The Relationship between Nearshore Wave Conditions and Coarse Clastic Beach Dynamics

Submitted by

Ralph Philip Brayne

to the University of Exeter

as a thesis for the degree of Doctor of Philosophy in Physical Geography

in April 2015

I certify that all material in this thesis which is not my own work has been identified and that no material has previously been submitted and approved for the award of a degree by this or any other University.

…….....

Abstract

Beaches composed of pebble to boulder-sized material are a common feature of rocky coastlines globally and provide effective protection against wave attack. However difficulties with the proximal deployment of wave gauges and measuring the transport of coarse clasts in the field has limited research in this area. The overarching aim of this thesis is to use contemporary 'off-the-shelf' technology in a series of interlinked, field-based experiments to improve quantitative understanding of relationship between coarse clastic beach dynamics and the nearshore wave conditions.

In the first of the empirical chapters (Chapter 3), indigenous clasts implanted with motion loggers provided a unique insight into the threshold-entrainment within the littoral zone on: (1) an exposed macro-tidal field site in Abbotsham, UK and; (2) a fetch-limited system in Flathead Lake, USA. The threshold-entrainment was positively related to the power of waves that prevailed over the hour-long experiment and accurately predicted with the equations of Lorang (2000). The relationship between clast mass and power of individual incident waves linked to each entrainment event was more complex. There was the propensity of large clasts to occasionally become entrained by exceedingly weak waves. The processes behind this result remain unclear.

Comprehensive experiments measuring variability in the concurrent wave conditions along the inner shore platform and offshore are presented in Chapter 4, along with daily longshore clast displacement and depth of activation measurements across the adjacent coarse clastic beach at Abbotsham. The longshore transport rate varies in concert with the longshore component of wave power, which is dependent on interactions between incident waves and shore platform morphology. These findings are used in Chapter 5 to model the (positive) longshore flux of clastic material towards the economically-valuable natural barrier, which has diminished in recent years. It was found that a disproportionately large fraction of positive transport was generated by storm events, the effectiveness of which was moderated by water depth. Net annual positive transport was predicted to increase with sea level rise and storminess. However, the increased influx was small in comparison to the volume of the barriers itself, and therefore unlikely to halt, or ameliorate future degradation.

The experiments presented in this thesis provide new insight into nearshore wave transformations and the relationship between wave properties and clast transport at a time when sea level rise and the potential increase in storminess is threatening coastlines globally.

Acknowledgements

There are a few of people I would like to thank for their contributions and support throughout the PhD process. I have been very lucky to have three wonderful supervisors; Dr Larissa Naylor, Dr Liam Reinhardt and Dr Mark Lorang. I thank Larissa for envisaging and securing the PhD position in the first instance. Larissa's enthusiasm, ideas and consistent support has been a big help throughout the project and made my PhD a great learning experience. Liam has not only spent many, and often consecutive, hours discussing work, ideas and progress, he has always provided his undivided attention, often at the 'drop of a hat', to each of the many and varied challenges for which I have sought his advice. For this I am hugely grateful. I would like to thank Mark for his detailed support and enthusiasm throughout the project. Mark funded much of the Flathead Lake field work and he and his family made my two trips to Montana huge fun. Mark has also shown belief in me and my work and has presented me with some very memorable opportunities. I would also like to express my gratitude to Professor Chris Caseldine for his academic advice during the final stages of the write-up.

I wish to thank Andrew Bell for his invaluable local knowledge and help with field work. Moreover, I thank Andy and his partner, Sarah Fellgate, for their stunning generosity during my UK field work. Not only did they house and feed me during each of my many field visits, they treated me as a family member. A large fraction of the empirical data that underpins this thesis was only made possible through their charity. I thank Chris Gottschalk for his technological support. Chris has not only provided me with code to process raw outputs from the pressure transducers, his skilful troubleshooting has fixed numerous computing and instrument issues.

I would finally like to thank my family for their consistent support throughout the PhD process, and in particular my dad, Peter, for his endless enthusiasm and his advice. Finally, I would like to thank my partner, Katharina, for her love and support throughout the PhD process.

Table of Contents

List of Tables

List of Figures

Lettering

Acronyms	
CCB	Coarse Clastic Beach
CCO	Channel Coast Observatory
DGPS	Differential Global Positioning System
DoA	Depth of Activation
LSD	Longshore Displacement
LSTR	Longshore Transport Rate
MAVS	Modular Acoustic Velocity Sensor
MHWN	Mean High Water Neap
MHWS	Mean High Water Spring
ML clast	Motion Logger Clast
MLWN	Mean Low Water Neap
MLWS	Mean Low Water Spring
MSL	Mean Sea Level
RFID	Radio Frequency Identification
SSG	Smart Sand Grain
UTC	Universal Coordinated Time
Symbols	
ξ	Surf similarity parameter
α	Wave approach angle
α_1	Clast shape factor
α_{M0}	Mean wave approach angle: Offshore
α_{Ms}	Mean wave approach angle: South shore platform position
a'	Beach porosity
C_g	Wave group velocity
C_r	Swash reduction faction
δ_I	Uncertainty associated with locating the position of an RFID clast
δ_m	Uncertainty associated with measuring the position of an RFID clast
δ_S	Uncertainty associated with the mean displacement of the RFID sample
δ_{TC}	Total uncertainty associated with the displacement of an RFID clast
d	Depth of Activation
D	Clast diameter
D_{50}	Intermediate clast diameter
D_{50O}	Intermediate diameter of clasts used to extrapolate K
D_{50P}	Intermediate diameter of clasts of the submersed beach
E	Wave energy
E_{HSb}	Wave energy: Based on breaker height
E_{Ru}	Wave energy: Based on wave run-up
f	Wave frequency
f_{BF}	Friction factor: Beach face
F_{drg}	Fluid drag force
F_{iwt}	Immersed weight force
F_{wav}	Wave force

g	Acceleration due to gravity
h	Water depth
H	Wave height
h_b	Water depth: Breaker position
h_C	Water depth: Central shore platform
h_{MAVS}	Water depth at the position of the MAVS at Flathead Lake
H_{rms}	Root mean squared wave height
H_S	Significant wave height
H_{S0}	Significant wave height: Offshore
H_{Sb}	Significant breaker height
H_{Sc}	Significant wave height: Central shore platform position
H_{Sn}	Significant wave height: North shore platform position
H_{Ss}	Significant wave height: South shore platform position
h_T	Tidal elevation
I_{LS}	Longshore immersed weight transport rate
I_t	Immersion time
κ	Breaker index
k	Wavenumber
K	Correlation coefficient: Longshore transport
K_D	Stability coefficient: Hudson Formula
K_P	Variable correlation coefficient: Longshore transport
K_r	Stability coefficient: Lorang equations
λ_0	Wavelength: Offshore
λ_P	Peak wavelength
λ_{P0}	Peak wavelength: Offshore
M_{Ru}	Critical entrainment mass: Based on wave swash
M_{HSb}	Critical entrainment mass: Based on breaker height
n	Number of clasts within the sample
φ	Pivoting angle
P	Wave power
P_0	Wave power: Offshore
P_c	Wave power: Central shore platform position
P_{LS}	Longshore component of wave power
P_{LSs}	Longshore component of wave power: South shore platform position
P-value	Probability of the relationship given the null hypothesis
Q_{LS}	Longshore volumetric transport rate
ρ_s	Clast density
ρ_w	Water density
R_u	Run-up elevations
$R_{u2\%}$	2% exceedance run-up elevation
θ	Beach Slope
Θ	Shields parameter
τ	Shear stress
τ_{BF}	Shear stress applied to the beach face
t	Time taken
T	Wave period

T_P	Peak wave period
T_{P0}	Peak wave period: Offshore
U	North component of fluid velocity
$\bar{U}$	Mean longshore displacement of clasts
U_{avg}	Average swash velocity
U_{max}	Maximum swash velocity
V	East component of fluid velocity
w	Width of beach over which clasts were transported
W	Vertical component of fluid velocity
X	Horizontal swash excursion

1 : Thesis Structure, Background and Aims

1.1 Thesis Structure

This thesis is divided into six chapters. Chapter 1 (this chapter) serves as a preface to the thesis in which (1) the thesis structure and (2) background information contextualising the following research are described, and (3) specific thesis aims defined. It is emphasised that the background section (1.2) in this chapter serves only as an overview of the dynamics of coarse clastic beaches. Focussed literature reviews for each specific research topic are located at the beginning of the empirical chapters (3 to 5).

Chapter 2 presents a physical description of the two contrasting beaches on which field experiments were conducted. The empirical portion of the thesis is organised with respect to the specific research areas, each of which are addressed in a designated, self-titled chapter. The three empirical chapters are structured in paper form, and begin with a focussed introductory review, followed by aims, methods, results, discussion and conclusion sections. Chapter 6 includes a synthesis of all of the thesis results and the final thesis conclusions.

Chapter	Title
1	Thesis Structure, Background and Aims
2	Field Sites Description
3	The Threshold-entrainment of Surficial Beach Clasts: Observations and Predictions
4	Shore Platform Control on Nearshore Wave Properties and Longshore Transport
5	Importance of Storm Events and Mean Sea Level on the Longshore Transport Rate at Abbotsham Beach and Implications for Future Nourishment of the Pebble Ridge
6	Synthesis and Conclusions

Table 1.1: Thesis Chapters.

1.2 Background

1.2.1 Introduction

Coastlines globally are at increased risk of erosion as a result of climate change (IPCC, 2007, 2013). Global sea level rise, resulting from thermal expansion of oceanic waters and the melting of terrestrial-based ice, will increase the exposure of coastlines to wave impact and the risk of inundation (e.g. Lorang & Stanford, 1993; MacDonald & O'Connor, 1996; Chini et al., 2010). In addition, climate change has been linked to a recent increase in the height and period of waves in a number of regions (e.g. Bacon & Carter, 1991, 1993; Bouws et al., 1996; Kushnir et al., 1997; Weiss et al., 2005; Wolf & Woolf, 2006; Dodet et al., 2010; Hemer et al., 2013). The combined effects of sea level rise and increased storminess will mean all forms of coastal defence systems will be increasingly relied upon. However, a lack of research into dynamics of coarse clastic beaches (CCBs) means the evolution of these systems in response to a change in the hydrodynamic forcing is poorly understood. Given this context, Paris et al. (2011) call for an increase in storm-based studies to improve understanding of how CCBs might respond to future conditions.

Coarse deposits comprised of pebble to boulder-sized clasts (as defined by Blair & McPherson, 1999) are a common feature of rocky coastlines globally (Nott, 2003a). They exist in a range of geomorphic settings (see Etienne & Paris, 2010; Paris et al., 2011) and are particularly prevalent at higher latitudes. Whilst coarse clastic beaches and barriers have social and economic value as natural sea defence systems (Lorang, 2000), cobbles and boulders emplaced on high cliff tops and at an extensive distance inland are important sedimentary signatures, and provide information about the magnitude of extreme palaeo-waves (e.g. Nott, 2003a).

Understanding the resilience of coarse deposits is therefore of practical importance to assess the: (1) vulnerability of a coastline to erosion and inundation and; (2) risks imposed by catastrophic wave events to coastal inhabitants. This thesis is concerned with the former of these two categories which is focused on littoral and beach processes. However, the vast majority of investigative work into sediment dynamics within the littoral zone has focused on sandy beaches (see Figure 1.1). Furthermore, until recently no detailed

common terminology existed to refer to clasts with an intermediate diameter greater than 2 mm (Blair & McPherson, 1999; see Table 1.2).

Table 1.2: Clast size grading as defined by Blair & McPherson (1999). A 'coarse clast' is considered here to have a b-axis greater than 2 mm. The size categories addressed in this thesis are shaded in red. Figure adapted from Blair & McPherson (1999).

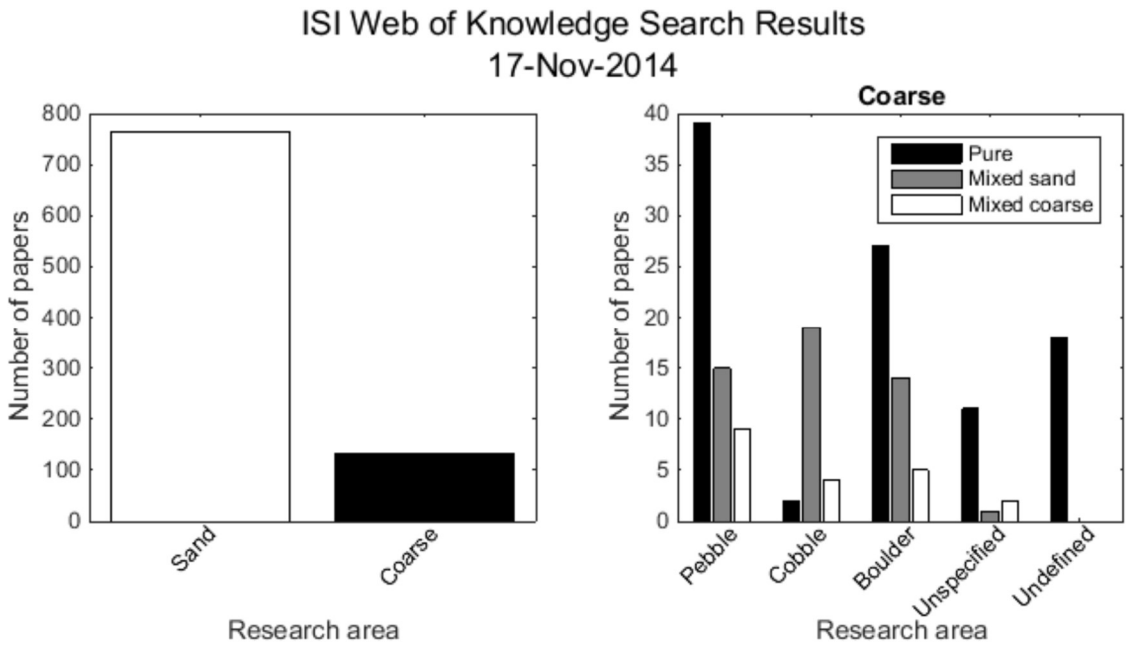

Figure 1.1: Number of found scientific papers versus sediment size. Right: 'Unspecified' refers to papers concerned with coarse clasts (as defined by Blair & McPherson, 1999) in general, and 'Undefined' to papers in which clast size could not be defined. Notably, papers composed of a mixture of coarse size grades can satisfy more than one category and hence the sum of papers in the right graph is greater than the total number of coarse papers identified (left graph). The graphs were constructed from the results from refined ISI Web of Knowledge searches, based on the Boolean criteria in Appendix 1, and conducted on 17 Nov 2014.

The beach and barrier literature address aspects including structure and organisation (e.g. Oak, 1984; Isla, 1993; Bluck, 1999, 2011; Orford et al., 2002), various cross-shore (e.g. Oak, 1984, 1986; Lorang, 2000, 2002; Masselink & Li, 2001; Austin & Masselink, 2006; Masselink et al., 2010; Bertoni & Sarti, 2011; Chen et al., 2011; Lee et al., 2007a; Matias et al., 2012; Williams et al., 2012; Jamal et al., 2014; Almeida et al., 2015) and longshore (e.g. Carr, 1971; Hatorri & Suzuki, 1978; Van Wellen et al., 2000; Ruiz de Alagria-Azaburu & Masselink, 2010) morphodynamic processes, in addition to various hydrodynamic processes (e.g. Horn, 2002, 2006; Horn & Li, 2006; Lee et al., 2007a; Matias et al., 2012).

However, the energetic and hostile conditions typical of CCBs make the deployment of scientific equipment difficult because of the risk of being impacted by mobile clasts or swept away. Meanwhile, the inability to generate large-amplitude, low-frequency waves in an artificial tank means the applicability of laboratory experiments is limited. Much of the field work into the dynamics of CCBs consider their morphodynamics over an extended period of time (e.g. Bluck, 1967, 2011; Johnston, 2001; Orford et al., 2002; Bertoni &

Sarti, 2011; Orford & Anthony, 2011), and conceptual understanding of the processes causing the observed response is greatly supplemented by numerical studies (Lorang, 2000, 2002; Van Wellen et al., 2000; Masselink & Li, 2001; Lee et al., 2007a; Chen et al., 2011; Williams et al., 2012; Jamal et al., 2014).

Recent improvements to monitoring equipment have enabled researchers to obtain detailed, event- (e.g. Carr, 1971, Hatorri & Suzuki, 1978; Oak,1986; Ruiz de Alagria-Azaburu & Masselink, 2010; Poate et al., 2013) and process-based (e.g. Foot & Horn, 1999; Horn et al., 2002; Austin & Masselink, 2005, Horn 2006; Horn & Li, 2006; Pedrozo-Acuña et al., 2008; Masselink et al., 2010; Poate et al., 2013; Almeida et al., 2014) field measurements occurring over a temporal frequency of days and seconds respectively. However, measuring morphodynamic processes of CCBs remains a challenge and general understanding of these diverse features greatly lags that of their sandy counterparts.

1.2.2 A Conceptual Model of Coarse Clastic Beach Dynamics

Coarse clastic beaches differ in a number of ways from those composed of sand. These peculiarities modify the nearshore hydrodynamics and therefore clast transport, making CCBs dynamically-distinct from sand beaches (Buscombe & Masselink, 2006). Perhaps the most notable difference between CCBs and sand beaches is the size of the constituent clasts. For a clast to become entrained, the hydrodynamic force must exceed its immersed weight (Shields, 1936: see Chapter 3 for full review on the threshold-entrainment). Coarse clasts that compose CCBs require large hydrodynamic forces to become entrained. It is generally understood that the exertion of such forces is unique to shoaling waves and, unlike sand beaches, CCBs are generally unaffected by residual currents (e.g. Lorang, 2000). Furthermore, the large interstitial spaces between coarse clasts make the beach matrix highly porous. The resulting hydraulically conductive beach face enhances asymmetries between the up-rush and backwash and enables CCBs to maintain extremely steep slopes (Bagnold 1940; Packwood, 1983; Masselink & Li, 2001), which in turn dominates the nearshore hydrodynamics and clast transport.

This section provides an overview of the interrelationship between the hydro- and morpho-dynamics of CCBs. It should be noted that unlike sand systems, coarse clasts can be organised into barriers as well as beaches. Where barriers are characterised by a landward-dipping back-beach, beaches are backed by a stable feature, which inhibits rollover. Orford (2002) noted all barriers have beach components, but all beaches are not necessarily part of a barrier system. The following section does not distinguish between beaches and barriers, but for brevity considers the dynamics of the two features together.

1.2.2.1 Process Zones & Beach Morphodynamics

Near-bed fluid motions generated by waves are closely related to the shoaling process and hence process zone on the beach (e.g. Pedrozo-Acuña et al., 2008). For this reason, clasts on CCBs tend to be shape- and size-sorted according to process zone (e.g. Bluck, 1967, 2011; Orford, 1975). Clast transport and beach morphodynamics are therefore considered here with respect to each process zone.

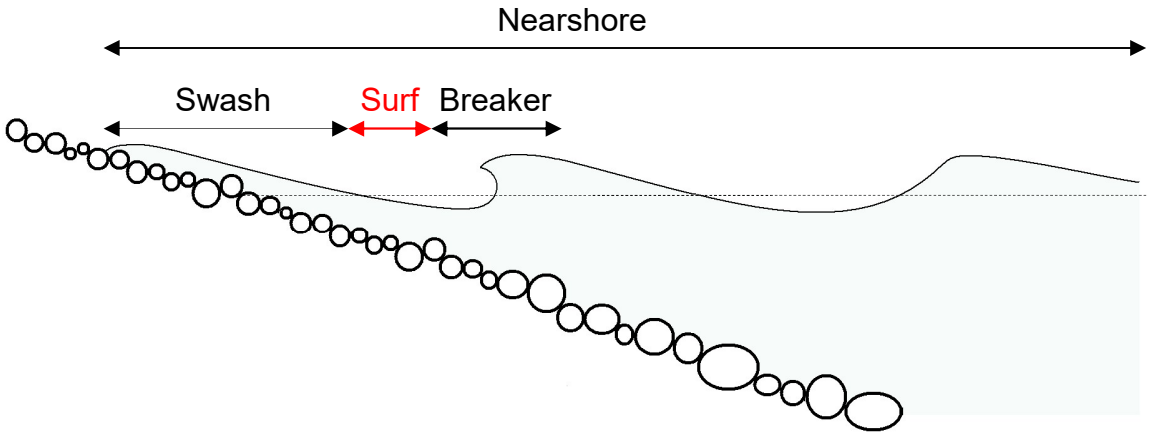

Figure 1.2: Diagram of process zones on a coarse clastic beach. Coarse clastic beaches often lack an effective surf zone (red) and the breaker conjoins the swash zone.

The forward-pitching and subsequent collapse of the waves in the breaker zone generates turbulent fluid motions. The characteristics of wave breaking is important for two reasons because it: (1) determines the forces exerted on clasts, and therefore clast transport within the breaker zone (e.g. Pedrozo-Acuña et al., 2008) and; (2) controls the dissipation of wave energy and therefore surf and swash competence (e.g. Battjes, 1974; Holman, 1986; Hughes, 2004; Hsu et al., 2012). Three discrete breaker types are identified

when transitioning from a dissipative to reflective setup, namely; spilling, plunging and surging. The breaker type can be expressed with respect to the offshore wave steepness and beach slope to give a 'Surf Similarity' parameter (Battjes, 1974):

$$\xi = \frac{tan\theta}{\sqrt{H_0/\lambda_0}} \qquad \textbf{Equation 1.1}$$

where Θ is the beach slope, H_0 is the offshore wave height and λ_0 is the deep water wavelength. The steepness of the beach face means CCBs tend to be characterised by plunging ($0.5 < \xi < 3.3$) and surging ($\xi > 3.3$) breakers (Battjes, 1974; Pedrozo-Acuña et al., 2008), which are described below.

The crest of a plunging wave becomes over-steepened and is projected forward before impacting with the water surface in front of the wave. This process results in an overturning, aerated and highly turbulent wave bore (Komar, 1997). Pedrozo-Acuña et al. (2010) measured extremely high impulsive pressures generated by plunging breakers impinging on a gravel beach. The pressure impulses were attributed to the significant vertical velocities associated with plunging breakers. They proposed the plunging breakers can fluidise the beach matrix and momentarily compromise the shear strength of the beach. In these circumstances, clasts are entrained more readily and Pedrozo-Acuña et al. (2008) suggested the process would ultimately enhance the onshore transport of clasts with the wave swash. The rotational and energetic nature of plunging breakers might aid sediment transport in the breaker zone, however the rapid dissipation of energy constrains the competence of the wave bore in the surf and swash zone (e.g. Battjes, 1974; Holman, 1986; Hughes, 2004; Hsu et al., 2012).

Surging breakers are the most reflective of the breaker types and are characterised by minimal turbulence and energy dissipation. Surging waves lack the rotation associated with plunging waves, but can still apply large forces on clasts. The minimal turbulence that is characteristic of surging waves means energy is conserved resulting in relatively competent wave swash. In fact, for given offshore wave steepness and beach slope, the largest run-up elevations are associated with surging breakers (Battjes, 1974; Holman, 1986; Hughes, 2004; Hsu et al., 2012).

The surf zone on a low-gradient sand beach can extend for hundreds of meters and dominate its nearshore sediment budget (Komar, 1997). Conversely, the steep profile of CCBs results in the compression of the process zones. Indeed, CCBs generally lack an effective surf zone (Orford, 2002), and the breaker zone conjoins the swash zone. The majority of transport occurs on CCBs within the area between the mean surface elevation and maximum run-up on the beach, termed the swash zone (Van Wellen et al., 2000). The characteristics of the wave swash are therefore important to the morphodynamics of CCBs (Lorang, 2002). Yet, due to the Lagrangian nature of the swash zone and the inability to monitor swash dynamics with traditional fixed instruments, it is the least well-understood of the process zones (Puleo et al., 2000).

The powerful up-rush of wave swash exerts large forces on surficial clasts and can mobilise them upslope through sliding, rolling or saltating. The competence of the up-rush is reduced as it: (1) decelerates due to gravity; (2) loses energy to friction with the beach face, and; (3) loses mass as fluid percolates into the porous beach face. The backwash is aided by gravity and can down-comb clasts, which have reduced pivoting angles in the seaward direction. However, fluid loss into the beach matrix can be so large that it is difficult to visually define the backwash on the beach surface. The combination of wave asymmetries and fluid loss into the beach face results in the wave swash being more competent than the backwash. Consequently, clasts are more likely to be transported onshore, against the beach slope (Lorang, 2000). This fundamental bias is a key driver in the development of CCBs and is the reason the beach exists in the first instance.

Swash asymmetries are also considered to contribute to the cross-shore size- and shape-sorting of clasts commonly exhibited by CCBs (e.g. Bluck, 1967, 2011; Orford, 1975). Orford (1975) noted that storm conditions result in an onshore transport bias at the beach crest and the localised retention of coarse clasts, and an offshore bias at the beach base and the accretion of fine and coarse clasts alike. Whereas in calm conditions, coarse clasts are left in place and the fines are transported furthest up the beach. The interplay between storm and calm conditions results in the coarsest clasts being located at the seaward margin and beach crest, with a central band of fine clasts between the two.

Bluck (1967) observed disc-shaped clasts to move up the beach more easily with the wave swash, and the effective down-combing of prolate- and roller-shaped clasts by the backwash. This process sorts clasts so that the crest is populated with discs and beach base with prolates and rollers. However, the findings of Oak (1986) indicate the cross-shore size and shape sorting described by Orford (1975) and Bluck (1967) are absent from beaches comprised primarily of boulder-sized clasts. Oak (1986) argued that 'boulder beaches' are distinguishable from other CCBs by the following properties: (1) an up-beach fining of clasts, (2) an abundance of broken clasts, (3) a positively-skewed size distribution of clasts, (4) an absence of sphericity grading and (5) a low foreshore gradient.

Longshore features, such as berms have also been identified as being interrelated with the characteristics of the wave swash. Berms refer to a break in the beach slope due to the accretion of coarser clasts at the maximum run-up elevation. They form through positive feedback between the hydrodynamics and clast transport, which is briefly described here: Towards the limit of swash run-up, the competence of the flow is diminished as fluid is lost through infiltration into the beach matrix. Coarse clasts are rapidly deposited, but the weaker back-wash is still capable of removing fine clasts down slope. The resulting steep, armoured and highly-porous deposit of coarse clasts further enhances the causative asymmetries between the up-rush and back-wash, and hence promotes the continuation of the depositional process. Over successive tidal cycles this process leads to the gradual onshore migration and accretion of the berm (Duncan, 1964; Buscombe & Masselink, 2006).

The maximum shoreward extent of wave swash not only determines the extent of the beach that is subjected to wave action, but the exceedance of the shoreward position of the beach crest by the wave swash can result in the accretion or erosion of material at the beach crest. Where wave swash exceeds the beach crest, one of three things can happen:

(1) if the competence of the wave swash is such that is unable to transport clasts from the beach face onto the beach crest, the crest will be neither built nor eroded;

(2) if the swash can mobilise and transport sediment from the beach face and deposit them on the beach crest, the crest height will increase (overtopping);

(3) if, however, the swash is competent enough to mobilise sediment at the beach crest, the beach crest will be eroded and material deposited at the back beach (overwashing). This process results in a lowering of the crest elevation and, for unconstrained barrier systems, results in the net transport of material shoreward in a process termed 'rollover' (e.g. Carter & Orford, 1993).

The morphodynamics of CCBs are further complicated by the periodic fluctuation of the sea surface elevation as a function of tides. Importantly, the tides vary the elevation of the swash zone and hence are a key determinant of the run-up elevation (Lorang, 2002; Bluck, 2011). Bluck (2011) demonstrated the dependence of the structure of CCBs on the tide and suggested the width and height of CCBs is strongly related to tidal range. He showed the cross-shore size- and shape-sorting of clasts was maintained at contrasting field sites, but the zonal width was elongated by the tidal range.

Where the CCB extends well below chart datum, the tides may act simply to vary the portion of beach subjected to wave action at any given instant. Alternatively, the tidal state on beaches fronted by a low gradient shore platform can also moderate the amount and form of wave energy reaching the beach face (see Chapter 4 for full review on shore platform control on wave transformations). A number of recent field studies have demonstrated the considerable attenuation of wave energy across horizontal and sloping shore platforms (e.g. Ogawa et al., 2011, 2012; Beetham & Kench, 2011; Bezerra et al., 2011; Marshall & Stephenson, 2011; Ogawa, 2013), which effectively moderate the amount of wave energy available to do geomorphic work at the shoreline (Ogawa, 2013).

The described morphodynamic processes have, so far, only been considered in the cross-shore plane. However, it is often the case that waves approach the beach at an oblique angle, which can transport material in the longshore plane (e.g. Carr, 1971, Hatorri & Suzuki, 1978; Oak, 1986; Ruiz de Alagria-Azaburu & Masselink, 2010). The steep profile of the CCB means wave refraction is

minimised (Van Wellen et al., 2000). Instead of sediment transport being determined by a steady, longshore current generated by the refraction of oblique wave fronts (as is the case on sandy beaches; Longuet-Higgins, 1970; Komar, 1997), mobile clasts are transported obliquely up the beach with the wave swash before being transported seaward within the backwash. The cumulative effect of the resulting saw-tooth transport pathway is the net transport of clasts along the beach (Sherman & Nordstrom, 1985). The longshore transport of clastic material can dominate the transport budget and morphology of coastlines (Komar, 1997; see Chapter 4 for a detailed review of longshore transport on CCBs).

1.3 Thesis Aims

The field work presented in this thesis takes advantage of newly-available, 'off-the-shelf' technology to advance quantitative understanding of the interrelationship between nearshore processes and the dynamics of beaches composed of pebble- to boulder-sized clasts. As described in section 1.2, the dynamics of coarse clastic beaches are complex and dependent on the interrelationships between hydrodynamic, sediment transport and morphodynamic processes. Masselink & Puleo (2006) illustrated the interlinked nature of variables with a conceptual diagram (see Figure 1.3).

Figure 1.3: A conceptual diagram of the interrelationship between the hydrodynamic, clast transport and morphodynamic processes of coarse clastic beaches. Each of the physical components addressed within each thesis aim is highlighted accordingly. Red, green and blue represent thesis research aims 1, 2 and 3 respectively. Figure adapted from Masselink & Puleo (2006).

The thesis research aims to improve understanding of the relationship between the nearshore wave mechanism and clast transport on coarse clastic beaches. This broad thesis aim is divided into three specific research areas that address a range of physical processes highlighted above. Figure 1.3 indicates the particular processes which form the focus of each of the research aims/empirical chapter, which are described below.

1. To obtain process-based field measurements of the threshold-entrainment of surficial clasts in relation to the nearshore wave properties and compare these observations with pre-existing force-balance equations of Lorang (2000).

The threshold-entrainment of surficial clasts defines the morphodynamic threshold of the beach itself (e.g. Lorang, 2002). The ability to predict the mobility/stability of surficial clasts is therefore of practical use because it describes the resilience of a beach to wave action and possible erosion. The importance of the threshold-entrainment has motivated a number of researchers to derive predictive force-balance equations (e.g. SPM, 1984; Lorang, 2000; Nott, 2003a). Lorang (2000) derived the most detailed and applicable process-

based equations to predict: (1) the largest clast that will become entrained, and; (2) the smallest clast that will remain stable when acted upon by waves. However, a lack of relevant field data has meant these valuable equations have not been extensively tested (e.g. Oak, 1986; Lorang 2000), and their accuracy remains largely unknown. Chapter 3 presents novel Lagrangian field experiments that include the deployment of off-the-shelf motion loggers implanted within natural clasts to provide process-based measurements of the threshold-entrainment within the littoral zone. The observations are subsequently compared with the predictions made with the equations of Lorang (2000).

2. To quantify shore platform control on nearshore wave conditions at Abbotsham and its influence on the longshore transport rate on the adjacent coarse clastic beach.

Shore platforms are a major feature of rocky coastlines and represent an interface between incident waves and coastal cliffs or beaches (Kirk, 1977; Emery & Kuhn, 1982; Ogawa, 2013). A number of recent field studies have improved understanding of the relationship between wave attenuation and platform morphology (e.g. Ogawa et al., 2011, 2012; Beetham & Kench, 2011; Bezerra et al., 2011; Marshall & Stephenson, 2011; Ogawa, 2013). However, no one has yet linked variations in wave transformations across shore platforms to a particular geomorphic response. Meanwhile, relatively little research has been conducted into the longshore transport rate on coarse clastic beaches, which requires accurate measurement of the longshore displacement of clasts and the thickness of the mobile portion of the beach, which is especially difficult to obtain.

Chapter 4 first considers the influence of shore platform morphology on wave transformations and thus wave force acting on the adjacent beach. Here, wave properties measured by an offshore wave buoy are compared with concurrent measurements from three wave gauges deployed along an inner section of the intertidal shore platform (directly adjacent to the base of the CCB) in order to understand nearshore wave transformations as a function of platform morphology and resulting longshore variability in the wave force. Second, these data are considered with respect to daily field observation of the longshore

displacement of between 45 and 118 natural pebbles, cobbles and boulders, traced with Radio Frequency Identification (RFID) technology on the adjacent beach. Additional depth of activation measurements are presented and considered in terms of the power of incident waves at the inner shore platform. Lastly, the depth of activation findings are combined with the longshore displacement observations in order to estimate the longshore transport rate through Abbotsham beach.

3. To estimate the net annual longshore transport rate through Abbotsham beach and quantify the importance of storm events and mean sea level on this process, and the resulting implications for the future nourishment of the '*Pebble Ridge'.*

The longshore transport of greywacke clasts through Abbotsham beach (in North Devon, UK) is thought to be vital for the nourishment of the economically- and socially-valuable coarse clastic barrier (colloquially termed the 'Pebble Ridge') that protects the settlements of Westward Ho! and Northam Burrows (see section 2.2). Storminess within the northeast Atlantic has been observed to increase over the past 50 years (Bacon & Carter, 1991, 1993) and a number of reports predicted a continuation of this trend as a result of climate change (e.g. Bouws et al., 1996; Wolf & Woolf, 2006). Meanwhile, global sea level rise and the current isostatic adjustment of the UK is predicted to result in a rapid rise in mean sea level relative to Abbotsham (UKCP09, 2009). It is therefore important to understand the sensitivity of the beach to a change in storminess and sea level rise, and to consider how future variability might affect the rate of longshore transport toward the Pebble Ridge. A simple empirical model is developed in Chapter 5 to quantify the: (1) current net annual longshore transport rate towards the Pebble Ridge; (2) sensitivity of the net annual longshore transport rate to storm events, and; (3) sensitivity of the net annual longshore transport to mean sea level rise.

2 : Field Site Description

2.1 Introduction

The experiments presented within this thesis were conducted at two contrasting field sites. The principal field site for this project was a 250 m stretch of beach at Abbotsham, North Devon, UK. Here, experiments were conducted to address all research questions raised in this thesis, and the findings supplied to interested end users (The North Devon Biosphere Reserve and North Devon and Somerset Coastal Advisory Group) to help inform their management strategies. A number of smaller, detailed experiments were conducted at a secondary, contrasting beach on a freshwater lake in Montana, USA. Chapter 2 provides a description of the geographical setting, beach properties and wave climate at both field sites, with a particular emphasis on the origin and management issues of the wider coarse clastic system that Abbotsham beach comprises.

2.2 Abbotsham, North Devon, UK

2.2.1 Geomorphological Setting

The stretch of coastline between the mouth of the Taw-Torridge estuaries and Westward Ho! is low-lying and composed of estuarine clays (see Figure 2.1). The clay deposits within the intertidal zone form a low gradient foreshore, which is generally covered in a layer of sand (Keene, 1996). The back beach features developed sand dunes to the north and intertidal flats to the south. Between Westward Ho! and the Gore lie the elevated Bideford and Bude formations. Here, the carboniferous geology is characterised by steeply-dipping sandstone and shale (Arber, 1974). This stretch of coastline is fronted by a wide intertidal rocky shore platform, and backed by sea-cliffs of varying height.

Keene (1996) proposed the morphology south of Westward Ho! is the product of coastal processes and the local geology. He suggested much of the coastal features evident today were formed by wave action during the last interglacial period. The coastal features were subsequently covered in a layer of glacial till during the following ice age when sea level was much lower. The succeeding marine transgression, as a result of the current interglacial phase, has again exposed the relict coastline to wave action, which has cut the glacial till and thereby exposed the shore platform and formed sea cliffs. In a number of locations, extensive wave action has re-exposed the underlying carboniferous

formations. Of utmost importance for the current thesis research is the exposed sandstone cliffs at the Gore, beneath which lays the debris from one or more catastrophic cliff falls. It is these poorly sorted sandstones units that are thought to form the source of the coarse clastic system of greywacke clasts that extends 11.5 km along the Bideford Bay coastline.

2.2.2 The Bideford Bay Coarse Clastic System

Abbotsham beach comprises one section of an inter-/supra-tidal coarse clastic system, made up of pebble- to boulder-sized greywacke clasts. The morphology of the feature and large size of constituent clasts distinguishes this coarse clastic system from others in the UK (May, 2007), and *Natural England* has declared a section of the feature as a '*Site of Special Scientific Interest'*.

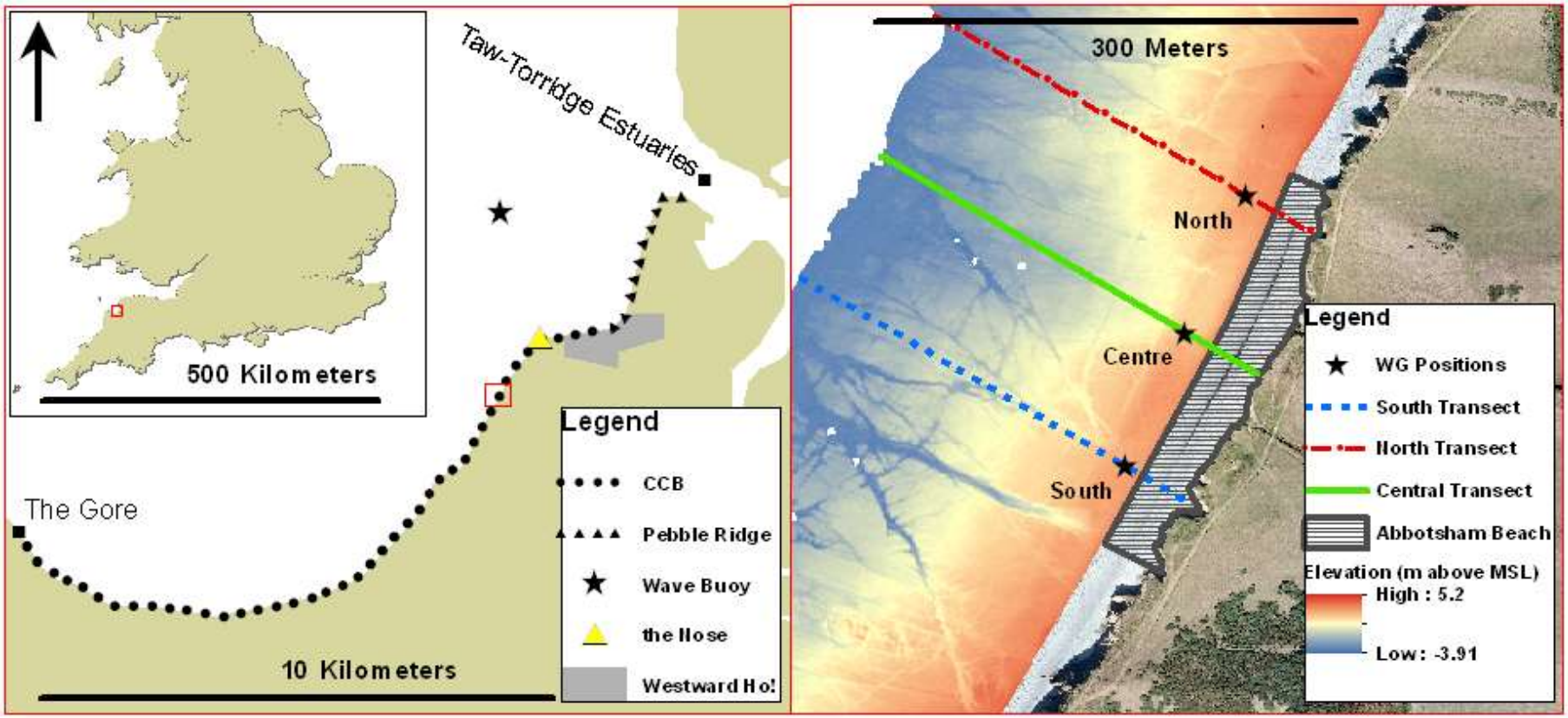

Figure 2.1: Map of Abbotsham beach and the surrounding area. Left: Map of Bideford Bay indicating the positions of the Bideford Bay wave buoy and field site (Abbotsham) with an inset showing their locations relative to the English and Welsh land mass. Right: An aerial view of the experimental beach displaying a true colour image of the CCB (grey) and shoreward land mass (green), and digital elevation map of the rocky shore platform. Three topographic transect lines are shown; these intersect the three positions in which wave gauges were deployed (black stars). Aerial image (2007) and LiDAR data (2010) used to construct these plots was obtained from the Channel Coastal Observatory (CCO).

Between *the Gore* and Westward Ho! (Approximately 11.5 km; see Figure 2.1), coarse clasts accumulate at the cliff-platform junction. Assemblages range from a thin scattering of cobbles and boulders, to beaches (such as that at Abbotsham) rising up to 8 m above the shore platform. Here, the glacial till cliffs form an irregular back beach with both outcrops and cliff debris regularly punctuating the clastic system.

Conversely, the 2.5 km stretch of coastline between Westward Ho! and the mouth of the Taw-Torridge Estuaries is low-lying. Here, clasts form a south-south-west/north-north-east aligned barrier, fronted by a low-gradient sandy beach and backed by low-lying marshland. Despite being colloquially termed the ‘Pebble Ridge’, the feature is actually composed of pebble- to boulder-sized clasts. The dimensions of the Pebble Ridge vary along the feature, with an approximate height and thickness of up to 7 m and 25 m respectively (Halcrow, 1980). Crow Point at the north of Northam Burrows represents the end of the coherent Pebble Ridge, beyond which lies the mouth to the Taw-Torridge Estuaries.

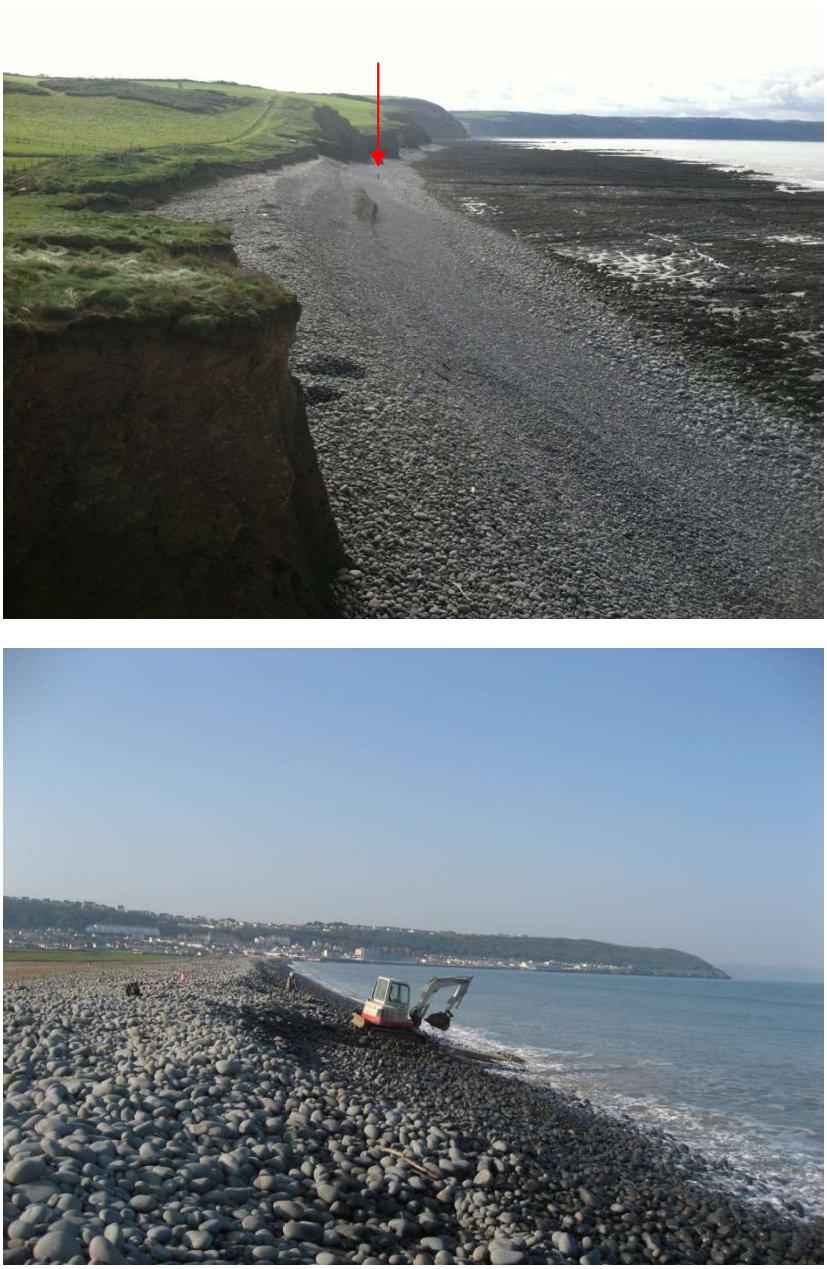

Figure 2.2: Images of the coarse clastic beach at Abbotsham (top) and Pebble Ridge (bottom). Top: The image of Abbotsham beach was taken at low tide, and the red arrow highlights the position of a person (for scale). Bottom: Image along the Pebble Ridge (at high tide) with the town of Westward Ho! and The Nose visible at the end of the feature. Note: The digger in the bottom image was laying down a walk-way across the Pebble Ridge.

2.2.3 System Origin

The most widely accepted hypothesis (i.e. Keene, 1996; Kirby, 1996; Pethick, 2007; Orford, 2005; May, 2007; Halcrow, 2008) is that the majority of greywacke material originated from a single source in the cliffs at the Gore. Keene (1996) suggested clastic material was released by a series of catastrophic cliff falls that occurred between the 16th and 17th century, and was subsequently transported northwards by wave action, forming the coarse clastic

feature that is evident today. This hypothesis is based on the lithological mismatch of the greywacke clasts with their surroundings in all areas except the cliffs at the southernmost extremity of the feature, the Gore. The hypothesis is in agreement with experimental evidence of Naylor et al. (2010), who documented the extensive northward displacement of 48 clasts over one month at the Nose under low to moderate wave conditions. Further evidence to support Keene's hypothesis is apparent in the progressive sorting and rounding of clasts when heading northward from the Gore (Stuart & Hookway, 1954).

2.2.4 System Evolution & Management Issues

The hypothesised origin of the Pebble Ridge implies it is a relatively contemporary and dynamic feature that is the product of an exhaustive supply of greywacke material from a southern source. This assumption is reflected by the findings of a number of studies that reported significant morphological changes in recent years (e.g. Stuart & Hookway, 1954; Halcrow, 1980, 2008). Keene (1996) monitored the time-varying position of the Pebble Ridge using a series of geo-rectified photographs taken during the 19th and 20th centuries. The most significant changes have been observed at its southern portion, which has retreated between 150 m and 200 m over the past 100 years. Meanwhile, clasts have accreted at the northern end of the feature, which has consequently prograded seaward. This process has resulted in the anti-clockwise rotation of Pebble Ridge as a whole (see Figure 2.3).

Keene (1996) proposed the documented retreat and rotation of the Pebble Ridge represents a general transformation from the past, well-nourished, drift alignment to a modern, unnourished, swash alignment. Notwithstanding the reduced source of material, Orford (2005) suggested the current disjointed positioning of the Pebble Ridge relative to the *Nose* (west of Westward Ho!; see Figure 2.1) has greatly-reduced (or even halted) nourishment, and the Nose now acts an impassable barrier to the northward conveyer of clasts.

Figure 2.3: (Top) Aerial and (Bottom) profile diagrams of the recent rotation and retreat of the Pebble Ridge. Top: aerial view of the recent anticlockwise rotation of the Pebble Ridge, from drift- to swash-alignment (Figure taken from Pethick, 2007). Bottom: Time-varying position of the southern portion of the ridge fronting Westward Ho! and Northam Burrows. Historic records have shown the southern portion of the ridge to have retreated almost 200 m shoreward between 1861 and 1947 (Figure adapted from May, 2007).

The long-term dynamics of the Pebble Ridge have important implications for Westward Ho!. A number of sea front businesses experienced temporary closures due to inundation and erosion when the ridge was breached by storm waves (Pers. Comm. Andrew Bell, Coordinator of the North Devon Biosphere Reserve, February 2014). Perhaps a more worrying consequence of the reducing capacity of the ridge to defend the backshore from wave attack is the potential inundation of an old landfill site situated inland of the Pebble Ridge at Northam Burrows, and subsequent release of pollutants into the Taw and Torridge estuaries.

A number of researchers have considered the future of the Pebble Ridge in light of a reduction in nourishment and increase in relative sea level (e.g. Orford, 2005; Pethick, 2007; Halcrow, 2008). Pethick (2007) predicted the rate of retreat at the southern portion of the ridge will be sensitive to sea level rise and (given the sea level projections of DEFRA, 2006) estimated it to increase from the current 1 m to 2 m per annum up to 4 m per annum by 2100. Slade (1962) pointed out the southern portion of the Pebble Ridge must recede a further 130 m until the feature is swash-aligned. Once at this orientation, longshore transport will be minimal (Pethick, 2007). Such change is likely to have a serious impact on the town of Westward Ho!, which will experience significant erosion and become increasingly exposed to large Atlantic storm waves.

Attempts have been made by the local authorities to maintain the Pebble Ridge and mitigate against erosion. In 1947, three timber groynes were built just north of Westward Ho! and were reported to have been “fairly effective” in slowing the local rate of retreat (Halcrow, 1980). In 1974 a complete set of large-scale, cross-shore gabion groynes were implemented across a 1500 m stretch of the ridge to aid the local retention of clasts. The success of the groynes was unclear due to the simultaneous re-nourishment scheme (described below). Despite the southern end of the ridge experiencing minimal erosion in the years following, erosion rates at the north end of the ridge were more pronounced. It was later hypothesised that this could have been due to a reduction in the flux of material towards the north as a direct consequence of the presence of the gabion groynes (Halcrow, 1980). The life-span of the groynes was limited and by 1980 they had been completely demolished by natural processes.

Other management strategies have included the artificial nourishment of the Pebble Ridge with non-local and recycled material. Additional rock armouring was also implemented to protect the old landfill site (Northam Burrows) against wave action. The large-scale recycling of clastic material at the northernmost end of the feature was conducted on two occasions, in 1978 and 1979 respectively. Here, an unknown quantity of material was recycled from the north to the south of the Pebble Ridge (Halcrow, 1980). A subsequent programme of material recycling from Grey Sand Hill to the southern ridge was started in 1981, but has since ceased (Halcrow, 2008). It is estimated that between 1000

m^3 and 6000 m^3 of coarse clastic material was redistributed by trucks to counter longshore transport on any given year (Halcrow, 2008).

Despite an earlier call for the implementation of proactive defence schemes (e.g. Halcrow, 1980), all such efforts have now stopped and any intervention along the Pebble Ridge is solely reparation in response to significant storm damage (Pers. Comm. Andy Bell, Coordinator of the North Devon Biosphere Reserve, November 2011). Orford (2005) advised against resuming the past 'hold-the-line' approach, commenting that resisting the natural retreat of the Pebble Ridge will result in it being subjected to an increased wave force as the dissipation of wave energy is reduced with sea level rise. He suggested a 'hold the line' approach would ultimately lead to enhanced longshore transport and therefore loss of material northward into the mouth of the Taw-Torridge Estuaries. Instead, the consensus of the most recent management reviews (e.g. Orford, 2005; Pethick, 2007; Halcrow, 2008) is to treat the Pebble Ridge as a transient feature and allow it to retreat naturally. Orford (2005) stated that, if necessary, reparation work should recycle material to the back of the ridge to reduce the risk of it being swept into the estuary.

In the long term, the Pebble Ridge is predicted to lose its coherent structure as its volume diminishes and longshore transport reduces (due to the general swash alignment and lack of available material for transport). The rate of degradation will depend on future sea level rise, the wave climate and nourishment rate. The lack of studies monitoring the transport of coarse clastic material in Bideford Bay has meant obtaining such information was highlighted by Orford (2005) in internal report to *English Nature* as a primary recommendation to assist the coastal advisory group in developing future management strategies.

2.2.5 Abbotsham Beach

Abbotsham beach was chosen as the site at which to conduct experiments for the following reasons: Abbotsham beach is strategically situated between the widely-accepted source of clastic material (the Gore) and the Pebble Ridge. It follows that a significant proportion, or perhaps all, clasts that comprise the Pebble Ridge had at some point migrated through Abbotsham beach. The beach at Abbotsham was uninterrupted by cliff debris and outcrops and

relatively uniform in composition. Unlike the Pebble Ridge, human activity at Abbotsham was minimal and it is fronted by a rocky shore platform upon which wave gauges could be secured. Moreover, the beach at Abbotsham is backed by low cliffs with a number of small bluffs well-suited for mounting the DGPS base station. Despite the relative isolation of Abbotsham, it is the most accessible part of the coastline between the Gore and the Nose.

Figure 2.4: Images of Abbotsham beach. Top: Image of the coarse clastic beach at Abbotsham displaying an exposed cliff-top bluff on which the DGPS was mounted. Bottom: Image of the experimental beach at Abbotsham (facing south). The fronting rocky shore platform (right) and backing cliffs (left) are clearly visible.

2.2.6 Shore Platform Morphology

The shore platform fronting the experimental beach is approximately 225 m wide and has a mean elevation of -1.1 m and mean cross-shore gradient of 2.1 %. The shore platform therefore corresponds with the 'Type A' of the morphological categories specified by Sunamura (1992), which is characterised by a seaward aspect (see Figure 2.5). The platform exhibits small-scale (< 1 m) faults and gullies owing to the differential weathering of its mudstone, siltstone, sandstone and feldspar components (Keene, 1996). Also noticeable are

horizontally-extensive, yet topographically-small-scale (< 2 m) anomalies. Crucially, an embayment can be seen to intersect the central beach (central transect) with the shore platform elevated to the north and south (see Figure 2.1 & Figure 2.5).

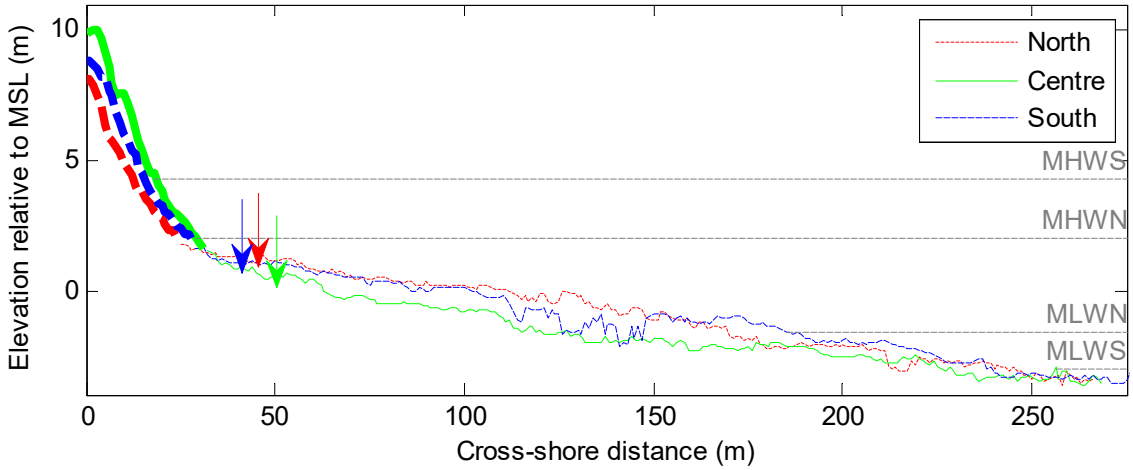

Figure 2.5: Profile of the CCB and shore platform across the three cross-shore transects indicated in Figure 2.1. The shore platform is indicated with thin lines, the CCB with thick lines, and cross-shore position in which wave gauges were deployed is marked with arrows. The mean high and low tide elevation during spring and neap conditions are indicated with the horizontal dashed lines. LiDAR data used to construct these plots was obtained from the CCO and the tidal elevations obtained from the Reeds Nautical Almanac.

2.2.6.2 Beach Fabric

The beach fabric description is based on the properties of the ~400 surficial clasts that were systematically sampled over the duration of the field work at Abbotsham (see section 4.5.1 for full explanation of the sampling method). Abbotsham beach is composed of pebble- to boulder-sized clasts, which were most clearly sorted according to their cross-shore position. The mean B-axis diameter of surficial clasts found on the beach face was 0.14 m (a medium-sized cobble).

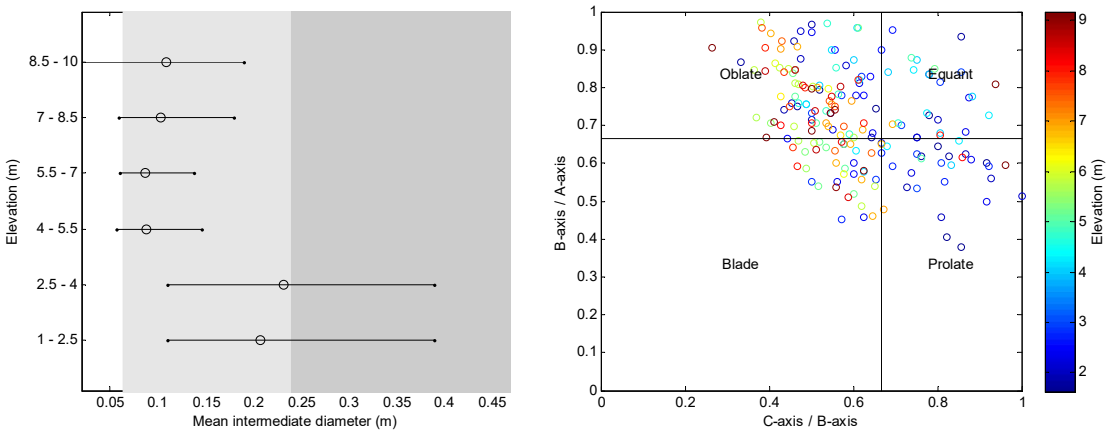

Figure 2.6: Elevation versus mean intermediate diameter (left), and Zingg plot of shape (right) of clasts on Abbotsham beach. Left: Mean intermediate diameter of the clasts versus elevation on the beach. The shading indicates the size categorisation (white = pebble, light grey = cobble, dark grey = boulder) and horizontal bars represent the maximum and minimum values in the zone. Between 20 and 40 clasts were included in each elevation bin. Right: Zingg plot of clast shape on Abbotsham beach. Data points are coloured with respect to elevation on the beach.

The cross-shore size- and shape-distribution of clasts was consistent with the description of Bluck (2011) (see Figure 2.6). The largest clasts populated the seaward margin of the beach, often resting directly on the shore platform (1 to 2 m above mean sea level, MSL). Clast size reduced rapidly towards the central beach zone (5 to 6 m above MSL), where the finest clasts (coarse pebbles) were located. Continuing up the beach, the mean clast diameter coarsened slightly to that of a fine cobble at the storm crest and back beach (8 to 10 m above MSL). All four shape end-members (e.g. equant, oblate, blade and prolate) were present within the sample. The distribution of clast shape appears to vary with elevation, with clasts at the seaward margin being relatively equant, and oblate- and blade-shaped clasts becoming more prevalent with elevation. The shape-sorting observed at Abbotsham beach is supported by the description provided by Bluck (2011) of a similar beach in south Wales.

Excavation (to approximately 1 m below the beach surface) revealed clasts underlying the middle and upper beach face to be similar or slightly finer than at the surface. This trend appeared to reverse at the lower beach face, where clasts coarsened slightly with depth. The arduous nature of beach excavations meant the composition of the beach greater than 1 m below the surface in any area is unknown.

2.2.6.3 Beach Profile

Abbotsham beach extended from a definitive bottom boundary, at approximately 1 m above MSL, to over 10 m above MSL at the highest point along the storm crest. Typically, the beach gradient was very steep (with an average of between 11 ° and 16 °) and reaches a maximum of up to 30 degrees just seaward of the beach crest. Additional, small-scale berms occasionally developed at the high water mark but were rapidly washed-out by both moderate and storm conditions. The beach profile varied along Abbotsham beach with the crest elevation peaking in the centre (see Figure 2.5). The cross-shore position of the crest was relatively straight. Where the low-lying cliffs retreated shoreward, an extensive back beach was found. Where cliffs protruded seaward, there was an absence of a back beach and the beach face intersected the cliff face.

2.2.6.4 Wave Climate & Tidal Regime

With exception to one controversial paper suggesting the occurrence of a tsunami in the Bristol Channel (Bryant & Haslett, 2002), the region is widely considered to be subject to wind-generated waves only. Bideford Bay is exposed to large amplitude, long period waves generated in the Atlantic Ocean. The most powerful waves are usually generated by winter storms associated with the strong eastward airflow between the Azores high and Icelandic low pressure system (Rodwell et al., 1999). The winter wave climate therefore fluctuates in concert with the phase of the North Atlantic Oscillation (Wolf & Woolf, 2006).

Analysis of the half-hourly wave statistics provided by the wave buoy over a period of almost four years (01 June 2009 to 31 April 2014) show the wave climate of Bideford Bay is dominated by swell waves generated in the Atlantic Ocean (see Figure 2.7). The modal significant wave height is relatively modest (0.8 m). However, the distribution is positively-skewed such that significant heights of almost 10 m were occasionally measured (Figure 2.7A). The modal peak period is 12 s, which is indicative of swell waves that have travelled an extensive distance from the point of generation (Figure 2.7B). The modal mean wave direction is 281 degrees. The vast majority of incident waves approach the coastline from a narrow range of directions (between 270-300 degrees) due

to the limited exposure of Bideford Bay to the Atlantic Ocean, which is constrained by the English and Welsh land mass (Figure 2.7C).

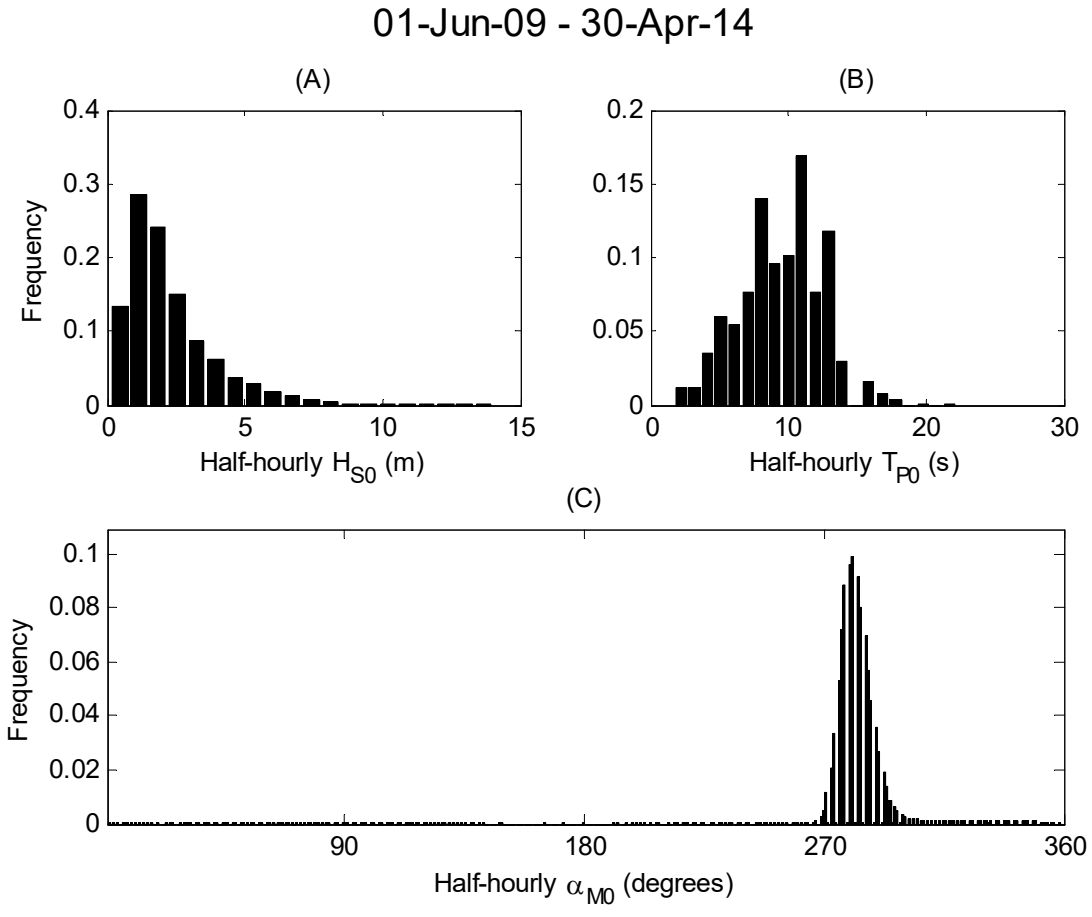

Figure 2.7: Frequency distribution of the half-hourly significant height (A), peak period (B) and mean direction of waves (C) measured by the Bideford Bay wave buoy. (A) The modal significant height is 0.8 m, however the distribution is positively skewed such that wave with significant heights greater than 2, 4 and 6 m account for 25, 5 and 0.4 % of the time respectively. (B) Peak wave period: The modal wave period is 12 s, however the peak period can be as little as two seconds (associated with local wind waves) and as much as 28 s: (C) Mean wave direction. The modal mean wave direction is 281 degrees. Ninety-four percent of waves approach the coastline from between 270 and 300 degrees. Graphs are constructed using data from the Bideford Bay wave buoy from between 01 June 2009 and 30 April 2014. Data Obtained from the CCO.

Abbotsham beach is situated within the macro-tidal setting of the Bristol Channel. The mean spring tidal range is approximately 7.2 m (Reeds Nautical Almanac). Beach base is elevated approximately 1 m above MSL and only the bottom half of the beach is submerged during highest spring tide (see Figure 2.5). Moreover, the beach is sub-aerial the majority of the time and only subject to hydrodynamic processes during the higher tidal states. The precise relationship between the Bideford Bay wave climate and wave conditions

adjacent to the experimental beach is dominated by the tides, the details of which are addressed in Chapter 4.

2.3 Flathead Lake, Montana, USA

Further field experiments were conducted at a secondary site on the eastern shore of Flathead Lake. The experimental beach setting is in sharp contrast with Abbotsham in terms of its geographical setting, beach composition and wave climate. These experiments were conducted along with Dr Mark Lorang from Flathead Lake Biological Station, University of Montana. Unlike the maritime setting of Abbotsham, Flathead Lake provided a controlled environment analogous to a large wave tank. The spectrum of waves that developed in the fetch-limited system was generally dominated by a narrow frequency band and lacked the secondary and tertiary frequencies that often complicate the wave field in exposed maritime environment. Moreover, Flathead Lake lacks daily tides that fluctuate the cross-shore positions of the process zones. The simple hydrodynamics of this setting were ideal for the process-based threshold-entrainment field experiments presented in this thesis.

2.3.1 Geographical Situation

Flathead Lake is situated at the southern end of the north-south oriented Rocky Mountain Trench in north-west Montana, USA. Despite the precise origin of the trench being unknown, the scale of the feature, which extend over 1000 km, implies it is the result of tectonic processes (Soward, 1965). It is thought that Flathead Valley and the Flathead Lake basin were scoured out by the Cordilleran ice sheet and in-filled by melt water from its retreating Flathead glacial lobe (Hofmann & Hendrix, 2010). The lake is flanked by the Mission (east) and Salish (west) mountain ranges, which are elevated 1200 m and 760 m above lake level (approximately 880 m above MSL) respectively. The major tributary to the lake is the Flathead River, which enters at the north and exits at the south. The lake exit is regulated by the Kerr dam, which varies the lake level and is described further in section 2.3.3.

The lake has a maximum length of 45 km and width of 24 km. The mean and maximum depth is 52 m and 115 m respectively (Lorang et al., 1993b). On the eastern side, the lake bed slopes steeply down to an elongate trench (> 90 m deep) that runs parallel with the shoreline. The bathymetry on the west side of

the lake is shallower and more gently-sloping. The geology of the Flathead Lake area is characterised by a mixture of crystalline bedrock and glacial till. The shoreline around Flathead Lake is determined by the local geology and includes the following: a dissipative beach composed of deltaic sand on the north shore; rocky, crystalline bedrock compose of metamorphosed siltstone, carbonate and sandstone to the west (LaFave et al., 2004) and; steep, reflective coarse clastic beaches composed of glacial till on the east and south shores (Lorang et al., 1993a). These coarse clastic beaches are composed of a mixture of sedimentary, metamorphic and igneous rock types, and include metacarbonate, quartzite, argillite and diorite lithologies (LaFave et al., 2004).

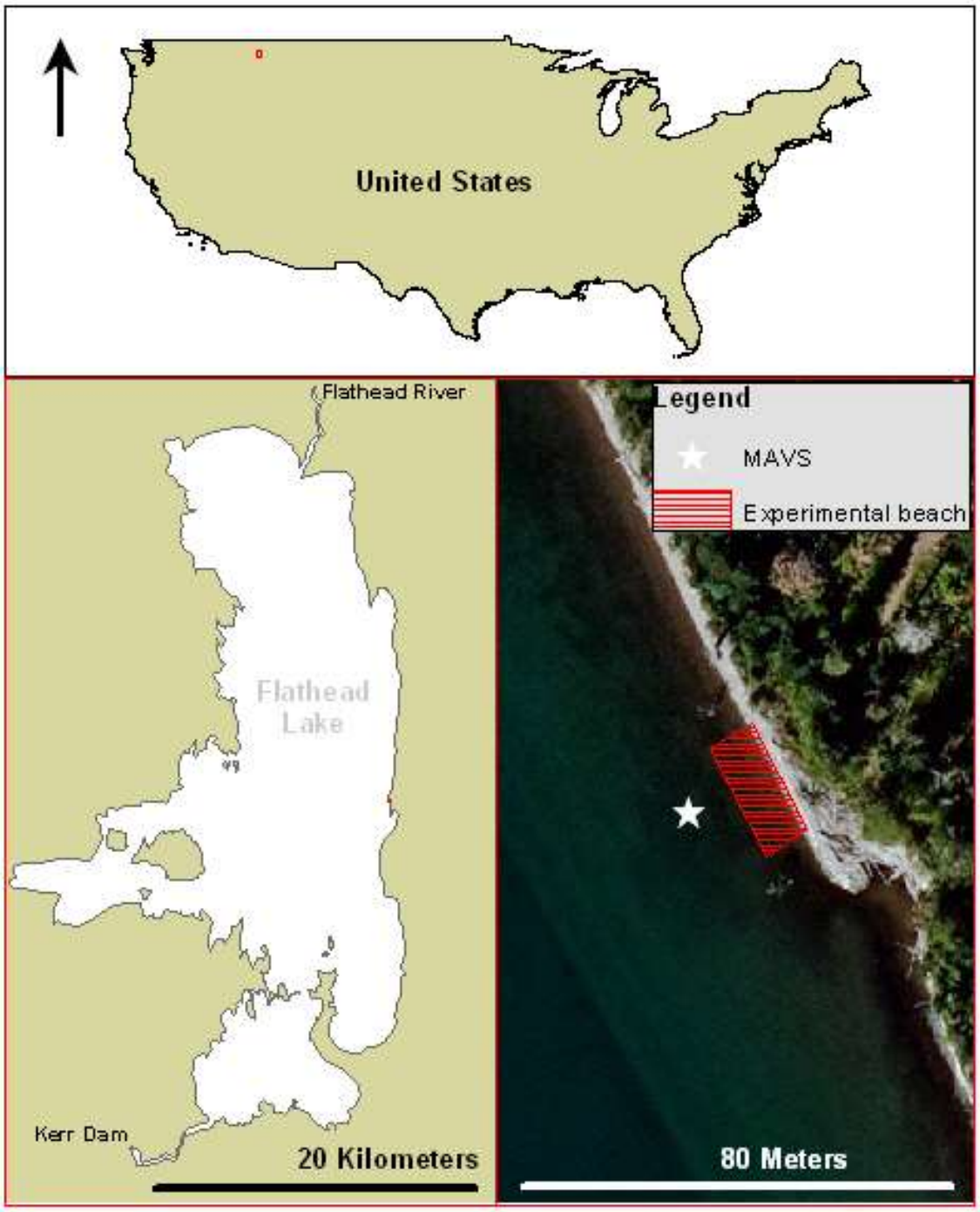

Figure 2.8: Map of the experimental beach at Flathead Lake and the surrounding area. Aerial image of the experimental beach and position of the wave gauge on the eastern shore of Flathead Lake (bottom right), with inset of Flathead Lake, indicating the position of the experimental beach (bottom left), and inset of the USA mainland indicating the position of Flathead Lake (top). Aerial imagery obtained from the Montana State website (www.geoinfo.msl.mt.gov) and USA outline from the United States Census Bureau (www.census.gov).

2.3.2 Beach Profile & Fabric

Experiments were conducted on a 30 m stretch of coarse clastic beach just north of Woods Bay on the east shore of Flathead Lake. The beach was unbounded to the north and extended southward to form a spit, backed by a shallow lagoon filled with drift wood. The cross-shore profile of the beach extended from well below full-pool elevation (see section 2.3.3 for definition) to the beach crest, which was elevated approximately 0.25 m above lake level. The average beach gradient was 7 degrees and, like at Abbotsham, increased from the beach base to a maximum (8 degrees) just seaward of the beach crest.

The surveyed beach was composed of a mixture of pebbles and cobbles (see Figure 2.9). Within the portion of the surveyed beach below mean surface elevation, the mean B-axis diameter of surficial clasts fined in the shoreward direction. Clasts with the finest mean B-axis diameter (64 mm) were located at mean surface elevation and included a range of pebbles and fine cobbles. The sub-aerial beach was composed of very well-sorted fine cobbles (mean B-axis diameter = 70 mm). As demonstrated in Figure 2.9, all four shape end members (e.g. equant, prolate, blade and oblate) were represented across the beach, but no significant relationship was found between shape and cross-shore position. The experimental beach was not excavated and hence the internal composition is unknown. The shore face, beach crest and back beach also incorporated a variable number of pieces of drift wood, which ranged from small branches to whole tree trunks.

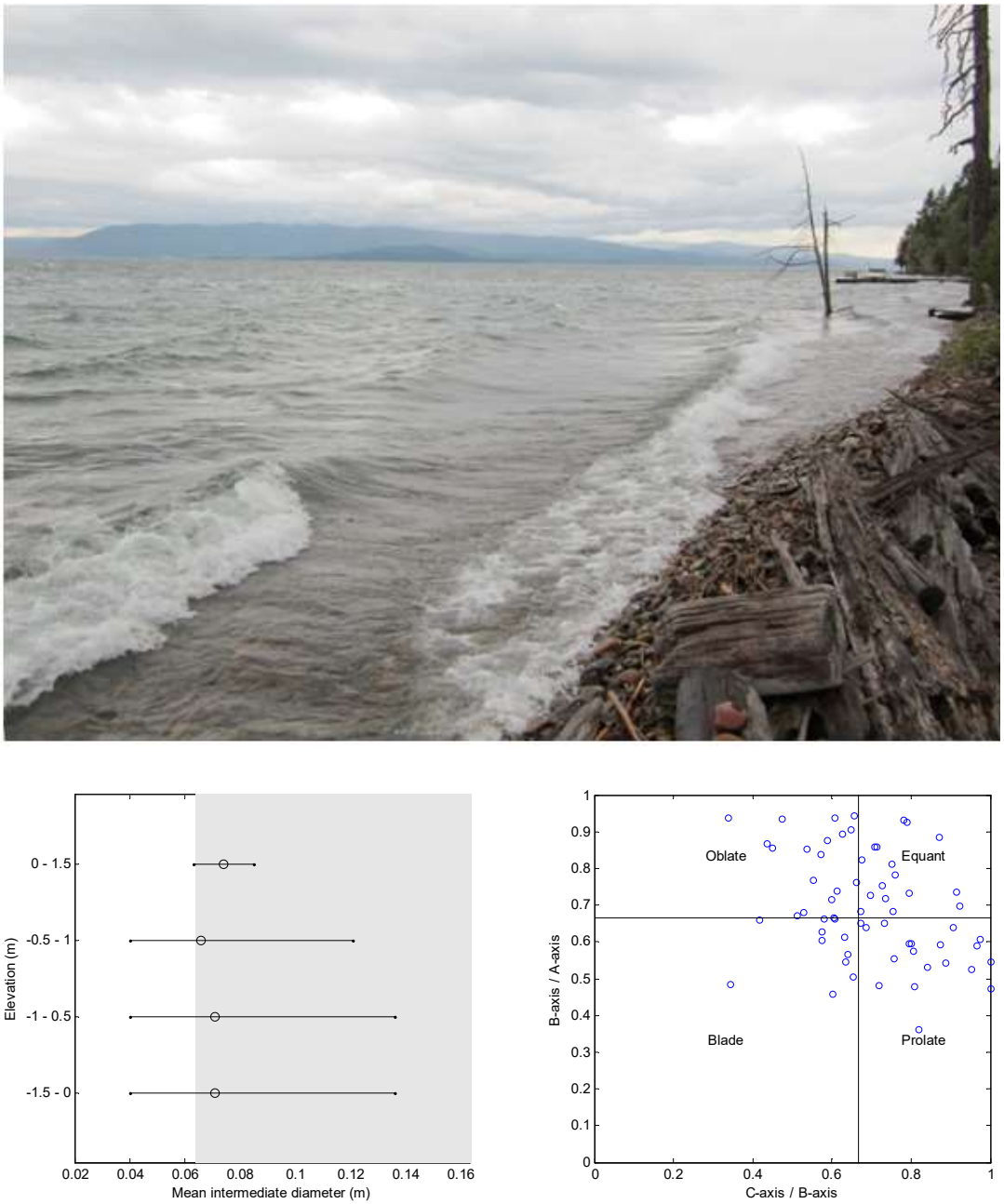

Figure 2.9: Image of the experimental beach on Flathead Lake (top); elevation versus mean intermediate diameter (bottom left) and Zingg plot of shape (bottom right) of clasts on the experimental beach at Flathead Lake. Bottom left: Mean B-axis diameter of between 25 and 27 clasts systematically selected along each of the four cross-shore transects using an adaptation of the 'pebble count' method (e.g. Wolman, 1954). The shading of the plot indicates the size categories (white = pebble, light grey = cobble), and horizontal bars indicate the finest and coarsest clasts located within each zone.

2.3.3 Wave Climate & Tides

Although Flathead Lake lacks astronomical tides, the surface elevation is artificially varied by the Kerr Dam. The lake level is fluctuated on an annual basis so that maximum elevation, ‘full pool’, is reach at the end of May and maintained until October, before the water level is lowered by two meters to the ‘low-pool’, winter level. The dam control on elevation of Flathead Lake means the experimental beach is only subjected to hydrodynamic forcing for approximately half the year (May to October), and remains sub-aerial for the winter months.

The experimental beach is exposed to waves from almost 180 degrees. The effective fetch over which waves can develop is limited in all directions and varies from between 11 km due west, and 25 km to the north-north east. The rapid spin-up and -down of waves is driven by winds associated with the passing of local and large-scale storm fronts. The wind is channelled along the lake by the Mission and Salish mountain ranges and prevails from the south in the summer and north in the winter (e.g. Lorang et al., 1993b).

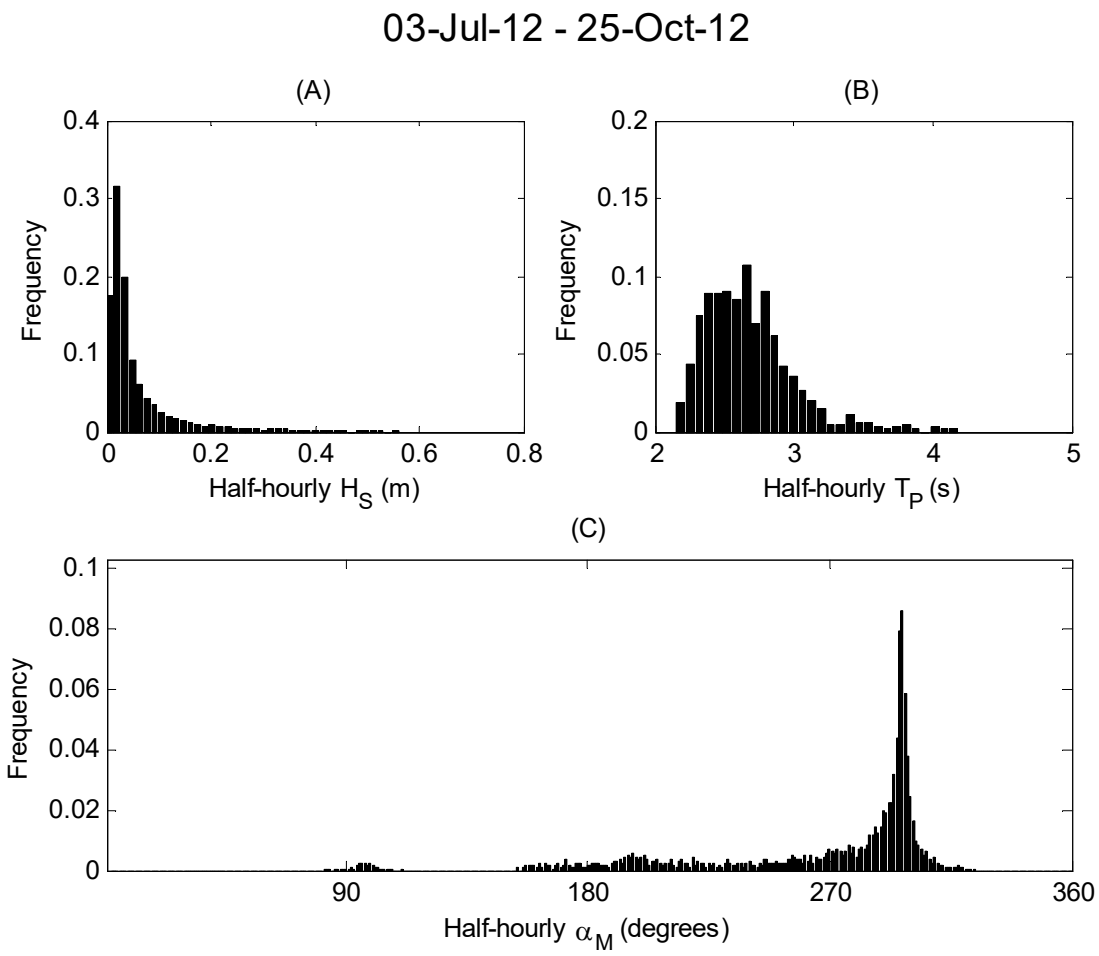

Figure 2.10: Frequency distribution of the half-hourly significant height (A), peak period (B) and mean direction (C) of waves measured adjacent to the experimental beach at Flathead Lake. (A) Although the modal wave height is less than 0.02 m, the exponential distribution shows heights greater than 0.1, 0.3 and 0.4 m account for 13.3, 1.5 and 0.004 % of the time respectively. (B) Peak wave period: The modal wave period is 2.8 s, but can occasionally exceed 4 s. (C) Mean wave direction: The modal mean wave direction is 281 degrees. Ninety-four percent of waves approach the coastline from between 270 and 300 degrees. Graphs are constructed using data obtained from adjacent to the experimental beach between 03 July 2012 and 25 October 2012.

No long-term empirical wave data were available for the field site at Flathead Lake. The wave conditions adjacent to the experimental beach were however measured between 03 July & 25 October 2012 (see section 3.4.4 for details) for the purpose of the experiments described in this thesis. These data are used here to describe the wave climate at the experimental beach. Field measurements demonstrate a general absence of waves during the deployment. Although the significant wave height was negligible (< 0.05 m) for over 60 % of the time, the positively-skewed distribution showed the half-hourly significant wave height to occasionally exceed 0.5 m. The distribution of wave heights is indicative of a system in which long periods of quiescence are punctuated by brief periods of storminess (consistent with the findings of Lorang

& Stanford, 1993). The modal peak wave period is small 2.8 s and typical of a fetch-limited system. However, longer period incident waves were measured, with peak periods greater than 4 s.

The location of the experimental beach means it is exposed to storm waves from a wide range of directions. All of the recorded waves came from between 210 and 360 °. However a strong modal peak is evident at 300 degrees. The vast majority of incident waves approached the beach with a southerly component of obliquity.

3 : Threshold-entrainment of Surficial Beach Clasts: Observations and Predictions

3.1 Introduction

The threshold-entrainment of surficial clasts is synonymous with the morphodynamic threshold of the beach itself, and is therefore of utmost importance when considering resilience to geomorphic change and potential erosion. The importance of this fundamental parameter has motivated researchers to derive process-based equations to predict the threshold-entrainment of coarse clasts (e.g. Hudson 1953; Lorang, 2000; Nott, 2003a). However, a general lack of corresponding field data has meant the accuracy of these equations remains largely unknown.

Previous field experiments have identified the threshold-entrainment through monthly and post-storm beach surveys by relating the mass of the heaviest displaced clast to the most powerful incident waves recorded between surveys (e.g. Oak, 1985). The advent of compact motion loggers has made it possible to adopt a real-time approach to measuring the threshold-entrainment by implanting devices within natural or synthetic clasts. A number of researchers have developed their own motion logger clasts (ML clasts) (e.g. Abeywardana & Hu, 2009; Frank et al., 2013), and explored the theory of tracing the clast's trajectory using inertial navigation techniques (Spazzapan et al., 2004; Abeywardana & Hu, 2009; Frank et al., 2013). Motion loggers have been utilised by a number of recent studies to measure clast transport in rivers (e.g. McNamara & Borden, 2004; Tremblay et al., 2010; Gendaszek, 2012; May & Pryor, 2014). Meanwhile, comparable wave-based studies have been confined to the laboratory (e.g. Frank et al., 2013), and a comprehensive literature search suggests motion loggers have not yet been deployed within the littoral environment.

This chapter presents novel field experiments observing the real-time entrainment of cobbles using 'off-the-shelf' motion loggers. Entrainment events are related to the corresponding 'threshold wave series' (see section 3.3.1 for definition), as measured by a proximal wave gauge. The results from the field experiments are cautiously compared with equation outputs of Lorang (2000), which aim to predict the threshold-entrainment mass of surficial beach clasts as a function of the wave conditions.

3.1.1 Threshold-entrainment: Conceptual Model Evolution

For a clast to become entrained, the forces exerted by the flowing fluid must be sufficient to destabilise it from its stationary position. In physical terms, the fluid drag force must exceed the immersed weight force of the clast (Shields, 1936). This condition is called the threshold-entrainment, and hence the mass of the entrained clast is a measure of wave competence (Lorang, 2000).

Figure 3.1: A simple diagram showing the forces acting on a surficial clast subjected to wave action. Where: φ is the pivoting angle; F_{drg} is the fluid drag force; F_{iwt} is the immersed weight force (figure adapted from Lorang, 2000).

Shields (1939) expressed the threshold-entrainment simply by scaling the shear stress against the immersed weight of the clast in question, and termed the relationship the 'Shields Parameter' (Θ).

$$\Theta = \frac{\tau}{(\rho_s - \rho_w)gD} \qquad \textbf{Equation 3.1}$$

Where: τ is the shear stress acting on the clast; ρ_s and ρ_w are the densities of the clast and water respectively; g is acceleration due to gravity and D is the clast's diameter. Although the Shields entrainment function was originally derived for steady flow conditions, wave tank experiments later showed the expression to be applicable to oscillatory flow conditions as well.

The relationship between immersed weight and the critical shear stress forces have been developed to predict: (1) the masses of the lightest clast that will remain stable (e.g. Hudson 1953; Lorang, 2000) and heaviest clast that will

become entrained (e.g. Lorang, 2000) by predefined wave conditions; (2) the height of the wave that displaced a clast of given mass (Nott, 2003a). Equations within the second category are central to the growing body of literature dedicated to discriminating between historic tsunami and storm wave impacts (e.g. Nott, 2003a, 2003b; Mastronuzzi & Sansò, 2004; Noormets et al., 2004; Williams & Hall, 2004; Barbano et al., 2010; Switzer & Burston, 2010; Lorang 2011).

Because fluid motions (and the associated bed shear stress) are a function of the wave profile (Doering & Bowen, 1995), these practical equations substitute the shear stress acting on a clast for measurable quantities such as; the offshore significant wave height (H_{S0}; SPM, 1984); the breaker height (H_b; Oak, 1986; Lorang, 2000; Nott, 2003a); or swash characteristics (Lorang, 2000), which are a function of the breaker height (H_b) and wave period (T) (e.g. Hunt, 1959; Battjes, 1974). The following section describes the equations derived specifically to determine the stability of surficial clasts situated on a CCB or similar man-made structure. Such equations consider the gradient of the feature and, in line with the general understanding of the hydrodynamics of CCBs, consider clasts to be most easily entrained up-slope.

3.1.1.2 Hudson Formula

The Hudson Formula was the earliest expression to predict the stability of individual clasts on a man-made rubble structure. Published by Hudson in 1953 and later adapted in the Army Corps of Engineers' Shore Protection Manual (SPM, 1984), the Hudson Formula is based on the previous work of Irribarren (1938) and Irribarren & Nogales Y Olano (1950). The minimum mass of an individual clast that will remain stable was expressed with respect to the density of the clast, the deep water significant wave height (H_{S0}), the beach slope (θ) and stability coefficient (K_D), which varies with the shape, roughness and interlocking nature of clastic material:

$$W = \frac{\rho_s {H_{S0}}^3}{K_D \left(\frac{\rho_s - \rho_w}{\rho_w}\right) cot\,\theta} \qquad \textbf{Equation 3.2}$$

Unlike the other input variables, the stability coefficient cannot be easily measured, and was instead estimated from wave tank experiments. The Shore Protection Manual (SPM, 1984) prescribed the stability coefficient according to

clast properties, placement and location (i.e. head or trunk of structure). Optimal K_D values were found to vary from between: 1.1 and 1.2 for smooth, rounded quarry stones subject to breaking waves at the trunk and head of the structure respectively; 16 and 31.8 for manufactured dolos subject to non-breaking waves at the trunk and head of the structure respectively.

Despite the equation being derived for man-made coastal protection structures, Oak (1986) reasoned that these artificial features are located in similar areas, and are composed of similar material to natural CCBs. Oak carefully compared threshold-entrainment predictions made with the Hudson Formula with direct field observations of the monthly and post-storm positions of 300 boulders over a two year period at Kaima beach, Australia. A stability coefficient (= 2.3) associated with rough, angular quarry stones subjected to non-breaking waves situated at the head of the structure was selected. Comparisons with the field observations showed the Hudson Formula to underestimate the wave height required to entrain finer boulders and greatly overestimate the wave height required to entrain coarser boulders.

Although the Hudson Formula is simple and easy to use, it does not account for the considerable effects of friction and permeability of the 'beach' face (e.g. Wang, 1974). Perhaps the most significant limitation of the Hudson Formula is that it does not consider wave period, which is linked to wave power and hence ability to do work (Lorang, 2000). The lack of wave period in the Hudson Formula could lead to the partial or complete erosion of protection structure composed of clasts greater than the predicted entrainment mass (e.g. Bruun & Günbak, 1977).

3.1.1.3 Lorang Formula

Noting the limitations of the Hudson Formula, Lorang (2000) derived two process-based threshold-entrainment equations which do consider wave period and beach porosity. The equations were based on the principles of Shields entrainment function (Equation 3.1) and developed the shear stress term for the face of a CCB. Lorang (2000) argued that the shear stress force applied by wave swash is a function of the fluid density, absolute swash velocity, and friction factor. He distinguished oscillatory flow conditions from steady state

conditions by considering both the maximum (U_{max}) and average swash velocity (U_{avg}); the latter being dependent on wave period.

$$\tau = f_{BF}\rho_w|U_{max}|\left|U_{avg}\right| \quad \textbf{Equation 3.3}$$

Lorang adapted an expression of Hughes (1995) to estimate the frictional resistance (f_{BF}) imposed by the beach-face, in which he considered in terms of the swash run-up height (R_u) and the median diameter of surficial clasts (D_{50}):

$$f_{BF} = \frac{8}{\left(2.5\ln\left(30\frac{R_u}{D_{50}}\right)\right)^2} \quad \textbf{Equation 3.4}$$

In the absence of direct swash velocity measurements, the maximum swash velocity is given as:

$$U_{max} = \sqrt{gH_{Sb}} \quad \textbf{Equation 3.5}$$

where H_{Sb} is the significant breaker height. Average swash velocity is simply given by dividing the horizontal excursion of the wave swash (X) by the time taken (t):

$$U_{avg} = \frac{X}{t} = \frac{R_u cot\theta}{(\frac{1}{2}T)} = R_u 2f\ cot\theta \quad \textbf{Equation 3.6}$$

where f stands for frequency and T stands for period. It follows that:

$$\tau = f_{BF}\rho_w U_{max} R_u 2f\ cot\theta \quad \textbf{Equation 3.7}$$

Lorang (2000) argued that the energy of the wave swash is equal to the energy of the breaking wave (E_{Hsb}):

$$E_{H_{Sb}} = \frac{1}{8}\rho_w g {H_{Sb}}^2 \quad \textbf{Equation 3.8}$$

Such that:

$$E_{R_u} = \frac{1}{8}\rho_w g {R_u}^2 \quad \textbf{Equation 3.9}$$

He therefore recommended that the threshold-entrainment should be scaled according to wave energy:

$$|F_{wav}| = \tau_{BF}.{R_u}^2$$ **Equation 3.10**

It follows that:

$$|F_{wav}| = f_{BF}\rho_w U_{max}{R_u}^3 2f\ cot\theta$$ **Equation 3.11**

The immersed weight (F_{iwt}) of the clast is a function of the buoyancy and mass of the clast (M_{Ru}):

$$F_{iwt} = (\rho_s - \rho_w)g\frac{M_{R_u}}{\rho_s}$$ **Equation 3.12**

Lorang included a non-dimensional variable, analogous to K_D in the Hudson Formula, which accounts for the pivoting angle (φ), shape factor (α_1) and packing coefficient (C_p) as follows:

$$K_r = \frac{C_p}{\alpha_1} tan\ \varphi$$ **Equation 3.13**

The critical threshold-entrainment condition is met when the wave force equals the immersed weight force:

$$F_{iwt} = |F_{wav}|$$ **Equation 3.14**

and thus:

$$(\rho_s - \rho_w)g\frac{M_{R_u}}{\rho_s} = f_{BF}\rho_w U_{max}{R_u}^3 2f\ cot\theta$$ **Equation 3.15**

The threshold-entrainment of a given clast subject to a given swash force will vary depending on the exposure of the clast to the wave force and pivoting angle, such that:

$$K_r = \frac{\rho_s\ f_{BF}\ U_{max}\ {R_u}^3\ 2f}{M_{R_u}\left(\frac{\rho_s - \rho_w}{\rho_w}\right) g\ tan\ \theta}$$ **Equation 3.16**

Making clast mass the subject Equation 3.16 gives:

$$M_{R_u} = \frac{\rho_s\ f_{BF}\ U_{max}\ {R_u}^3\ 2f}{K_r\left(\frac{\rho_s - \rho_w}{\rho_w}\right) g\ tan\ \theta}$$ **Equation 3.17**

By introducing the significant breaker height (H_{Sb}), which is scaled to a greater energy than the run-up height (R_u), the equation was modified to estimate the mass of the lightest clast that will remain stationary:

$$M_{H_{Sb}} = \frac{\rho_s \, f_{BF} \, U_{max} \, R_u \, {H_{Sb}}^2 \, 2f}{K_r \left(\frac{\rho_s - \rho_w}{\rho_w}\right) g \, tan \, \theta}$$ **Equation 3.18**

Lorang (2000) compared predictions from his threshold-entrainment equations with the aforementioned field data of Oak (1986). In the absence of direct measurements he estimated swash run-up from the equation initially proposed by Hunt (1959) and adapted by Battjes (1974):

$$R_{u2\%} = C_r \, H_S \, \xi$$ **Equation 3.19**

where: C_r is an empirically-derived reduction factor, found to be 0.55 for plunging waves (van der Meer & Stam, 1992); H_S is the significant wave height; ξ is the surf similarity parameter and is expressed in relation to the beach slope, wave height and deep water wavelength (see Equation 1.1). The deep water wavelength is expressed as follows:

$$\lambda_0 = \frac{gT^2}{2\pi}$$ **Equation 3.20**

Lorang (2000) demonstrated that Equation 3.17 provided reasonably accurate predictions when he compared his results with the observations of Oak (1986). For wave heights less than 2 m, the estimated maximum entrainment mass was within a factor of two to three of observations, and less than a factor of two for wave heights greater than 4.25 m. He suggested the larger discrepancy between observed and predicted threshold-entrainment when the wave height was small indicated the dominance of friction over hydraulic forces. He concluded that where wave height exceeded 4.25 m, hydraulic forces became dominant and the equation predicted the critical entrainment mass accurately.

3.1.1.4 Limitations

Conceptual understanding of the threshold-entrainment is restricted by a lack of corresponding field data and is based largely on the force-balance equations described above. Practical difficulties associated with monitoring clast dynamics and measuring the nearshore hydrodynamics means the exact physical relationship between wave mechanics and clast entrainment remains unclear. Previous investigation by Oak (1986) into the entrainment of boulders was limited by the temporally-coarse monthly and post-storm field observations. The frequency of these surveys is inconsistent with the intra-wave time scale within

which the entrainment process occurs. Consequently, these data provide limited insight into the detailed wave-clast interactions that determine the threshold-entrainment.

3.2 Chapter Aims & Specific Research Questions

Chapter 3 presents novel field data using motion loggers implanted within natural clasts to observe the threshold-entrainment within the littoral zone. These data are compared with outputs from the process-based equation of Lorang (2000). This chapter aims to answer the following research questions:

Q3.1: Are the measured variables sensitive to the threshold-entrainment?

Defining the threshold-entrainment of clasts within the littoral setting using real-time rotational data from implanted motion loggers has not previously been attempted. It is therefore important to establish whether the combination of the tiltmeter time series from the motion loggers and proximal wave measurements are sufficient to define the threshold-entrainment and explore its relationship to the wave force.

Q3.2: What is the relationship between the threshold-entrainment and wave power?

The power of a wave ($\propto H^2T$) determines its ability to do work. Direct observations and theoretical argument suggest that increasingly powerful wave conditions will be able to entrain increasingly heavy clasts (Lorang, 2000). However, the precise relationship between wave power and the threshold-entrainment mass of coarse clasts has not been extensively measured, and the temporally-coarse frequency of the monthly and post-storm field observations (e.g. Oak, 1986) does not correspond with the entrainment process itself. A novel benefit of using implanted motion loggers to measure entrainment is knowledge of the precise timing of entrainment events and hence the ability to attribute each entrainment event to the 'threshold wave series' (see section 3.3.1 for definition) overlying the clast at that time. The motion logger experiments provide novel, process-based insight into the threshold-entrainment, which current data sets do not.

Q3.3: Are the model variables and structure of the equations of Lorang (2000) appropriate to predict the threshold-entrainment on a wave-by-wave basis? How well does the observed and predicted threshold-entrainment correspond?

Equation 3.17 and Equation 3.18 derived by Lorang (2000) are the most up-to-date threshold-entrainment equations for use on CCBs. Importantly, the equations use the statistics that describe the general characteristics of the prevailing wave conditions to estimate the heaviest clast that will be entrained and lightest clast that will remain stable. The threshold-entrainment considered in relation to the threshold wave series is not directly comparable with the generalised statistics-based equations of Lorang (2000). Equation outputs are compared with the empirically-derived threshold-entrainment, defined at two differing frequencies. Here, comparisons are made with the threshold-entrainment observed first over the experimental run (approximately one hour) and second at a temporal frequency consistent with the entrainment process itself. The data sets not only provide opportunity to test the Lorang equations in general, but also their applicability at various temporal frequencies.

3.3 Methodological Approach

Previous studies observed the entrainment of coarse clasts from their displacement between monthly and post-storm surveys. The inability to determine precisely when each clast was entrained meant entrainment was automatically assigned to a cumulative wave parameter, such as the significant height and mean period of the most powerful waves measured between beach surveys (e.g. Oak, 1986). This method requires minimal equipment and effort but provides a limited description of the entrainment process, which occurs on a temporal scale of seconds (e.g. Frank et al., 2013).

A new method is presented here to measure the real-time entrainment of clasts and relate entrainment events to a ‘threshold wave series’ (see section 3.3.1 for definition) using two fundamental components: (1) ten to fifteen off-the-shelf motion loggers, each implanted within a natural beach clast and deployed in unison during a number of experimental runs (see section 3.4.2) and; (2) a wave gauge deployed directly adjacent to the experimental beach (see section 3.4.4). The experiments were conducted in two contrasting environments; firstly,

in the fetch-limited, freshwater setting at Flathead Lake and secondly at the exposed, macro-tidal, maritime setting at Abbotsham. The same methods and equipment (with different host clasts to reflect each of the natural settings) were used at both experimental sites.

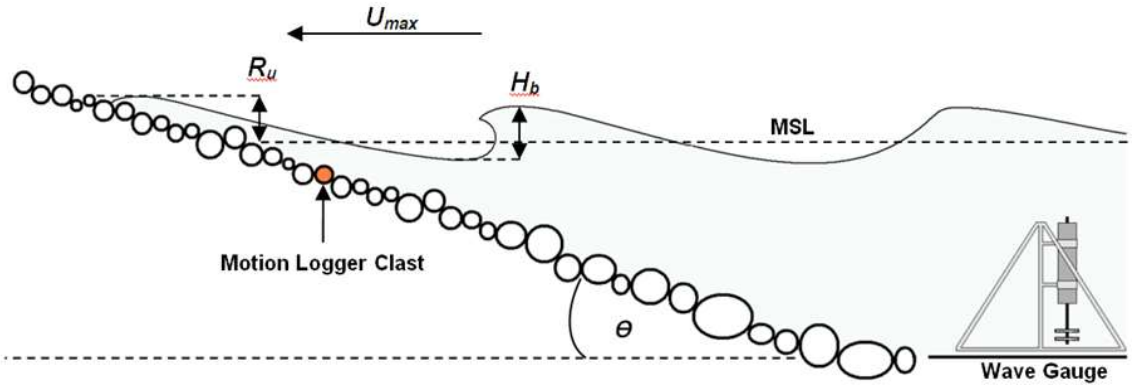

Figure 3.2: Diagram of the threshold-entrainment experiment setup indicating the variables important to the threshold-entrainment equations of Lorang (2000). Where: R_u is the maximum run-up elevation; U_{max} is the maximum swash velocity; H_b is the breaker height; θ is the beach slope and; MSL stands for mean sea level.

Clast entrainment was inferred from the three-dimensional tilt time series measurements from the motion loggers. Each entrainment event logged by each ML clast was related to the: (1) characteristics of the incident waves that prevailed over the hour-long experiment; (2) individual incident wave (or 'threshold wave series') overlying the entrained ML clast at the time of entrainment. The observed and predicted threshold-entrainment is analysed firstly on an experimental basis and subsequently with respect to the threshold wave series.

3.3.1 Definition of the Threshold Wave Series

The 'threshold wave series' is defined as the most powerful individual up-crossing wave profile estimated to be overlying the ML clast at the time of entrainment (see Figure 3.3). In essence, this approach attempts to identify the *individual wave* that entrained the ML clast. However, it is acknowledged that the natural wave field is not monochromatic but composed of a spectrum of waves with varying amplitudes, wavelengths and phases. The power of the associated incident wave is inferred from the surface profile when passing the wave gauge, which at any given point in time is the product of interactions between the various components of the wave spectrum. Hence, this approach in reality defines entrainment events in relation to the spectrum of incident

waves estimated to be acting on the ML clast at the time of entrainment, hereafter referred to as the 'threshold wave series'. The concept of a threshold wave series is akin to boat wakes which are a packet of wave energy composed of a dominant boat wake and series of smaller waves that travel as a visible wave-group (e.g. Bauer et al., 2001).

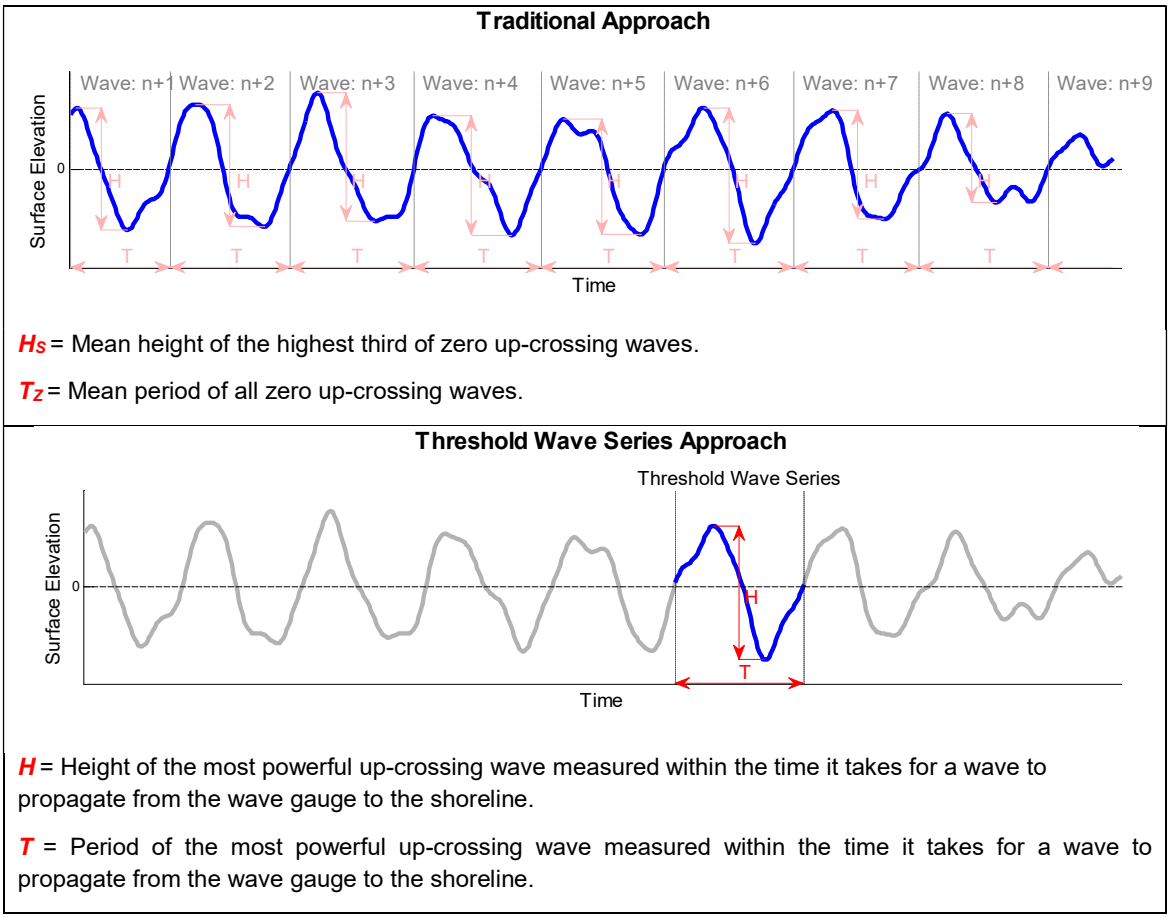

Figure 3.3: Illustration of the difference between traditional cumulative approach (top) and threshold wave series approach (bottom) to quantifying the wave force.

3.3.2 Compatibility of Motion Logger Data & Threshold-entrainment Equation Outputs

The equations of Lorang (2000) were not intended to predict the threshold-entrainment at a frequency consistent with the entrainment process itself, but instead use the general statistics that describe multiple polychromatic incident waves that compose a storm event. Considering this, it is logical to start by forcing the threshold-entrainment equations with the general wave statistics measured during each of the experimental runs and compare the mass of the heaviest ML clast that was entrained (at least once) within the intervening period with equation predictions. The threshold-entrainment was subsequently

considered as a function of the threshold wave series. Here, it was assumed that the weakest threshold wave series associated with the entrainment of each ML clast represents the minimum power required to entrain that clast. The threshold-entrainment equations were forced with the properties of the weakest threshold wave series in order to compare the observed and predicted critical entrainment mass.

3.4 Experimental Equipment & Configurations

3.4.1 Host Clast Selection & Modifications

Fifteen (plus two spare) natural clasts from both the Flathead Lake and Abbotsham field sites were chosen to host the motion loggers. Clasts selected for the experiments ranged from medium to coarse cobbles. At Flathead Lake, the selected ML clasts represented the largest size fraction in the nearshore zone. Clast selection at Abbotsham (where the B-axis of the largest clasts approximated 1 m) was limited by the requirement to transport selected clasts to and from the isolated beach by wheelbarrow.

The motion loggers were fitted inside a 35 mm diameter cylindrical hole cored through each clast using a water-cooled diamond-encrusted corer. The position and orientation of the cored hole was determined by the ability to grip the clasts in the drilling vice. Clasts were generally cored through their A- or B-axis. The hole cored through each clast was sealed at one end with cloth tape. To compensate for the mass loss from the coring process, lead shots were mixed evenly into uncured marine epoxy resin and the mixture poured into the unsealed end of each clast. A plastic-wrapped motion logger was subsequently dipped in the resin and held in the desired position until the resin had cured. Effort was made to ensure the motion logger was held as close to the centre of the clast as possible with its X-axis approximately aligned with the A-axis of the host clast. The motion logger was removed from the hardened epoxy resin, leaving an impression that would hold the device securely within the clast during the experiments. Before deployment, the ML clasts were painted bright orange to aid post-experiment retrieval.

Figure 3.4: Image of an adapted ML clast (A01) from Abbotsham, displaying the motion logger mould. Scale: Cored hole is 35 mm in diameter.

Despite the aforementioned attempt to compensate for mass loss of the modified ML clasts, the process resulted in up to a 25 % reduction in mass. In addition to the usual clast measurements the densities of the ML clasts were obtained from displacement experiments. Details for all ML clasts from Flathead Lake and Abbotsham are provided in tables 3.1 and 3.2 respectively.

Name	A-axis (mm)	B-axis (mm)	C-axis (mm)	Mass (kg)	Mass loss (%)	Volume (m^3)	Density (kg/m^3)
F01	80	72	61	0.369	25	1.30E-04	2.80E+03
F02	88	75	61	0.509	20	1.90E-04	2.70E+03
F03	95	67	61	0.546	19	2.00E-04	2.70E+03
F04	102	68	65	0.589	19	2.30E-04	2.60E+03
F05	117	74	58	0.648	16	2.80E-04	2.00E+03
F06	111	78	77	0.744	16	2.80E-04	2.60E+03
F07	115	71	69	0.787	14	3.10E-04	2.50E+03
F08	113	93	64	0.877	13	3.20E-04	2.80E+03
F09	125	106	69	1.112	11	4.30E-04	2.60E+03
F10	126	125	84	1.424	15	5.50E-04	2.60E+03
F11	152	95	75	1.473	10	5.60E-04	2.60E+03
F12	132	113	86	1.529	5	5.90E-04	2.60E+03
F13	136	114	90	1.606	24	6.40E-04	2.50E+03
F15	146	96	95	1.933	9	7.40E-04	2.60E+03

Table 3.1: ML clast properties for the Flathead Lake experiments.

Name	A-axis (mm)	B-axis (mm)	C-axis (mm)	Mass (kg)	Mass loss (%)	Volume (m^3)	Density (kg/m^3)
A01	121	84	65	0.902	13	3.30E-04	2.70E+03
A02	111	80	78	0.993	14	4.00E-04	2.50E+03
A03	115	90	87	1.267	11	4.80E-04	2.60E+03
A04	121	101	81	1.273	10	5.00E-04	2.50E+03
A07	141	100	79	1.528	10	5.80E-04	2.60E+03
A08	139	122	82	2.029	7	7.50E-04	2.70E+03
A09	145	109	99	2.139	8	7.80E-04	2.80E+03
A10	135	114	93	2.160	8	8.30E-04	2.60E+03
A12	131	123	94	2.208	7	8.10E-04	2.70E+03
A13	159	117	80	2.300	8	8.60E-04	2.70E+03
A14	149	128	90	2.415	9	9.40E-04	2.60E+03
A15	140	132	96	2.422	7	9.10E-04	2.70E+03
A16	157	116	87	2.455	8	9.10E-04	2.70E+03

Table 3.2: ML clast properties for the Abbotsham experiment.

3.4.2 Motion Loggers

Onset HOBO Pendant G (*UA-004-64*) motion loggers were used to measure the three-dimensional tilt and acceleration (*g*) of clasts. The loggers are housed in a tough, watertight polypropane case. Their compact (58 mm × 33 mm × 23 mm) design means they can be fitted within natural clasts as small as a medium-sized cobble.

Figure 3.5: Image of (left) *Onset Pendant G Data Loggers* (*UA-004-64*) and (centre) *BASE U-1* optical USB and coupler device.

The HOBO motion logger measures three-dimensional tilt and acceleration at a specified frequency of between 1.54×10^{-5} Hz and 10 Hz. They have a stated accuracy of ± 1.03 m/s² from -20 °C to 70 °C and time drift of approximately a minute per month (or 0.083 seconds per hour) at 25 °C (*Onsetcomp* website, 2012). A maximum of 21,688 tilt and acceleration readings can be stored in the logger's 64 kilobyte internal memory. Motion loggers must be retrieved in order to access the data, which is downloaded via an *Onset BASE U-1* optical *USB* driver using *Onset*'s tailored *HOBOware* software.

The motion loggers were programmed to sample at a frequency of 4 Hz, which limited the duration of each motion logger run to approximately 1.5 hours. This was rapid enough to capture intra-wave motions and corresponded with the frequency of the wave gauge (see section 3.4.4). Loggers were programmed to record their three-dimensional tilt and acceleration. The motion loggers could not be programmed with a future start time, but instead required hand-activation with a magnetic coupler (located on the *BASE U-1* optical USB device). Running motion loggers were finally placed and sealed within their host clasts ready for immediate deployment.

3.4.3 Timescale and Cost of Making a Motion Logger Clast

The process of adapting natural clasts to house motion loggers was relatively expensive and time consuming. The following costing is based on the UK experiments, for which all raw materials needed to be purchase. Coring the clasts required a specialist pillar drill and water-cooled system used by a stone mason. It took one day and cost £234 to have 15 clasts professionally cored. Making the epoxy moulds, which held the motion loggers firmly in place, was a painstaking process that demanded the attention of the worker for the entire curing period (lasting between 4 and 12 hours). It should be noted that all the ML clasts were treated at once, and the time required to complete this task might not vary much by either reducing or increasing the number of clasts being treated.

Each mould was formed from a substantial amount of epoxy resin with lead shots mixed in. Approximately two 260g *Plastic Padding* epoxy/hardener sets (£15.00 each) and 1 kg of lead shots (approximately £5) were used on the ML clasts. Finally, the *HOBO Pendant G* motion loggers cost approximately £53 a piece and the single *BASE U-1* optical USB reader required to download data cost £45. In total, the process of adapting 15 clasts to house motion loggers is estimated to have taken between two and three working days and cost approximately £75 per motion logger clast.

3.4.4 Wave Gauge

The nearshore incident wave profiles and direction of propagation was provided by *Nobska*‘s third generation Modular Acoustic Velocity Sensor (MAVS). The MAVS measures the instantaneous surface elevation using a pressure transducer and the concurrent three-dimensional fluid velocities with two acoustic modules. The stated accuracy of the pressure transducer and fluid velocities and time drift is 0.5 % full scale, 0.03 m/s and 0.15 seconds per month respectively (www.nobska.net/, 2012). The MAVS is a self-contained unit with the dimensions 83 mm × 635 mm. It can be deployed vertically or horizontally. For vertical deployment the device can be configured to run with the acoustic baskets facing up or down.

The MAVS is powered by a custom-built battery pack comprised of 18 AA alkaline batteries, the durability of which depends on the sampling regime. The

device can be programmed to sample at frequencies between 2 Hz and 50 Hz, with a burst length of 1024, 2048 or 4096 samples and burst interval of 90 s and greater. The MAVS is connected to the computer using a customised MAVS to VGA cable, and programmed via *Crosscut* software. Data is stored internally in binary format on a 4GB compact flash card. The data is accessed by removing the MAVS' watertight shell, retrieving the flash card from its dock, and extracting the data with a flash card reader. *MAVSpack1* software was used to convert the downloaded data from binary to text format. Conversion of the pressure record to surface elevations and fluid velocities to directions were executed by an adapted MATLAB routine (written by Chris Gotschalk).

The MAVS device was programmed to sample at a frequency of 4 Hz, which captured the profiles of high frequency wind waves at Flathead Lake and corresponded with the sampling frequency of the motion loggers. The Shortest burst interval (90 s) was selected to obtain the most comprehensive wave record possible. Configuration for the first experiment (on 3 July 2012) was an exception, where the burst interval was set to 900 s. The MAVS was deployed vertically at both field sites with its: baskets down at Flathead Lake due to the dimensions of the MAVS frame and the shallow deployment of the device; baskets up in Abbotsham to maintain a low centre of gravity and maximise stability in the energetic nearshore zone.

The MAVS device was held securely by steel mooring frames. The Flathead Lake mooring frame consisted of a triangular base and a supported mast with grips to hold the MAVS device vertically (see Figure 3.6). The frame was anchored to the Lake bed by loading the triangular base with bricks and large clasts from the surrounding area. The MAVS frame for Abbotsham incorporated the same supported mast and vertical grip design. However, with consideration to the exposure of the shore platform to powerful oceanic waves, the frame was fixed by the insertion of a solid metal cylinder at the base of the mast into a corresponding hole cored into the shore platform. The frame also featured a rudder system to maintain its orientation whilst being impacted by shoaling waves. The orientation of the MAVS device was noted using a hand-held compass in light of local magnetic variation. The MAVS was deployed approximately 16 m and 30 m offshore from the ML clast deployment zone at the Flathead Lake and Abbotsham field sites respectively.

Figure 3.6: Images of the MAVS and its mooring frames at Flathead Lake and Abbotsham. Left: MAVS mooring frame used in the Flathead Lake experiments (without MAVS device and not positioned correctly). Right: Custom designed mooring frame holding the MAVS device on the shore platform at Abbotsham.

3.5 Data Collection

Between 10 and 15 motion loggers were deployed in unison on six occasions (or 'runs') at the US and UK field sites combined. At Flathead Lake, one run was conducted on 03 and 18 July 2012 respectively, and three runs were conducted on 23 July 2012. However, only one run was conducted at Abbotsham, on 14 October 2012, for reasons explained in section 3.5.1.

Before each deployment the internal time for the motion loggers and pressure transducer were synchronised to Universal Coordinated Time. Once activated, the ML clasts were then placed in the swash zone in a line with the clasts' A-axes aligned parallel to the shore. The low energy wave climate at Flathead Lake meant ML clasts could be retrieved immediately after the experimental run. The turbid and energetic nearshore at Abbotsham prevented clast retrieval until low tide the following day. Additional measurements of the initial and final position of every motion logger clasts was measured with a DGPS for each of the three experimental runs conducted at Flathead Lake on 23 July 2012.

3.5.1 Procedural Deviations

The large range of equipment required and the novelty of the experiments resulted in some methodological variability, as explained below.

Flathead Lake, 03-Jul-2012:

Out of the 15 available motion loggers, only ten were deployed because the epoxy mould in five of the host clasts had not yet fully cured. Furthermore, the ten deployed ML clasts were relocated (by hand) within the swash zone on two separate occasions during the experimental run. The full capabilities of the MAVS wave gauge were not yet fully understood, and it was programmed to have a burst interval equal to the burst length (900 s). Consequently, approximately half the logged entrainment events could not be included in the wave-by-wave analyses (see Table 3.3).

Abbotsham, 14-Oct-2012:

All fourteen of the deployed clasts were buried by the day following the experiment when ML clasts were to be retrieved. This hindered clast recovery and indeed lead to the loss of two ML clasts and data stored within their implanted motion loggers. In light of the forecasted increase in wave power and poor clast retrieval rate, the decision was taken to cancel the remaining planned experiments. Consequently, only one experimental run was conducted at Abbotsham.

3.6 Data Processing

3.6.1 Entrainment Identification

The motion loggers were programmed to record their three-dimensional tilt and acceleration at a frequency of 4 Hz (see Figure 3.8). For the logger outputs to be of any use they must first be converted into an understandable metric from which entrainment events can be identified. It is very difficult to accurately infer the magnitude of a transport event from non-continuous (i.e. digital) acceleration readings. Conversely, the change in the ML's three-dimensional tilt between successive time steps are additive and can be used to determine the rotation that the ML clast has made between time steps. Identification of entrainment events was therefore based on the tilt-meter readings. It is

acknowledged that this is a constricted lens given that it is insensitive to non-rotational transport (e.g. sliding).

3.6.2 Rotation through an Axis

Motion logger rotations were inferred from the three-dimensional tilt record using an algorithm developed to analyse change in the a_i, b_i and c_i axis tilt vectors (see Appendix 3). To capture clast rotation through an axis (that does not necessarily correspond to those of the motion logger), the cross product was taken between the tilt vectors a_i, b_i, and c_i to give the tilt vectors for the coupled *ab*, *ac* and *bc* logger axes, where:

$$ab = (a_i . b_{i+1}) - (b_i . a_{i+1}) \quad \textbf{Equation 3.21}$$

$$ac = (c_i . a_{i+1}) - (c_{i+1} . a_i) \quad \textbf{Equation 3.22}$$

$$bc = (b_i . c_{i+1}) - (c_i . b_{i+1}) \quad \textbf{Equation 3.23}$$

The angle of rotation derived from the *ab*, *ac* and *bc* tilt vectors between time(*i*) and time(*i*+1) were given such that:

$$Angle\ of\ Rotation = a\sin\left(\frac{\sqrt{{ab_i}^2 + {ac_i}^2 + {bc_i}^2}}{\pi . 180}\right) \quad \textbf{Equation 3.24}$$

And, the angle between rotational axes:

$$Angle\ between\ Axes = ab_i . ab_{i+1} + ac_i . ac_{i+1} + bc_i . bc_{i+1} \quad \textbf{Equation 3.25}$$

Where the angle of rotation was greater than 90°:

$$Angle\ between\ Axes = 180 - (ab_i . ab_{i+1} + ac_i . ac_{i+1} + bc_i . bc_{i+1}) \quad \textbf{Equation 3.26}$$

3.6.3 Defining Discrete Rotational Events

The algorithm (which is illustrated in Figure 3.7 and displayed in Appendix 3) assumes time steps when the angle of rotation is non-zero to be the first of a series of additive rotations that compose a discrete '*event*'. Subsequent rotations were multiplied by the cosine of the angle between the initial and subsequent rotational axes (-1 ≤ *cosine(angle)* ≤ 1) and added to the event total.

A discrete rotational event was terminated when either: (1) the rotational total of the event did not increase for more than one second or; (2) the initial rotational total was exceeded by a subsequent reversal. Event termination prompted the algorithm to continue the process one time step on from the beginning of the preceding (and now-terminated) event. In the exceptional case following an entrainment event (see section 3.6.5 for entrainment definition), processing was resumed from the beginning of the pause or reversal that terminated the preceding event.

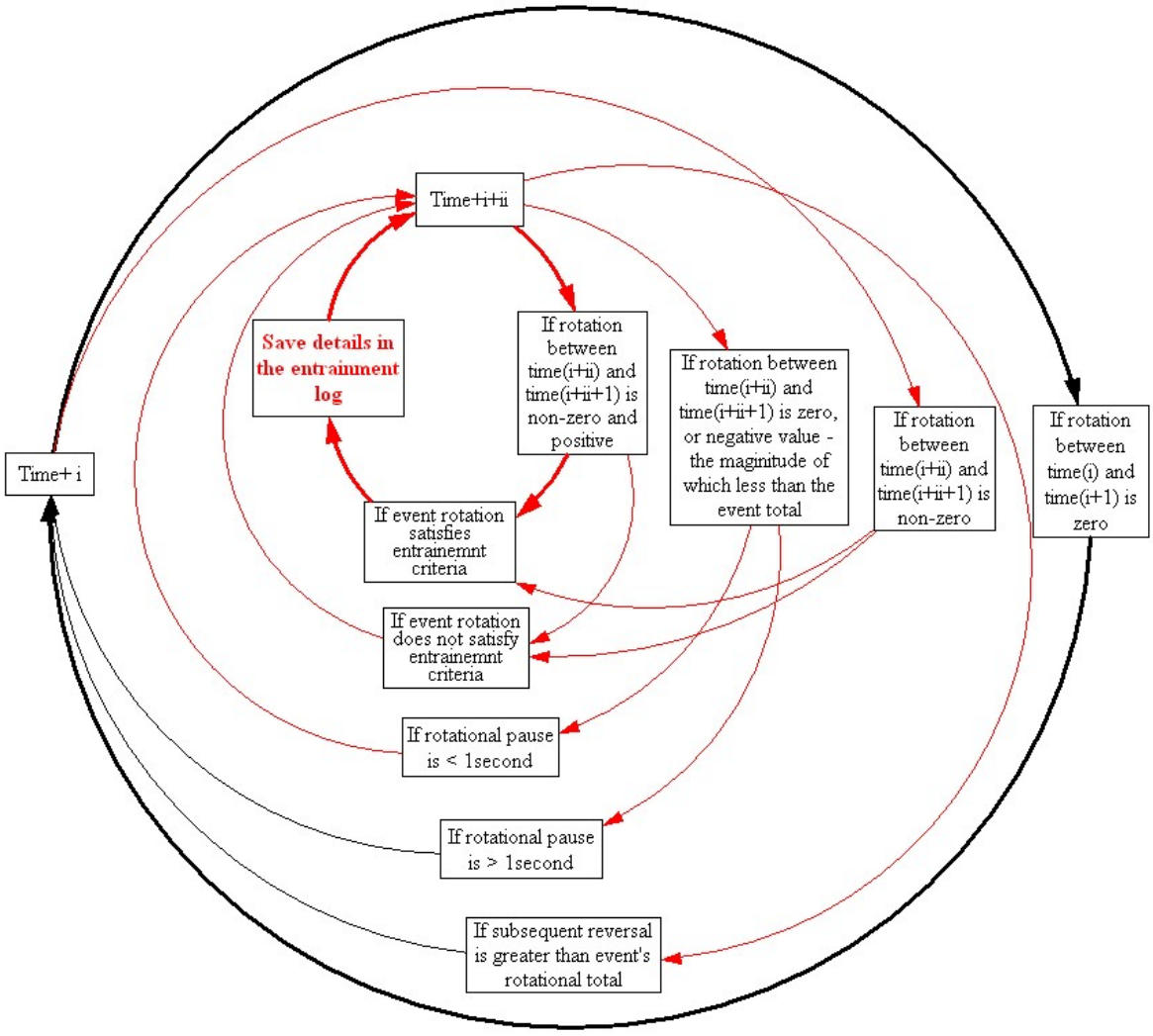

Figure 3.7: Flow diagram depicting the workings of the entrainment algorithm. Figure created with *Vensim* software.

It is important to note that this method focussed on the entrainment of clasts and does not provide data with which the time-varying position of the clast could be inferred. Where an event satisfied the entrainment criteria, the start and end time along with the rotational total and clast name was recorded.

3.6.4 Testing the Rotational Algorithm

The ability of the algorithm to detect rotation was tested by comparing observed and computed rotations made by a motion logger. For this: a motion logger was fixed inside a cylindrical glass jar at an obscure angle; the jar was rolled along a horizontal surface and the number of revolutions of the jar noted (3); comparisons were made between observed and computed number of revolutions.

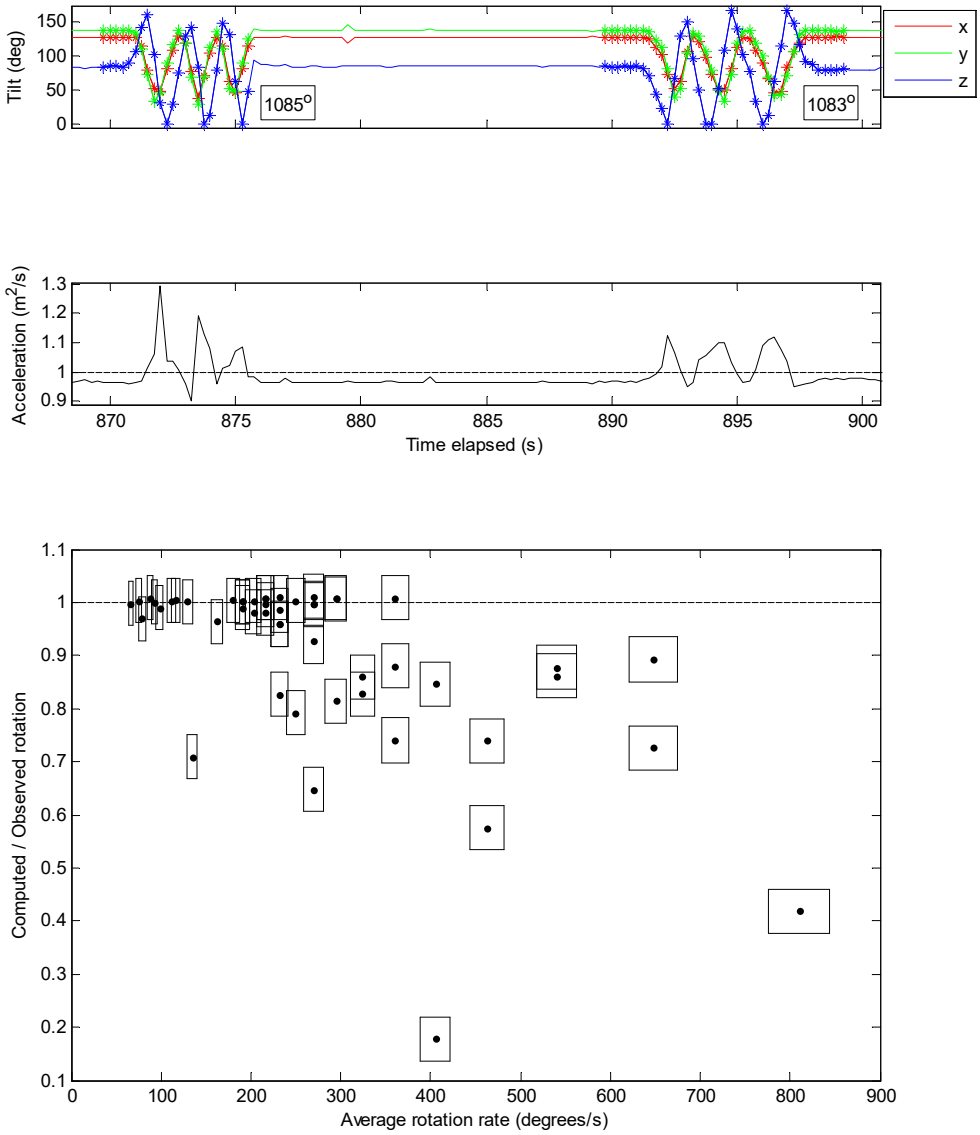

Figure 3.8: Time series of the three-axial tilt (top) and total acceleration (middle) from the jar-encased motion logger, and correlation between the observed and computed rotation versus rotation rates with a 4 Hz sampling frequency (Bottom). Each separate 'event' constituted a 1080 ° rotation of the jar and motion logger. Bottom: The dashed horizontal line denotes agreement between the observed and computed rotation. The rectangles represent an estimate of the proportional human-related uncertainty in precisely determining the rotation of the motion logger (22.5 °).

The algorithm provided rotational estimates between 0.18 and 1.01 times that observed. Near perfect rotational estimates were recorded at slow to medium revolution rates (< 360 °/s). However, underestimation of the rotational event became increasingly significant with rotational rapidity. This resulted from the inability to capture rotations exceeding 180 ° between sample time steps (which most likely results from the jerky motion of the operator's hand when initialising jar revolutions). In these instances, the algorithm recorded a smaller rotation in the reverse direction, which was not included in the event total, and resulted in the rotational event being underestimated. While the generation of such rapid rotations seems very plausible for surficial clasts impacted by a breaking wave front, the limited memory capacity of the motion loggers meant increasing the sample frequency to better capture fast rotations was not a viable option.

3.6.5 Entrainment Definition

It was crucial to define the minimum rotation required to identify the transition between no motion and entrainment. The entrainment criterion was based on the rotation required for a clast to roll from its resting position to the top of the adjacent stationary clast where the pivoting angle between the two clasts was zero. At this point, the mobile clast was considered to have become removed from its stable pre-transport setting, and therefore entrained.

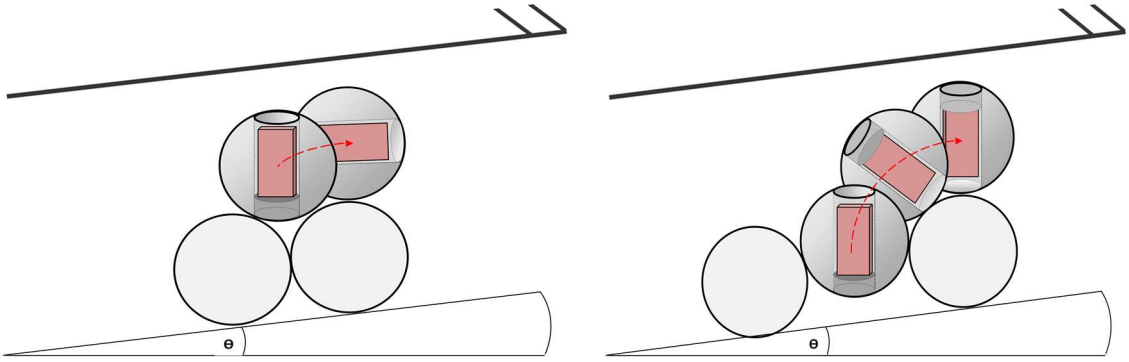

Figure 3.9: A simple diagram of the upslope entrainment of an exposed (left) and embedded (right) ML clast. Where θ stands for beach slope.

The rotation required to satisfy the entrainment criteria varies depending on the pivoting angle and hence pre-transport setting. While clasts with small initial pivoting angles might only be required to rotate slightly, well-bedded clasts with large pivoting angles must rotate almost 180 ° to satisfy the entrainment criteria. However, it was not possible to continually monitor the pivoting angles of all ML

clasts during the field experiments. The entrainment criterion was therefore set at 180 ° in order to capture the most significant transport events. Although this definition of entrainment is highly constrained, it is set to consider only significant entrainment events.

3.6.6 Identification & Quantification of the Threshold Wave Series

Identifying the threshold wave series that entrained a ML clast was a challenging process because the precise cross-shore position of the ML clasts at any given moment in time is uncertain. However, direct observations at Flathead Lake indicated all clasts remained between the breaker and swash zones during each of the experimental runs. The energetic and turbid nearshore obscured visual observation of the ML clasts at Abbotsham, but it seems reasonable to assume that they too remained on the beach face throughout the experimental run.

Entrained ML clasts were conservatively assumed to be underlying, and therefore entrained by, the most powerful threshold wave series located in between the MAVS and shoreline at that time (see Figure 3.2). In order to identify the wave field between the MAVS and the shoreline at the time of entrainment, knowledge of the time taken for an incident wave to propagate from the cross-shore position of the MAVS to the shoreline was required. This was estimated using linear wave theory, where:

$$t = \int_{0}^{h_{MAVS}} \frac{dx}{\sqrt{\frac{g}{k}\tanh kh}} \qquad \textbf{Equation 3.27}$$

in which: x is the cross-shore distance; h is the water depth, which varies in the x direction; h_{MAVS} (= 1.28 m) is the water depth at the position of the MAVS; k (=$2\pi/\lambda$) is the wavenumber and λ is the wavelength, which was solved iteratively using:

$$\lambda = \frac{gT^2}{2\pi}\tanh\left(\frac{2\pi h}{\lambda}\right) \qquad \textbf{Equation 3.28}$$

The time taken for an incident wave to propagate from the MAVS to the shoreline was conservatively estimated using the 5th percentile of measured wavelengths during each field experiment. Time lag estimates corroborated with

direct observations and were between 8 and 9 seconds at Flathead Lake and approximately 10 seconds at Abbotsham.

The threshold wave series was identified using the zero up-crossing method, with which the start and finish of an individual wave is defined by the point at which the instantaneous water surface rises above mean elevation. The wave height was taken as the difference between the trough and crest elevation. The wave period was given by the length of the wave divided by the sample frequency of the wave gauge. It is important to highlight the non-continuous measurements of the MAVS. Entrainment events that occurred outside the wave gauge's burst could not be linked to a threshold wave series and were therefore discarded.

3.7 Results

The motion logger field experiments provided a unique insight into the real-time dynamics of natural clasts within the littoral zone. In total, five experimental runs were conducted in Flathead Lake and one at Abbotsham (see summary of results in Table 3.3 and Table 3.4). The threshold-entrainment was observed with a varying success at the contrasting field sites, and the results are thus presented with respect to location.

Flathead Lake

Run	Start time (Local)	H_s (m)	T_z (s)	Breaker type	No. of clasts deployed / retrieved	Heaviest ML clast (kg)	Lightest ML ML clast (kg)	No. of ML clasts entrained at least once	Total no. of registered entrainment events	Total no. of discarded entrainment events	Heaviest ML clast entrained (kg)	Lightest ML clast not entrained (kg)
1	03-Jul-2012 23:30:00	0.52	3.1	Spilling	10/10	1.473	0.369	10	329	168	1.473	N/A
2	20-Jul-2012 18:18:00	0.10	2.3	Plunging	13/13	1.606	0.369	0	0	0	N/A	0.369
3	23-Jul-2012 18:47:00	0.36	2.7	Plunging	13/13	1.606	0.369	11	50	0	1.529	1.112
4	23-Jul-2012 22:08:00	0.21	2.3	Plunging	14/14	1.933	0.369	7	37	4	1.473	0.546
5	24-Jul-2012 01:40:00	0.30	2.6	Plunging	14/14	1.933	0.369	11	48	2	1.933	1.424

Table 3.3: Table of empirical values for each of the Flathead Lake motion logger experiments. The 'not applicable' abbreviation (N/A) indicates experimental runs in which either no ML clast was entrained or no ML clast remained stationary.

Abbotsham

Run	Start time (Local)	H_s (m)	T_z (s)	Breaker type	No. of clasts deployed / retrieved	Heaviest ML clast (kg)	Lightest ML ML clast (kg)	No. of ML clasts entrained at least once	Total no. of registered entrainment events	Total no. of discarded entrainment events	Heaviest ML clast entrained (kg)	Lightest ML clast not entrained (kg)
1	14-Oct-2012 16:25:00	0.66	4.7	plunging	15/12	2.455	0.902	12	374	70	2.455	N/A

Table 3.4: Table of empirical values for each of the Abbotsham motion logger experiments. The 'not applicable' abbreviation (N/A) indicates no ML clast remained stationary in the experimental run.

3.7.1 Flathead Lake

The significant wave height and mean period measured by the MAVS during each experiment ranged from 0.1 m and 2.3 s in the calmest experiment, to 0.52 m and 3.1 s during one of the most intense storms of the entire field campaign. The wave spectrum tended to be dominated by a narrow frequency band, which simplified the process of identifying individual threshold wave series (see Figure 3.10). The surf similarity parameter for the peak component of the spectra was inversely related to wave power and varied from between 0.5 and 0.8, which is indicative of spilling and plunging waves.

(A)

(B)

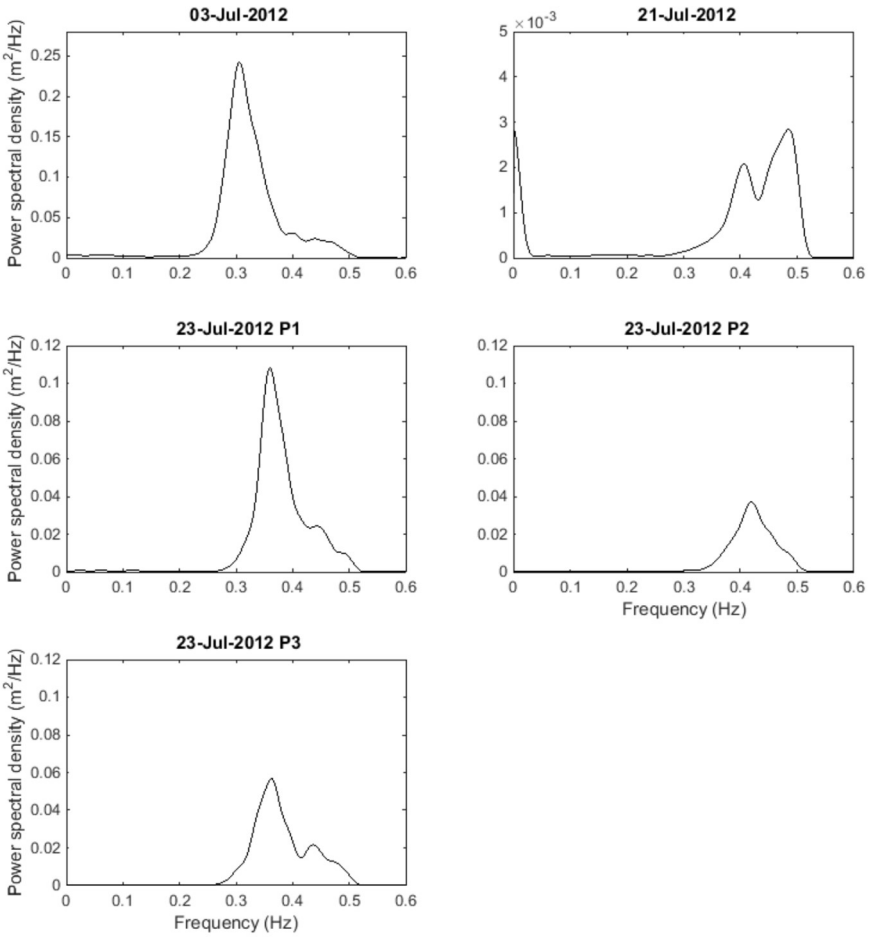

Figure 3.10: (A) Image of the beach at Flathead Lake during the experimental run on 03 July 2012 and (B) Wave Spectrum measured by the MAVS during each of the five ML experiments at Flathead Lake.

3.7.1.2 Motion Logger Time Series Data

The raw tilt and acceleration records showed clast motions to vary from small-scale fluctuations about a relatively fixed orientation, to major one-way shifts in the orientation of one or more axes. The mobility of clast was closely related to the prevailing wave conditions. The motion of clasts was often synchronised and appeared to be coincident with the measurement of particularly large incident waves. During each experiment, the magnitude of the measured clast accelerations was inversely related to clast mass, and heavier clasts tended to remain stationary for a greater proportion of the time.

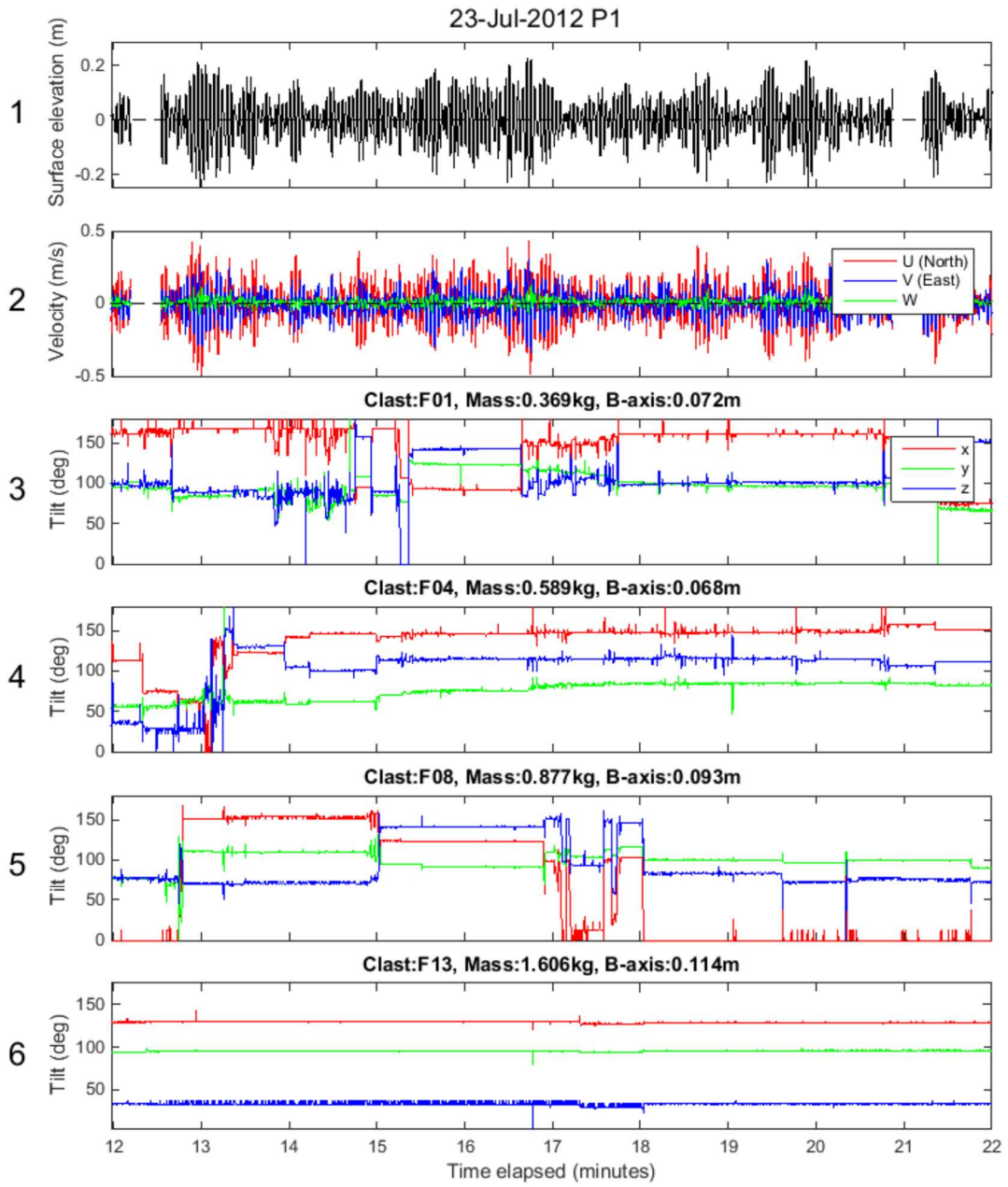

Figure 3.11: Time series of the: surface elevation (1) and three-dimensional velocity measured by the MAVS (2); three-dimensional tilt record from increasingly heavy ML clasts ((3) 0.369 kg; (4) 0.589 kg; (5) 0.877 kg; (6) 1.606 kg) measured on the first experimental run on 23 July 2012. A number of motion events, identifiable by the significant shift in the tilt of one or more ML axes, are evident in the record of all ML clasts. Some of these clast motions appear to be synchronised and correspond with the presence of particularly large waves (see the record MAVS and ML record at approximately 16 minutes and 40 second). While the three smaller clasts were mobilised on multiple occasions, the largest clast remained stationary throughout the experiment.

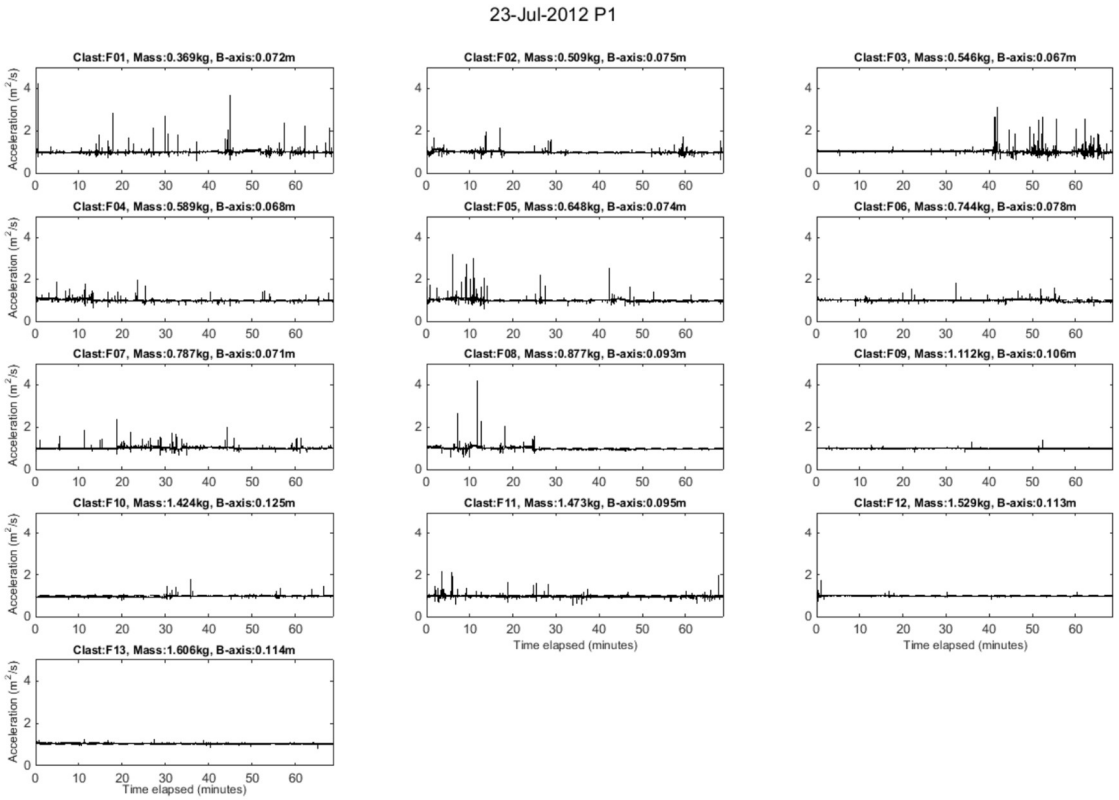

Figure 3.12: Time series of the acceleration of each of the ML clasts deployed on run 1, 23 July 2012. The total acceleration of a stationary clast adds up to one. Clasts are organised according to mass, which increases from left to right and top to bottom. In general, lighter clasts are more mobile that heavier clasts.

Analysis of the three-dimensional tilt records with the algorithm enabled the identification of major rollover events coherent with entrainment. The entrainment criterion was satisfied on one or more occasions in all but one of the experimental runs (on 20 July 2012). Indeed, with exception to F13; each ML clast was entrained at least once throughout all experiments at Flathead Lake. It is also noted that the acceleration signatures concurrent with clast rollover were both subtle and highly variable (see Figure 3.13). This supports the previous assertion that entrainment should be based on clast tilt (rollover) and not the acceleration record.

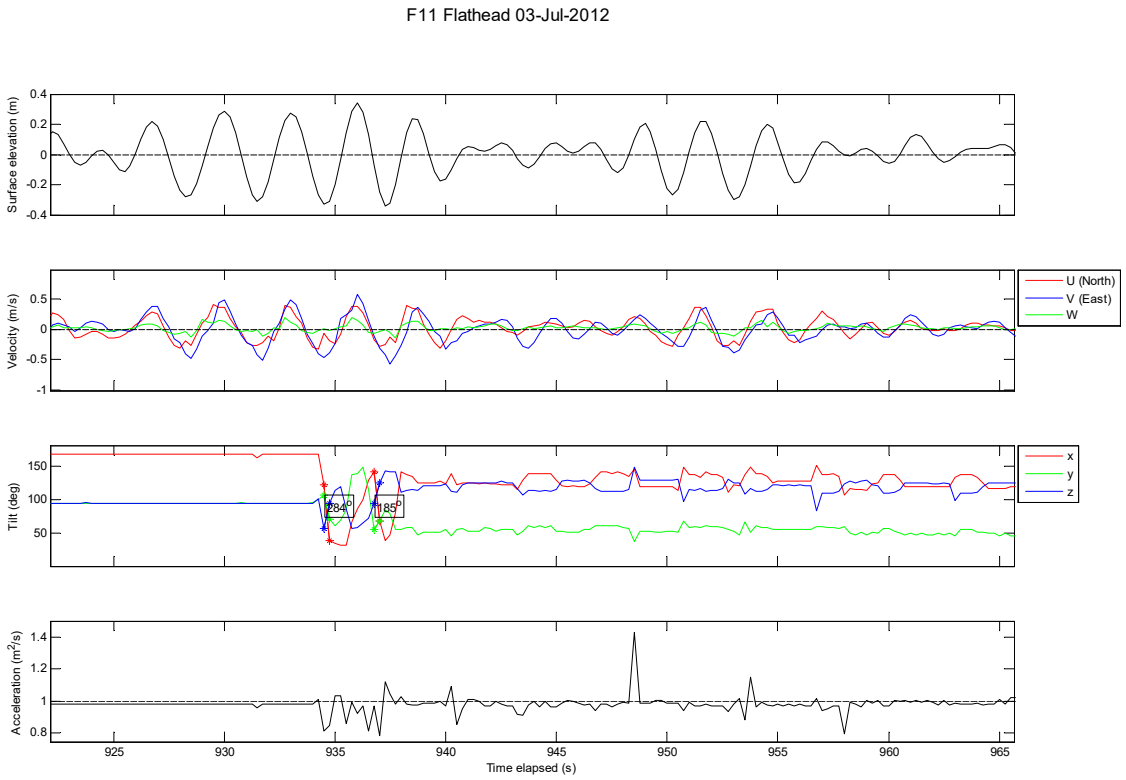

Figure 3.13: An excerpt of the concurrent: surface elevation (top) and three-dimensional fluid velocity (second) time series from the MAVS and; three-dimensional tilt (third) and acceleration (bottom) time series from F11 ML clast during the first experimental run on 3 July 2012. The MAVS pressure record indicates the presence of a large set of incident waves. The three-dimensional fluid velocity reflects the surface profile. Two discrete entrainment events coincide with the wave set. The first rollover measured 284 °, and is quickly followed by a successive roll of 185 °. Despite the rollover event being clearly captured in the three-dimensional tilt record, the associated acceleration record is far more subtle and unclear. See the Electronic Appendix 1 for all such time series plots.

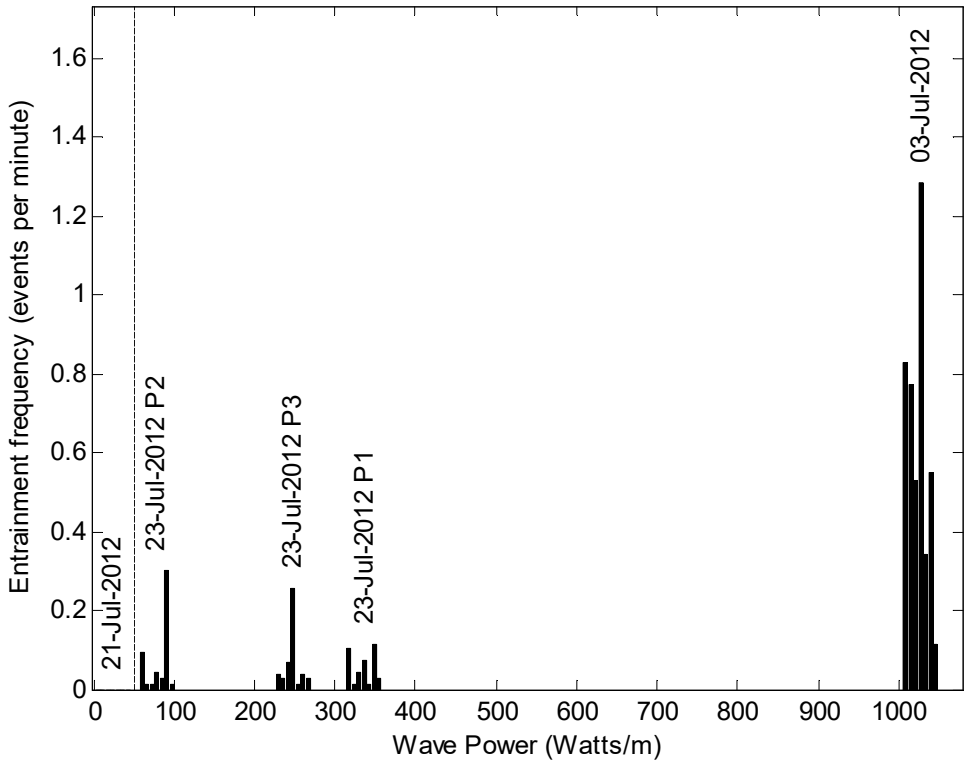

Figure 3.14: Entrainment frequency for a subset of seven ML clast (F01, F02, F04, F05, F06, F07 & F11) that were deployed in all Flathead Lake experiments versus the power of prevailing waves. The vertical dashed line highlights a critical boundary between experimental runs in which none (20 July 2012) and all (P2, 23 July 2012) of the clasts were entrained. The entrainment frequency tends to increase with wave power and on 03 July 2012, F05 exceeded one entrainment event per minute.

The frequency with which clasts were entrained was positively related to the prevailing wave power and increased from zero in calm conditions (on 20 July 2012) to a maximum of approximately one entrainment event per minute per clast in the most powerful storm event (on 3 July 2012). There appeared to be no clear relationship between entrainment frequency and the mass of the ML clast. Instead, the entrainment frequency was highly variable with one clast occasionally being entrained a significantly greater number of times than its neighbours.

3.7.1.3 Motion Logger Clast Displacement

This section briefly explores the link between the novel real-time motions of clasts and their x, y displacement over each of the three experimental runs on 23 July 2012. For reasons addressed in the discussion section (3.8.2.1) of this chapter, clast displacement cannot be reconstructed from the motion logger data, but is obtained from supplementary DGPS measurements made before

and after each run. It is important to note the lack of DGPS data on 05 and 21 July 2012 means a quantitative assessment of the displacement of ML clasts in these runs not possible.

A number of factors affected the accuracy of DGPS measurements and their compatibility with the motion logger records should first be noted. Dense woodland situated just shoreward of the experimental beach at Flathead Lake impeded the DGPS' connection with passing satellites and consequently the accuracy of measurements. The DGPS data is accurate to approximately 0.38 m and is insensitive displacements that do not exceed this distance.

Moreover, there was a slight mismatch between the timing of DGPS measurements and the motion logger record. The positions of each of the ML clasts were measured when they were initially deployed, however clast motions were only analysed after ten minutes had elapsed from the time at which the first ML clast was set running. This 'settling-in' period was crucial to ensuring clasts motions included in the analysis were the result of wave action and not the handling of field worker. ML clast retrieval (when the final positions were measured) was timed to occur after the motion loggers had finished running. Although this was a relatively simple and succinct task at Flathead Lake, it is inevitable that some ML clasts remained *in-situ*, and were perhaps displaced, during the short period (e.g. minutes) after the motion loggers ceased recording.

Despite the DGPS measurements not being a perfect counterpart to the motion logger records, they provide a general context for ML clast displacement during the experimental runs. Figure 3.15 shows that in all three of the experimental runs conducted on 23 July 2015 ML clasts were not displaced far from the positions in which they initially deployed and, most importantly, were not displaced outside the nearshore zone. The poor accuracy of the DGPS meant ML logger clasts were often recorded as having not moved at all. In reality this is most unlikely, not least because of errors associated with taking precise DGPS measurements.

Figure 3.15: Displacement of ML clasts over each of the three experimental runs conducted on 23 July 2012. Arrows indicate clast displacement, red dots indicate the measured position of clasts and white patches represent the uncertainty associated with the DGPS measurements. Aerial imagery of the experimental beach (taken in 2009) was obtained from the Montana State website (www.geoinfo.msl.mt.gov).

Table 3.5 to Table 3.7 presents the number of logged entrainment events alongside ML clast displacement. These data showed that the sum of multiple entrainment events did not necessarily correspond to considerable x, y displacement. This finding was typified by F07 during 23 July 2012 P2, which was entrained on 22 separate occasions yet was only displaced by 0±0.38 m. It seems most likely that this situation indicates a scenario in which the clast is successively entrained to-and-fro about a stationary point.

Confusingly, three ML clasts that were not entrained during the allotted observation time were recorded as having been displaced by 0.75±0.38 m. There are a number of potential explanations for this, including:

(1) ML clast displacement occurring in the initial 10 minute 'settling in' period;
(2) erroneous DGPS measurements;
(3) ML clast displacement resulting from non-rotational entrainment event(s).

It is not possible to further explore the precise relationship between clast entrainment and displacement. However, an improved positional monitoring scheme is proposed in the discussion section of this chapter to develop the basic interpretation presented here.

23-Jul-2012 P1		
Clast Name	**Entrainment No.**	**Displacement Distance (m)**
F01	3	0.00±0.38
F02	2	0.75±0.38
F03	1	1.34±0.38
F04	5	0.75±0.38
F05	19	0.75±0.38
F06	1	1.11±0.38
F07	3	0.00±0.38
F08	7	0.00±0.38
F09	1	1.11±0.38
F10	0	0.00±0.38
F11	2	0.00±0.38
F12	0	0.00±0.38
F13	0	0.00±0.38
F15	4	0.75±0.38

Table 3.5: Number of entrainment events and displacement distance recorded for each ML clast deployed in the first experimental run on 23 July 2012.

23-Jul-2012 P2		
Clast Name	**Entrainment No.**	**Displacement Distance (m)**
F01	7	0.00±0.38
F02	1	0.00±0.38
F03	0	0.00±0.38
F04	1	1.11±0.38
F05	3	0.00±0.38
F06	2	0.00±0.38
F07	22	0.00±0.38
F08	0	0.75±0.38
F09	0	0.00±0.38
F10	0	0.75±0.38
F11	1	0.00±0.38
F12	0	0.00±0.38
F13	0	0.00±0.38
F15	0	0.00±0.38

Table 3.6: Number of entrainment events and displacement distance recorded for each ML clast deployed in the second experimental run on 23 July 2012.

23-Jul-2012 P3		
Clast Name	**Entrainment No.**	**Displacement Distance (m)**
F01	7	0.00±0.38
F02	1	0.75±0.38
F03	15	0.00±0.38
F04	3	0.00±0.38
F05	5	0.75±0.38
F06	1	0.00±0.38
F08	6	0.00±0.38
F09	0	0.00±0.38
F10	1	0.00±0.38
F11	2	0.00±0.38
F12	1	0.00±0.38
F13	0	0.00±0.38
F14	0	0.00±0.38
F15	0	0.75±0.38

Table 3.7: Number of entrainment events and displacement distance recorded for each ML clast deployed in the third experimental run on 23 July 2012.

3.7.1.4 Comparisons of the Observed & Predicted Threshold-entrainment

The observed threshold-entrainment was compared with predictions made with the equation of Lorang (2000). The comparisons were conducted in two separate ways (as explained in section 3.3.2). First, the threshold-entrainment was considered with respect to the prevailing power, based on the significant height and mean period of incident waves measured during each of the experimental runs. Secondly, in section 3.7.1.5, comparisons are made with the outputs of the equations when forced with the characteristics of the weakest threshold wave series associated with each clast.

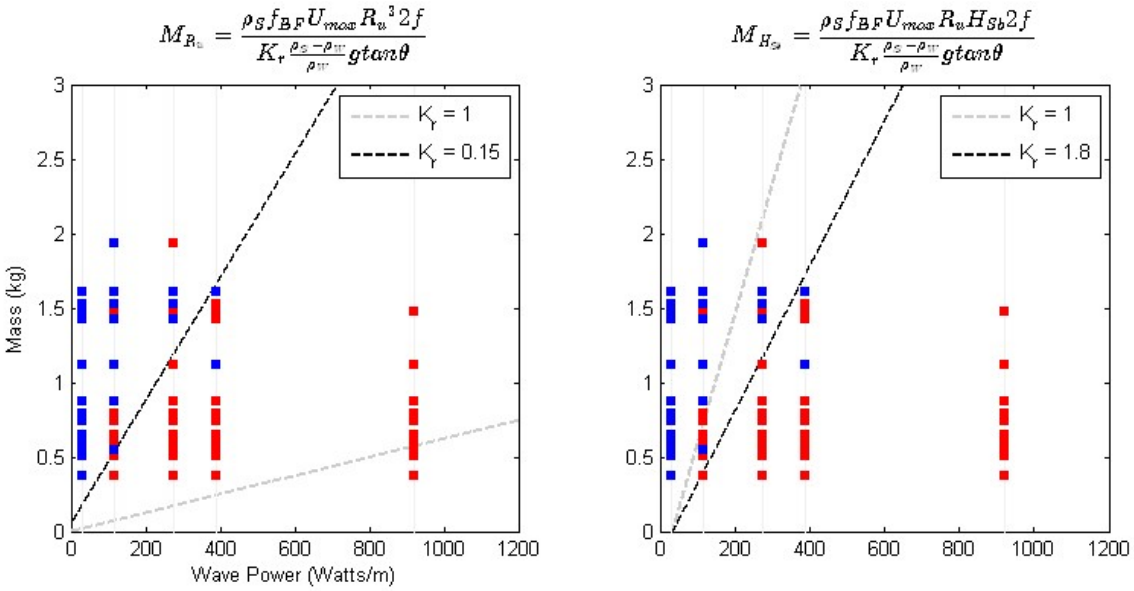

Figure 3.16: Clast mass versus prevailing wave power for each of the five experimental runs at Flathead Lake (left & right). Red points represent clasts that were entrained at least once during the experiment and blue points indicate clasts that remained stable. The dashed horizontal lines represent the threshold-entrainment predicted with Equation 3.17 (left) and Equation 3.18 (right). The predicted threshold-entrainment for each equation is demonstrated with two K_r values. The grey dashed lines indicate the un-optimised equation outputs, for which the stability coefficient was set to one. The black line shows the threshold-entrainment where the K_r values have been tailored to best replicate the observed threshold-entrainment.

The initial comparison is similar to those conducted by Lorang (2000) and Oak (1986), who forced various threshold-entrainment equations with the significant wave height and mean period of waves associated with the most powerful conditions measured between beach surveys. Figure 3.16 demonstrates a positive relationship between the likelihood of clasts becoming entrained and prevailing wave power. However, the precise dynamics of individual clasts is more variable. Indeed, the maximum entrainment mass is generally greater

than the minimum stable mass, which somewhat complicates the relationship between the threshold-entrainment and prevailing wave power.

Outputs from the two Lorang equations straddled the observed threshold-entrainment. While the un-optimised Equation 3.17 systematically under-predicted the critical entrainment mass, Equation 3.18 (which is scaled to a higher wave energy) marginally over-estimated the observed threshold-entrainment. Optimal results were found when K_r was reduced to 0.15 and 1.8 for Equation 3.17 and Equation 3.18 respectively. Here, clasts heavier than the predicted threshold-entrainment tended to remain stationary, lighter clasts were generally entrained on at least one occasion during the course of the experimental run.

3.7.1.5 Relating Clast Entrainment to the Threshold Wave Series

A key benefit of using motion logger data is knowing precisely when an entrainment event occurred, and hence the ability to relate entrainment to the properties of an *individual wave* or 'threshold wave series'. In this section, clast entrainment is considered with respect to the weakest associated threshold wave series. This is firstly demonstrated for each experimental run (see Table 3.8 and Figure 3.17) before the results from all experiments are compiled in order to consider the absolute weakest wave that entrained each of the ML clasts (see Table 3.9 and Figure 3.18).

ML clast name	Mass (kg)	03-July-2012			21-July-2012			23-July-2012 P1			23-July-2012 P2			23-July-2012 P3		
		H (m)	*T* (s)	*P* (Watts/m)	*H* (m)	*T* (s)	*P* (Watts/m)	*H* (m)	*T* (s)	*P* (Watts/m)	*H* (m)	*T* (s)	*P* (Watts/m)	*H* (m)	*T* (s)	*P* (Watts/m)
F01	0.369	0.20	3.0	135	N/E			0.08	3.8	25	0.08	2.5	17	0.18	2.5	93
F02	0.509	0.09	2.3	20	N/E			0.30	2.8	287	0.09	2.5	24	0.09	3.3	30
F03	0.546	0.14	3.0	64	N/E			0.06	3.3	13	N/E			0.13	2.8	56
F04	0.589	0.13	4.0	68	N/E			0.27	3.3	267	0.05	2.3	5	0.15	3.3	82
F05	0.648	0.14	3.0	69	N/E			0.18	3.3	121	0.13	2.3	43	0.09	3.0	24
F06	0.744	0.20	3.5	153	N/E			0.04	2.0	4	0.04	2.0	3	0.18	3.8	124
F07	0.787	0.20	3.5	153	N/E			0.12	4.0	55	0.04	3.3	6	0.24	3.0	196
F08	0.877	0.32	3.3	373	N/E			0.09	2.0	17	N/E			0.12	3.3	54
F09	1.112	0.20	3.0	135	N/E			N/E			N/E			0.16	3.0	87
F10	1.424	N/D			N/E			0.41	2.8	521	N/E			N/E		
F11	1.473	0.39	2.8	489	N/E			0.13	2.3	45	0.17	2.8	94	0.14	3.8	80
F12	1.529	N/D			N/E			0.02	2.0	1	N/E			N/E		
F13	1.606	N/D			N/E			N/E			N/E			N/E		
F15	1.933	N/D			N/D			N/D			N/E			0.07	2.3	12

Table 3.8: Table of the weakest threshold wave series identified for each of the ML clasts during each of the Flathead Lake experiments. Where a ML clast was not entrained, and thus no threshold wave series was identified, cells are shaded in light grey and assigned the term 'N/E'. Where a ML clast was not deployed, cells are shaded in dark grey and assigned the term 'N/D'.

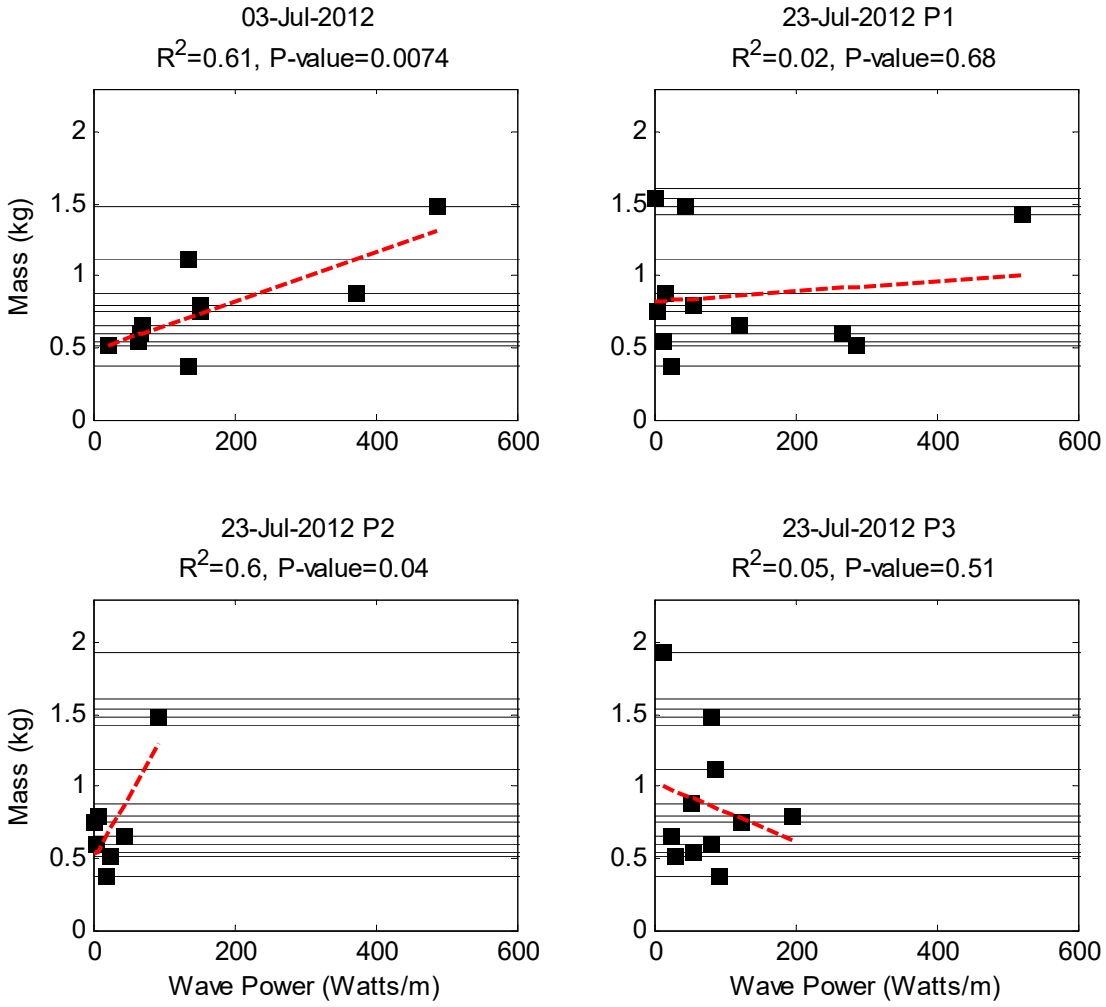

Figure 3.17: Clast mass versus power of the weakest threshold wave series for each of the experiments in which an entrainment event was registered (i.e. all experimental runs except 21 July 2012). The horizontal lines highlight the clasts deployed during the experimental run. The lines of best fit are red and dashed.

The power of the weakest threshold wave series associated with each ML clast is highly variable and dependent on the prevailing wave conditions. While a statistically significant positive relationship between the entrainment mass and wave power is evident during the relatively energetic conditions on 03 July and second experimental run on 23 July 2012, no trend is evident during the other two experimental runs. Importantly, the positive relationships observed on 03 July and the second run on the 23rd of July are quite different and clast entrainment was not exclusive to the most powerful incident waves. A number of ML clasts were observed to be entrained by exceedingly weak threshold wave series (< 50 Watts/m), which were far less powerful than a wave with the significant height and mean period measured during each experimental run.

The weakest threshold wave series from all experimental runs were compiled in order to identify the absolute minimum wave power required to entrain each clast. The grouped data shows no clear relationship between power and the critical entrainment mass (see Figure 3.18) and each clast (with exception to F10) has been entrained at least once by an exceedingly weak wave. It was assumed that F10 is an outlier and is therefore not included in the following comparison with the predictions from the threshold-entrainment equation.

ML clast name	**Mass (kg)**	**Absolute weakest threshold wave series**		
		H (m)	*T* (s)	*P* (Watts/m)
F01	0.369	0.08	2.5	17
F02	0.509	0.09	2.3	20
F03	0.546	0.06	3.3	13
F04	0.589	0.05	2.3	5
F05	0.648	0.09	3.0	24
F06	0.744	0.04	2.0	3
F07	0.787	0.04	3.3	6
F08	0.877	0.09	2.0	17
F09	1.112	0.16	3.0	87
F10	1.424	0.41	2.8	521
F11	1.473	0.13	2.3	45
F12	1.529	0.02	2.0	1
F13	1.606	N/E		
F15	1.933	0.07	2.3	12

Table 3.9: Table of the weakest threshold wave series identified for each of the ML clasts over all of the Flathead Lake experiments. Where a ML clast was not entrained cells are shaded in light grey and assigned the term 'N/E'.

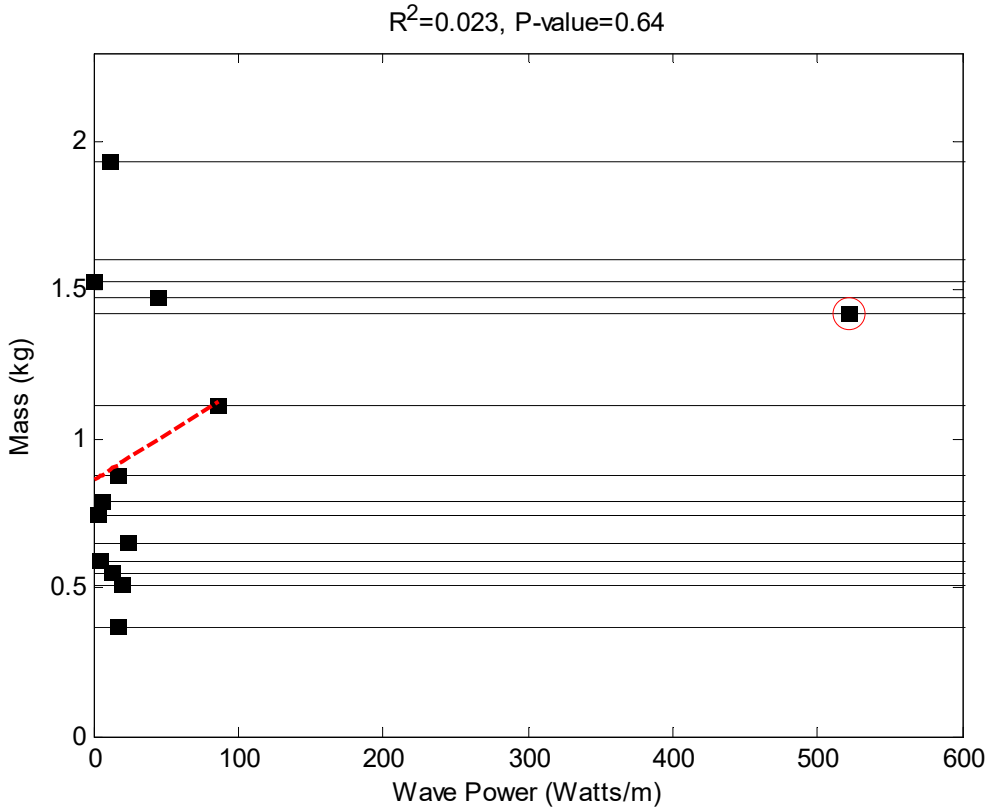

Figure 3.18: Clast mass versus power of the weakest threshold wave series identified over all experimental runs at Flathead Lake. The horizontal lines highlight the clasts deployed for at least one of the Flathead Lake experiments. The line of best fit is red and dashed. There is no clear trend between the clast mass and the weakest threshold wave series. The critical entrainment mass was exceedingly weak (< 100 Watts/m) for all but one (F10 - encircled) outlier.

Large disagreement was found between the observed threshold-entrainment and predictions made with the un-optimised threshold-entrainment equations despite optimising the stability coefficients (see Figure 3.19). Here, K_r values between 0.1 and 1 were systematically tested and it was found that the smallest possible coefficient (K_r = 0.1) provided the best prediction for both equations (i.e. Equation 3.17 and Equation 3.18). Despite this, Equation 3.17 still systematically underestimated the critical entrainment mass. Equation 3.17 and Equation 3.18 only accounted for 6 and 11 % of variability in the observed threshold entrainment respectively; however the significance of both of the trends was particularly low (*P-value* equalled 0.49 and 0.33 respectively).

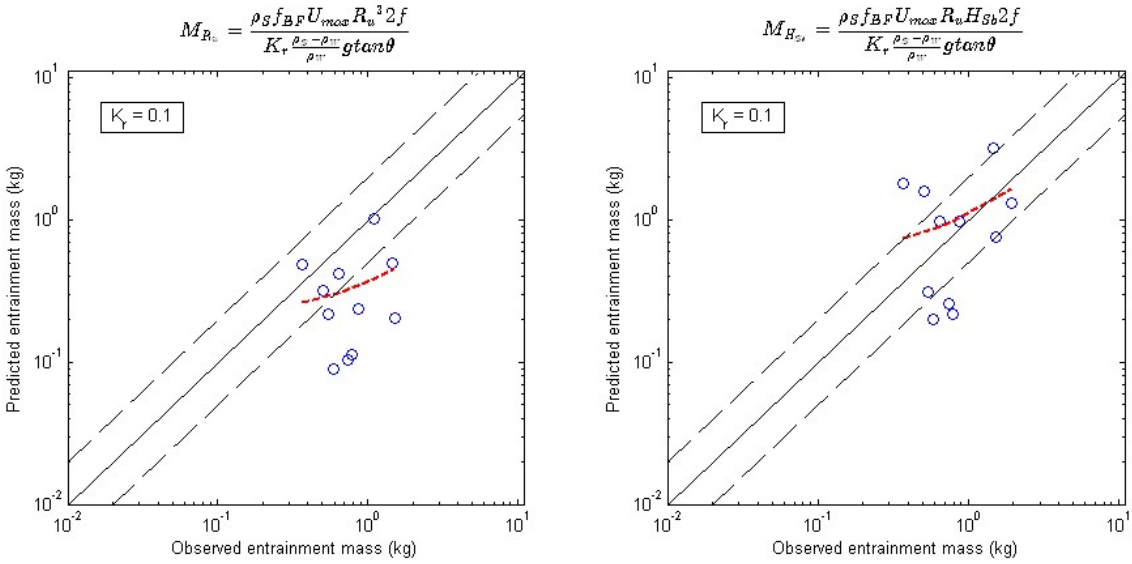

Figure 3.19: Observed versus predicted critical entrainment mass. Predictions were made by forcing Equation 3.17 (left plot) and Equation 3.18 (right plot) with the characteristics of the weakest threshold wave series associated with each of the ML clasts. The diagonal solid line denotes agreement, and the diagonal dashed lines are a factor of two either side of agreement. The line of best fit is plotted on each graph in red. Agreement between the observed and predicted entrainment mass is poor, which is reflected in the basic correlation statistics. The R^2 and *P-value* for: Equation 3.17 (left) is 0.055 and 0.49 respectively; Equation 3.18 (right) is 0.11 and 0.33 respectively.

3.7.2 Abbotsham

In addition to the five Flathead Lake experiments, motion loggers were also deployed at Abbotsham in a less successful experiment. The experimental run coincided with relatively calm conditions (H_S < 1 m) considering the exposure of the field site. Notwithstanding this, the dominant component of the wave spectra measured during the Abbotsham experiment (3719 Watts/m) was over four times more powerful than that measured during the stormiest ML run at Flathead Lake (869 Watts/m) (see Figure 3.20). Also present were multiple higher-frequency components (up to 0.5 Hz) that complicated the wave field and ability to attribute clast entrainment to a threshold wave series.

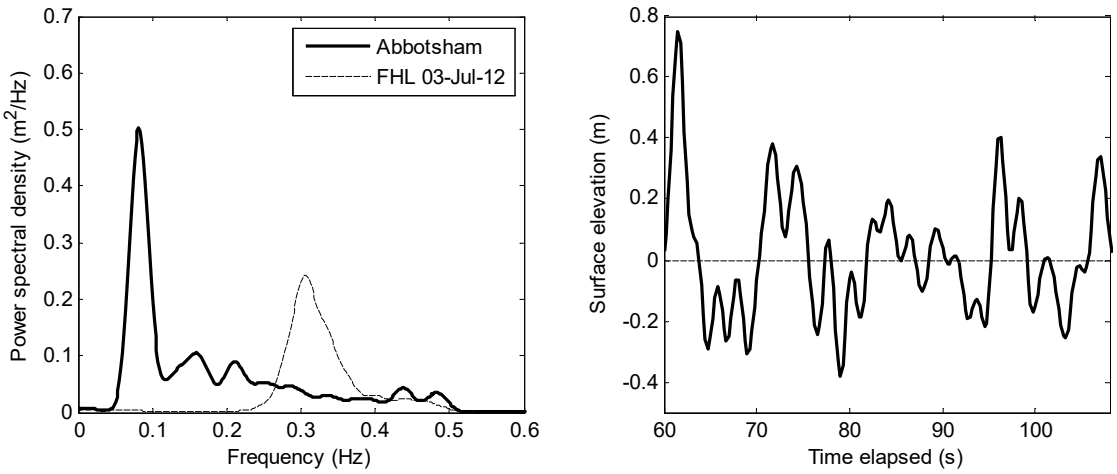

Figure 3.20: Wave spectral plot during the Abbotsham and stormiest Flathead Lake (FHL) ML experiment (left) and excerpt of the nearshore surface elevation time series during the Abbotsham ML experiments (right).

Figure 3.21: Aerial photo of the experimental beach at Abbotsham indicating the position of the wave gauge and the 20 m transect along which the ML clasts were deployed.

The energetic shore break made ML clast deployment difficult. It was not possible to accurately measure the initial deployment positions of each individual ML clast. The transect along which ML clasts were deployed is approximated in Figure 3.21 from the few DGPS measurements that could be made. Of course, the beach was only accessible the following day; long after the motion loggers had ceased recording. It is therefore not possible to conduct

a meaningful comparison between clast entrainment and x, y displacement (which was conducted in section 3.7.1.3).

3.7.2.2 Motion Logger Time Series Data

Despite the (relatively) powerful wave conditions, a misjudgement in the size of clasts selected meant the Abbotsham ML clasts were only marginally heavier than those deployed in Flathead Lake (see Table 3.1 & Table 3.2). The time series data from the deployment demonstrate two modes of behaviour characterised by either constant motion or sustained stillness. The dynamics of the ML clasts was not synchronised, and while some clasts were in motion others remained stationary. This is demonstrated in an excerpt of the acceleration time series of the ML clasts displayed in Figure 3.22, where number of clasts (e.g. A01, A03, A04, A07, A09, A13, A12) settled within the first 30 minutes while others (e.g. A02, A08, A14, A15, A16) remained highly mobile throughout the experiment. The tendency to either settle or remain mobile appears to be independent of clast mass.

The reasons for the abovementioned trends are (as discussed in section 3.8.4) uncertain. However the fact that the ML clasts were buried up to 0.5 m within the beach matrix by the following day suggests that the threshold-entrainment of all ML clasts was far exceeded, and conditions were energetic enough to mobilise a large fraction of the surrounding clasts and for considerable vertical mixing (burial) to occur.

Notably, the burial depth of ML clasts is particularly large in relation to the seemingly comparable values reported in section 4.10.3 (Chapter 4), which were obtained from a series of bespoke depth of activation experiments conducted in a range of conditions. However, the depth to which motion loggers were buried and the measured depth of activations differ in terms of the datum relative to which they were measured. The depth of activation experiments focussed on the mobilisation of successive layers of sediment below the beach surface and was reported relative to the lowest of the local beach elevations measured on day 1 and 2. This way, the localised accretion of sediment (between day 1 and 2) would not inflate the measured depth of activation. Conversely, the depth to which the ML clasts were buried would increase with the vertical mixing but also the local accretion of material.

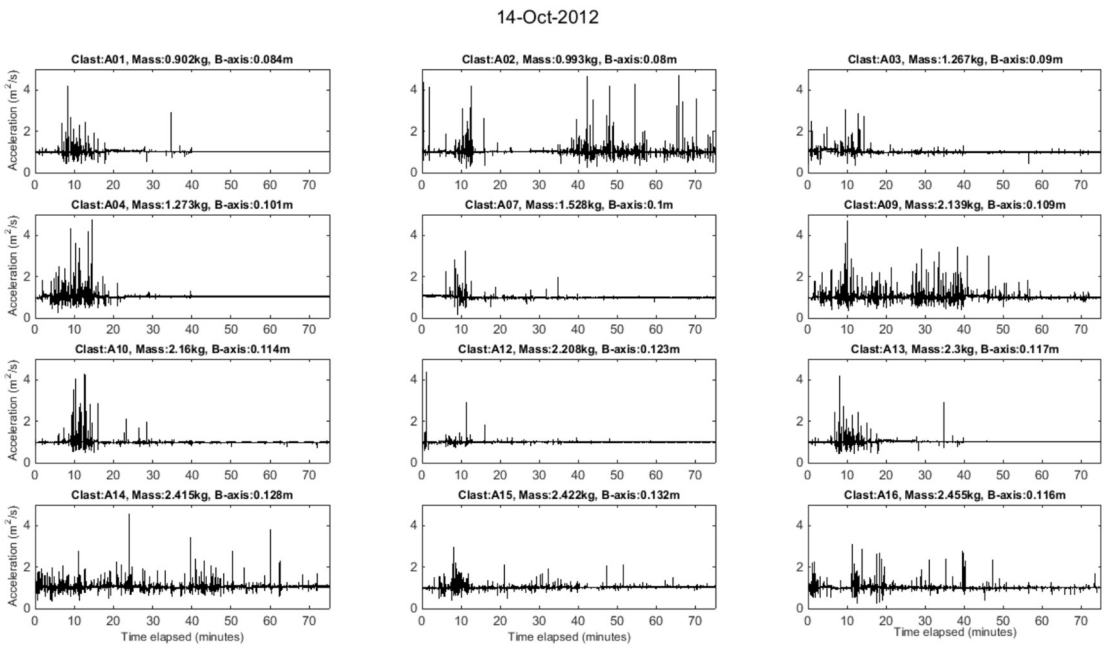

Figure 3.22: Time series of the acceleration of each of the ML clasts deployed at Abbotsham on 14 October 2012. Time series plots are organised according to clast mass, which increases from left to right and top to bottom. The total acceleration of a stationary clast adds up to one. Clast accelerations were much larger during the Abbotsham experiments, and accelerations greater than 4 g were recorded on numerous occasions.

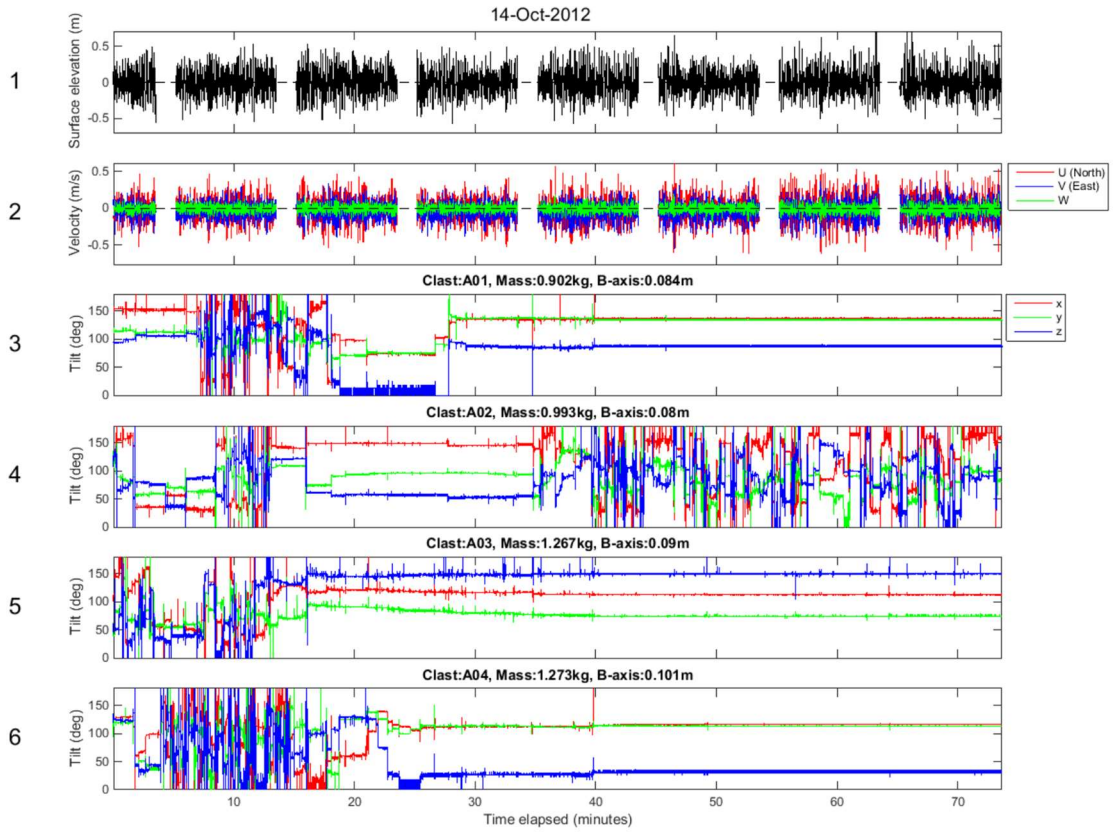

Figure 3.23: Time series of the: surface elevation (1) and three-dimensional velocity (2) measured by the MAVS; three-dimensional tilt record from increasingly heavy ML clasts (3 to 6) measured at Abbotsham. Maximum wave height was approximately 1 m and maximum fluid velocity of 0.5 m/s. The ML time series show clast motions to be rotational, with the tilt throughout each of the three axes regularly changing. ML clasts were either extremely active or remarkably still. All four clasts were initially mobile before settling abruptly after approximately 20 minutes. While A01, A03 and A04 remain stationary, A02 was entrained again at 35 minutes and was in continual motion for the remainder of the experiment.

The energetic and complex sea state during the Abbotsham ML experiment meant the ability to identify the threshold-entrainment and attribute it to a threshold wave series was highly complex. Firstly, the observational methods employed here assume that each clast is in a surficial position and directly exposed to fluid flow. However, it was impossible to determine whether a ML clast is stationary because the hydrodynamic force was not great enough to destabilise it from its surficial position, or whether it was buried within the beach matrix and not directly exposed to the wave force. Secondly, many components of the of the wave spectrum that interacted to create the surface profile above the MAVS device travel at varying speeds. The simple translation of the profile measured at the MAVS to the position of the ML clasts (approximately 30 m away) is therefore highly erroneous. For these reason these data are deemed

unsuitable for the current threshold-entrainment investigations, and are instead discussed as a physical limitation to the methodology.

3.8 Discussion

3.8.1 Observed versus Predicted Threshold-entrainment

The threshold-entrainment identified in the motion logger record was compared with predictions made with the equations of Lorang (2000). This was conducted in two ways: firstly on an experimental basis, for which the observed and predicted threshold-entrainment were considered in relation to the wave conditions that prevailed throughout each run (see section 3.8.1.1); secondly on a wave-by-wave basis, for which the observed and predicted threshold-entrainment were considered in relation to the weakest associated threshold wave series (as discussed in section 3.8.1.2).

3.8.1.1 Experiment-based Analysis

The initial comparison was similar to previous works of Oak (1986) and Lorang (2000) and utilised the equations in the intended way. Here, Equation 3.17 and Equation 3.18 were forced with the significant height and mean period of the most powerful conditions that prevailed during each experimental run. It was found that while the stability coefficient was set to one, predictions from both equations straddled the observed threshold-entrainment (see Figure 3.16). Here, Equation 3.17 systematically underestimated the threshold-entrainment, while Equation 3.18 provided slight over estimates. Good correlation was achieved by using stability coefficients of 0.15 and 1.8 for Equation 3.17 and Equation 3.18 respectively.

The stability coefficient in the Lorang equations is comparable to the K_D constant in the Hudson Formula, and describes the shape, roughness and interlocking nature of clasts. Extensive wave tank experiments were previously conducted (SPM, 1984) to explore values of the stability coefficient required to predict the unit size of component clasts for the structure to remain unaltered when subjected to waves of given height. Values presented in SPM (1984) ranged from between 1.1 for smooth, rounded clasts under breaking waves at the structure head, to 31.8 for concrete dolos subject to non-breaking waves at the structure trunk. Importantly, the stability coefficient was in all instances used to increase the stabilising, immersed weight force (i.e. > 1).

The stability coefficient required to predict a comparable 'no damage' scenario for Equation 3.17 would be even less than the optimal value (0.15), and is therefore outside the value range identified for its counterpart in the Hudson formula. However, optimal correlation using Equation 3.18 (which is scaled to a higher wave energy due to the substitution of wave height for run up elevation) was found when the stability coefficient was set to 1.8. Consultation with the list of proscribed K_D values in the Shore Protection Manual (SPM, 1984) shows the tailored stability coefficient closely matches those found for a smooth, rounded clast under non-breaking waves (1.9) or rough, angular clasts under breaking waves (1.3 to 1.9) located at the beach head. Considering the wide range of K_D values (1.1 to 31.8), the K_r value for Equation 3.18 corresponds closely with its counterpart in the Hudson Formula under similar circumstances. A more comprehensive understanding of the accuracy of the threshold-entrainment equations and optimal K_r values requires further field data using a range of clast shapes and sizes.

3.8.1.2 Threshold Wave Series Analysis

Analysing the threshold-entrainment at a frequency consistent with the entrainment process itself demonstrated clasts were occasionally entrained by exceedingly weak waves. Predictions of the critical entrainment mass produced by forcing Equation 3.17 and Equation 3.18 with the characteristics of the weakest threshold wave series was systematically less than that observed (see Figure 3.19). Reasonable agreement could only be achieved when the stability coefficient in both equations was reduced to 0.1. However, the stability coefficients found for the Hudson Formula are greater than 1, and thereby increase the stabilising forces (and reduce the critical entrainment mass) in the threshold-entrainment equations (see SPM, 1984). Although not explicitly stated in the literature, it is intuitive that the K_r value for the most exposed and precariously positioned clast should theoretically be one. Conversely, the optimal K_r values (of 0.1) act to reduce the stabilising expression and its function is therefore at odds with the comparable K_D factor found for the Hudson Formula.

No clear relationship was found between the critical entrainment mass and wave power of the weakest threshold wave series (see Figure 3.18). However, it is somewhat confounding that the threshold-entrainment based on the

weakest threshold wave series is smaller than that identified on an experimental basis. It was found that individual threshold wave series were associated with the entrainment of ML clasts far heavier than the un-optimised Lorang (2000) equations predicted. In fact, the potential entrainment of clasts far larger than predicted for given wave conditions could have serious implication for the practical application of the equations. It is therefore important to establish whether this is a genuine result, or a product of limitation(s) to the methodological approach.

The entrainment of clasts far heavier than the predicted critical entrainment mass perhaps indicates the importance of physical factors not described by the shear stress approach of Lorang (2000). The effect of the pressure gradient force (dp/dx) is reported to have a significant impact on the threshold-entrainment of sand grains (e.g. Madsen, 1974; Sleath, 1999; Foster et al., 2006). Foster et al. (2006) proposed the threshold-entrainment is determined by the combination of the shear stress and pressure gradient forces which can add or oppose each other. The ML clasts were located in the breaker and swash zones, where the wave profiles, and thus pressure gradients, reach their most critical values. The entrainment by the weakest threshold wave series was perhaps only achieved through the combination of these two forces under steep breaking waves. The influence of the pressure gradient force cannot be investigated with the current entrainment datasets, but would instead require wave measurements in the precise location of ML clasts.

Alternatively, the variable characteristics of the individual threshold wave series associated with each clast might indicate limitations to the threshold wave series approach. As described in section 3.8.3, interaction between the various spectral components might well continue within the short distance between the MAVS and position of the ML clast, and hence reduce the relevance of the MAVS measurement. Meanwhile, these detailed spectral intricacies are smoothed out in the cumulative, experiment-based wave parameters, with which an improved relationship was found. In any case, uncertainty surrounding the threshold wave series approach cannot be further explored here, but required improved wave measurement ideally in the precise position of each ML clast.

3.8.2 Defining Threshold-entrainment with Motion Loggers

3.8.2.1 Defining Clast Motion

Although motion logger outputs included the three-dimensional time series of acceleration, clast entrainment was defined purely with respect to rotation, based on analysis of the three-axial tiltmeter readings. The method was therefore insensitive to non-rotational (sliding) motions. The decision to not include clast accelerations within the analyses was made because of the difficulty with which large, coherent motions could be accurately distinguished from non-coherent vibrations ('noise') at a sample frequency of 4 Hz. These difficulties were due to the temporally fine nature of an acceleration signal and relatively coarse sample frequency. Conversely, change in the three-dimensional tilt between time series are additive and, as long as the clast did not rotate more than 180 ° between (0.25 s) time steps, rotation could be accurately resolved.

Where clast rotation between time steps was greater than 180 °, the algorithm would register a rotation of 360 ° minus the actual rotation in the opposite direction. This would not only underestimate the rotation that had been made, but the reversed sign of the initial rotation would mean it would not be included as part of any continuation. Considering the energetic nature of the littoral zone, it seems likely that clasts would make excessively rapid rotation, and that the current methodology is only partially sensitive to rotational motions under shoaling waves.

The ability to fully-capture rapid clast rotations and include clast accelerations in the analyses would simply result from an increased ML sample frequency. The sampling frequency of the motion loggers used in the present investigation was limited to 4 Hz. However, comparable wave tank experiments utilising custom-built motion loggers programmed them to sample at a frequency of 50 Hz (Frank et al., 2013). In principal, the trajectory of the clast can be reconstructed from the fully-resolved three-dimensional acceleration record, through a process called 'inertial navigation'. Given knowledge of its initial orientation, the clast's trajectory could be converted into three-dimensional geographic coordinates, as described by Abeywardana et al. (2009). It is not difficult to imagine the numerous applications, in both littoral and fluvial environments, of a 'smart' clast

with inertial tracking capabilities. In terms of the present investigation, knowledge of the precise position of the clast at any given moment would help relate entrainment events to the overlying threshold wave series.

3.8.2.2 Defining Clast Entrainment

No entrainment criterion has previously been defined in terms of the rotation of an individual clast. A novel entrainment criterion was defined here in terms of the rotation required for a clast to become removed from its stable position. Considering a number of bedding scenarios, the rotational requirement was provisionally set at a relatively high value of 180 °. In reality, the rotational requirement for a clast to become removed from its stable position depends on the pivoting angle between the ML clasts and surrounding beach clasts. The importance of the pivoting angle on clast stability meant both Hudson (1953) and Lorang (2000) included descriptive terms in their threshold-entrainment equation within the K_D and K_r coefficients respectively. However, it was not possible to measure the pivoting angles of each ML clast throughout the experimental runs, the influence of which was therefore not explored.

3.8.3 Threshold Wave Series Limitations

Each entrainment event logged during a MAVS sampling burst was linked to the threshold wave series that was estimated to be overlying the ML clast at that time. The MAVS was deployed approximately 16 m and 30 m off the beach at Flathead Lake and Abbotsham respectively. Although the proximal wave measurements was an improvement on previous threshold-entrainment field studies (e.g. Oak, 1986), linking clast entrainment to an individual threshold wave series was challenging. The inability to track the location of ML clasts from the tilt and acceleration time series meant their precise position at any given moment was unknown. The ML clasts were however observed to not migrate out of the breaker/swash zone at Flathead Lake, but uncertainty associated with the precise whereabouts of the clast at each moment in time complicated the process of linking clast entrainment to a threshold wave series. It was assumed that the clast was underlying, and hence entrained by, the most powerful incident wave located between the MAVS and beach at the time of entrainment.

Further error might have resulted from the quantification of the threshold wave series. Importantly, the threshold wave series refers to the surface profile as a

function of the interaction of a spectrum of waves overlying the MAVS device. The preceding analysis considers the threshold wave series measured at the position of the MAVS device as a discrete entity and representative of the force acting on the ML clasts some distance away in the breaker/swash zone. In reality, the complex interaction between the various components of the wave spectrum are likely to continue within the short distance between the position of the MAVS and the breaker/swash zone, and influence the fluid force exerted on the ML clasts. It was for this reason that identification of the threshold wave series in the Abbotsham dataset was deemed too complex and is highlighted here as a limitation to the current method.

Moreover, the force exerted by a wave of given power is strongly influenced by the breaking process and therefore breaker type (Pedrozo-Acuña et al., 2008). The Surf Similarity numbers during the Flathead Lake and Abbotsham experiments suggest that the breaker zone was characterised by spilling and plunging waves respectively, the latter of which is characterized by a strong cross-shore gradient in the wave force. Plunging breakers generate turbulent, rotational fluid motions which results in the rapid dissipation of energy (Pedrozo-Acuña et al., 2008). It follows that the process zone in which a ML clast is located will have a significant impact on the force exerted by a given threshold wave series. The ability to trace the real-time position of the ML clast based on its inertia would not only aid the process of linking clast entrainment to a threshold wave series, but exploration of clast entrainment as a function of process zones.

3.8.4 Abbotsham Experiments & Threshold Exceedance

The Abbotsham-based experiments were complicated by a number of factors and highlighted some limitations and potential improvements to the current methodology. The wave conditions during the experimental run were highly complex, and included multiple incident wave frequencies. This is perhaps a key limitation to the methodological approach, because the wave field at exposed sites is often complex and a function of waves from multiple origins. Despite the conditions being relatively calm for the exposed field site, the low-frequency component of the swell was far more powerful than conditions observed during the most intense storm in Flathead Lake. Yet, the ML clasts selected for the experiment were only marginally larger than those deployed in

the USA. As a result the threshold-entrainment of all the ML clasts was far exceeded.

Perhaps of most interest was the disparity in the mobility of ML clasts at any given time. While some clasts remained highly mobile, the other apparently random selection was remarkably still. It is hypothesised that this pattern could be indicative sheet flow conditions, in which ML clasts were mixed vertically into the beach matrix. This scenario corresponded with the fact that ML clasts were buried down to 0.5 m on retrieval the following day. Alternatively, ML clasts which remained in motion might well have migrated, on the flooding tide, up the beach within the breaker/swash zone, whilst the others became stranded beyond these energetic process zones. Although these data are of limited use to understanding the threshold-entrainment they do provide insight into the intra-wave dynamics and show a large fraction of surficial clasts at Abbotsham to be highly mobile during calm conditions.

The Abbotsham experiments would have been improved by simply choosing larger clasts to house the motion loggers. These clasts would not be in continual motion and clast rollover would be a distinguishable event. The simple, low energy wave field generated in the fetch-limited setting of Flathead Lake enabled detailed process-based measurement to be obtained and clast entrainment to be related to a threshold wave series with a reasonable error margin. However, trying to apply the same methodology at the exposed, macro-tidal setting of Abbotsham was highly complex. Perhaps a better approach for the exposed field site would be to coarsen the sample frequency of the motion loggers and investigate the threshold-entrainment of clasts over a period of weeks or months. These data would provider limited process-based insight into the threshold-entrainment, but would yield a large-scale dataset with which to test and refine the equation of Lorang (2000).

3.8.5 Methodological Improvements

Experiments presented in this chapter constitute a novel approach to making field measurements of the threshold-entrainment in the littoral zone. They provided detailed, real-time data on a temporal scale which corresponds to the entrainment process. Moreover, they have highlighted some of the challenges and limitations associated with adopting a real-time approach to measuring

clast entrainment. It is hoped the current experiments will form an initial pilot for future motion logger field experiment. A few suggestions are made here to help subsequent studies build on the findings of the current investigation.

3.8.5.1 Motion Logger Clast Sample

It should be emphasised that the number of motion loggers used in the present experiments was determined by the available funds. The Flathead Lake and Abbotsham experiments incorporated a relatively small number of ML clasts, which were confined to a single zone of the beach. The experiment would be improved by increasing the sample to include a large range of class sizes in a variety of nearshore positions. To avoid a situation where (as in the Abbotsham experiment) the entire sample of ML clasts is far below the critical entrainment mass, the masses of ML clasts should range significantly in order to ensure the sample straddles the threshold-entrainment. Manufactured clasts would allow control of size, shape and density of clasts, and is therefore worth consideration (e.g. Maniatis et al., 2013).

3.8.5.2 Motion Logger Analysis

The current investigation measured clast motion through a highly-constricted rotational criterion, and was therefore insensitive to non-rotational motions. Meanwhile, the ML sampling frequency of 4 Hz meant that rotations greater that 720 °/s were not fully-captured. The ability to accurately analyse the acceleration time series and resolve rapid clast rotations is dependent on the sampling frequency of the ML device. The limited memory capacity of the *HOBO Pendent G* motion loggers meant that it was not possible to increase the sample frequency without reducing the already-brief run time of 1.5 hours. The ability to sample at such a high frequency would enable the full resolution of the acceleration and tilt time series data, and perhaps the migration pathways of an individual clast to be traced throughout time (Abeywardana et al., 2009). These improvements would help ascertain the real time position of clasts relative to the swash/breaker zone and reduce the uncertainty with which clast entrainment could be linked to an individual threshold wave series.

The suggested analytical improvements are dependent on the development of motion logger technology. Frank et al. (2013) presented findings from wave tank experiments using custom-built “Smart Sand Grains” (SSG). Like the HOBO

motion loggers, the SSG sensors were equipped with a tri-axial accelerometer to measure three-dimensional acceleration. However, the SSG sensors have a very large (flash card) memory capacity and are able to sample at a rate of 50 Hz. Data from the SSGs can be wirelessly transmitted, negating the need to relocate clasts in order to access data. It is suggested here that the use of motion loggers with similar capabilities to the SSG within the current field experiments would have greatly improved the entrainment analyses, and ultimately the ability to measure the threshold-entrainment.

3.8.5.3 Wave Measurements

The proximal position of the MAVS provided detailed measurements of the wave conditions from directly adjacent to the experimental beach. However, wave measurements would be improved by instrumentation of the swash zone in a fashion similar to Masselink et al. (2010). They deployed a cross-shore array of wave gauges between the breaker and swash zone. The array would both reduce uncertainty associated with linking individual waves to entrainment events but would also increase the relevance of the hydrodynamic measurements. An additional benefit to comprehensive instrumentation in the swash zone would be the ability to determine the break point and instantaneous pressure gradient force in the position of the ML clasts, which has been noted to have a significant role in the incipient motion and entrainment of sediments (Foster et al., 2006).

Run-up elevation is a key component of the Lorang equation. The Lagrangian nature of the swash zone makes the direct measurement of the run-up complex and beyond the means of traditional fixed instruments. In the current investigation, run-up was not measured directly but instead calculated using Equation 3.19. However, it is possible to measure wave run-up directly from geo-rectified image sequences of the wave swash (e.g. Holman & Guza, 1984). Here, the leading edge of the wave swash could be traced throughout time and enable the measurement of the run-up elevation, which could be directly input into the equations. This would improve confidence with which predictions made with the equations (and in particular Equation 3.17) could be critiqued, and would be a significant improvement on the current investigation.

3.8.5.4 Key Recommendations for Future Research

A brief overview of the key improvements identified in the results and discussion section of this chapter is provided here:

- Improvements resulting from increasing the modest 64,000 byte memory capacity of the HOBO motion loggers would be twofold:

  (1) ML clasts could be deployed for a longer period of time and capture the spin-up and spin–down of passing storms in addition to peak storm conditions. Increasing the deployment time would extended the (currently limited) field observations made and permit the exploration of the threshold-entrainment over a longer time scale (e.g. weeks, month).

  (2) The sampling frequency could be increased from 4 Hz. This would improve the resolution of particularly rapid rotations and therefore sensitivity of the method to entrainment events.

- The memory capacity of “off-the-shelf” motion loggers could be vastly increased with the right commercial incentives. Notwithstanding this, motion loggers can be custom-built with a particular specification in mind (e.g. Frank et al., 2013), which would negate the need to wait for the cooperation of a third party. It is recommended that the latter of these options is preferable for prompt research.
- Although the inhospitable and energetic nearshore at Abbotsham prevented the measurement of the time-varying positions of ML clast to be assessed, all clasts were clearly visible and accessible in Flathead Lake experiments. This enabled the initial and final position of each of the ML clasts to be measured with a DGPS unit for the three experimental runs conducted on 23 July 2012. However, the limited accuracy of measurements and the slight mismatch with the timing of the motion logger run meant these data could only be used to provide general context about the migration of ML clasts. A primary recommendation for similar experiments conducted in comparable setting would be to accurately measure the position of ML clasts at regular intervals throughout each experimental run. These data would

provide improved insight into the link between real-time motions and the net transport of coarse clasts in the natural beach setting.

- Wave run-up height measurements made with a digital camera would improve the assessment of the threshold-entrainment equations as these data could be used to force Equation 3.17 negate the need for wave run-up to be calculated from MAVS measurements, which were made outside the surf zone. This would address suspected issues about the importance spectral interaction shoreward of the MAVS wave gauge and the confidence with which the accuracy of the threshold-entrainment equations could be assessed.

3.9 Conclusion

The deployment of off-the-shelf motion loggers implanted within adapted natural host clasts provided real-time data on clast dynamics within the littoral zone. The ML clasts were deployed for a total of five one hour-long experiments in Flathead Lake, and once at Abbotsham. Although the exceedance of threshold conditions and highly complex wave field rendered the Abbotsham data set unsuitable for detailed analyses, the fetch-limited, reductive environment of Flathead Lake provided a perfect setting to make detailed process-based analysis of the threshold-entrainment. An algorithm was developed to: (1) infer rotation through a single axis from the three-dimensional tilt record of the motion logger, and; (2) classify entrainment events. Each entrainment event was related to a ‘threshold wave series’ measured by the proximal MAVS device and considered to be overlying the ML clast at the time of entrainment.

The five Flathead Lake experiments coincided with a range of conditions. No clasts were entrained during the calmest experimental run, and multiple entrainment events were logged by each clast deployed during the most intense storm on 03 July 2012. The threshold-entrainment was first considered on an experimental basis, for which the likelihood of a clast becoming entrained increased with prevailing wave power. The Lorang equations were forced with the corresponding significant wave height and mean period from each of the experimental runs. While Equation 3.17 systematically underestimated the critical entrainment mass, Equation 3.18, which is scaled to a higher wave energy, provided more favourable predictions. Moreover, optimal agreement

was found when the K_r value was set to 1.8, which matches the K_D values found for a comparable scenario using the Hudson Formula.

However, the threshold-entrainment based on the weakest threshold wave series differed significantly, and indicated the occasional entrainment of particularly heavy clasts by exceedingly weak waves. Here, the predicted critical entrainment mass, obtained by forcing the Lorang equations with the height and period of the weakest threshold wave series correlated poorly with observations. Reasonable agreement between the observed and predicted critical entrainment mass could only be achieved by using a particularly small K_r value (0.1) of less than one, which is outside the range found for the Hudson Formula. However, the validity of the threshold-entrainment observations as a function of the threshold wave series remains unclear.

A number of alterations are suggested to improve the methodology and the confidence with which the accuracy of the threshold-entrainment equations can be assessed. Key suggestions included: increasing the sample frequency of the motion loggers in order to resolve rapid clast rotations and even trace the position of clasts through its inertia; measuring the time-varying position of ML clasts with a DGPS to provide insight into the link between real-time motions and x, y displacement. Moreover, measurement of the wave properties across the process zones and the direct measurement of run-up elevation from image record made with a digital camera focussed on the experimental beach would be an improvement on the current run-up estimate used to force the equations. Despite these suggested improvements, the current investigation provides new insight into the threshold-entrainment on coarse clastic beaches.

4 : Shore Platform Control on Nearshore Wave Properties and Longshore Transport

4.1 Introduction

4.1.1 Shore Platform Control on Wave Transformations

Horizontal and gently sloping shore platforms are a common feature of rocky coastlines globally (Trenhaile, 1987; Sunamura, 1992). Until recently, the influence of shore platform morphology on wave transformations had been unexplored (e.g. Farrell et al., 2009; Ogawa et al., 2011, 2012; Beetham & Kench, 2011; Bezerra et al., 2011; Marshall & Stephenson, 2011; Ogawa, 2013). However, understanding the role of shore platforms has become particularly important because storminess is predicted to increase in many regions (e.g. Bouws et al., 1996; Kushnir et al., 1997; Weiss et al., 2005; Wolf & Woolf, 2006; Dodet et al., 2010; Hemer et al., 2013) and the vulnerability of rock coasts has been increasingly recognised (Naylor et al., 2010; Trenhaile, 2011). These data are also essential for informing the development of sediment transport, cliff erosion and rock coast evolution models (Naylor et al., 2010).

A number of recent field studies have explored wave transformations across various shore platforms using concurrent measurements from a cross-shore array of wave gauges (e.g. Ogawa et al., 2011, 2012; Beetham & Kench, 2011; Bezerra et al., 2011; Marshall & Stephenson, 2011; Ogawa, 2013). These studies have typically been conducted in micro- and meso-tidal environments during calm and moderate wave conditions. They showed water depth to moderate incident wave energy propagating across the shore platform through the process of wave breaking (e.g. Farrell et al., 2009), and that energy within the infragravity frequencies becomes progressively more dominant with reducing depth (Marshall & Stephenson, 2011; Ogawa, 2013). Ogawa et al. (2011) concluded that the morphology of the shore platform is a key determinant of the wave energy available to do geomorphic work at the shoreline.

A number of recent papers explore geological control of shore platforms on the formation of sand and coarse clastic beaches (e.g. Trenhaile, 2002, 2004, 2005) as well as the cross-shore structure of sand beaches in a variety of settings (e.g. Jackson et al., 2005; Backstrom et al., 2009; Jackson & Cooper, 2009; Kennedy & Milkins, 2014). However, an extensive literature search found no published work that presents field data demonstrating shore platform control

on nearshore wave transformations and the geomorphological response of a coarse clastic beach.

4.1.2 Longshore Transport on Coarse Clastic Beaches

Early field work into the dynamics of CCBs provided valuable information about the longshore displacement (LSD) of pebbles in response to various wave conditions (e.g. Carr, 1971; Hattori & Suzuki, 1978). They related the longshore displacement of visually-traced pebbles to the longshore component of wave power measured nearby. The advent of contemporary, passive tracing techniques (e.g. Radio Frequency Identification (RFID) technology) has improved the ability to locate and identify individual tracers, even when buried (Allan et al., 2006). Recent field work utilising RFID technology has provided critical insight into the magnitude and direction of sediment transport on mixed sand and gravel beaches (e.g. Osborne, 2005; Allan et al., 2006; Curtiss et al., 2009; Dickson et al., 2011; Miller et al., 2011) as well as pure gravel beaches (e.g. Bertoni et al., 2010; Naylor et al., 2010).

These studies found useful, and occasionally confounding, information about the LSD of clasts in relation to the nearshore wave conditions. Tracer studies on fine pebble beaches (e.g. Carr, 1971; Hattori & Suzuki, 1978) and mixed sand and gravel beaches (e.g. Osborne, 2005; Curtiss et al., 2009; Miller et al., 2011) showed the direction of transport to be determined by the angle of obliquity of incident waves. Carr (1971) on a fine pebble beach in the UK and Hattori & Suzuki (1978) on a sand and gravel beach in Japan, measured the rapid displacement of tracer clasts of up to 343 m/day and 400 m/day respectively. Hattori & Suzuki (1978) found a strongly positive relationship between the longshore component of wave power and the mean longshore displacement of the traced sample, which varied between 2 and 60 m/day. However, similar efforts to relate the longshore component of wave power to the longshore displacement of tracers on a mixed sand and gravel beach has yielded a less clear relationship (Miller et al., 2011).

These studies also highlighted the moderating effect of burial on a clast's longshore displacement. Carr (1971) observed the rejection of coarse clasts by the beach matrix, resulting in the tendency for them to be located at the beach surface. The highly exposed surficial position of coarse clasts results in a

positive relationship between clast size and longshore displacement. This trend has also been observed with pebbles and cobbles on a mixed sand and gravel beach (Osborne, 2005). Importantly, Carr (1971) noted a general reduction in the expected longshore displacement of all traced clasts during energetic conditions. He pointed out that only the top layer of sediment is mobilised in calm conditions, and the probability of any given surficial clast becoming buried is low. Conversely, in energetic conditions, the vertical extent of the mobile layer is large and clasts are more likely to become buried, reducing their exposure to the hydrodynamics and hence (longshore) displacement. Carr (1971) thereby demonstrated the longshore displacement of clasts is not necessarily proportional to the volume of sediment transported longshore, which is dependent on the thickness of the mobile layer.

Van Wellen et al. (2000) noted that the volume of material transported longshore is of utmost importance, which has been largely overlooked (e.g. Carr, 1971; Hattori & Suzuki, 1978; Allen et al., 2006; Curtiss et al., 2009; Bertoni et al., 2010; Dickson et al., 2011). Measurement of the volume of sediment transported longshore (from hereafter referred to as the 'longshore transport rate' or 'LSTR') using tracers, requires knowledge of the:

(1) longshore displacement of the sample of traced clasts;
(2) width of the beach over which clasts are being transported;
(3) vertical extent of the mobile layer (see Figure 4.1).

Although quantities 1 and 2 are easily measureable through traditional tracer studies, quantifying subsurface transport (quantity 3) presents a serious logistical challenge (Komar, 1997).

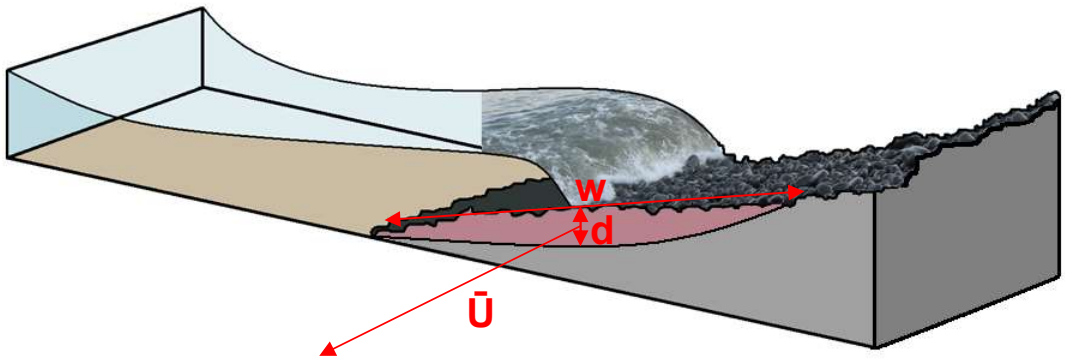

Figure 4.1: A three-dimensional diagram of a slice of the experimental beach showing the mobile layer (maroon) and the three quantities required to estimate longshore transport. Where: *Ū* is the mean longshore displacement of clasts; *d* is the thickness of the mobile layer; *w* is the beach width over which clasts were mobilised.

The mobile layer refers to the portion of beach material transported by hydrodynamic processes. A number of methods to measure the thickness of the mobile layer have been proposed and employed in the marine environments. Nicholls (1989) inserted vertical column of aluminium blocks into a pebble beach and considered the thickness of the mobile layer to equal the depth to which individual blocks were displaced (termed the depth of activation) after being subjected to wave action. Curoy et al. (2009) adopted much the same approach on a mixed sand and pebble beach, but instead of using aluminium blocks they use painted pebbles (40 mm to 50 mm in diameter).

The principles with which both researchers measure the depth of activation (DoA) correspond to sand-based techniques which have been widely practiced (e.g. King, 1951; Komar & Inman, 1970). More recent LSTR studies conducted on mixed sand and gravel beaches have defined the DoA by the burial depth of RFID-traced clasts across the beach (e.g. Miller et al., 2011). Despite this method providing DoA measurements corresponding to those obtained using a more traditional rod and washer method, it is obvious that this technique is only appropriate where the DoA is less than the detection range of the locating device.

Considering the importance of, and challenge presented by, obtaining DoA measurements, a number of researchers have conducted intensive experiments focussed purely on quantifying the DoA on sandy beaches (for full review of the literature see Anfuso, 2005). These experiments related the measured depth of activation to the breaker height and consistently demonstrated a positive

relationship between the two variables (e.g. Sunamura & Kraus, 1985; Jackson & Nordstrom, 1993; Ferreira et al., 2000; Anfuso, 2005; Curoy et al., 2009). Furthermore, for a given wave height, the greatest activation depths were achieved by plunging breakers (Anfuso, 2005).

A couple of field studies have measured the DoA on sand and mixed sand and gravel beaches (e.g. Osborne, 2005; Miller et al., 2011), yet no published report of such measurements being made on a pure coarse clastic beach were found. The presence of sand greatly affects the hydraulic conductivity of the beach matrix (Krumbein & Monk, 1943), meaning the DoA on even a mixed sand and gravel beach may vary significantly from beaches composed purely of coarse clasts. The relationship between the wave force and DoA on a CCB therefore remains unknown.

4.2 Chapter Aims & Specific Research Questions

Chapter 4 presents a large data set obtained from Abbotsham to explore the relationship between nearshore processes and the longshore transport rate, estimated through the combination of the observed longshore displacement and depth of activation of clasts, on the adjacent coarse clastic beach. This chapter aims to answer the following specific research questions:

Q4.1: What is the influence of the shore platform on wave transformations and hence the nearshore wave properties?

Shore platforms play a key role as an intermediate between incident waves, generated some distance offshore, and the shoreline. A number of recent studies have shown various shore platforms to have a considerable moderating effect on the shoreward propagation of incident wave energy. However, a comprehensive literature search suggests there is no published report addressing the refraction of incident waves across an irregular shore platform and likely impact on the local approach angle and energy of incident waves at the shoreline. This chapter aims firstly to address the role of the shore platform on wave transformations and therefore the wave force acting on the coarse clastic beach at Abbotsham.

Q4.2: What is the relationship between the nearshore wave conditions and longshore transport rate on Abbotsham beach?

Longshore transport processes can dominate the morphology of a coastline and are the cause of multiple problems for coastal engineers (Komar, 1997). Much effort has been made to define the relationship between wave force and longshore transport rate on sandy beaches. These studies have shown large quantities of sand is transported longshore by the current setup when oblique wave fronts shoal. However, CCBs are dynamically distinct from their sandy counterparts and hence the applicability of the sand-based results is unknown. Difficulties with measuring the thickness of the mobile layer has meant the majority of studies have focussed on the longshore displacement of coarse clasts (e.g. Carr, 1971; Hattori & Suzuki, 1978; Allen et al., 2006; Curtiss et al., 2009; Bertoni et al., 2010; Dickson et al., 2011) and not the longshore transport rate (e.g. Nicholls & Wright, 1991). This multidisciplinary chapter therefore has the overarching aim of developing a quantitative relationship between the nearshore wave force and longshore transport rate at Abbotsham beach.

4.3 Methodological Approach

This chapter presents field measurements of the wave climate within Bideford Bay and the inner shore platform at Abbotsham in addition to daily clast transport measurements on the adjacent CCB. The data were collected over nine field trips spanning an 18 month period (see Table 4.1). Geomorphic control imposed by the shore platform on wave transformations and resulting nearshore wave mechanism is inferred from spatial variability in concurrent wave properties measured by the Bideford Bay wave buoy and wave gauges deployed at three equidistant positions aligned along the inner section of the 225 m wide sloping shore platform. Wave data incorporated in this experiment span a wide range of conditions, which is in contrast to the temporally-limited data sets presented in the pre-existing literature. While previous field studies have provided detailed insight into the geomorphic control on wave attenuation across a variety of shore platforms, the along-shore array of wave devices provides insight into the lateral difference in attenuation and redistribution of wave energy as a function of shore platform morphology.

High-frequency field experiments tracing the daily displacement of a sample of between 47 and 118 tracer clasts were also conducted at Abbotsham beach, which amounted to a total of 15 daily clast transport observations. These data were considered in terms of the longshore displacement of clasts, which was analysed in relation to the estimated longshore component of wave power. In the absence of consistent measurements of wave height, period and direction from adjacent to the section of beach on which comprehensive clast transport observations were made, the key wave descriptors were estimated from the analysis of relationships presented within this chapter. The estimated longshore component of wave power is used to describe variability in the observed longshore displacement of tracer clasts.

Additional depth of activation experiments were conducted to measure the thickness of the mobile layer in response to the wave conditions. The DoA was measured by the daily displacement depth of a vertical column of tracer clasts buried within the beach matrix. In total, five DoA experiments were conducted in up to three locations across Abbotsham beach. These experiments were conducted in both calm and storm conditions, and the DoA was related to the maximum power of waves estimated to have been impinging directly on the DoA column during the intervening 24 hour period.

The following methods and results section are both divided into three exploring: (1) shore platform control on nearshore wave transformations, (2) longshore clast displacement and (3) depth of activation on the beach. The results from each experimental component are carefully combined in the discussion section in order to determine the wave-related longshore transport rate through a section of Abbotsham Beach.

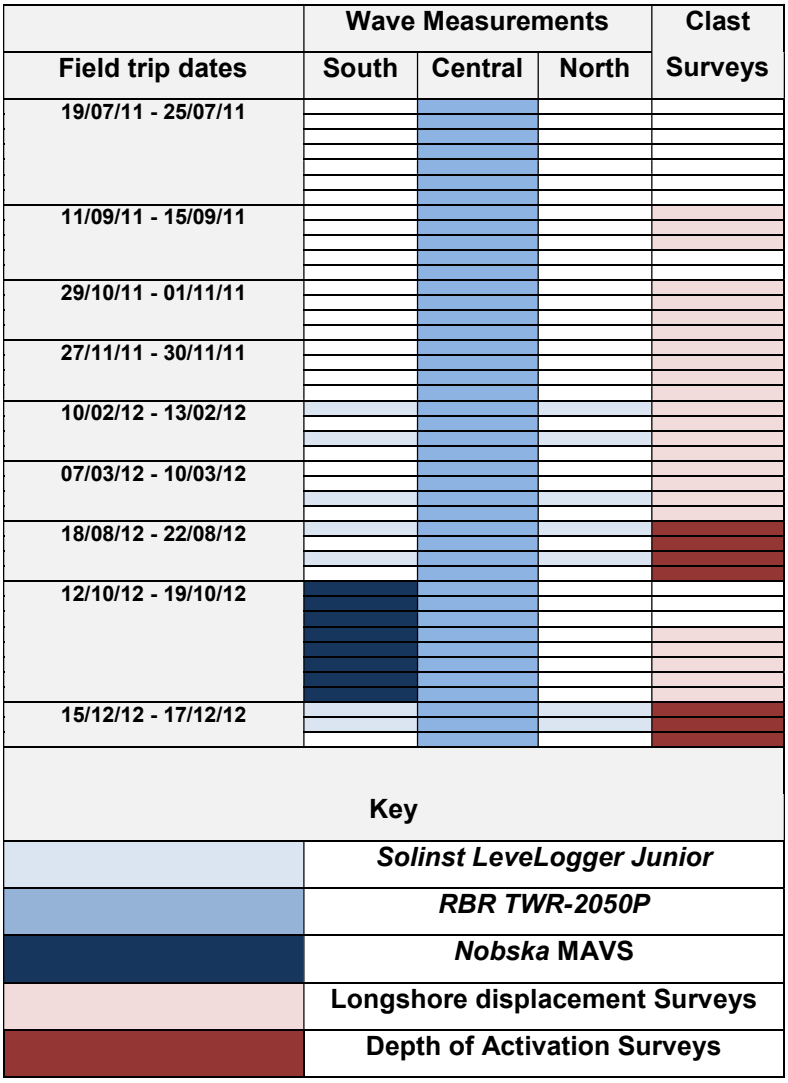

Table 4.1: Schedule of the field work at Abbotsham including the wave devices deployed at each of the three longshore positions, and timing of the longshore displacement and depth of activation surveys. See section 4.4 for description of the *Solinst*, *RBR* and *Nobska* wave gauges.

4.4 Methods I: Wave Measurements

Long-term regional wave measurements were obtained from a *Datawell* Directional *WaveRider Mk III* buoy moored in 10 m deep waters approximately 3.3 km north of the experimental beach. The buoy, which is maintained by the Channel Coast Observatory (CCO), samples continuously at a frequency of 3.84 Hz and streams data to the shore station where it is processed. Wave statistics are output on a half-hourly basis and made available for download from the CCO website. The buoy has been deployed in Bideford Bay since June 2009, with sampling only being briefly interrupted for servicing or by storm damage.

For the purpose of this investigation, additional nearshore wave measurements were made at three locations along the inner shore platform fronting Abbotsham beach. The three deployment positions were approximately 93 m apart and located between 6 and 8 m away from the base of the CCB (see Figure 2.1). At each of the deployment positions a 60 mm (diameter) by 300 mm (deep) cylindrical hole was made in the shore platform using a hand-held core drill and diamond-encrusted corer. Depending on the type of instrument deployed, the holes were used to either house the wave gauges or anchor the devices' mooring frame to the shore platform.

Three types of wave gauge were used with differing measurement capabilities and sampling regimes. An *RBR TWR-2050P* pressure transducer is a compact device which was housed within the central deployment hole and programmed to sample at a frequency of 4 Hz during each field visit (see Table 4.1). The burst and interval regime was varied between 2048 samples and 512 seconds and 4096 samples and 1024 seconds according to the duration of deployment. An additional two *Solinst LeveLogger Junior* pressure transducers were occasionally deployed within the north and south holes to sample in conjunction with the *RBR TWR-2050P* pressure transducer. These simple, inexpensive devices could only be programmed to run continuously, and have a maximum sample frequency of 2 Hz. Their memory is limited and they can only store 32,000 readings, which translates to approximately four hours of continuous measurements, or one high tide phase.

Figure 4.2: Images of the weighted *RBR TWR-2050P* pressure transducer about to be inserted into the deployment hole at the central inner shore platform.

The *RBR* and *Solinst* pressure transducers only measure the instantaneous surface elevation and lack a directional component. A third generation *Nobska Modular Acoustic Velocity Sensor* (MAVS) was deployed at the south position in a one-off five day experiment to measure the direction (as well as surface profile) of waves overlying the inner shore platform. For a full description of the deployment of the MAVS see section 3.4.4.

4.4.1 Data Processing

In line with the Bideford Bay wave buoy statistics, data output from each of the deployed devices was analysed on a half-hourly basis. All pressure time series were post-processed in MATLAB in order to extract the significant height, peak period and mean approach angle of incident waves. Where time series data with differing sampling frequencies were to be compared, the highest frequency time series was coarsened, using MATLAB's resample function, to match the other dataset(s) prior to analysis. Nortek's WDS MATLAB function was used to extract the wave direction from the pressure and three-dimensional velocity time series of the MAVS. The direction of the most powerful frequency present was recorded and used in the following analyses.

4.5 Methods II: Longshore Clast Displacement

4.5.1 Clast Selection

Clasts were selected using an adaptation of the 'Pebble Count' method (see Wolman, 1954). A selection grid was constructed using two 50 m measuring tapes extended: (1) cross-shore from the seaward to the shoreward extremity of the beach (30 m), and; (2) 40 m along-shore. Considering the finite length of the experimental beach and the anticipated net northward transport of clasts (see section 2.2.2), the selection grid was positioned at the southern extremity of Abbotsham beach (see Figure 4.6).

Surficial clasts were selected at 2 m increments in the longshore direction and 3 m increments in the cross-shore direction. In total, there were ten longshore rows, each including 20 clasts. Clasts that were removed from the beach to be tagged were first assigned a unique grid reference number so they could be returned to their original position. Sampled clasts that were broken during the export or drilling process were replaced with clasts selected from the corresponding grid position during the following field trip.

It should be noted that six of the 200 RFID tags failed from the outset. Moreover, in the subsequent processing and analysis phases of the research, it was found that recorded digits of two RFID tags deployed throughout all field experiments conducted at Abbotsham beach were duplicated. This situation arose because, for brevity, only the last four digits of the exceedingly long RFID number were recorded in the field. It was thought that this would be sufficient given the relatively small number of tracer clasts deployed at Abbotsham (less than 500 in total). However, this assumption was proven to be incorrect. The two tracer clasts with duplicate recorded RFID numbers were excluded from the following analyses to prevent potentially large errors that could arise from having two clasts with the same recorded identification number. Consequently, 192 operational tracer clasts with a unique recorded identity number were deployed in the initial sample and their properties are displayed in Table 4.2.

	Initial Sample				
Size	**Count**	**Equant**	**Blade**	**Prolate**	**Oblate**
Medium Pebble	1	0	0	1	0
Coarse Pebble	0	0	0	0	0
Very Coarse Pebble	11	4	5	2	0
Fine Cobble	107	9	22	8	68
Coarse Cobble	48	8	8	15	17
Fine Boulder	25	3	2	2	18
Medium Boulder	0	0	0	0	0

Table 4.2: Size (Blair & McPherson, 1999) and shape (Zingg, 1939) categorisation of the initial sample of tracer clasts deployed at Abbotsham.

The accuracy with which the dynamics of beach clasts can be inferred from a sub-sample of tracers is dependent on the variability of clast transport and sample size (Lee et al., 2007b). In the absence of previous clast transport measurements, the initial deployment of a semi-arbitrary number of (192) tracer clasts was intended to inform an optimal sample size for the beach. It was however found that the initial sample was about the maximum number of clasts that a loan worker could locate and survey within a day.

The experimental beach was only recharged with more tracer clasts once, in February 2012, the majority of tracers in the central (cross-shore) region of the beach had been lost. For this, a grid was constructed in the same position as before and clasts were systematically selected along the five rows spanning the depleted region. Clasts were removed for tagging and returned to their precise grid position during the following field trip (one month later). In total, the central beach was recharged with 100 clasts. However, the RFID tag in one of the clasts was not operational and the properties of the 99 working clasts are displayed in Table 4.3.

	Recharge 1				
Size Grading	**Count**	**Equant**	**Blade**	**Prolate**	**Oblate**
Medium Pebble	0	0	0	0	0
Coarse Pebble	0	0	0	0	0
Very Coarse Pebble	32	8	6	11	7
Fine Cobble	65	11	8	3	43
Coarse Cobble	2	0	1	0	1
Fine Boulder	0	0	0	0	0
Medium Boulder	0	0	0	0	0

Table 4.3: Size (Blair & McPherson, 1999) and shape (Zingg, 1939) categorisation of the first recharge of tracer clasts at Abbotsham.

The beach was again recharged with traced clasts for a five day field trip in October 2012. At this time, the majority of the original and recharge samples had become removed from the experimental beach. It was planned to recharge all cross-shore zones in an operation similar to the initial installation work. However, poor weather hindered field efforts and meant that that only six of the top rows were recharged with 120 tracer clasts and the bottom beach was left unrepresented. The properties of the 120 operational clasts sampled in October 2012 are displayed in Table 4.4.

	Recharge 2				
Size	**Count**	**Equant**	**Blade**	**Prolate**	**Oblate**
Medium Pebble	0	0	0	0	0
Coarse Pebble	0	0	0	0	0
Very Coarse Pebble	31	5	12	11	3
Fine Cobble	85	11	14	5	55
Coarse Cobble	4	2	0	0	2
Fine Boulder	0	0	0	0	0
Medium Boulder	0	0	0	0	0

Table 4.4: Size (Blair & McPherson, 1999) and shape (Zingg, 1939) categorisation of the second recharge of tracer clasts at Abbotsham.

4.5.2 Clast Tracing Method

Considering the aforementioned benefits of RFID technology (e.g. Allan et al., 2006) and the relatively coarse clasts at Abbotsham beach, tracing clasts with RFID tags was considered to be the best approach. The RFID system comprises of four main components, including a:

(1) transponder tag,
(2) pole antenna,
(3) duplex (HDX) long-range reader and
(4) personal digital assistant (PDA).

The transponder tags are glass-encased and come in a range of sizes; 12mm, 23mm and 32mm in length. Only the 23mm and 32mm tags were used in these experiments due to the size-dependent signal strength and the coarseness of clasts being traced. The RFID tags lack batteries, but instead include a small capacitor that is wirelessly charged by the short magnetic pulse emitted from the reader. The power harnessed by the RFID tag is used to transmit a unique signal back to the reader.

The *HDX* long range reader is housed within a backpack that is worn by the worker during clast searches. The reader moderates the voltage through the antenna and converts the return signal from a detected RFID tag into its unique identification number. The reader is also connected (via cable) to a waterproof PDA where the identification number of detected tags is displayed within *Oregon RFID*'s custom-made *PTlogger* application. The pole antenna is an ergonomic construction of plastic tubing designed to maximise the worker's search swath. The antenna consists of a long pole with a hand grip in the centre, and hoop at one end within which the wire circuit that emits the electronic signal is housed.

The detection distance of an RFID tag is dependent on its orientation relative to the antenna. When connected to the HDX reader, RFID tags buried up to 1 m below the beach surface can be identified (Allan et al., 2006). This has proven to be particularly advantageous for the monitoring of clasts on exposed beaches where a considerable portion of tracer clasts were buried at any given time (e.g. Osborne, 2005; Allan et al., 2006; Curtiss et al., 2009; Dickson et al., 2011; Miller et al., 2011).

4.5.3 Clast Tagging

Each transponder tag was first inserted into a silicone sleeve to help absorb shock. Each silicone-encased tag was then inserted inside a 6 mm (diameter) × 40 mm (deep) hole drilled into each of the sampled clasts using a hand-held drill and hardened masonry bit. The tag was finally sealed inside the clast using marine epoxy resin. The axis through which a clast was drilled depended on its size and the ability to grip it within the drilling vice. It was however found that drilling clasts through their A-axis reduced the risk of breakage, and was adopted whenever possible.

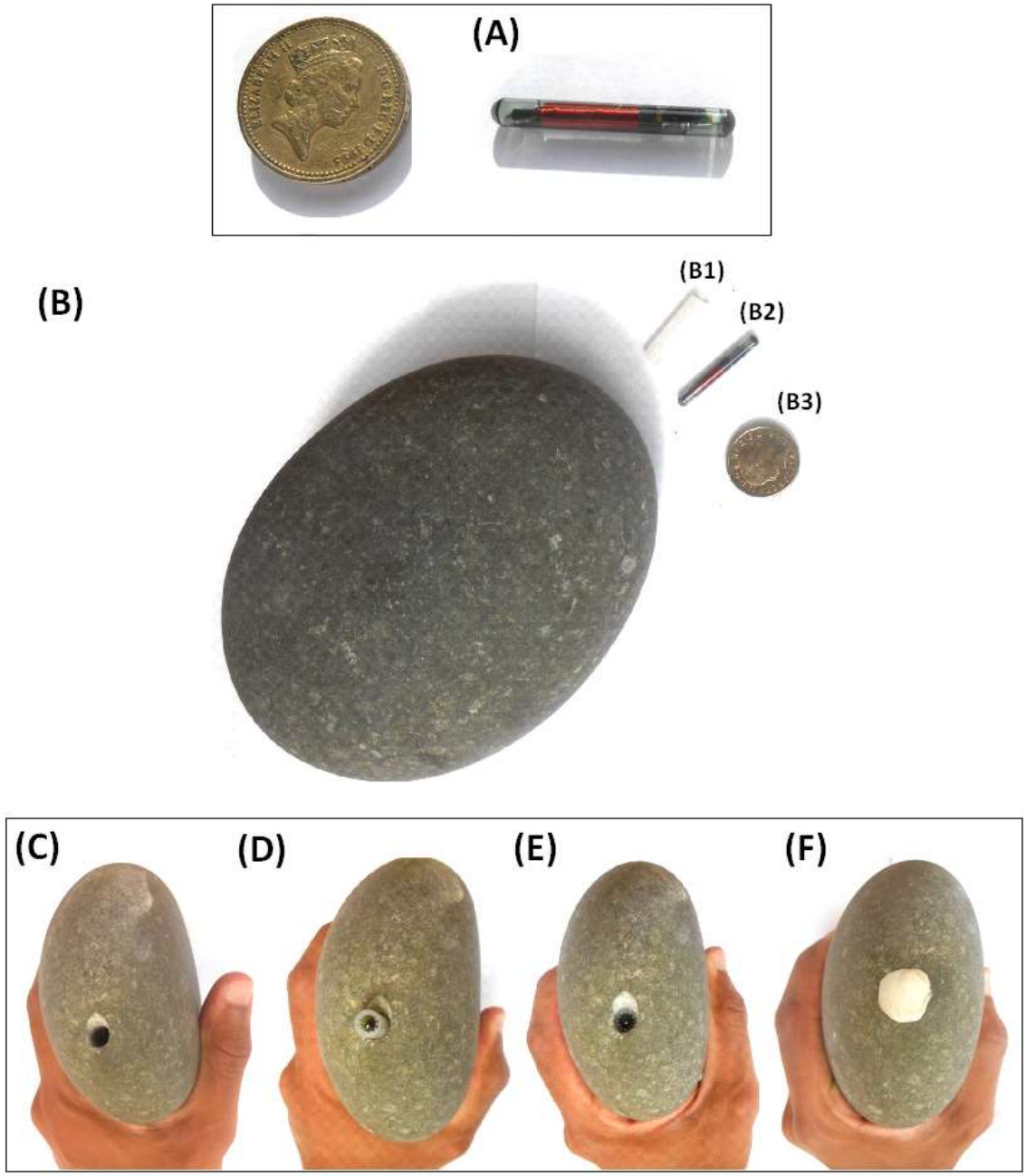

Figure 4.3: Images of: (A) a 32 mm RFID tag placed next a one pound coin; (B) the host clast, (B1) protective silicone sheath, (B2) RFID tag, (B3) one pound coin; (C) the host clast with 6 mm hole drilled through its A-axis; the host clast with silicone-encased RFID tag partially (D) and fully (E) inserted into the hole; (F) the host clast with silicone-encased RFID tag sealed inside with epoxy resin.

The limited battery life of the hand-held drill and the remote location of the experimental beach meant it was easiest to remove the finer clasts and adapt them close to a power supply. The coarsest clasts at the seaward extremity of the beach were immovable and had to be drilled and tagged *in-situ*.

Figure 4.4: photo of a selection of clasts displaying the marine epoxy cap after being fitted with RFID tags. Scale: The ruler is approximately 270 mm in length.

The tag, sleeve and resin were of a significantly lower density than the clast. The tagging process therefore resulted in a slight decrease in the mass of each clast. The percentage mass loss of 101 of the RFID host clasts weighed before and after the tagging process was between 2.4 % and 0.1 %. The relative mass loss was non-linearly and inversely related to the original clast mass. Importantly, the weighed sample constituted the finer fraction of the sample that could be removed from the beach. The percentage mass loss is therefore expected to be less than 0.1 % for coarser, immovable clasts.

An inherent limitation of this particular tracing method is that the hole drilled into each host clast probably weakens its structure and makes it more vulnerable to impact fragmentation. Depending on how the clast is split, the newly-liberated fragment within which the RFID tag is located could be a very different size and shape to the original (selected) clast. Moreover, the RFID tag could become completely removed from the host clast and remain un-housed within the beach matrix. One mitigating factor of employing this method at Abbotsham is that the local greywacke clasts are hard and generally lack faults, which would lead to further structural weakness.

The whole tagging process was both time and cost effective. Drilling, tagging, sealing and measuring the weight and three-axel dimensions of a single clast took approximately five minutes. It should be noted that tagged clasts had to be left for a further 1 to 2 hours until the epoxy resin had cured. RFID tags are relatively inexpensive and, including a silicone sheath, cost approximately £1.60

each from *Oregon RFID ltd.* A hardened masonry bit (approximately £3.00 each) treated between 10 and 15 greywacke clasts before deforming. Notably, the greywacke clasts were particularly hard and the lifespan of a drill bit is expected to vary depending on rock type. Over 100 newly-tagged clasts could be sealed with a 260 g tin of *Plastic Padding* epoxy resin, which cost approximately £15.00. Considering all the required materials, tagging a single clast is estimated to have cost around £2.00.

4.5.4 Data Collection

Longshore displacement surveys were conducted during a series of three to five day windows when spring low tide occurred between 1200 and 1600 UTC. In total, the dispersion of the traced sample was monitored over six field trips. During each field trip, daily clast searches were conducted with the RFID system to locate as many of the tracer clasts as possible. The worker conducted along-shore sweeps of the beach, starting at its shoreward extremity and finishing on the largely-exposed shore platform. The long-shore extent of the clast search-sweeps was determined by the detection rate along the search swath. Search-sweeps were continued for at least a distance equal to that between the two previously detected tracer clasts. Exception to this rule was made at the north or south extremity of the Abbotsham beach survey zone (see Figure 2.1) where the search-sweep was terminated. It was also insured that the parallel search swaths overlapped for full beach coverage. Located clasts were marked with a fluorescent flag, on which the unique RFID number was written with a permanent marker pen.

Field trip	Survey dates	Number of complete surveys conducted on
1	11-Sep-11 to 13-Sep-	1
2	29-Oct-11 to 01-Nov-	3
3	27-Nov-11 to 30-Nov-	2
4	10-Feb-12 to 13-Feb-	2
5	07-Mar-12 to 10-Mar-	3
6	14-Oct-12 to 19-Oct-	4

Table 4.5: Schedule of survey dates and the number of complete surveys conducted on consecutive days. The number of consecutive surveys is occasionally fewer than the survey dates suggest. This is due to equipment failure during field trips, which meant the beach was not fully surveyed on one or more of the survey dates.

Once the experimental beach had been comprehensively searched with the RFID unit, the positions of the located clasts were measured using a DGPS. The last four to five digits of the RFID number, along with the point identification number on the DGPS, was recorded in a field notebook. In addition, it was noted whether the clast could be located by sight or not. Following the measurement of the position of each recovered tracer clast, the flag was collected and clast left in place.

4.5.5 Data Processing

The abovementioned ability to visually locate detected RFID clasts is of particular importance when considering uncertainty. Depending on its orientation, an RFID tag can be detected up to 1 m away. Where clasts could not be visually located, uncertainty (δ_l) was taken as the detected position ±1 m. Further uncertainty was associated with DGPS measurements (δ_m), which was conservatively estimated as 0.1 m. Of course, longshore displacement measurement required knowledge of the position of a clast at two instances in time. Total uncertainty associated with the displacement of each clast (δ_{TC}) between time 1 (*t1*) and 2 (*t2*) is:

$$\delta_{Tc} = \delta_{lt1} + \delta_{mt1} + \delta_{lt2} + \delta_{mt2} \qquad \textbf{Equation 4.1}$$

Where *n* stands for the number of clasts in the sample, uncertainty associated with the mean displacement of the entire sample was given as:

$$\delta_S = \frac{1}{n}\sqrt{{\delta_{Tc1}}^2 + {\delta_{Tc2}}^2 + {\delta_{Tc3}}^2 + {\delta_{Tc4}}^2 + \cdots} \qquad \textbf{Equation 4.2}$$

Further errors might have arisen by the worker: (1) misreading the RFID or DGPS numbers from the displays on the respective devices; (2) miswriting/misreading the RFID number on the marker flag; (3)

miswriting/misreading the RFID and/or DGPS number written in the field notebook. Although great care was taken during each stage of the field work to accurately transcribe data, the was inefficient and would have increased the likelihood of human error affecting the results. To minimise the impact of any erroneous data points, tracer clasts that were either displaced greater than the 99th percentile or less than 1st percentile of the sample between consecutive surveys were systematically deleted from the dataset during the data processing phase.

Although the entire stretch of Abbotsham beach was surveyed for these experiments, the position of the selection grid and the timing of the field visits meant that only the southerly portion of the experimental beach was at all times populated with tracer clasts. Furthermore, the observed longshore variability in wave properties demonstrate that the wave force acting on Abbotsham beach is not uniform and the beach should be compartmentalised according to the platform morphology (see sections 4.7.2 & 4.7.3). Considering this, only the transport of tracer clasts within a 100 m longshore zone located adjacent to the south wave gauge position were analysed in the high-frequency, daily clast longshore displacement analyses. The longshore displacement of clasts are configured with respect to the orientation of Abbotsham beach (which is aligned at 31 °) so that positive and negative values represent longshore transport northwards towards the Pebble Ridge (31 °) and southwards towards the Gore (211 °) respectively.

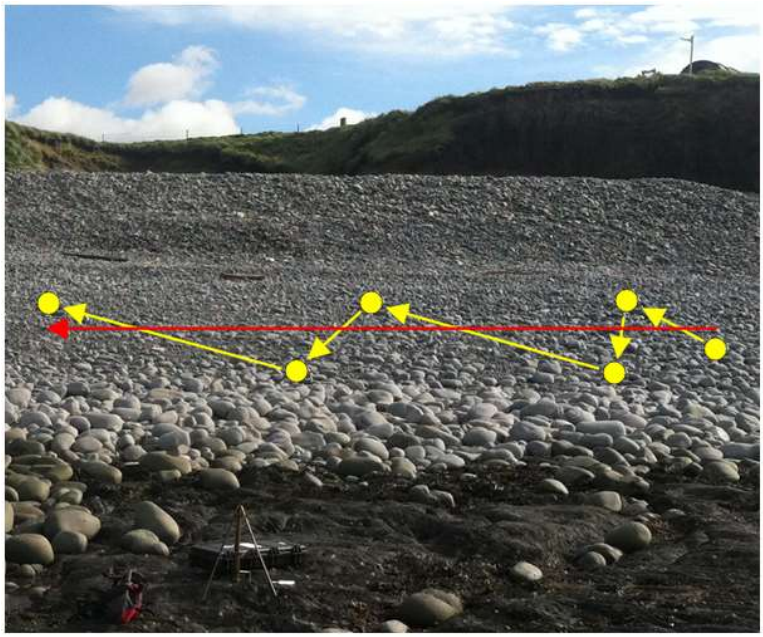

Figure 4.5: Diagram depicting the difference between real-time clast transport (yellow) and the longshore displacement (red arrow) resulting from the cumulative sum of the longshore component of all transport events occurring over an extended period of time (e.g. days).

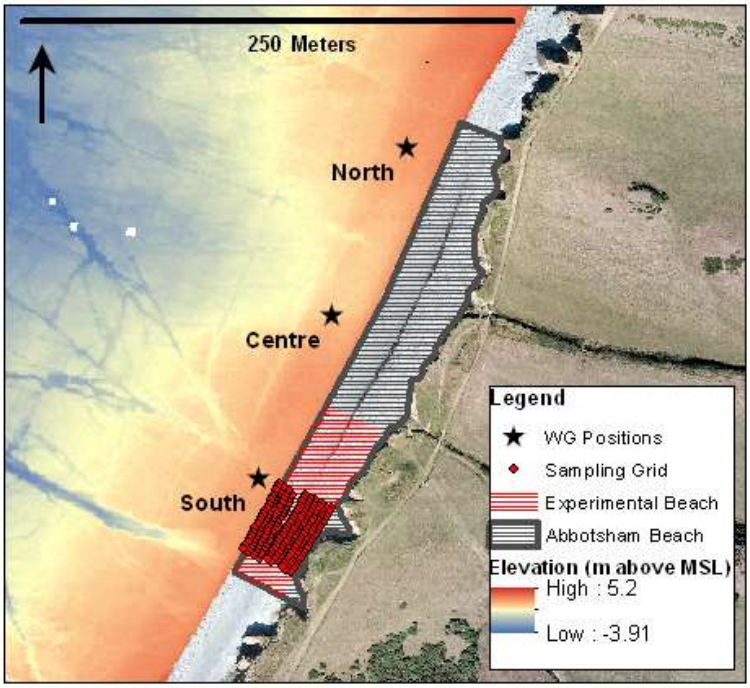

Figure 4.6: An aerial view of the experimental beach displaying a true colour image of the CCB (grey) and shoreward land mass (green), and digital elevation map of the rocky shore platform, with the position of Abbotsham beach, the experimental beach and sample grid. The three positions in which wave gauges were deployed are indicated with black stars. The stretch of Abbotsham beach that was surveyed each day is shaded with black lines and the experimental beach on which the LSD of clasts is analysed in detail is shaded with red lines. The positions in which clasts were selected and deployed (i.e. the 'selection grid') are highlighted with red dots. Aerial imagery and LiDAR data used to construct these plots was obtained from the CCO.

On any given day a proportion of the located tracer clasts are positioned above and below the depth of activation. The proportion of clasts located on either side of this boundary depends on (1) the DoA between the beach surveys and (2) the depth to which the RFID sample have been previously buried. This presents a problem because the transport of tracer clasts is therefore influenced by the historical wave conditions. For example, it is intuitive that the mean transport of the sample might be suppressed following a storm due to a large proportion of RFID clasts being buried deep within the beach matrix. This is a particular issue when attempting to estimate the longshore transport rate of the mobile layer (which is necessary for the longshore transport estimate; see section 4.10.4.2). To minimise the effect of wave contingency on the estimated longshore displacement of the mobile layer, the experimental beach was separated into five vertical bins, each two meters in extent. Within each bin, only tracer clasts that had been displaced a greater distance than the 10th percentile of the zonal distribution were included in the collective transport analyses.

4.5.6 Relating Clast Transport to the Nearshore Wave Properties

In his 1970 paper, Longuet-Higgins explained the lateral thrust that is applied when oblique wave fronts shoal using the momentum flux concepts he developed with Stewart (1964). He expressed the longshore flux of momentum (generally referred to as the longshore component of power, P_{LS}) in relation to the offshore energy density (E), group velocity (C_g) and approach angle (α) of breakers, such that:

$$P_{LS} = \left(EC_g\right)_b \sin\alpha_b \cos\alpha_b \qquad \textbf{Equation 4.3}$$

Where H_{rms} ($\approx H_S/1.41$, after Longuet-Higgins, 1952) stands for the root mean squared wave height:

$$E = \frac{\rho_w g {H_{rms}}^2}{8} \qquad \textbf{Equation 4.4}$$

The group velocity is variable a dependent on the wave length (λ) and water depth. The specific group velocity equations and scenarios in which they are used are presented in Table 4.6.

Shallow water: defined as less than 1/20th of the deep water wavelength ($= \frac{gT^2}{2\pi}$), the group velocity:

$$C_g = \sqrt{gH} \quad \textbf{Equation 4.5}$$

Intermediate water: defined as between 1/20th and a half of the deep water wavelength, the group velocity:

$$C_g = \frac{1}{2}\left(1 + \frac{2kh}{\sinh(2kh)}\right)\left(\frac{gT}{2\pi} tanh \frac{2\pi h}{\lambda}\right) \quad \textbf{Equation 4.6}$$

where the wavenumber:

$$k = \frac{\lambda}{2\pi} \quad \textbf{Equation 4.7}$$

and the wavelength:

$$\lambda = \frac{gT^2}{2\pi}\tanh\left(\frac{2\pi h}{\lambda}\right) \quad \textbf{Equation 4.8}$$

which, given λ features on both sides of the equals sign, is solved iteratively.

Deep water: defined as water depth greater than half the deep water wavelength, the group velocity:

$$C_g = \frac{1}{2}\frac{gT}{2\pi} \quad \textbf{Equation 4.9}$$

However, it should be noted that a deep water scenario is most unlikely to occur at the inner shore platform at Abbotsham.

Table 4.6: Wave group velocity equations used in shallow, intermediate and deep water.

The practice of relating longshore transport to the longshore component of wave power is well established within the coastal engineering discipline. Despite the simplicity of this approach, it has been proven to provide a good description of the net longshore transport of sediment over an extended period of hours and days (see Komar, 1997 for review). In fact, much research effort has been invested in the derivation of the proportionality coefficient (represented by the symbol '*K*') that relates the longshore component of wave power to the immersed weight transport rate. These field studies have generally been conducted on sandy beaches and (with exception to Nicholls & Wright, 1991) the longshore transport rate of CCBs has generally been overlooked.

Equation 4.3 was originally applied to extensive sandy beaches where the cross-shore position of the breaker zone determines the width of the transport zone. Conversely, the coarse clastic beach at Abbotsham is spatially confined

in the cross-shore direction, and longshore transport is related to the longshore component of wave power measured adjacent to the beach base.

4.5.7 Inferring the Nearshore Wave Height & Approach Angle

Equation 4.3 expresses longshore component of power in terms of the height and approach angle of incident waves. However, measurement of the height and approach angle of waves adjacent to the 'experimental beach' (where comprehensive clast transport observations were made) was intermittent and coincided with only five survey dates (see Table 4.1). Meanwhile, the height and direction of waves were measured continuously by the Bideford Bay wave buoy. The half-hourly height and approach angle of waves adjacent to the beach are based on wave buoy measurements, which were corrected according to the condition- and tide-dependent transformations undergone by shoaling waves at Abbotsham (see section 4.7). Specifically, the offshore significant wave height was corrected with respect to the relationships displayed in Figure A2 (Appendix 4) and offshore mean approach angle was corrected with respect to the relationships displayed in Figure 4.12.

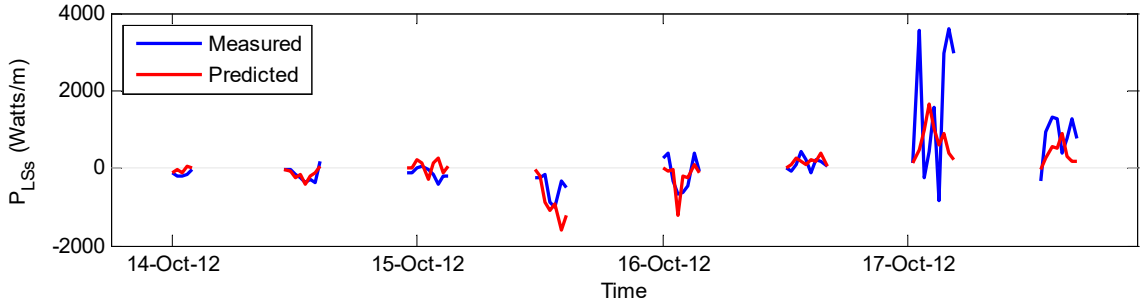

Figure 4.7: Time series of the measured and predicted longshore component of wave power.

The longshore component of wave power based on the inferred nearshore wave height and approach angle was tested against corresponding values based on direct measurements made with the MAVS (see Figure 4.7). The direction and magnitude of the predicted longshore component of wave power corresponds well with that observed. Exception to this general rule was evident during the first high tide on 17 October 2012, where the discrepancy between the observed and predicted P_{LS} was momentarily up to 3209 Watts/m. Nevertheless, there is good agreement between daily-mean values (against which daily-mean longshore clast transport is analysed). Agreement is reflected

in a high R^2 value of 0.95 and a relatively low *P*-value of 0.028 considering there are only four data points in the analysis.

It is acknowledged that the data used to relate the properties of waves overlying the south shore platform with those measured by the wave buoy were used in the initial comparison (from which the inferred values were extrapolated), and hence it is not an independent test. It is however argued that height, period and direction measurements made adjacent to the south platform spanned a wide range of conditions enabling robust trends to be established.

4.6 Methods III: Depth of Activation

4.6.1 Clast Selection

Clasts required for the DoA experiments were subjectively selected according to their shape and size. In general, discs with a mean B-axis diameter of between 60 mm and 80 mm were chosen to construct the DoA columns. Discs were selected because of: (1) their stability when resting on their C-axis, which improved the ease with which the DoA column could be constructed; (2) their small vertical extent (when resting on their C-axis), which increased the number of clasts comprising a DoA column and thus the resolution of measurements. Beforehand, DoA clasts were fitted with RFID tags using methods described in section 4.5.3. For each experimental day, the total number of sampled clasts depended on the number of DoA columns constructed and the prevailing wave conditions. As few as five clasts were used to construct a DoA column in calm conditions, and as much as 11 clasts comprised a DoA column for stormy measurements (see Table 4.9).

4.6.2 Data Collection

Like the LSD experiments, the daily DoA was measured during a three to five day period when spring low tides occurred between 1200 and 1600 UTC. In total, two field trips were dedicated to measuring the DoA, and were conducted between:

18 & 22 August 2012;
15 & 17 December 2012.

Each DoA experiment spanned a 24 hour period, during which the beach was subjected to two high tides.

The experimental setup included the construction of two to three vertical columns of RFID-traced clasts at specific positions across the beach face. The DoA transect was located in the centre of the experimental beach, directly adjacent to the central wave gauge. The precise positions of the DoA columns were located each day using the 'stakeout' function on the Leica DGPS, which enables the worker to pin-point a three-dimensional position to within a few centimetres. Column construction required excavation of beach material before in-filling the pit with a vertical column of tracer clasts, tightly surrounded by the excavated material. The precise position of each of the columned clasts was measured with the DGPS. Care was taken to make sure that the in-filled material was as compact as the surrounding beach matrix.

The final task in the experimental setup was to measure the beach profile using a DGPS. The following day included a detailed clast search with the RFID unit before the cross-shore profile was again measured and the beach at the precise position of the DoA column carefully excavated to reveal the uppermost clast that remained in place. For each DGPS measurement extreme care was taken to hold the pole as upright as possible so as to minimise positional errors. The accuracy stated by the DGPS was at all times less than 0.02 m. Given that the DoA is based on two measurements (i.e. the position of the uppermost DoA clast on day 1 and day 2), and that it is in fact impossible to hold the pole perfectly upright, the uncertainty associated with the measured DoA was estimated to be 0.05 m.

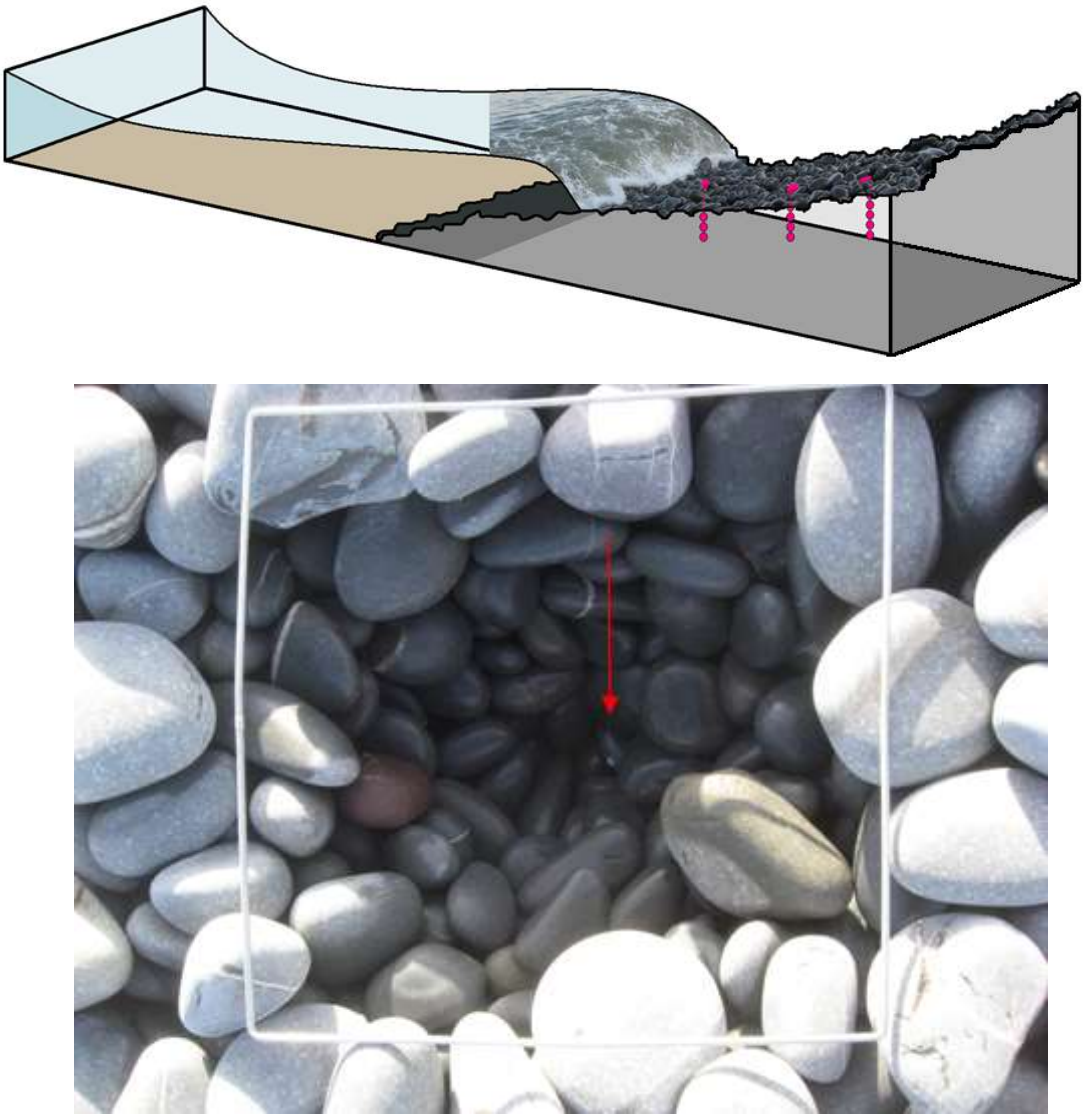

Figure 4.8: (Top) Three-dimensional diagram of three DoA columns (pink spheres) extending vertically into the beach matrix and (Bottom) DoA column excavated (on 17 December 2012) to reveal the uppermost clast that remained in place. The light grey epoxy cap of the clast can just be seen and is pointed out by the red arrow. The quadrat in the bottom image is 0.5m×0.5m.

4.6.3 Data Processing: Defining the Depth of Activation & Wave Mechanism

The three-dimensional positional data from the DoA experiments were firstly translated onto a common cross-shore plane. A program was written to find, for each DoA column during each experiment, the uppermost clast that remained unmoved between the first and second day. Factoring in the uncertainty associated with DGPS measurements, an 'unmoved' clast was considered to have a difference in the measured position on the first and second day of less than 50 mm. The DoA was defined as the elevation difference between the uppermost columned clast that was unmoved and the lowest surface elevation

directly above the DoA column measured on the first and second day. The DoA was related to the power of waves impinging directly onto the DoA column. This was estimated by obtaining the significant height and peak period of waves at all times when the tidal elevation intersected the top of the DoA column.

4.7 Results I: Nearshore Wave Climate

Equation 4.3 expresses the longshore component of wave power in terms of the height and approach angle of waves adjacent to the beach. The height and approach angle of incident waves are dependent on interactions with the morphology of the sea bed. This section explores the control exerted by the shore platform on nearshore wave transformations, and hence the longshore component of power measured adjacent to the CCB at Abbotsham.

4.7.1 Central Shore Platform

Measurements of the wave height and approach angle by the Bideford Bay buoy (offshore) are compared with the concurrent properties of waves overlying the central inner shore platform (nearshore) in order to demonstrate geomorphological control on the wave properties adjacent to the beach. The wave record from the central position is the most comprehensive of the three nearshore deployment positions (see Table 4.1). Wave measurements obtained from the central nearshore platform during all field trips amounts to 300 hours of submersed measurements and coincide with conditions in which the offshore significant height (H_{S0}) and peak period (T_{P0}) measured by the Bideford Bay wave buoy ranged from 0.8 m and 3 s to 3.7 m and 12.5 s.

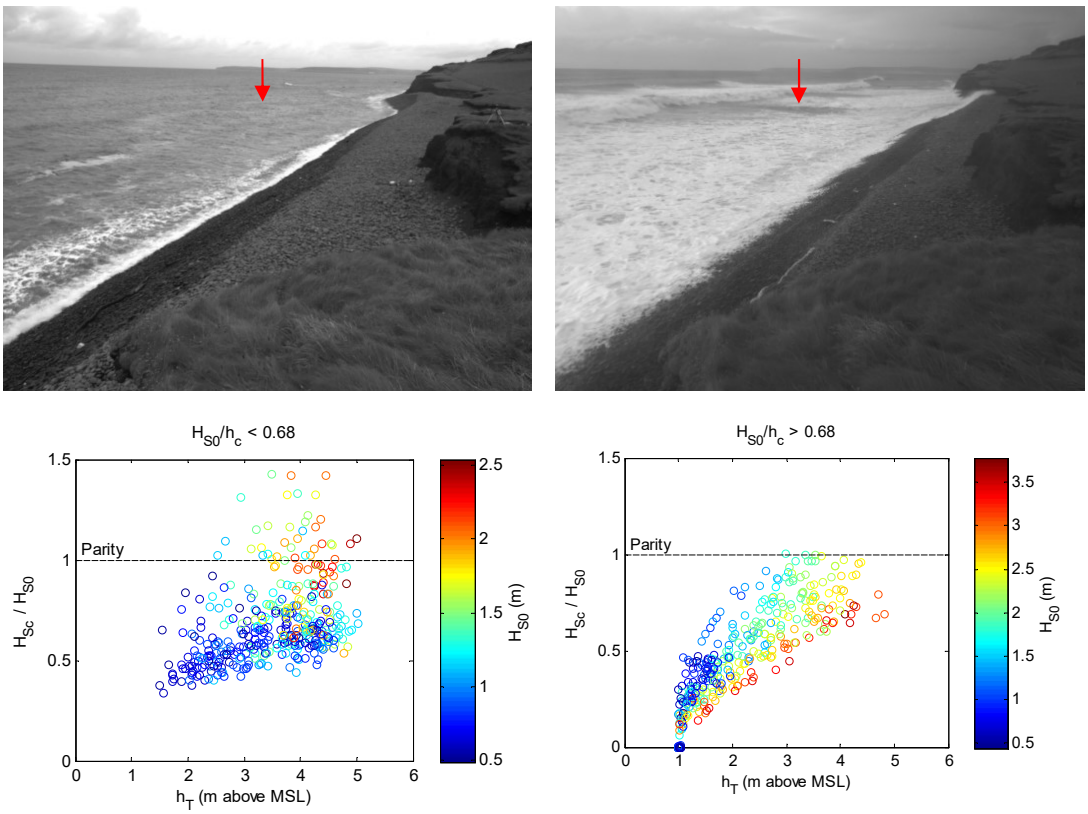

Figure 4.9: (Top) example image of an occasion when the break point is landward (left) and seaward (right) of the wave gauge positions and (bottom) the ratio of the central nearshore (H_{Sc}) to offshore (H_{S0}) half-hourly significant wave height versus the tidal elevation (h_T) when the break point is considered to be landward (left) and seaward (right) of the wave gauge. Red arrows on the images (top) indicate the approximate position of the central wave gauge. The colour of the data points in the bottom graphs indicates the corresponding offshore significant wave height. This figure is constructed using all wave measurements obtained from the central shore platform throughout all field experiments. The break point (H_{S0}/h_c = 0.68) is defined according to the findings of Kuo & Kuo (1974).

Tides play a key role in moderating the nearshore wave height at Abbotsham (see Figure 4.9). However, two differing trends were observed depending on the cross-shore position of the break point. Where waves of significant height are estimated to break seaward of the wave gauge (e.g. H_{S0}/h_c > 0.68), the relationship between the relative nearshore wave height and tidal elevation is simple. The dissipation of wave energy (and therefore reduction in wave height) is inversely related tidal elevation. At each point in the tidal cycle, the extent to which waves overlying the inner shore platform were attenuated was directly proportional to the offshore wave height. These results indicate that the breaker zone tends to migrate seaward with decreasing water depth and/or increasing offshore wave height, thereby widening the turbulent surf zone and increasing wave attenuation. This process results in a situation in which the ratio between

the nearshore wave height and local water depth (h_c) becomes fixed regardless of the offshore wave height (see Figure 4.10).

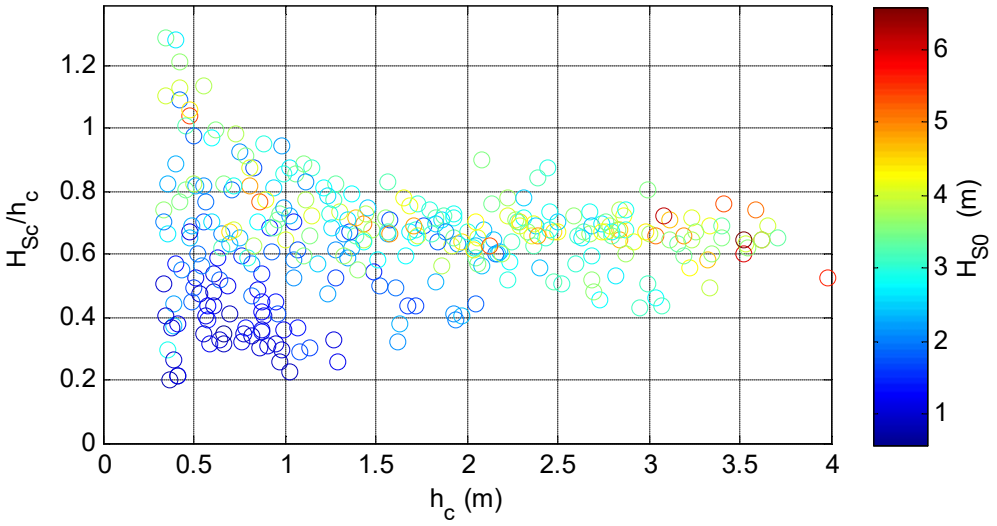

Figure 4.10: Ratio of the nearshore significant wave height (H_{Sc}) to local water depth (central shore platform; h_c) versus the local water depth. Data used in the figure were selected at times when the break point was estimated to be seaward of the wave gauge (i.e. H_{S0}/h_c > 0.68). The graph demonstrates that when the break point is seaward of the wave gauge, the nearshore wave height is limited by water depth and the ratio between the two is maintained regardless of variability in the offshore wave height.

When incident waves overlying the inner shore platform are largely unbroken, the relationship between the offshore and nearshore wave height differs considerably. In these circumstances, one might expect the nearshore wave height to be equal to or indeed greater than that offshore as the height of shoaling waves increases. However, a somewhat confounding relationship is found in which the nearshore heights of unbroken waves are systematically smaller than offshore. For each point in the tide, the relative nearshore wave height is inversely related to the offshore wave height, which is opposite to the breaker/surf zone measurements. The puzzling trend is explained later when the increasing importance of wave refraction in calm conditions is explored. Importantly, calm conditions are characterised by the refraction of wave energy away from the central position and its concentration at the north and south of the experimental beach.

4.7.2 Longshore Variability

Comparisons between wave height at the central position relative to the concurrent measurements to the north and south demonstrate systematic longshore variability in the shoaling process and incident wave energy along the

inner shore platform (see Figure 4.11). The measured heights of waves along the inner shore platform occasionally vary by greater than 0.5 m. The precise transformations incident waves underwent, and therefore the distribution of wave energy at the inner shore platform, is dependent on the offshore wave conditions and water depth.

When the break point is seaward of all three wave gauges, the cross-shore attenuation of incident waves dominates the energy profile along the inner shore platform. The reduced water depth over the elevated platform to the north and south enhances local wave attenuation and results in a systematic reduction in the local wave height relative to the central position. Deeper waters in the central embayment enabled a greater amount of incident wave energy to propagate across the shore platform and reach the shoreline.

Further evidence to support this observation is apparent in the morphology of the adjacent coarse clastic beach. Lorang (2002) noted that the beach building process is defined by incident waves transporting material from the beach face to the beach crest, and the elevation to which wave swash can transport clasts is dependent incident wave energy. It follows that the crest height of a developed beach provides an indication of nearshore wave energy during storm events. The beach crest adjacent to the central embayment is elevated relative to that at the north and south and is considered to be reflective of the uneven energy profile of incident waves along the inner shore platform during low-frequency, high-magnitude events (see Figure 2.5).

As the tidal elevation increases and/or offshore wave height decreases, wave attenuation across the shore platform reduces and the wave height at the north and south positions can exceed that measured in the centre. It is not possible to determine the extent to which the observed amplification of the measured wave height is due to (1) the conservation of power as unbroken incident waves shoal and/or (2) the local focussing of energy as wave fronts are refracted away from the central embayment towards the elevated peripheries. Interestingly, the amplification of wave height at the north and south position correspond with a reduction in the expected wave height at the central position. This perhaps indicates the role of shore platform morphology in the refraction of wave fronts and lateral distribution of wave energy at the inner shore platform. The

magnitude of variability in particularly calm wave conditions is such that wave height at the north and south can be up to 2.5 times greater than that measured at the central position.

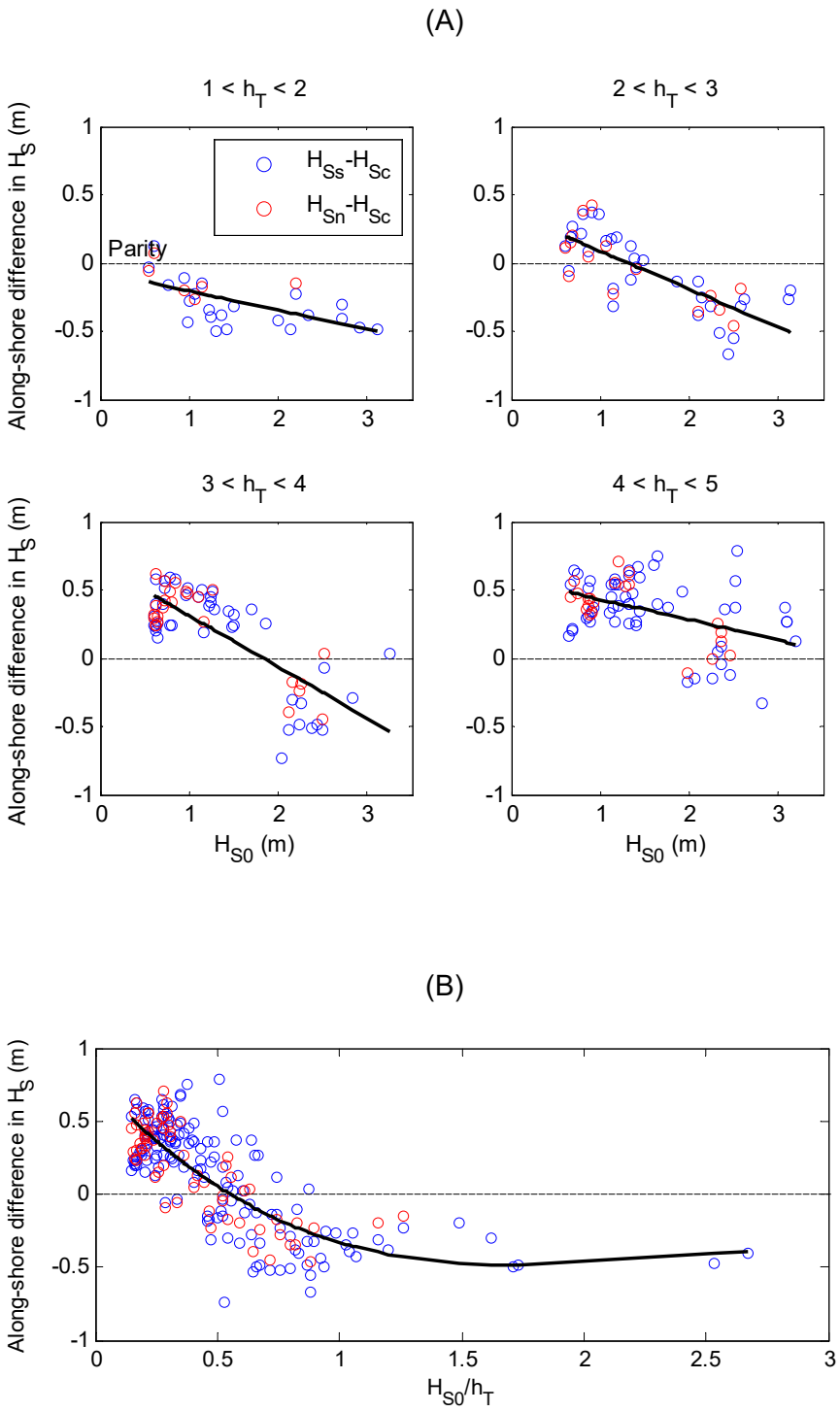

Figure 4.11: Difference in the concurrent half-hourly significant wave height between the: north (H_{Sn}) and central (H_{Sc}) (red data points); south (H_{Ss}) and central position (blue data points); versus (A) the offshore significant wave height and (B) the ratio between the offshore wave height and tidal elevation. (A) The wave height measured in the central embayment tends to be smaller than at the south and north positions when the offshore wave height is small (e.g. H_{S0} < 2.5 m) and/or tide is high (e.g. h_T >3.5 m). (B) The water depth and offshore wave height are combined on the X-axis in a dimensionless expression which describes the cross shore position of the break point. The height of unbroken waves at the north and south shore platform tends exceed that in the centre. Conversely, the height of waves in the central embayment exceeds those at the north and south when the break point extends offshore.

4.7.3 Approach Angle: South Position

The deployment of the MAVS for a five day period enabled the measurement of the nearshore approach angle of waves at the south position. The deployment coincided with highly variable conditions in which the offshore significant height and peak period ranged from 0.7 m and 8.3 s, to 3.1 m and 12.5 s respectively. The ability to infer the nearshore wave direction is crucial to the following clast transport analyses because: (1) the nearshore approach angle is one of the requisite variables for estimating the longshore component of wave power (see Equation 4.3); (2) only five of the clast transport surveys coincided with the deployment of the directional wave gauge (see Table 4.1).

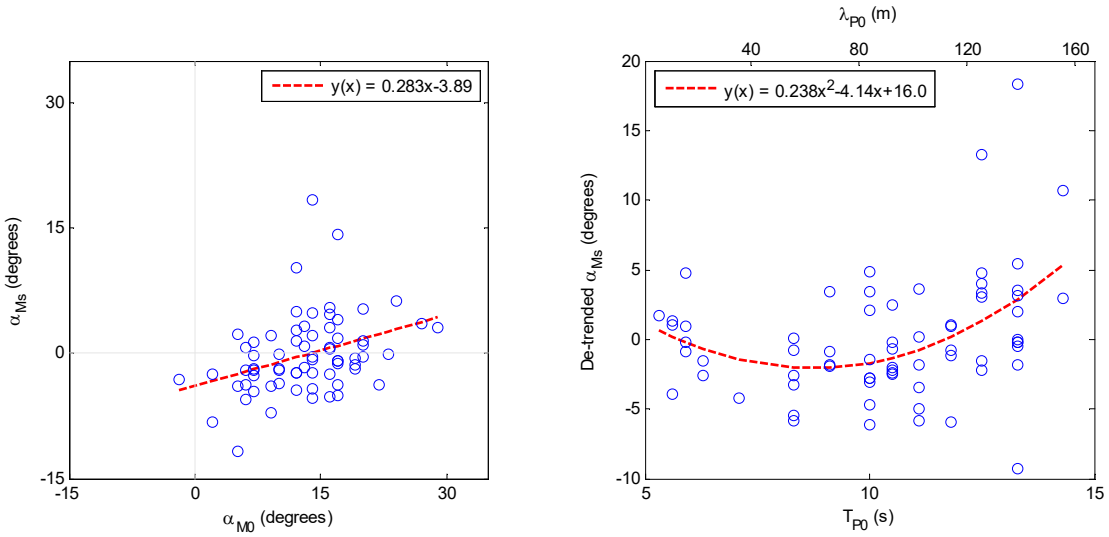

Figure 4.12: (Left) half-hourly mean approach angle measured nearshore (by the MAVS; α_{Ms}) versus corresponding, concurrent offshore measurements (by the wave buoy; α_{M0}); (Right) nearshore approach angle (de-trended for variability related to the offshore approach angle) versus peak offshore period/wavelength (λ_{P0}). Left: The nearshore approach angle is positively related to the approach angle offshore (R^2 = 0.13, *P-value* = 0.0026). Right: Once de-trended for variability related to the offshore approach angle, a secondary, non-linear relationship is observed between the nearshore approach angle and offshore wave period (R^2 = 0.19, *P-value* = 0.0002).

There is a positive, linear relationship between the concurrent offshore and nearshore approach angle (see Figure 4.12). Waves at the inner shore platform are more shore normal than offshore, which implies approaching waves refract considerably when shoaling. Furthermore, both positive and negative approach angles were measured nearshore, which is in contrast to the exclusively positive approach angles measured by the Bideford Bay wave buoy.

Having de-trended the nearshore approach angle for variability in the approach angle offshore, a secondary non-linear relationship is observed with the

offshore peak period. This trend is understandable considering the vertical extent of wave action and hence interaction with underlying morphology is determined by wavelength. The distribution shows incident waves with peak periods between 6 s and 12 s are most strongly refracted, and tend to approach the beach with a southerly-directed (negative) approach angle. The trends displayed in Figure 4.12 corroborate with the understanding that low period wave conditions are characterised by the enhanced refraction of wave fronts towards the elevated south (and north) shore platform, and the subsequent localised focussing of wave energy.

4.8 Results II: Longshore Displacement of Tracer Clasts

Radio Frequency Identification technology facilitated the detection of a high percentage (up to 80 %) of the tracer sample during each full survey following initial deployment. As time progressed, an increasing number of the tracer sample passed through the experimental beach and the proportion of the total number of tracer clasts that were re-detected reduced accordingly (see Figure 4.13 and Table 4.7). Despite this, the two recharges conducted after initial deployment meant the beach was, on all survey dates, populated with tracer clasts.

The collective longshore displacement of clasts is considered here at various temporal frequencies. Whilst daily observations (section 4.8.1) enables longshore transport to be attributed to the specific wave conditions, observations made over a period of weeks and months (section 4.8.2) provides insight into the resulting direction and magnitude of net clast transport at Abbotsham.

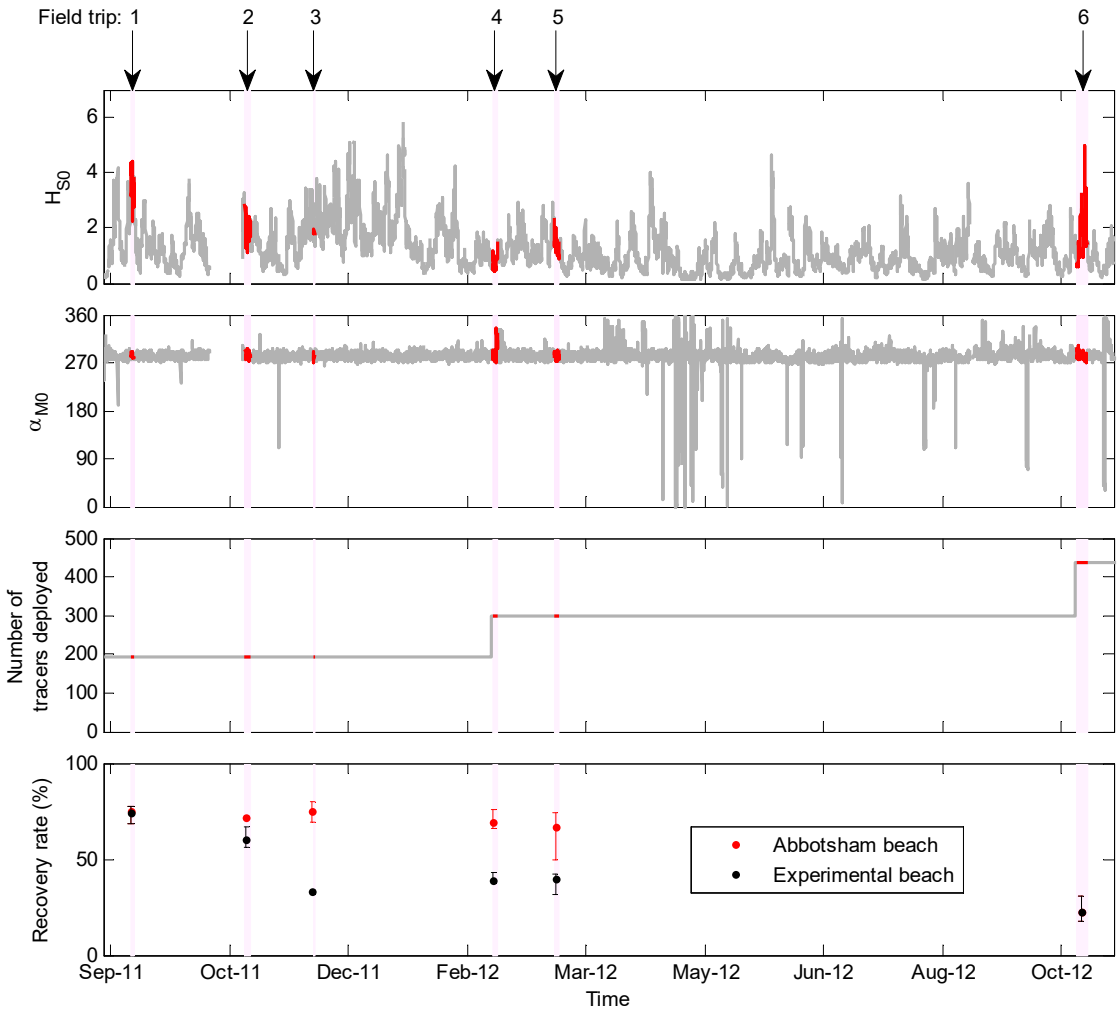

Figure 4.13: Time series of the: significant height (top) and mean approach angle (2nd down) of incident waves measured by the Bideford Bay wave buoy; number of tracer clasts deployed on the beach (3rd down) and the maximum (top of error bar), mean (point) and minimum (bottom of error bar) percentage of the total number of tracers clasts found on each of the six field trips (bottom). Individual field trips lasted for between two and five days, and are highlighted in pink.

4.8.1 Daily Observations

The daily clast displacement experiments coincided with a variety of wave conditions in which the maximum offshore significant height and corresponding peak period ranged from 0.67 m and 9.6 s (calm) to 3.43 m and 13.6 s (storm) (see Table 4.7). The dynamics of clasts was strongly related to the prevailing wave conditions, with the maximum daily displacement of a single clast ranging from 1.93±2.20 m/day in calm condition and 58.74±2.20 m/day in stormy conditions. Displacement distance was also related to clast mass and elevation up the beach (see Figure 4.16 and Figure 4.17). Despite the dynamic state of individual clasts, the cross-shore organisation of the sample remained relatively consistent throughout the experiments (see Figure 4.14).

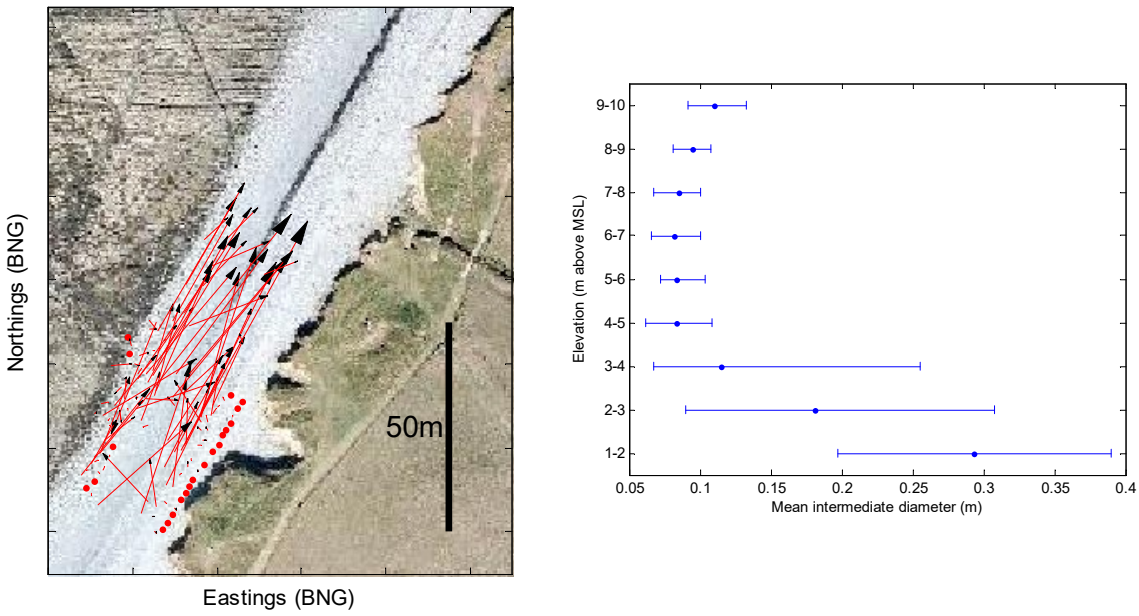

Figure 4.14: Displacement vectors of the located sub-sample of (118) RFID-traced clasts between 12 & 13 September 2011, superimposed onto aerial image of the experimental beach (left) and mean intermediate diameter of sampled clasts versus elevation on the beach (right). Left: Clasts tended to have an overwhelmingly positive longshore component of displacement with a maximum displacement of 58.74±2.20 m. Right: The error bars signify the minimum and maximum mean values for all of the experimental days. Despite the dynamics of the sample the cross-shore sorting of tracer clasts was conserved. Variability in the in the size of clasts located above 4 m was remarkably small, however variability increases significantly below 4 m and ranged by as much as 0.2 m.

Experimental Beach													
Column: 1	2	3	4	5	6	7	8	9	10	11	12	13	14
Dates	Mean H_{S0} (m)	Mean T_{P0} (s)	Mean α_{M0} (deg)	Mean H_{Ss} (m)	Mean α_{Ms} (deg)	Mean P_{LSs} (Watts/m)	No. Tracers deployed	No. / % recovered day 1	No. / % recovered day 2	No. / % recovered day 1 & 2	Mean displacement (m)	Minimum displacement (m)	Maximum displacement (m)
11-Sep-11 to 12-Sep-11	2.57	11.5	18.2	1.14	2.0	214	192	132 / 69	148 / 77	107 / 56	2.77 ± 0.16	-1.10±2.20	18.76±2.20
12-Sep-11 to 13-Sep-11	3.43	13.6	17.7	1.80	5.7	991	192	148 / 77	147 / 77	118 / 62	9.91±0.16	-2.07±1.20	58.74±2.20
29-Oct-11 to 30-Oct-11	2.39	16.0	14.3	1.29	9.1	1143	192	136 / 71	140 / 73	103 / 53	11.91±0.17	-0.89±1.20	48.75±2.20
30-Oct-11 to 31-Oct-11	1.71	14.0	14.4	1.00	4.7	313	192	140 / 73	138 / 72	98 / 51	4.96±0.18	-3.07±1.20	40.66±0.20
31-Oct-11 to 01-Nov-1	1.84	15.0	15.5	0.94	10.1	632	192	138 / 72	138 / 72	98 / 51	1.14±0.19	-1.92±1.20	12.10±2.20
27-Nov-11 to 28-Nov-11	2.20	13.1	13.9	1.26	3.9	432	192	133 / 69	154 / 80	57 / 30	5.07±0.25	-0.98±2.20	30.19±2.20
11-Feb-12 to 12-Feb-12	0.70	10.9	17.2	0.50	0.3	6	298	196 / 66	201 / 67	93 / 31	-0.22.±0.18	-11.58±2.20	2.91±2.20
12-Feb-12 to 13-Feb-12	0.67	9.6	12.7	0.50	-8.6	-137	298	201 / 67	227 / 76	105 / 35	0.06±0.17	-8.80±2.20	11.73±1.20
07-Mar-12 to 08-Mar-12	2.04	10.2	15.0	1.38	-1.2	-122	298	148 / 50	202 / 68	77 / 26	-1.92±0.23	-20.99±2.20	4.07±2.20
08-Mar-12 to 09-Mar-12	1.55	13.5	16.1	1.25	5.0	433	298	202 / 68	211 / 71	104 / 35	-1.55±0.20	-13.36±1.20	3.62±2.20
09-Mar-12 to 10-Mar-12	1.23	12.0	18.3	1.08	1.6	167	298	211 / 71	221 / 74	108 / 36	-0.30±0.19	-9.08±2.20	5.15±2.20
14-Oct-12 to 15-Oct-12	1.05	9.8	15.0	1.02	-1.5	-109	435	135 / 31	114 / 26	105 / 24	-1.10±0.10	-6.82±1.20	1.93±1.20
15-Oct-12 to 16-Oct-12	2.06	10.0	14.6	1.78	-0.8	-349	435	114 / 26	78 / 18	67 / 15	-0.62±0.23	-8.94±1.20	9.31±1.20
16-Oct-12 to 17-Oct-12	1.57	10.8	17.0	1.57	0.6	-21	435	78 / 18	90 / 21	47 / 11	0.50±0.32	-14.80±2.20	9.19±2.20
17-Oct-12 to 18-Oct-12	2.49	12.0	19.6	1.53	3.1	545	435	90 / 21	78 / 18	45 / 10	3.59±0.32	-7.87±2.20	39.30±2.20

Table 4.7: Table of empirical values for each of the longshore transport days, including: survey dates (1); mean offshore significant wave height (2), Peak period (3), approach angle (4); estimated mean nearshore (south) significant wave height (5), approach angle (6) and longshore component of wave power (7); number of tracer clasts that had been deployed before the initial survey date (8) and the number/percentage of which were detected across the experimental beach on the first (9), second (10) and both (11) of the coupled survey days; mean (12), minimum (13) and maximum (14) longshore displacement observed between survey days.

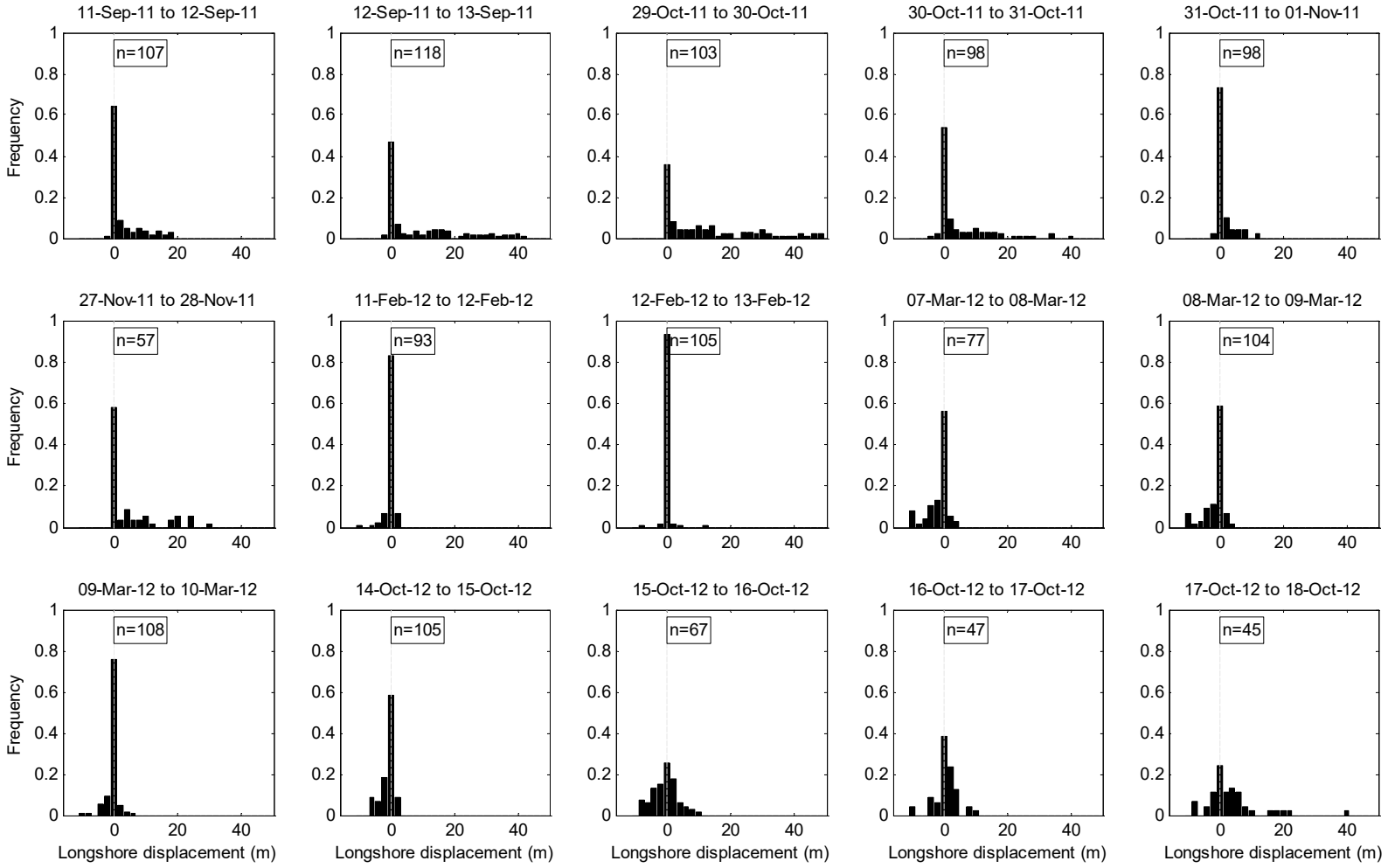

Figure 4.15: Frequency distribution of tracer clasts between daily surveys. The number of clasts located on both of the coupled survey days is displayed within the text box.

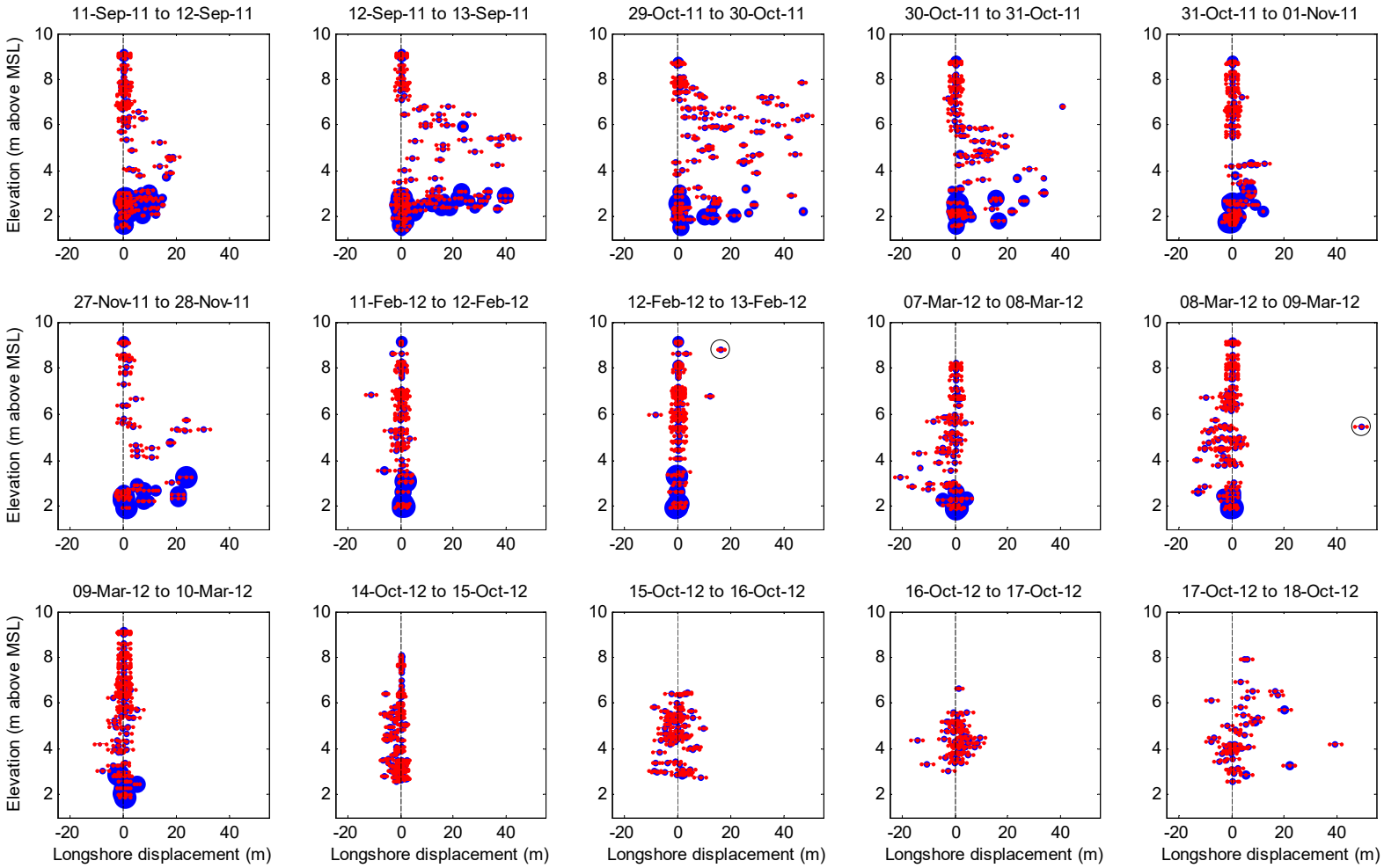

Figure 4.16: Mean elevation versus longshore displacement of individual clasts. The size of the blue data points is proportional to the B-axis of the clast and the red horizontal error bars represent uncertainty associated with measuring the displacement of each clast. Notably, between 12 and 13 February 2012 and 08 and 09 March 2012 a tracer clast with highly anomalous recorded displacement was identified (encircled in black). For reason outlined in the text these data points were considered to be spurious and excluded from the following analyses.

The direction and magnitude of the displacement of tracer clasts varied depending on the prevailing wave conditions. In the most powerful conditions (between 29 and 30 October 2011) coarse pebbles located on the central beach were displaced by up to 58.74±2.20 m to the north-north-east. Calm conditions displaced similarly sized and positioned clasts by as much as 20.99±2.20 m in the negative direction (between 07 and 08 March 2012). There was general conformity in the direction in which clasts were displaced between consecutive daily surveys. However, the magnitude of the displacement of individual clasts was highly variable. This characteristic demonstrates the stochastic nature of wave-clast-beach interactions and the fact that transport of two clasts with similar properties and pre-transport settings can differ greatly.

Despite precautions (outlined in section 4.5.5), it is immediately apparent in Figure 4.16 that two measured clast displacements are anomalous. In the first instance (between 12 and 13 February 2012; see encircled data point in Figure 4.16), a clast located shoreward of the storm crest was registered as being displaced 16.11±1.20 m in the positive direction, despite the wave conditions being the calmest recorded. Secondly, (between 08 and 09 March 2012) a single clast was supposedly transported 49.08±2.20 m in the positive direction whilst almost all other displaced tracer clasts were transported in the negative direction. Considering the improbability of these anomalous displacements being the result of hydrodynamic processes and the numerous ways in which they could have arisen from worker error or human interference, these data point were considered to be spurious, and accordingly omitted from the data set.

Between each of the coupled daily surveys the magnitude of modal clast displacement was less than two meters (see Figure 4.15). The proportion of clasts that remained relatively stationary (i.e. measured displacement < 1 m) reduced with prevailing wave power. For example, almost the entire sample remained stationary between 12 and 13 February 2012, but less than 30 % of the sample was stationary between 29 and 30 October 2012. In fact, an even smaller proportion of the sample was stationary between the final three coupled survey days in October 2012. However, this particular result was due to the under-representation of particularly coarse clasts at the beach base, and clasts seaward of the beach crest (see Figure 4.16).

Despite variability in the magnitude of clast displacement, consistent sample-wide trends do emerge. Most noticeable is the tendency for the displacement distance to

increase rapidly from the beach base to a maximum around the high water spring mark (approximately 4.3 m above MSL). The displacement of clasts reduced to zero above maximum run-up elevation, which approximated 5 and 8 m above MSL in the calmest and stormiest conditions respectively.

The observed relationship between the cross-shore position of a clast and its longshore displacement makes physical sense considering the elevation at which the displacement distance was greatest approximated the spring high water mark, and hence the area of the beach in which the most powerful breakers (within a tidal cycle) will impinge. Meanwhile, there is an equally intuitive inverse relationship between the maximum displacement distance and clast size/mass. It should be noted that only a small, and particularly fine, fraction of 121 tracer clasts were exported to the laboratory and weighed, but the A-, B- and C-axes of all tracer clasts were measured. The product of the three axial lengths of the regular, rounded greywacke clasts at Abbotsham is very strongly correlated to clast mass (see Figure 4.17). For this reason, clast displacement is considered here with respect to clast mass, which estimated from the lengths of its three axes.

Figure 4.17 shows that while the displacement distance of any one clast is variable, the maximum observed displacement is strongly related to clast mass. This finding is indicative of the multiple variables that influence the displacement of a clast, which might become buried or stranded beyond the influence of wave action. Clasts displaced the greatest distance are less likely to have been buried or stranded and thus it seems likely that the upper boundary will be a good indication of the mass control on displacement.

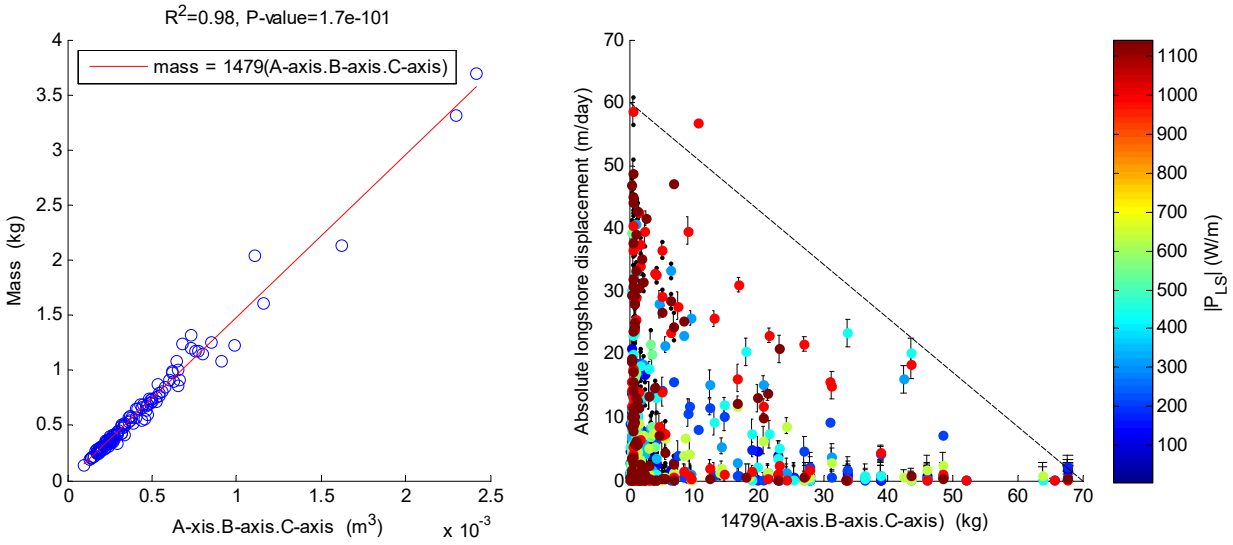

Figure 4.17: (Left) Relationship between the mass of a small subset of 121 particularly fine tracer clasts (that were exported to the lab for weighing) and the product of their three axial lengths; (Right) Absolute longshore displacement measured between each of the coupled daily surveys versus estimated mass (based on the relationship in the left graph). Data points are coloured according the estimated longshore component of wave power acting adjacent to the beach. Error bars represent the uncertainty associated with measuring the displacement of clasts. The dashed black line has been subjectively placed to highlight the relationship between the magnitude of the maximum longshore displacement of clasts and mass.

The mean longshore displacement of the tracer clasts located on successive coupled surveys is between -1.92±0.23 m/day and 11.91±0.17 m/day. Correlation analysis indicates a statistically significant relationship (i.e. *P-value* << 0.02) with the inferred longshore component of wave power, which accounts for 70 % the variability in the mean longshore displacement of tracers (see Figure 4.18).

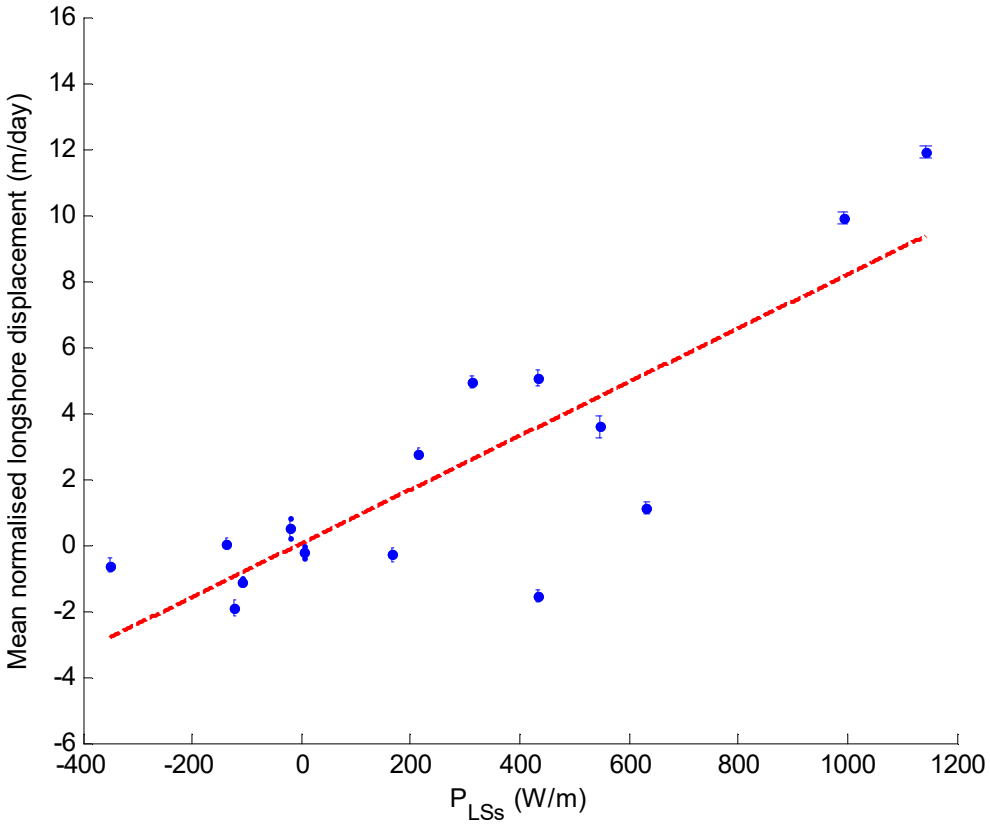

Figure 4.18: The mean longshore displacement of mobile tracers versus the estimated mean longshore component of wave power. The error bars represent the estimated error associated with the inability to locate and measure the exact position of tracer clasts. The line of best fit is plotted with a dashed red line. The longshore displacement of mobile tracers correlates well with the estimated longshore flux of wave energy (R^2 = 0.70, *P-value* = 9.87×10^{-5}).

4.8.2 Low Frequency Observations

4.8.2.1 Clast Displacement between Consecutive Field Trips

Further to the daily observations, the displacement of clasts between the interspersed field trips is considered here. The displacement of clasts are analysed in between the five field visits made from September 2011 to March 2012. Considering entire schedule of field work, one might logically question why these analyses do not include the displacement of tracer clasts between the: (1) initial deployment (in July 2011) and following September field visit; (2) March and October (2012) field trips.

This was not possible for the following reasons:

(1) The initial injection of tracer clasts onto the beach in July 2011 was conducted over a series of five days with only a fraction of the sample being deployed on any given day. Therefore, only a small number of tracer clasts from a very specific portion of the beach could be monitored between single survey days in July and September field visits.

(2) By October 2012, the majority of the initial and recharge tracer clasts had migrated out of the surveyed beach. Clasts traced throughout these field trips were not actively searched for during the subsequent October survey, for which the south beach was replenished with a new sample of tracer clasts.

Abbotsham Beach														
Column: 1	**2**	**3**	**4**	**5**	**6**	**7**	**8**	**9**	**10**	**11**	**12**	**13**	**14**	**15**
Dates	**Days between surveys**	**Mean H_{S0} (m)**	**Mean T_{P0} (s)**	**Mean α_{M0} (deg)**	**Peak H_{S0} (m)**	**Peak T_{P0} (s)**	**Peak α_{M0} (deg)**	**No. Tracers available**	**No. / % recovered time 1**	**No. / % recovered time 2**	**No. / % recovered time 1 & 2**	**Mean displacement (m/day)**	**Minimum displacement (m/day)**	**Maximum displacement (m/day)**
13-Sep-11 to 29-Oct-11	46	1.31	9.3	18.2	3.82	13.3	23	192	147 / 77	136 / 71	106 / 55	0.16±0.004	-0.13±0.026	1.86±0.026
01-Nov-11 to 27-Nov-11	26	1.37	11.9	19.1	3.43	13.3	13	192	138 / 72	133 / 69	93 / 48	0.75±0.008	-0.12±0.085	2.99±0.085
30-Nov-11 to 11-Feb-12	73	1.81	10.9	17.8	5.82	10.5	23	192	148 / 77	112 / 58	86 / 45	0.22±0.003	-1.28±0.030	1.38±0.030
13-Feb-12 to 07-Mar-12	23	1.29	10.2	16.0	2.64	16.7	24	298	227 / 76	148 / 50	133 / 45	0.11±0.007	-1.11±0.096	2.52±0.052

Table 4.8: Table of empirical values for wave and clast transport between field trips, including: survey dates (1) and the number of days between them (2); mean offshore significant wave height (3), peak period (4) and approach angle (5); offshore significant wave height (6), peak period (7) and approach angle (8) measured during the most powerful conditions; number of tracer clasts that had been deployed before the initial survey date (9) and the number/percentage of which were detected across Abbotsham beach on the first (10), second (11) and both (12) of the coupled survey dates, and; mean (12), minimum (13) and maximum (14) longshore displacement of tracer clasts observed between the survey dates.

Figure 4.19: Displacement vectors of individual clasts between consecutive field trips. The majority of the original sample (red arrows) was transport in the positive direction (northward) between field trips.

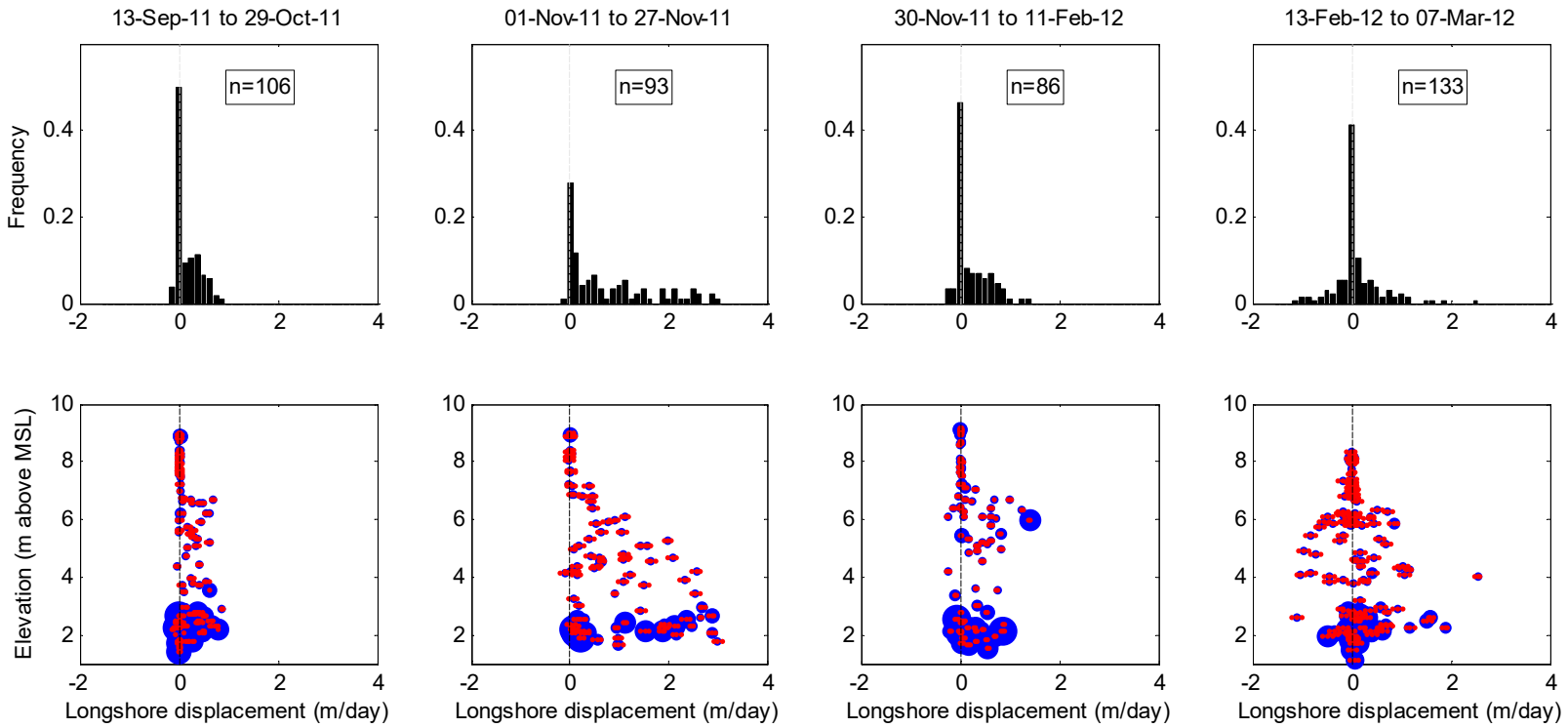

Figure 4.20: (top) Frequency distribution of longshore clast displacement and (bottom) mean elevation versus longshore displacement of individual clasts. In the bottom plots, the size of the blue data points is proportional to the B-axis of the clast and the red horizontal error bars represent uncertainty associated with the displacement of each clast.

Net displacement between field trips was overwhelmingly towards the north-north-east (i.e. positive-directed). Variation in the magnitude of clast displacement over the extended intervening time period meant the tracer clasts became dispersed outside the confines of the experimental beach. The wide distribution of the observed sample complicates the situation because, at any given time, clasts occupied quite different hydrodynamic zones (see section 4.7.2). For this reason no attempt is made to relate clast transport to the nearshore wave conditions (that have be inferred for the south position only), and wave buoy measurements are used to contextualise the observed transport.

Mean displacement of the sample was exclusively in the positive direction and varied between 0.11±0.007 m/day and 0.75±0.008 m/day. These values are over an order of magnitude smaller than rates measured between consecutive days, which is unsurprising considering field surveys were scheduled to coincide with spring tides (when the beach was most exposed to wave action). In contrast, at least one whole spring-neap tidal cycle was completed over the extended period intervening field trips. During neap tides, nearshore wave energy was minimised. So too was the period (within each tidal cycle) when waves acted on the beach, which in the most neap tidal cycle approximates zero.

The transport of individual clasts varied considerably within a given time frame. The modal longshore displacement between each of the coupled survey dates was approximately zero, but individual clasts were displaced at an average rate of up to 2.99±0.085 m/day (between 1 and 27 November 2011; see Table 4.7). As demonstrated by the daily transport observations, there was a complex relationship between clast mass and its displacement. Again the displacement of any one clast is highly variable but the maximum displacement between each field trip was strongly and inversely related to clast mass (see Figure 4.21). The upper limit of displacement appears to vary between survey periods, yet the boundary is particularly strong between 01 and 27 November 2011 when the magnitude of transport was greatest.

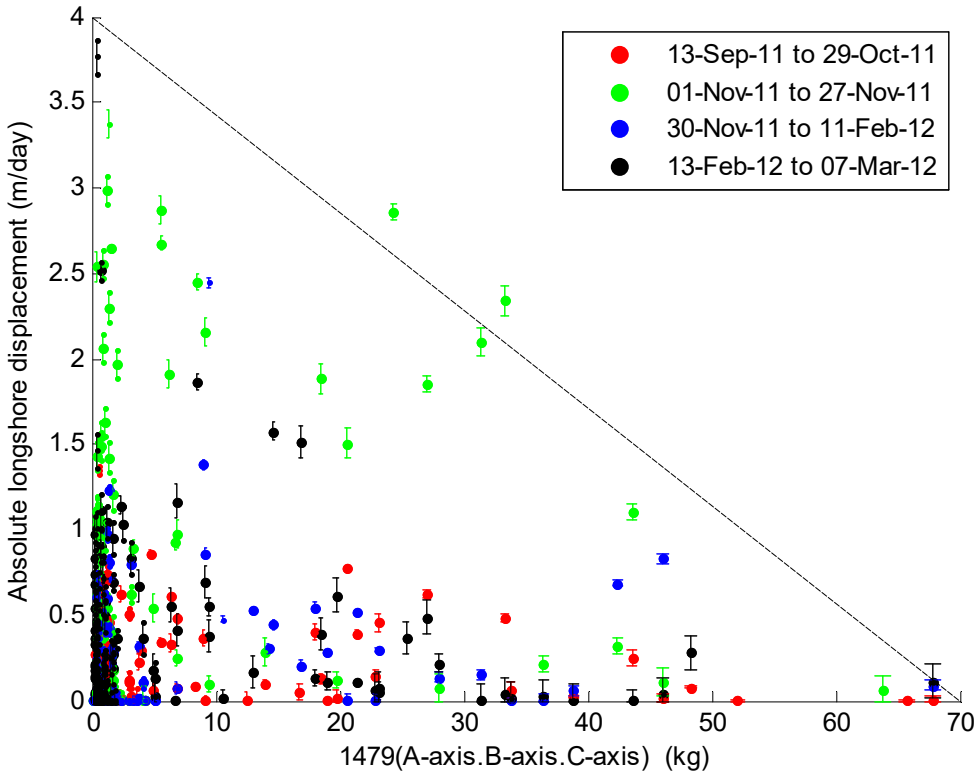

Figure 4.21: Absolute longshore displacement measured between each of the coupled field trips versus estimated clast mass (see Figure 4.17 for details). Data points are coloured according to each observational period. Error bars represent the uncertainty associated with measuring the displacement of each clast. The dashed black line has been subjectively placed to highlight the relationship between the magnitude of the maximum longshore displacement of clasts and their mass.

Clast displacement was uniformly in the positive direction between the first three coupled survey dates. However, a relatively even number of clasts were transported in the positive and negative directions between 13 February and 7 March 2012. The lack of uniformity in the displacement direction meant the mean longshore displacement of the entire sample was small in comparison that observed during the previous three observational periods. Neither the displacement of individual clasts nor the collective displacement of the sample as whole was clearly related to the average or peak wave conditions measured offshore. Moreover, no clear relationship was evident between the mean and maximum displacement of clasts (see Table 4.8).

The poor relationship between: (1) clast displacement and mean/peak wave conditions and (2) the displacement of individual clasts and the sample as a whole suggests observed transport was not generated by a single event, but was the culmination of the successive reworking of clasts on variety of

occasions. These low frequency observations are therefore of limited use for furthering understanding about the precise relationship between wave conditions and clast transport and highlight the value of the high-frequency, daily observation between which the (offshore) wave conditions remained relatively consistent.

4.8.2.2 Clast Displacement over a Six Month Period

The six-month transport observations (displayed in Figure 4.22) are based on the sub-sample of 98 clasts that were located across Abbotsham beach on 11 September 2011 and 10 March 2012. These two dates were selected because they were the most inter-dispersed surveys for which there was a large overlap in the sub-samples of tracer clasts detected. The recovery rate of the 192 available RFID clasts on both surveys was 69 % and 73 % respectively. However, 51 % of the original sample was located during both surveys and comprise the following longshore displacement observations.

The tracer sample was displaced 79.52±0.18 m to the north-north-east at an average rate of 0.44±0.001 m/day. The displacement distance of individual clasts was highly variable and ranged from between approximately -0.04±0.007 m/day and 1.07±0.007 m/day. Modal clast displacement was approximately zero (see Figure 4.22). Considerable displacement (i.e. > 1 m/day) was exclusively in the positive direction and normally distributed.

Figure 4.22 shows, in contrast to the daily transport observations, the longshore displacement of coarse clasts located on the lower beach approximated the longshore displacement of fine clasts located around MHWS elevation. This is most probably because throughout the spring-neap cycle clasts located lower on the beach were more frequently exposed to wave action than the elevated regions. Nearly all stationary clasts were located shoreward of the storm crest and clasts with the highest longshore displacement on the central and lower beach face. Like for the observations made between consecutive days and field trips, there was a strong inverse relationship between clast mass and maximum longshore displacement.

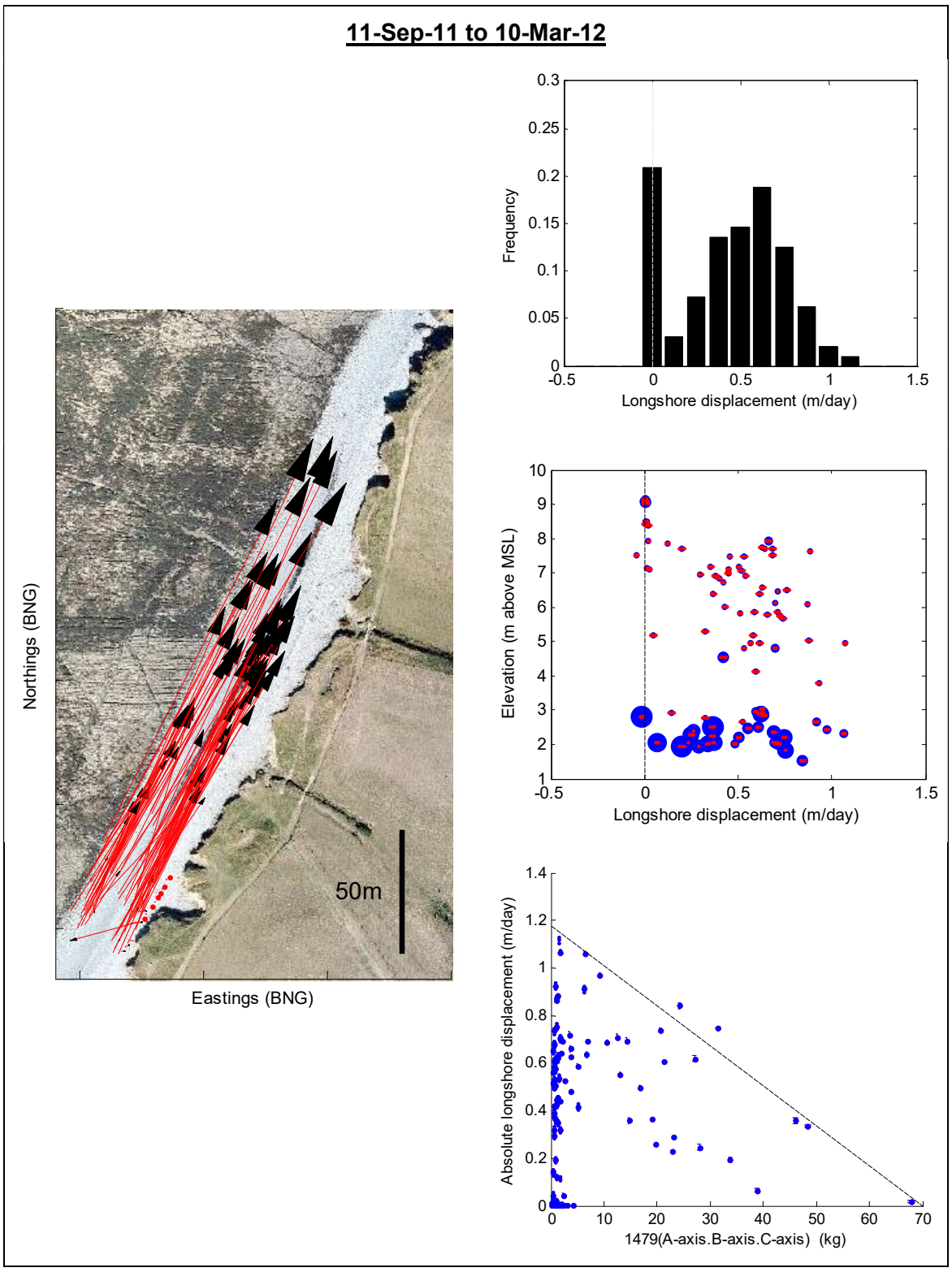

Figure 4.22: (Left) Displacement vectors of individual clasts; (top, right) frequency distribution of longshore particle displacement; (middle, right) mean elevation versus longshore displacement of individual clasts; (bottom, right) absolute longshore displacement of individual clasts versus estimated clast mass (see Figure 4.17 for details). The horizontal red bars in the middle right plot, and the vertical blue bars in the bottom right plot represent uncertainty with measuring the displacement of each clast (which in each case is relatively insignificant). The size of the data points in the middle, right plot is proportional to the B-axis diameter of the clasts.

It should be noted that considering long-term transport over the finite length of surveyed beach incorporates significant uncertainties. The recovery of traced clasts will be biased toward those which had not yet migrated out of the surveyed zone. Clasts with the greatest longshore velocities are less likely to have been located on the second beach survey and therefore less likely to be represented in the quoted six-month displacement estimate. The actual longshore displacement of the sample is likely to be greater than estimated.

4.9 Results III: Depth of Activation

The DoA experiments were conducted over two field trips, one coinciding with calm conditions and the other with one of the most intense storms of 2012. The daily DoA was measured repeatedly at three cross-shore positions, however the methodology was considered to be flawed at the most seaward position and excluded from the following analysis for reasons outlined here: The bottom beach at Abbotsham is composed of coarse cobbles and fine boulders. The inability to construct a DoA column of similar-sized clasts meant relatively fine DoA clasts were wedged between much larger units. The displacement of DoA clasts in the seaward position was strongly influenced by the packing of DoA clasts within the beach matrix and did not truly reflect the depth to which surrounding material was transported. Although it is not necessary for the DoA clasts to exactly reflect the surrounding beach matrix, it is important that they are similar in size in order to maintain natural packing. For this reason, only the data obtained from the central and uppermost DoA positions (i.e. 2 and 3 in Figure 4.23) are included in the following analysis.

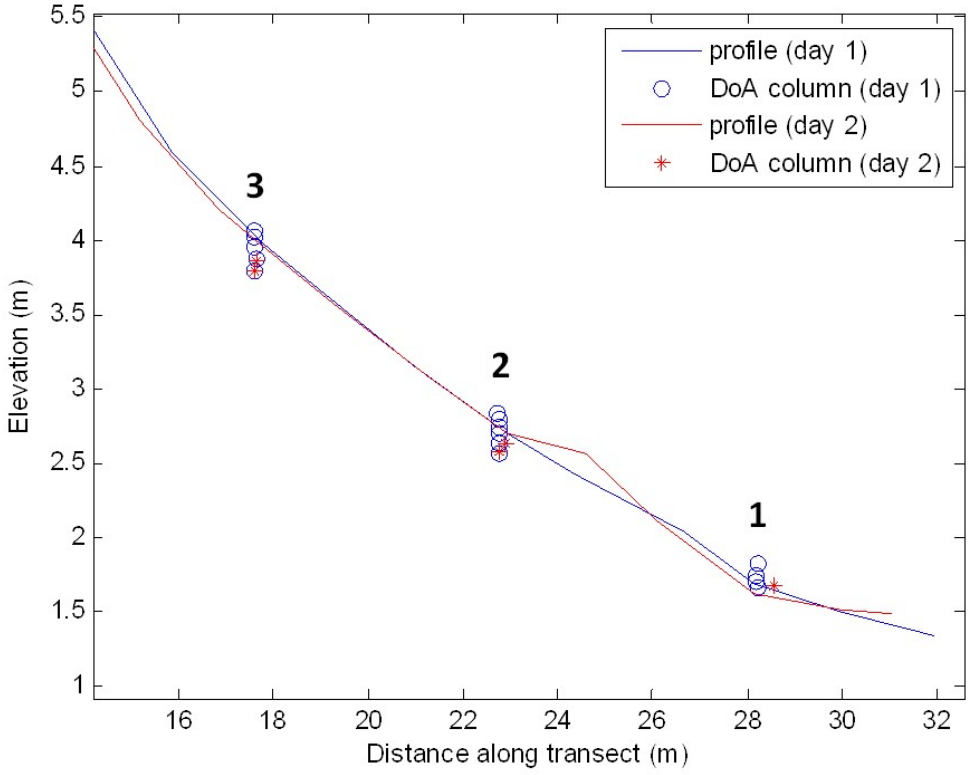

Figure 4.23: The cross-shore profile and position of DoA clasts on 18th (day 1) and 19th (day 2) of August, 2012. The numbers refer to the cross-shore position of the DoA columns.

The DoA was positively related to the power of the prevailing waves in both locations across the transect (see Table 4.7 for all empirical values), which in each daily experiment was greater at the uppermost position. The DoA was observed to be between $0.04^{+0.05}_{-0.04}$ m and 0.25±0.05 m in calm conditions. During the most powerful wave conditions the measured DoA was at least 0.42 m in the position of the uppermost DoA column (3; Figure 4.23). It was not possible to put an upper bound on this measurement because the entire DoA column was situated in the mobile layer and hence was displaced. The consistently greater activation depths measured at the uppermost DoA column likely results from the influence of the shore platform on the power of waves that impinged directly on the beach. The DoA was therefore analysed with respect to the estimated power of waves impinging directly on the DoA column.

Dates	DoA Column (m above MSL)	No. of DoA clasts deployed (day 1) / unmoved (day 2)	Elevation of uppermost DoA clast (day 1)	DoA (m)	h_{max} (m above MSL)	H_{Sc} (m)	T_{Pc} (s)	P_c (Watts/m)
18-Aug-12 to 19-Aug-12	2	6 / 2	2.84	0.16±0.05	4.4	0.42	10.7	1010
	3	5 / 2	4.06	0.14±0.05		0.44	8.4	1428
19-Aug-12 to 20-Aug-12	2	5 / 4	2.73	0.08±0.05	4.6	0.53	10.4	1593
	3	8 / 4	4.05	0.10±0.05		0.56	10.4	2263
20-Aug-12 to 21-Aug-12	2	6 / 4	2.77	0.09±0.05	4.6	0.35	8.1	698
	3	7 / 3	4.05	0.25±0.05		0.38	8.1	1037
21-Aug-12 to 22-Aug-12	2	8 / 5	2.74	$0.04^{+0.05}_{-0.04}$	4.4	0.71	8.3	2873
	3	8 / 0	4.02	$0.07^{+2.85}_{-0.05}$		0.67	7.7	3219
15-Dec-12 to 16-Dec-12	2	10 / 2	3.06	0.38±0.05	4.6	1.83	14.9	20490
	3	10 / 0	4.09	$0.47^{+2.72}_{-0.05}$		2.08	15.3	31359
16-Dec-12 to 17-Dec-12	2	11 / 4	3.10	0.33±0.05	4.4	1.70	14.2	17714
	3	9 / 0	4.25	$0.47^{+2.89}_{-0.05}$		2.21	14.8	36270

Table 4.9: Table of empirical values for the daily depth of activation experiments, including the: (1) dates over which experiments were conducted; (2) cross-shore position in a which depth of activation column was constructed (see Figure 4.23); (3) number of clasts deployed on day 1 and that remained unmoved by day 2; (4) initial (day 1) elevation of the uppermost DoA clast; (5) measured depth of activation between coupled survey days; (6) maximum tidal elevation between coupled survey days; (7) significant height, (8) peak period and (9) power of incident waves estimated to have impinged directly on the DoA column.

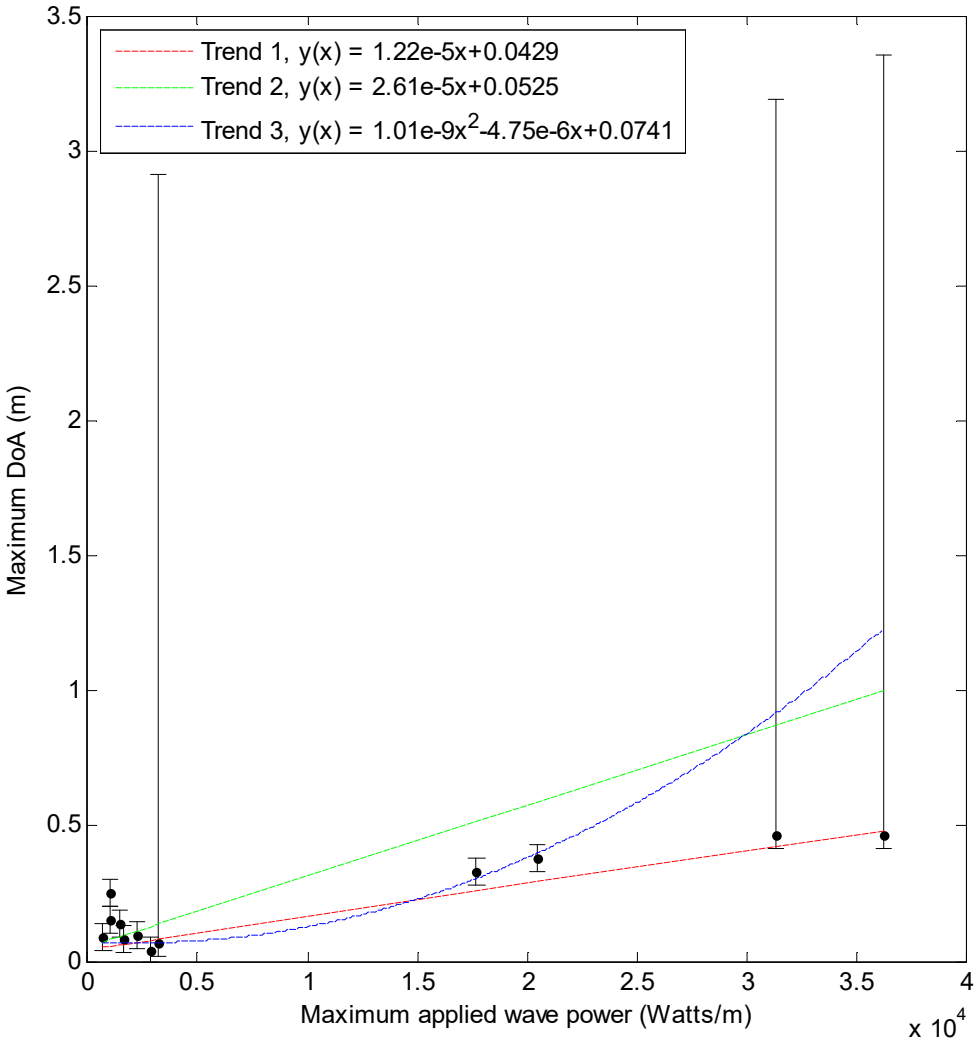

Figure 4.24: The daily depth of activation versus the maximum power of waves impinging directly on the depth of activation column. Where the entire DoA column was displaced, the DoA was not measured accurately and the actual DoA could have been anywhere between position of the lowermost DoA clast (on day 1) the beach base. In order to explore the impact of this uncertainty on the estimated volumetric transport rates (see section 4.10.4) three separate trend lines have been fitted to the data set. The red line of best fit is based on the absolute minimum DoA (R^2 = 0.85, *P-value* = 2.2×10^{-5}). Further hypothetical linear (green) and non-linear (red) trend lines have also been subjectively applied to the data set.

As displayed in Figure 4.24, the DoA was positively related to wave power. A general lack of data and the immeasurably large DoA achieved by powerful storm waves meant the precise relationship between the two variables remains unclear. A linear trend line was initially fitted the absolute minimum DoA, which was strongly correlated with the maximum applied wave power. However, while this trend might accurately represent the DoA in calm conditions, the actual DoA could be vastly greater than the trend suggests during powerful conditions. Two further hypothetical trends were therefore applied to the data set to quantify the

impact of this uncertainty on the estimated volumetric transport rates (see section 4.10.4).

4.10 Discussion

4.10.1 Shore Platform Control on Nearshore Wave Properties

Field data showed nearshore wave transformations to be complex, and shore platform morphology to influence shoaling, breaking, and the refraction of incident waves. The precise interaction between the shore platform and incident waves was dependent on the prevailing offshore wave conditions and tidal elevation. It should be noted that measurements were not sensitive to the assumption that wave properties at the position of the Bideford Bay wave buoy and seaward edge of the shore platform are consistent. The deployment of a wave gauge just beyond the littoral zone at Abbotsham is therefore highlighted as a key improvement to the experimental setup.

When the ratio between the offshore wave height and water depth was high, the surf zone extended across the shore platform and wave energy along the inner shore platform was saturated. Here, the nearshore wave height was linearly related to water depth and became independent of variability in the offshore wave conditions (e.g. Thornton & Guza, 1983; Sallenger & Holman, 1985; Farrell et al., 2009). Spatial variability in platform morphology resulted in systematic variability in incident wave energy along the inner shore platform. Enhanced attenuation across the elevated north and south shore platform meant wave height was consistently greater within the central embayment. The moderation of wave energy was mirrored in the morphology of the coarse clastic beach, which was built up adjacent to the central embayment. It should be noted that despite the reduced elevation of the platform seaward of the central position, half the wave energy was dissipated here during the stormiest high tide period.

A different trend was observed when waves propagated across the shore platform without breaking. Under these circumstances, the wave height measured at the north and south tended to be greater than at the central position. It is however unclear whether the observed amplification of waves at the elevated shore platform was simply the result of the shoaling process (in which power is conserved), or a result of a change in the local wave energy as

incident waves refract (as discussed below). The ability to determine the precise cause of this trend would require enhanced knowledge of the refraction patterns across the shore platform and therefore the deployment of an alongshore array (or better still a grid) of directional wave gauges.

While the attenuation of incident wave energy across shore platforms has been addressed by multiple studies, a comprehensive literature search suggests no published field studies have observed wave refraction in relation to platform morphology. Incident waves with peak periods between 6 s and 12 s were most strongly refracted by the shore platform morphology. These wave fronts were consistently refracted away from the central embayment and towards the elevated shore platform, to the north and south. It is hypothesised that this was a contributing factor to the systematic amplification of the incident wave height to the north and south of the central embayment during calm conditions. The five-day-long wave direction measurements made at the south position corresponded with these findings, and demonstrated the tendency of shorter period waves (characteristic of weak conditions) to approach the beach with a negative angle of obliquity and longer period waves (characteristic of powerful wave conditions) with a positive angle of obliquity.

4.10.2 Longshore Clast Displacement

Long-term observations over a period of six months demonstrated the overwhelming positive (northward) net displacement of clasts along the entire stretch of Abbotsham beach. This result supports the general understanding of the dynamics of the Bideford Bay coarse clastic system, in which clasts are progressively transported northward from the clastic source (the Gore) to the mouth of the Taw and Torridge Estuaries. Net positive displacement was also observed between field visits, which were separated by 23 to 73 days. However, the wide dispersion of clasts across Abbotsham beach made it difficult to relate the collective displacement of the sample to the nearshore wave conditions. No relationship was found between the longshore transport and the offshore wave conditions; but perhaps more surprising was the lack of a relationship between the collective mean and maximum displacement of clasts between each field trip. This was taken as an indication that the observed transport was the result of the progressive reworking of material by the various conditions that prevailed between each field trip.

The displacement of individual clasts was related to cross-shore position. Clasts located shoreward of the storm crest were protected from wave action and generally remained stationary. For the daily (spring tide) observations, fine clasts located around the spring high water mark tended to be displaced the greatest distance. However, over the spring-neap cycle, the lower beach was most exposed to wave action and was where the greatest clast displacement was observed. Regardless of the observational frequency and the intervening wave conditions, there was a strong inverse relationship between clast mass and the maximum displacement distance.

The magnitude of the longshore transport of clasts observed between experimental days was generally far greater due to the particularly high (spring) tides which field trips were deliberately scheduled to coincide with. The main benefit to the daily observation is that the wave conditions remained relatively consistent during the intervening 24 hour period, which enabled a strong relationship to be developed between the wave force and clast transport.

Of utmost importance was the estimation of the mean longshore transport of the mobile layer and its relationship to the prevailing wave conditions. Systematic longshore variation in wave conditions adjacent to Abbotsham beach meant it was best to divide the beach up into different hydrodynamic zones. The southerly injection of tracer clasts and timing of the field visits meant only the south zone of the beach was at all experimental times populated with tracer clasts and hence suitable for analysis. However, limited access to a directional wave gauge meant the wave record at the south position was incomplete. Consequently, local wave parameters had to be inferred for each of the experimental days. Improvement to the current investigation would result from relating the clast transport observations to direct measurements of the height and approach angle of incident waves.

The daily observations made for the purpose of this investigation enabled the development of a strong, quantitative relationship between clast transport and prevailing wave conditions. The results were consistent with the findings of Hattori & Suzuki (1978) and Miller et al. (2012), who found the magnitude and direction of the longshore displacement of clasts was linearly related to the longshore component of wave power.

The role of the shore platform in the determination of the longshore component of wave power adjacent to the CCB, and therefore the longshore displacement of clasts, was twofold. First, the shore platform morphology moderated the amount of incident wave energy that could propagate shoreward. Perhaps more interestingly, enhanced refraction of weaker waves, and resulting negative longshore component of power, was coupled with a reversal in the direction of net clast transport within the observational cell. Alternatively, energetic conditions were consistently associated with the positive transport of clasts towards the Pebble Ridge.

4.10.3 Depth of Activation

Measuring the DoA is a classic challenge in the sediment dynamics discipline. The DoA data presented in this chapter are the first known measurements on a beach comprised of pebble- to boulder-sized clasts. A positive trend was found between the absolute minimum DoA and maximum wave power. However, the scarcity of, and uncertainty associated with, these data provided scope for a wide range of possible trends. The data set could be vastly improved by simply increasing the number of observations in moderate and stormy conditions. These data would not only increase confidence in the current results, but could enable the inference of immeasurably large DoA's achieved by the most powerful conditions. Unfortunately, the laborious and time-consuming nature of the DoA experiments meant increasing the number of observations was beyond the scope of the current thesis.

Difficulties associated with constructing DoA column on the particularly coarse seaward portion of the beach meant measurements were only made in the central region of the beach, which is composed of fine pebbles. It seems probable that the DoA will vary depending on the size of beach clasts, which influences the threshold-entrainment (e.g. Lorang, 2000) and the hydraulic conductivity of the matrix (e.g. Krumbein & Monk, 1943). The applicability of these pebble-based measurements to the particularly coarse clasts located at the seaward margin of the beach is therefore unclear.

Overarching questions remain about how the measured DoA relates to the longshore transport rate. The displacement of the DoA clasts between consecutive days signifies the maximum depth to which clasts were mobilised

within the intervening time period. In reality, the thickness of the mobile layer is temporally variable and dependent on the instantaneous wave force (e.g. Foster et al., 2006). It is arguable that the average DoA is more meaningful than the maximum DoA values yielded by displacement experiments, and the use of these displacement data can result in a systematic over estimate of the LSTR (Van Wellen et al., 2000). Improvement would result from the ability to determine the real-time DoA, as has been conducted for a number of sand-based experiments (e.g. Foster et al., 2006). However, measuring of the real-time DoA in a sandy setting is difficult enough, and no published reports were found that described equipment or techniques for application on CCBs. Despite the crude nature of the DoA experiments, they have provided values for a hitherto unknown quantity at Abbotsham.

4.10.4 Longshore Transport Rate & the *K* Coefficient

A key aspiration in coastal engineering is the ability to predict the longshore transport rate in response to the lateral thrust applied by shoaling incident waves. Extensive empirical studies have shown the longshore transport of sand to be proportional to the longshore component of wave power (Komar, 1997), and have focussed on the empirical derivation of a dimensionless proportionality (*K*) coefficient that equates the two variables:

$$I_{LS} = KP_{LS}$$

Equation 4.10

where I_{LS} is the immersed weight of sediment transported longshore:

$$I_{LS} = (\rho_s - \rho_w) g a' Q_{LS}$$

Equation 4.11

in which ρ_s and ρ_w are the density of sediment and water respectively; g is the acceleration due to gravity; a' stands for porosity and; Q_{LS} is the volume of sediment transported longshore.

For sandy beaches, the *K* coefficient has been shown to be between 0.2 and 1.2 (Komar, 1997). Shoonees & Theron (1991) reviewed the results from numerous field studies and noted large variability within and between different data sets, but conclude that it is not possible to determine whether variability was due to natural factors or methodological error. They called for further comprehensive field data in order to improve understanding of the precise

relationship between the longshore component of wave power and transport rate on a range of beaches.

Field and laboratory studies by Kamphuis (1990) showed the *K* coefficient to be positively related to beach slope but negatively related to grain diameter:

$$K \propto \theta \left(\frac{H_b}{D_{50}}\right)\left(\frac{H_b}{\lambda_0}\right) \qquad \textbf{Equation 4.12}$$

Where Θ is the beach slope; H_b is the breaker height; D_{50} is the intermediate clast diameter and; λ_0 is the offshore wavelength. Komar (1997) highlighted the interrelationship between beach slope and grain diameter and suggested the dependency on slope will offsets the reduction in *K* with increasing clast diameter.

Van Wellen et al. (2000) noted that very few longshore transport field experiments have been conducted on coarse clastic beaches (e.g. Nicholls & Wright, 1991) and that their distinct hydrodynamics means the results of sand-based field studies are not necessarily applicable. Komar (1997) pointed out that the *K* coefficient for coarse clastic beaches is complicated by the requirement of a threshold-entrainment function. However, field data presented in this chapter show the threshold-entrainment of a large fraction of clasts is exceeded during relatively calm conditions at Abbotsham.

4.10.4.2 Estimating the Longshore Transport Rate

This section presents estimates of the daily longshore transport rate through the experimental beach at Abbotsham, which are analysed with respect to the nearshore wave conditions. Specifically, the estimated volumetric transport rate was converted (using Equation 4.10) into an immersed weight transport rate (I_{LS}) and related to the mean longshore component of wave power (P_{LS}) that prevailed over the intervening high tide period. The K coefficient is given by the gradient of the regression line that relates I_{LS} to P_{LS}.

However, calculating the longshore transport rate from the LSD and DoA measurement was complex. For reasons previously explained, the DoA and LSD experiments were not conducted simultaneously. It was therefore necessary to infer the mean DoA for each of the 15 daily LSD observations. This was conducted by sequentially extrapolating the mean DoA from the three trend lines displayed in Figure 4.24. Longshore transport was estimated each day by multiplying the (1) mean LSD with the (2) width of the mobile layer and (3) estimated DoA.

An important distinction is made between the longshore displacement of the located tracer sample (presented and plotted in Table 4.7 and Figure 4.18 respectively) and the longshore displacement used for the longshore transport estimates. The following analysis is concerned only with the transport of clasts within the mobile layer, and hence only tracers located lower on the beach than the most elevated tracers that were transported between coupled daily surveys are included. The exclusion of a considerable number of tracer clasts stranded shoreward of the storm crest and buried below the mobile layer (see section 4.5.5 for filtration method) results in the magnitude of longshore displacement of the mobile layer being somewhat greater than that of the tracer sample as a whole (see Table 4.10).

The width of the mobile layer was taken as the portion of the cross-shore beach profile (which was measured once every field trip) located below the most elevated position at which clast transport occurred. Estimation of the immersed weight transport rate requires knowledge of the density and porosity of beach clasts. The density of clastic material was taken as 2700 kg/m^3 and the porosity of the beach matrix was taken as 0.6 (after Nicholls & Wright, 1991). The

empirical values for the: mean displacement, width and mean DoA of the mobile layer, as well as the dependent longshore transport estimates are presented in Table 4.10.

Dates	LSD (m/day)	Mobile layer width (m)	DoA (m)			I_{LS} (kg/s)			Q_{LS} (m^3/day)		
			Trend 1	Trend 2	Trend 3	Trend 1	Trend 2	Trend 3	Trend 1	Trend 2	Trend 3
11-Sep-11 to 12-Sep-11	3.50	34.1	0.17	0.32	0.13	6.1	11.7	4.8	20	38	16
12-Sep-11 to 13-Sep-11	12.86	32.6	0.29	0.59	0.40	35.4	71.1	48.5	123	247	168
29-Oct-11 to 30-Oct-11	13.37	36.1	0.21	0.42	0.21	29.9	58.6	29.0	104	203	101
30-Oct-11 to 31-Oct-11	6.88	32.7	0.13	0.24	0.09	8.9	16.3	6.3	29	54	21
31-Oct-11 to 01-Nov-11	1.55	33.4	0.13	0.23	0.09	2.2	4.1	1.6	6	12	5
27-Nov-11 to 28-Nov-11	6.50	36.1	0.20	0.39	0.18	13.5	26.4	12.3	47	92	43
11-Feb-12 to 12-Feb-12	-0.25	35.1	0.07	0.10	0.07	-0.2	-0.3	-0.2	-1	-1	-1
12-Feb-12 to 13-Feb-12	0.06	35.1	0.07	0.10	0.07	0	0.1	0	0	0	0
07-Mar-12 to 08-Mar-12	-2.84	30.3	0.18	0.35	0.15	-4.7	-9.1	-3.9	-16	-30	-13
08-Mar-12 to 09-Mar-12	-2.48	30.9	0.18	0.34	0.14	-4.1	-7.9	-3.4	-14	-26	-11
09-Mar-12 to 10-Mar-12	-0.53	28.7	0.16	0.30	0.12	-0.7	-1.3	-0.5	-2	-5	-2
14-Oct-12 to 15-Oct-12	-1.42	31.8	0.11	0.20	0.08	-1.9	-3.3	-1.3	-5	-9	-4
15-Oct-12 to 16-Oct-12	-1.02	31.8	0.26	0.53	0.32	-2.3	-4.7	-2.8	-9	-17	-10
16-Oct-12 to 17-Oct-12	0.67	32.3	0.20	0.40	0.19	1.3	2.5	1.2	4	9	4
17-Oct-12 to 18-Oct-12	3.86	35.1	0.25	0.49	0.28	9.7	19.2	10.9	34	67	38

Table 4.10: Table of empirical values including the: mean longshore displacement of the mobile layer; width of the mobile layer; depth of action estimated with trend 1, 2 and 3 in Figure 4.24 respectively; immersed weight longshore transport rate estimated using DoA trend 1, 2 and 3 respectively; volumetric longshore transport rate estimated using DoA trend 1, 2 and 3 respectively.

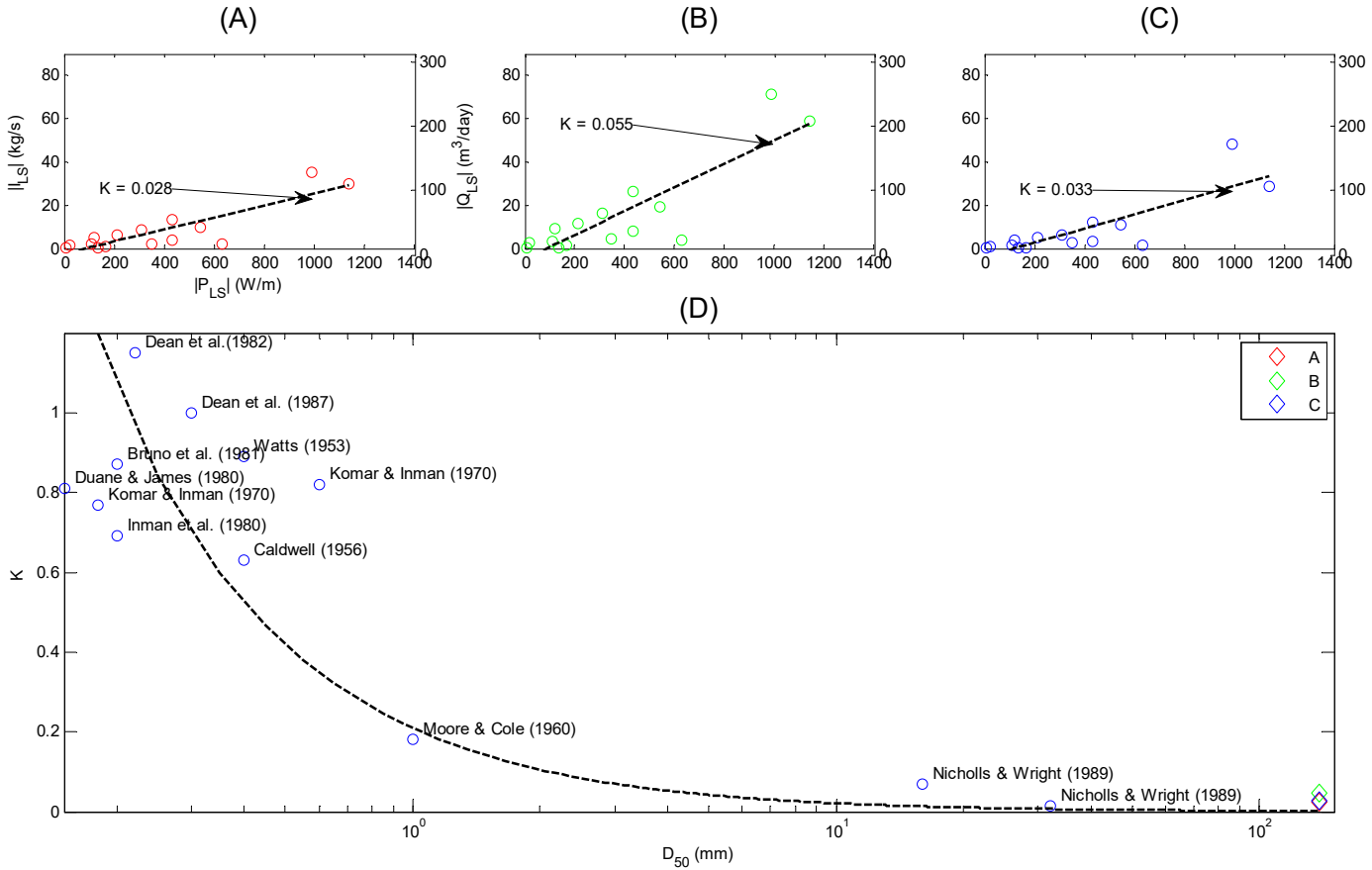

Figure 4.25: Absolute longshore component of wave power versus the absolute immersed weight transport rate, estimated using DoA trend 1 (A), 2 (B) and 3 (C) (see Figure 4.24 for DoA trends), and; the average *K* coefficient versus clast diameter (D). A-C: A positive linear relationship is evident between the longshore component of power and immersed weight transport rate (R^2 of 0.75, 0.75 and 0.68 for plots A, B and C respectively). The gradient of the distribution (*K*) varies depending on the trend used to extrapolate the DoA and varied between 0.028 (DoA trend 1) and 0.055 (DoA trend 2). D: Mean *K* versus intermediate clast diameter. The *K* values appear to be reciprocally related to the intermediate clast diameter. The trend line is given as $0.21/D_{50}$. Plot and results based on Komar (1997).

The magnitude of the estimated longshore transport rate ranges from negligible transport to between 35 kg/s and 71 kg/s (or 123 m^3/day and 247 m^3/day). There is a strong positive relationship between the longshore transport rate and longshore component of wave power, which accounts for between 68 % and 75 % of the variability. The *K* coefficients from the current experiments (which range from 0.028 to 0.055) are over an order of magnitude smaller than the majority of *K* coefficients derived for sandy beaches (Komar, 1997). This is not surprising considering the intermediate diameter of clasts on Abbotsham beach is over two orders of magnitude larger than the coarsest sand studied (e.g. Moore & Cole, 1960). Comparing the results with those from a number of previous experiments shows the *K* coefficient is reciprocally related to the intermediate clast diameter. The reduction in *K* with clast size demonstrates the efficiency with which an applied lateral thrust transports material is inversely proportional to the intermediate clast diameter. The precise reason for this is not known, but it seems likely that the large hydraulic forces required to mobilise coarse clasts and the spatially confined face of coarse clastic beaches are contributing factors.

4.10.4.3 Key Recommendations for Future Research

Primary recommendations for the continuation of the research presented in Chapter 4 are as follows:

- Nearshore wave measurements obtained for the current thesis research highlighted the importance of platform morphology in the shoreward propagation of wave energy and the refraction of wave fronts. However, improved understanding of the transformations incident waves undergo when propagating across the shore platform would be achieved by installing an array of three directional wave gauges at all of the nearshore wave gauge positions and a further three directional wave gauges at the outer edge of the shore platform, parallel with the nearshore array. This would not only improve understanding of the dissipation of wave energy across the shore platform but also the influence of shore platform morphology on the nearshore approach angle of incident wave and therefore the longshore transport on the coarse clastic beach.

- Access to a directional waves gauge was limited. It was therefore necessary to infer (from a limited data set) the height and approach angle of waves incident to the experimental beach between each of the coupled survey days. It would be better to measure the nearshore height and approach angle of incident waves during the period intervening each of the coupled beach surveys. This way, clast transport could be related to the longshore component of wave power calculated from direct measurements of the nearshore wave conditions rather than empirically inferred values from the offshore wave buoy.
- Large uncertainties were associated with the depth of activation at Abbotsham; which was immeasurably deep during storm conditions. For the current thesis research, time constraints imposed on the loan worker by the tides and daylight limited his capacity to excavate the beach and construct depth of activation columns. The help of one or two co-workers would lessen these constraints and allow time to extend the DoA columns (hopefully) below the maximum extent of storm wave action.

  It is also worth reviewing the current, laborious method of inserting tracer clasts into the beach matrix. Trial of the method proposed by Nicholls (1989) is advisable. He suggested inserting tracers through a piece of hollow metal piping that is hammered vertically into the beach matrix. If proven effective at Abbotsham, this method would almost certainly improve DoA column construction as well as reduce the disturbance of the internal structure of the beach.

4.11 Conclusion

Field experiments were conducted along an exposed, macro-tidal coastline at Abbotsham (UK) in order to quantify the magnitude and direction of the longshore transport on a coarse clastic beach and understand the variables important to this process. Comparisons between concurrent measurements of incident waves by the Bideford Bay wave buoy and up to three wave gauges deployed at predefined locations along the inner shore platform were used to demonstrate shore platform control on nearshore wave properties. Local variations in incident wave energy along the inner shore platform were determined by the process of wave shoaling, breaking and perhaps refraction.

When the surf zone extended across the shore platform (e.g. during storm wave conditions and/or when the shore platform was barely submerged), nearshore wave energy was saturated and linearly related to water depth. The profile of incident wave energy along the inner shore platform was inversely related to platform elevation. Wave energy was more attenuated at the elevated peripheral areas. This trend modified the profile of the coarse clastic beach, which was built up adjacent to the central embayment. In contrast, when waves propagated across the shore platform without breaking, the wave height was systematically greater at the north and south positions relative to the centre. It was not possible to determine from the current data set the extent to which this particular trend was the result of the conservation of power as incident waves shoal or, more interestingly, the local focussing of energy as wave fronts are refracted away from the central embayment towards the elevated peripheries.

Analysis of data from a directional wave gauge deployed at the south shore platform showed the consistent refraction of incident waves with peak periods between 6 s and 12 s away from the central embayment and towards the elevated platform to the south. In stark contrast to the strongly positive offshore approach angles, refracted wave fronts occasionally resulted in negative mean approach angles measured at the south shore platform. This result demonstrates a further and previously overlooked aspect of the mediating role of shore platforms on nearshore wave properties. Further experiments in a wide range of settings are required to understand the wider relevance of these findings

The nearshore wave data set was coupled with successive daily measurements of the position of RFID-traced clasts, which were utilised to estimate the direction and magnitude of net transport. The transport of individual clasts between each of the coupled surveys was stochastic and related to their cross-shore position and size. While clasts located on the beach face were most mobile, clasts located shoreward of the storm crest were protected from wave action and generally remained stationary. Of the clasts that were entrained, a negative relationship was observed between the maximum transport distance and clast mass.

The daily mean longshore displacement of the tracer sample was proportional to the longshore component of wave power. A particularly interesting finding was the negative net transport of mobilised clasts by shorter period waves, which was coherent with the refraction patterns as a function of platform morphology. These negative transport events demonstrate the geological control on not only the magnitude, but direction of clast transport on the beach.

Powerful conditions generated positive (i.e. directed towards the Pebble Ridge) clast transport across the monitored beach – the direction of net longshore transport. Observation of the net longshore displacement of tracer clasts between field trips was overwhelmingly in the positive direction. Indeed, transport observations over a six-month period showed clast transport to be almost exclusively positive. Yet, the height and approach angle of incident waves overlying the inner shore platform were still strongly moderated, which reduced the longshore component of power acting on the beach. The shore platform therefore plays a key role in moderating positive longshore transport during storm conditions. These data provide initial insight into the role that shore platforms play on nearshore wave transformations and ability of waves to transport coarse clasts.

Additional field experiments showed the DoA was positively related to wave power, and varied from between approximately 0.04 m to 0.25 m in relatively weak conditions and was greater than 0.42 m under the most powerful conditions. Storm-based measurements were hindered by the inability to extend the DoA column deep enough into the beach matrix to accurately measure the DoA. The absolute minimum DoA was related to wave power and used for the LSTR calculations. Given the large uncertainty associated with these data, two further hypothetical trends were created. The LSD and minimum DoA data were combined to provide a lower estimate the LSTR for given wave conditions. The magnitude of the longshore transport rate was estimated to have reached 123 m^3/day, 247 m^3/day and 168 m^3/day using DoA trend 1, 2 and 3 respectively. The proportionality (K) coefficient derived from each of the distribution was over an order of magnitude smaller than has been widely reported on sandy beaches. The findings show that, for a given longshore component of power, the transport along a coarse clastic beach is small in comparison to their sandy

counterpart. Further research in a range of locations is required to quantify the wider significance of these findings.

5 : Importance of Storm Events and Mean Sea Level on the Longshore Transport Rate at Abbotsham Beach and Implications for Future Nourishment of the Pebble Ridge

5.1 Introduction

Beaches composed of pebbles, cobbles and boulders differ from their sandy counterparts because they are not necessarily in a continual state of dynamism. For a clast to be transported, the hydrodynamic force must first exceed its immersed weight (Shields, 1936). Lorang (2000) noted the ability of a wave to entrain a clast is a function of its power (*P*):

$$P \propto H^2 T \qquad \textbf{Equation 5.1}$$

where *H* and *T* stand for the wave height and period respectively. Increasingly coarse clasts require increasingly powerful waves to become entrained. Indeed, the dynamics of systems comprised of boulders and with limited exposure to competent waves might be exclusive to low-frequency hurricane or tsunami events (e.g. Nott, 2003b; Goto et al., 2007, 2009, 2010; Maouche et al., 2009; Paris et al., 2010; Etienne & Paris 2010; Chen et al., 2011; Engel & May, 2012; Weiss, 2012; Nandasena et al., 2011, 2013). Conversely, the impact of low-frequency, high-magnitude events could perhaps be outweighed by the almost-continuous low-magnitude transport that occurs on exposed sand and pebble beaches.

Climate change has been linked to an increase in the frequency and intensity of high magnitude storm events, which could potentially alter the dynamics of CCBs globally (IPCC, 2013). A recent increase in the surface wind speeds as a result of climate change is thought to have increased mean wave height globally (Young et al., 2011; Hemer et al., 2013). Key to the current chapter is the measured and predicted increase in the storminess in the North Atlantic Ocean, which has direct implication for the Bideford Bay coastline. A 2 %/yr increase in the mean wave height measured in the north-east Atlantic Ocean has been detected by time-series analysis of wave data collected between 1962 and 1986 by moored instruments (Bacon & Carter, 1991). These findings are supported by climate-driven wind-wave model simulations which have generally found a similar systematic increase in the significant wave height owing to an increase in storminess, which is influenced by the state of the North Atlantic Oscillation (Kushnir et al., 1997; Weiss et al., 2005; Dodet et al., 2010).

Another effect of climate change is the thermal expansion of global oceanic waters and the melting of terrestrial-based ice. The consequential rise in global mean sea level is further accelerated in North Devon (and indeed the whole of southern England and Wales) by the current isostatic adjustment of the UK landmass. This is particularly important considering the attenuation of storm wave energy at Abbotsham is dominated by water depth across the shore platform. Any rise in sea level would result in an exponential increase in nearshore wave energy, which could affect the annual net longshore transport rate.

As described in section 2.2.2, the coarse clastic system in Bideford Bay is hypothesised to be a modern, transient feature nourished by an exhaustive supply of greywacke clasts sourced from the Gore. The process of longshore transport is particularly important in Bideford Bay because it is considered responsible for the northward transport of clasts from the Gore and the formation and maintenance of the valuable Pebble Ridge that protects the low-lying settlements of Westward Ho! and Northam Burrows.

Although a number of reports have assessed the future dynamics of the Pebble Ridge, a general lack of information about the local pathways and magnitude of clast transport has hindered understanding and the confidence with which morphodynamic predictions can be made. Given this, a recent internal report to *English Nature* highlighted the lack of studies quantifying the longshore transport rate and underscored the need for further investigation (e.g. Orford, 2005). Such work would help inform the coastal advisory group on future management strategies that are hinged on the influx of coarse clastic material to the Pebble Ridge.

5.2 Chapter Aims & Specific Research Questions

This chapter addresses the highlighted knowledge gap by modelling the longshore transport rate through a section of (Abbotsham) beach located between the Gore and Pebble Ridge. Here, empirical field observations are used to model the daily longshore transport over a multiannual period in order to assess the current annual net transport rate towards the Pebble Ridge and potential impact of sea level rise and/or increase in storminess on the annual net transport rate. The specific research questions are as follows:

Q5.1: What is the annual net volumetric transport rate towards the Pebble Ridge?

Q5.2: What effect will relative sea level rise have on the annual net volumetric transport rate towards the Pebble Ridge?

Q5.3: What is the relative importance of storms in generating longshore transport towards the Pebble Ridge? What effect would an increase in storminess have on the annual net volumetric transport rate towards the Pebble Ridge?

5.3 Methodological Approach

In this final empirical chapter the correlation coefficients (*K*) derived in Chapter 4 are combined with the nearshore wave climate to estimate the daily longshore transport rate through the experimental beach over a multiannual period (see Figure 5.1 for details of the model). A key component to the model is the long-term record of the height and approach angle of incident waves directly adjacent to the south beach cell. In the absence of continuous *in-situ* measurements, the multiannual nearshore wave record was modelled based on the tide-dependent relationships between the concurrent conditions measured by the Bideford Bay wave buoy and wave gauge deployed at the south shore platform. The modelled longshore component of wave power was finally used to estimate the longshore transport rate according to the correlation (*K*) coefficient derived in Chapter 4.

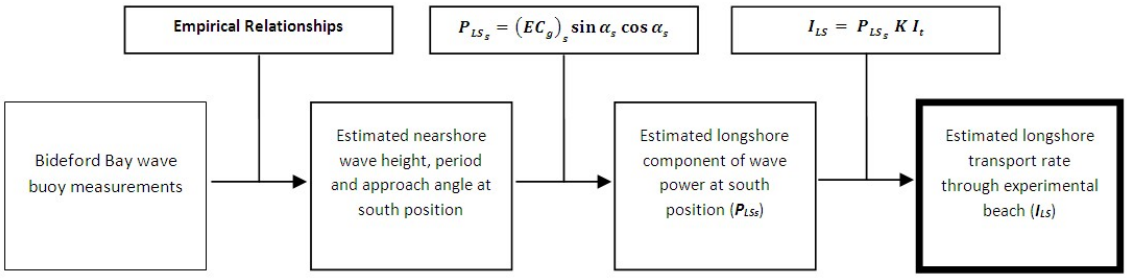

Figure 5.1: Simplified flow diagram depicting the construction of the empirical model. Where I_t stands for immersion time.

5.4 Defining Storm Events

It is imperative to first define what is meant by the term 'storm'. Storms are traditionally defined with respect to the distribution of wave heights measured in a specific area over a multiannual period. Currently, the Bideford Bay wave buoy has not been deployed long enough for the Channel Coast Observatory to give their definition of the storm threshold and, for the time being, is semi-arbitrarily set to H_{S0} > 4 m. Of course, any storm threshold has an arbitrary component and is dependent on the duration for which observations have been made. Furthermore, the ability to do geomorphic work is dependent on wave period and is proportional to wave power. Net longshore transport is considered with respect to the relative contributions made by the conditions in which the offshore wave power (P_0) exceeds the 90th, 95th and 99th percentiles of all daily-mean measurements made by the Bideford Bay wave buoy, which is graphed in Figure 5.2.

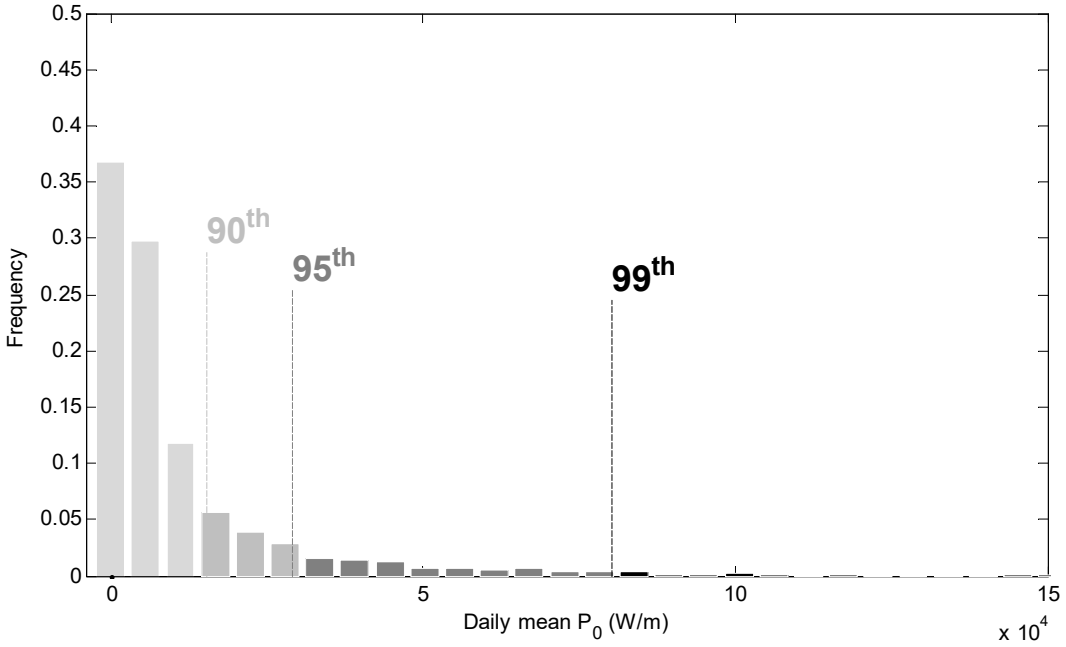

Figure 5.2: Frequency distribution of the daily-mean offshore wave power (calculated from Bideford Bay wave buoy measurements). The 90th (15,407 Watts/m), 95th (29,228 Watts/m) and 99th (80,235 Watts/m) percentiles of the distribution are indicated with dashed lines.

5.5 The Empirical Model

5.5.1 Hydrodynamic Model

Wave gauges were deployed on the intertidal shore platform during field visits only. Consequently, no long-term record of the nearshore significant wave height and mean approach angle currently exists for the south shore platform. Unlike period, the height and approach angle of incident waves can be strongly modified by the shoaling process. In the absence of consistent measurements, these key wave descriptors were modelled based on the empirical relationships developed between the concurrent wave conditions at the southern shore platform and those offshore.

5.5.1.1 Nearshore Wave Height

The half-hourly wave height measurements from the Bideford Bay wave buoy were corrected according to the condition- and tide-dependent transformations waves undergo when shoaling across the south shore platform. The four plots displayed in Figure 5.3 present the relative nearshore wave height at the south shore platform versus tidal elevation as a function of offshore wave height. When the prevailing offshore wave height is small, the relative nearshore wave

height (H_{S0}/H_{Ss}) increases non-linearly with tidal elevation. Once the water depth exceeds the offshore wave height, the nearshore wave height becomes more variable and ranges from between 0.7 and 1.7 times the offshore wave height. The relative nearshore wave height decreases with increasing offshore wave height, and the relationship with water depth becomes increasingly linear.

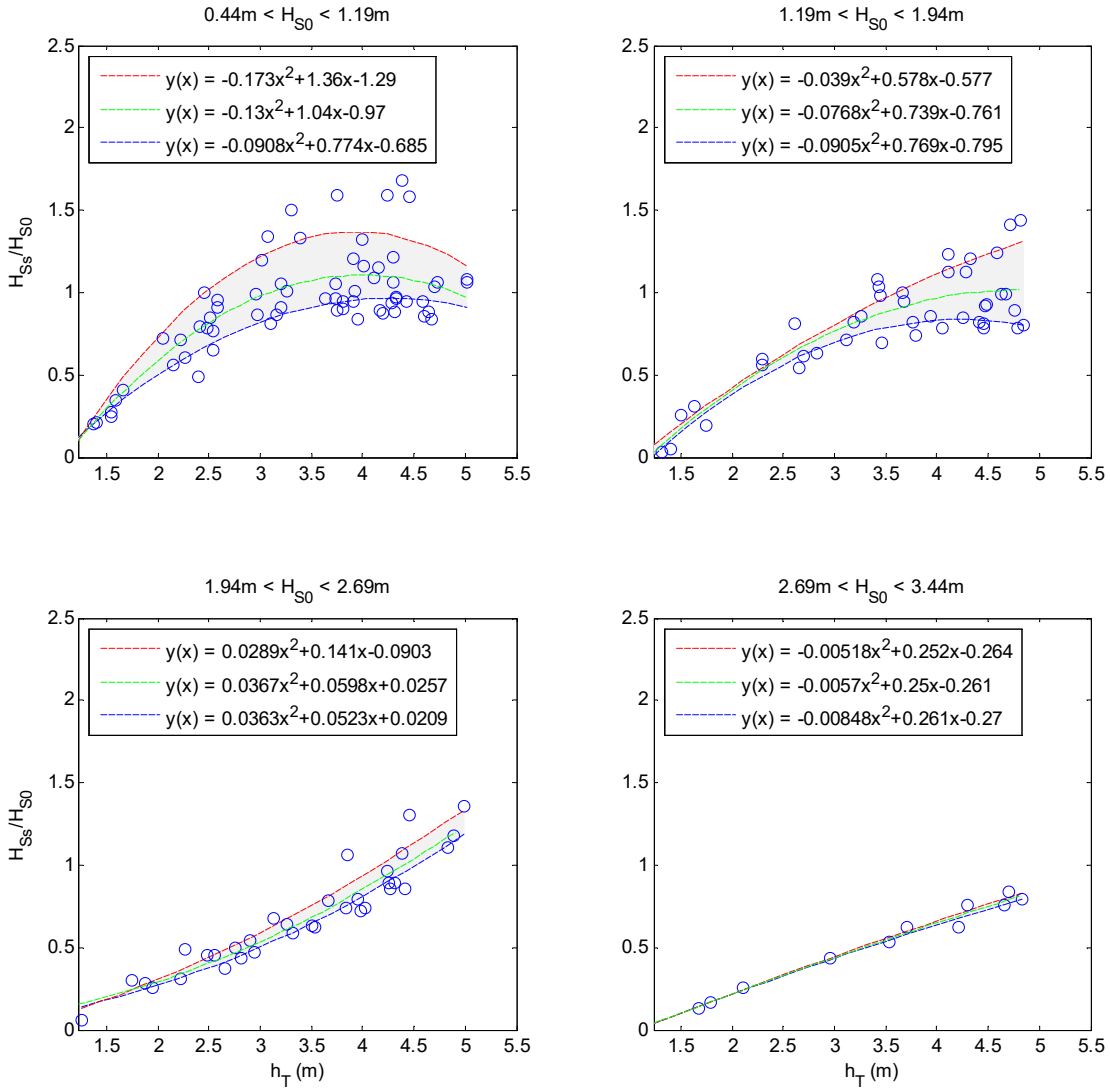

Figure 5.3: Ratio of the nearshore to offshore wave height versus tidal elevation. Plots separated with respect to the offshore wave height. The figure is constructed using all measurements made at the southern shore platform. In each plot, the distributions of all data, as well as the 5th and 95th percentiles are represented with second order polynomials (red and blue dashed lines respectively). The nearshore wave height is, in each case, positively related to water depth. Where the offshore wave height is small (H_{S0} < 1.94 m), the trend is non-linear such that the rate at which the wave height increases reduces with tidal elevation. Larger waves are more strongly moderated by the water-depth, which is reflected by the increasingly linear trends and reduced variability where H_{S0} > 1.94 m.

Wave Energy Saturation Point

The increasing dominance of attenuation through the process of breaking is typified during the most energetic conditions, when the nearshore wave height is linearly related to the tidal elevation. At this point, the wave energy at the inner shore platform is saturated and the nearshore wave height becomes a function of water depth (e.g. Thornton & Guza, 1983; Sallenger & Holman, 1985; Farrell et al., 2009). The saturation of wave energy is identifiable in Figure

5.3 by the relatively fixed ratio between the nearshore significant wave height and water depth, which is maintained regardless of variability in the offshore wave height. When the local water depth is greater than 1 m, the significant wave height is limited to approximately 90 % of the water depth. However, when the local water depth is particularly shallow (< 1 m), significant wave heights of up to 120 % of the water depth were measured.

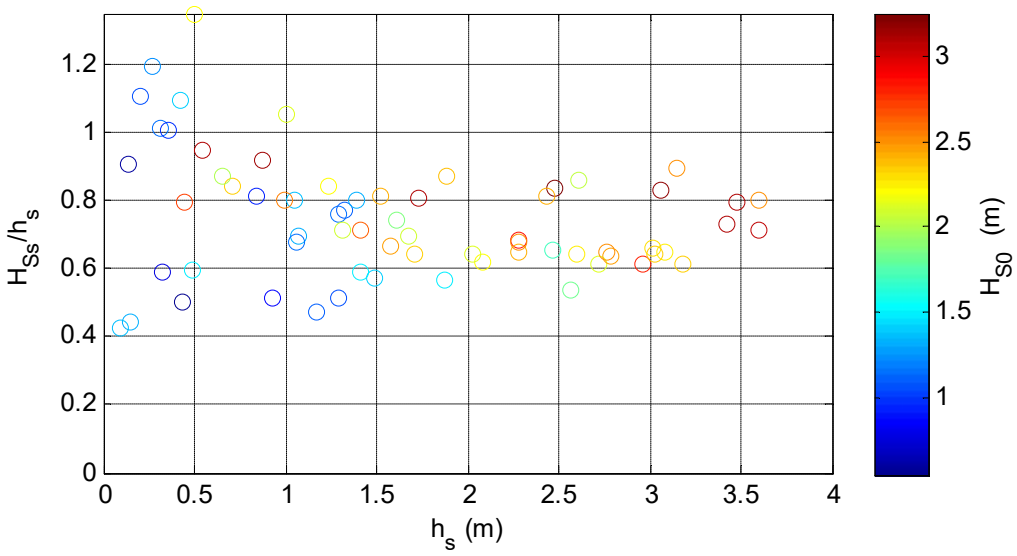

Figure 5.4: Ratio of the nearshore significant wave height (H_{Ss}) to local water depth (south shore platform; h_s) versus the local water depth. Data selected for the graphs were collected when the break point was considered to be seaward of the wave gauge (e.g. H_{Ss}/h_s < 0.68) and data points coloured according to the offshore wave height. The ratio between H_{Ss} and h_s is largely maintained regardless of variability in the offshore wave height. When the inner shore platform is barely submerged (0 m < h_s < 1 m) H_{Ss} was up to 140 % of the local water depth. However, at the higher tidal states (h_s > 1 m), when the nearshore wave height is larger, the significant wave height tends to be limited to between 85 and 90 % of the water depth. See comparable plot for the central shore platform in section 4.7.1.

Modelling the Nearshore Wave Height

The nearshore significant wave height was based on measurements from the wave buoy, which were corrected according to the condition- and tide-dependent transformations (displayed in Figure 5.3) that incident waves undergo when approaching the experimental beach. It is acknowledged that variability within the empirical relationship could have an impact on the overall results. The model therefore incorporates the spread of data using MATLAB's 'rand' function to randomly select either the polynomial representing the distribution as a whole (a), or the 5th (b) or 95th (c) percentile of the distribution to extrapolate the correction factor for the offshore wave height. One boundary

condition was applied to this process which limited the nearshore wave height according to the concurrent water depth at the inner south shore platform. The maximum H_{Ss}/h_s ratio was varied between 0.8 and 1. Ten iterations of the wave height component of the model were run in order to explore the impact of the uncertainty on the modelled wave height time series. The significant wave height was converted into the root mean wave height such that $H_{rms} = H_S/1.41$.

5.5.1.2 Nearshore Mean Approach Angle

As demonstrated in section 4.7.3 the nearshore approach angle of waves was only weakly related to the offshore approach angle. After de-trending the nearshore approach angle with respect to the concurrent offshore approach angle, a further relationship was observed between the nearshore approach angle and peak wave period. It was hypothesised that waves with peak periods between 6 and 12 seconds were most strongly refracted by the morphology of the intertidal shore platform, and as a consequence, tended to approach the beach with a negative angle of obliquity. Although significant, the relationship between peak period and mean approach angle is diffuse and individual half-hourly measurements can differ significantly from the second order polynomial that represents the distribution as a whole.

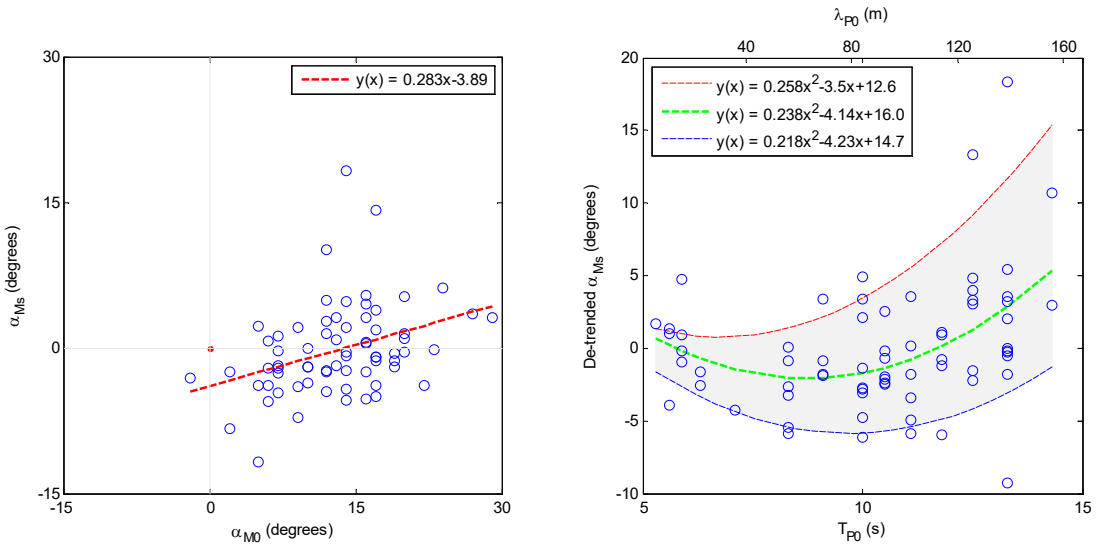

Figure 5.5: (Left) half-hourly mean approach angle measured nearshore (by the MAVS; α_{Ms}) versus corresponding, concurrent offshore measurements (by the wave buoy; α_{M0}); (Right) nearshore approach angle (de-trended for variability related to the offshore approach angle) versus peak offshore period/wavelength (λ_{P0}). This figure is identical to Figure 4.12 with exception to the two additional polynomials in the right plot, which represent the 5th (red dashed line) and 95th (blue dashed line) percentiles of the distribution. The model incorporates uncertainty in the dataset by extrapolating from each of these trend lines (see section 5.5.1.3).

5.5.1.3 Modelling the Mean Approach Angle

The half-hourly mean approach angle at the south shore platform was based on the offshore approach angle, which was corrected for the relationships displayed in Figure 5.5. Similar to the wave height model, variability in the empirical relationship was included with a random function that extrapolated the mean approach angle correction factor from either the distribution as a whole or the 5th or 95th percentile of the distribution. One boundary condition was applied to the model, which prohibited waves with excessively large periods from approaching the beach from a greater angle than concurrently measured offshore.

5.5.1.4 Abbotsham Tidal Record

The tidal elevation controls the amount of wave energy that can propagate across the shore platform and therefore the wave action on the beach. It is imperative to have an accurate, multiannual record of the tidal elevation for hydrodynamic model. No such data exists for Abbotsham and the process of generating an accurate tidal record was achieved by:

(1) obtaining the most complete record of tidal elevations from as close to Abbotsham as possible and which spans the deployment period of the Bideford Bay wave buoy.

(2) conducting orbital analysis on the tidal record to produce a comprehensive, celestial-based tidal elevation model that is free from highly erroneous or absent readings.

(3) isolating variability in the observed tidal record (obtained by step 1) that is due to meteorological processes.

(4) adjusting the amplitude of the modelled tidal curve (obtained by step 2) to match that at Abbotsham.

(5) adding meteorological-based variability (isolated in step 3) to the adjusted modelled tidal curve (from step 4) to account for fluctuations generated by wind and air pressure.

Steps 1-2:

The nearest tide gauge is located at Ilfracombe, approximately 24 km north-north-east of Abbotsham. The gauge has been located there since 1968 and provides mean surface elevation every 15 minutes. These data were made available by the British Oceanographic Data Centre and downloaded via their website (www.bodc.ac.uk). Unfortunately, the elevation time series from the tide gauge were regularly interrupted by erroneous or absent measurements. Using the T_TIDE harmonic analysis MATLAB toolbox (see Pawlowicz et al., 2002), a complete tidal elevation time series was generated using 64 constituents analysed in the incomplete Ilfracombe record.

Step 3:

The predicted and measured tidal elevations correlated well. However the measured tidal elevation was slightly more variable and the magnitude of the difference between the measured and predicted elevation occasionally exceeded 0.7 m. The apparently random nature of variability in the measured

record implied it was the result of meteorological processes, which are not included in the celestial-based T_TIDE predictions. The difference between the predicted and (where available) measured tidal record was taken to construct a corresponding time series of variability in surface elevation due to meteorological processes, which was later applied to the modelled tidal record (see Step 5).

Step 4:

Despite its close proximity to Abbotsham, Ilfracombe is situated beyond a major constriction point in the Bristol Channel, which funnels the tidal wave and thereby amplifies the tidal range (Archer, 2013). The amplitude of the predicted (Ilfracombe) tidal curve was incrementally suppressed with a scale factor until the rate of change matched field-based measurements at Abbotsham.

Step 5:

The time series of residual fluctuations attributed to meteorological processes (isolated in Step 3) was finally added to the modelled tidal elevation time series. As displayed in Figure 5.6 the adjusted tidal curve closely correlates with direct measurements from the shore platform at Abbotsham and hence provides a suitable record of the long-term tidal elevation at Abbotsham.

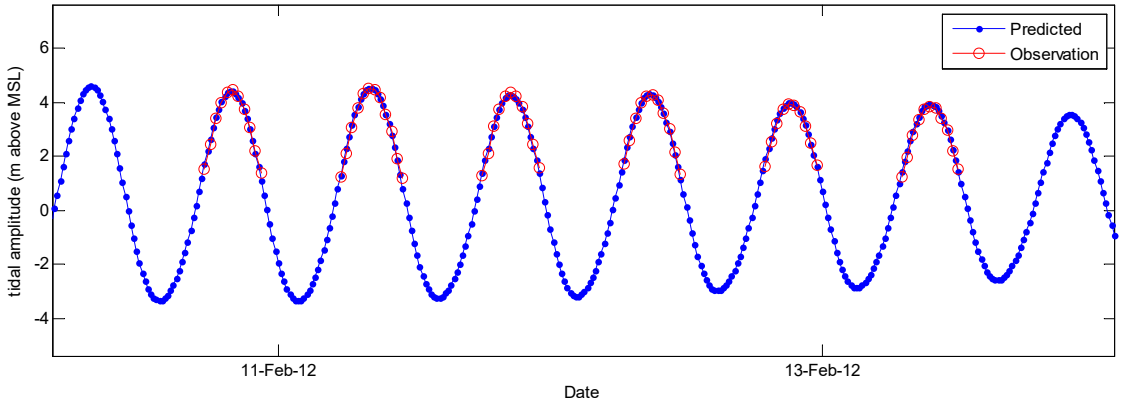

Figure 5.6: Time series of the predicted and measured tidal elevation at Abbotsham. The predicted tidal elevation closely matches the amplitude and shape of the measured tidal elevation. The tide gauge record is positioned where the seabed is below chart datum, and therefore captures the entire tidal cycle. The wave gauge was deployed on the inner shore platform, which is raised approximately 0.69 m above MSL, and hence only captured the higher tidal state. The Ilfracombe tide gauge data (on which the harmonic analysis was performed) was obtained from the British Oceanographic Data Centre. Harmonic analysis was conducted with T_Tide toolbox in MATLAB (For details see Pawlowicz et al., 2002).

5.5.1.5 Testing the Modelled Longshore Component of Power

The modelled half-hourly significant height and mean approach angle of waves adjacent to the experimental beach were expressed in terms of the longshore component of wave power. In section 4.5.7, values predicted using the modelled nearshore wave variables were compared with those directly obtained from (MAVS) measurements. However, as previously noted, measurements of the wave conditions at the south shore platform were sparse, and hence the entire data set was used to develop the empirical relationships used to model the height and approach angle of incident waves in the first instance. Consequently, there is no independent data with which to test the modelled longshore component of wave power against. The modelled longshore component of wave power could only be *validated* against the direct measurements used in its construction. Although this provides little insight into the general accuracy of the model, it does indicate the robustness of the relationships and modelling process.

Direct comparison between the modelled and observed daily-mean longshore component of power demonstrated good agreement (e.g. R^2 = 0.95). Although direct measurement of the height and approach angle of waves at the south shore platform was for a duration of four days only, the short deployment of the

MAVS coincided with a range of wave conditions during which the longshore component of power ranged from weakly negative (-290 Watts/m) to strongly positive (1154 Watts/m). Correlation between the measured and predicted daily-mean longshore component of power is a good indication of the accuracy of the wave height and approach angle models.

5.5.2 Clast Transport Model

The daily longshore transport rate was based on the *K* coefficients derived in Chapter 4. The model was initially run on three separate occasions using the *K* coefficient estimated with the; minimum (Run 1A); hypothetical linear (Run 2A) and; hypothetical non-linear (Run 3A) DoA trends respectively (see Figure 4.24). For each of these occasions, multiple variants of the *K* coefficient were deduced by re-sampling the wave-transport dataset in a statistical process termed 'jackknifing'. This included the systematic omission of each of the wave/transport observation from the regression analysis (by which the *K* coefficient was derived). The process produced 15 *K* values to be used in each model run, and provides a gauge of the robustness of the distribution and the precision of the modelled longshore transport rates.

The efficiency with which waves transport sediment is reciprocally related to clast diameter (see Figure 4.25). This is particularly important at Abbotsham where the beach clasts are size-sorted in the cross-shore plane, with the coarsest class situated at the beach base. It is argued here that for a given lateral thrust, the volume of material transported longshore per unit time will be greater during spring tide conditions when wave energy is distributed further up the beach face. Conversely, only the coarse cobbles and boulders that compose the bottom beach are subject to wave action during neap tides, and hence the correlation (*K*) coefficient should reduce accordingly. The correlation coefficient incorporated within the model (K_P) was therefore moderated with respect to the size of clasts on the immersed beach, such that:

$$K_P = K\left(\frac{D_{500}}{D_{50}}\right) \qquad \textbf{Equation 5.2}$$

Where D_{50O} is the mean intermediate diameter of submersed clasts used to empirically derive K, and D_{50P} is the mean intermediate diameter of submersed clasts on each of the modelled days.

5.6 Results

The coupled wave and clast transport models were run for the four year period during which the Bideford Bay wave buoy has been deployed and operational. The empirical models provided a time series of the daily wave conditions at the inner shore platform and volumetric transport rate through the experimental beach. The clast transport model was run three times using the: absolute minimum (Run 1A), hypothetical linear (Run 2A) and hypothetical non-linear (Run 3A) DoA trends (see Figure 5.7 for except of Run 1A and Electronic Appendix 2 for the entirety of all model runs). Outputs from the model runs were compared in order to determine the impact of the highly uncertain DoA on the modelled volumetric transport rates.

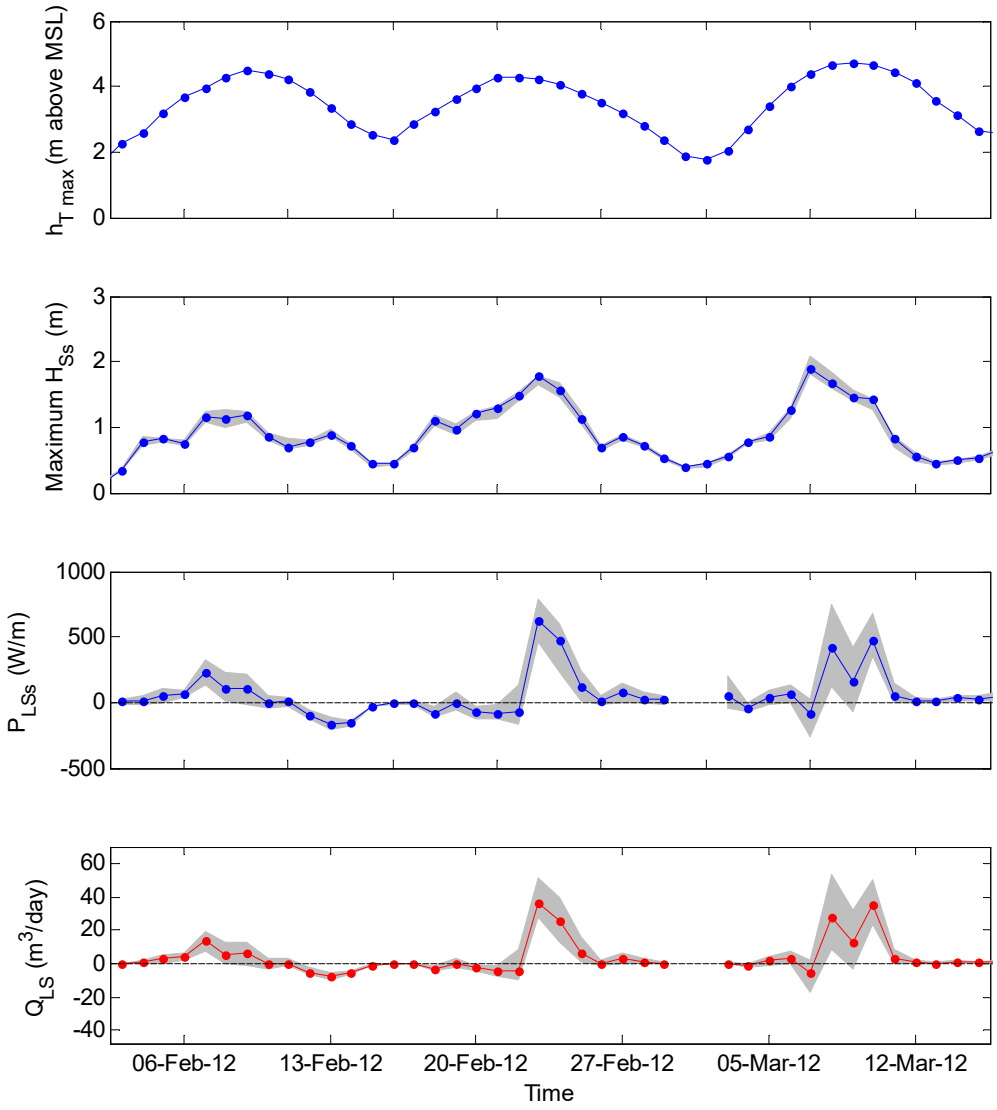

Figure 5.7: A six week excerpt of the time series of daily: maximum tidal elevation (top); maximum nearshore wave height (2nd down); longshore component of wave power (3rd down) and; longshore transport rate (bottom) modelled using the minimum depth of activation data set (i.e. Run 1A). The grey areas on the bottom three plots indicate, for each day, the range between the 5th and 95th percentile of model results. The maximum daily tidal elevation fluctuates with the spring-neap cycle, which in turn moderates the amount of wave energy reaching the inner shore platform. The daily mean longshore component of power was both positive and negative, and the 50th percentile of estimates varied from -260 Watts/m to 780 Watts/m. The longshore transport rate varies in concert with the longshore component of power, with the daily transport estimated to be between -17 m^3 and 54 m^3 respectively.

The daily mean longshore component of wave power adjacent to the experimental beach was both positive and negative. The magnitude of the negative longshore component of wave power was at all times small, suggesting that peak periods of greater than 12 seconds are inherent to powerful storm swells, which consistently approach the beach from a positive angle. The combination of powerful storm swells and positive approach angle

occasionally resulted in a large mean longshore energy flux of up to 3110 Watts/m.

As expected, incident wave energy at the inner shore platform was strongly moderated by depth and hence the tidal elevation. Days in which the greatest amount of energy reached the inner shore platform were confined to spring tidal conditions. Storm energy at all other times was effectively attenuated before reaching the inner shore platform and the experimental beach.

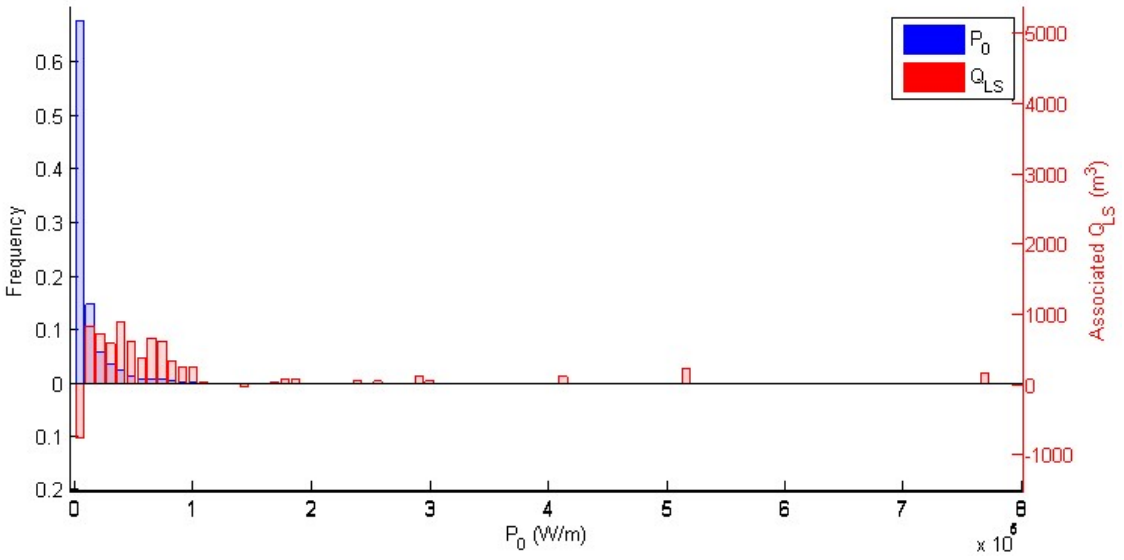

Figure 5.8: Frequency distribution of the daily-mean offshore wave power measured by the Bideford Bay wave buoy (P_0) with the associated net longshore transport (50th percentile of model outputs from Run 1A) superimposed on top. The second y-axes (right) indicates the volume (in m^3) of material transported. The modal daily offshore wave power is weak and the distribution is positively skewed such that increasingly powerful conditions occur at an exponentially decreasing frequency. Net negative longshore transport was generated by frequent, modal conditions. A disproportionate amount of positive transport is generated by infrequent, powerful wave conditions.

Of key importance is the relative contribution of storm events to the overall transport towards the Pebble Ridge. This is graphed in Figure 5.8, which considers net longshore transport in relation to the frequency distribution of the associated offshore wave power. The graph demonstrates a transport bias towards infrequent powerful conditions. The associated volume of material transported is considered in terms of the most powerful 10, 5 and 1 % of conditions measured by the Bideford Bay wave buoy over its four year deployment. This simple analysis is complicated by the numerous model iterations that result from uncertainty in the hydrodynamic and clast transport components of the models. Three new time series were generated based on the

5th, 50th and 95th percentiles of the 300 model iterations. Analyses were conducted on the three scenarios to address the range of possible scenarios, as displayed in Table 5.1.

	Run 1A			Run 2A			Run 3A		
Percentile of total model iterations	**5th**	**50th**	**95th**	**5th**	**50th**	**95th**	**5th**	**50th**	**95th**
Average net longshore transport (m^3/yr)	-195	1339	2988	-390	2649	5917	-256	1527	3460

Table 5.1: Net annual longshore transport estimates from all model runs.

The average net annual transport varied considerably between the 5th, 50th and 95th percentile of model outputs. Net transport based on the 5th percentile of model outputs was in the negative direction and clearly disagree with direct observations of net (positive) clast displacement at the field site (see section 4.8.2). However, the majority of model iterations suggest net transport is toward the Pebble Ridge and are consistent with direct observation and the general understanding of the dynamics of the Bideford Bay coarse clastic system. The 50th percentile of net annual transport based on the absolute minimum DoA (Run 1A) was estimated to be 1339 m^3. However, Run 1A is likely to systematically (and perhaps significantly) underestimate the storm-based DoA. Forcing the model with the hypothetical DoA trends (Run 2A and 3A) increased positive, storm-based transport and hence annual net transport estimates.

	All Model Runs		
	5th	**50th**	**95th**
Conditions in which P_0 exceeds	**Associated proportion of total positive transport (%)**		
90th percentile	69	59	53
95th percentile	53	42	37
99th percentile	13	11	10
Conditions in which P_0 exceeds	**Associated proportion of net positive transport (%)**		
90th percentile	-	84	60
95th percentile	-	60	41
99th percentile	-	15	11

Table 5.2: The relative importance of storm events in generating positive transport towards the Pebble Ridge. P_0 stands for offshore wave power. The results are mean values from Runs 1A, 2A, and 3A. Variability between model runs was very small and at all times less than 1 %.

Analysis of the 5th, 50th and 95th percentile time series from all model runs indicates the general importance of storms in the transport of material towards the Pebble Ridge (see Table 5.2). Model outputs show that between: 53 % and 69 % of positive transport was generated by the most powerful 10 % of conditions; 37 % and 53 % of positive transport was generated by the most powerful 5 % of conditions and; 10 % and 13 % of positive transport was generated by the most powerful 1 % of conditions.

While longshore transport by powerful conditions was almost exclusively in the positive direction, both positive and negative transport was generated by weaker waves. This further increased the relative contribution of storm-based transport to the overall net flux towards the Pebble Ridge. The contribution of the most powerful conditions to overall net transport is considered for the 50th and 95th percentiles, which predicted positive net transport. Here, between: 60 % and 84 % of the net positive transport was generated by the most powerful 10 % of conditions; 41 % and 60 % of the net positive transport was generated by the most powerful 5 % of conditions and; 11 % and 15 % of the net positive transport was accounted for by the most powerful 1 % of conditions.

5.7 Discussion

This chapter presents a four year time series of the predicted daily longshore transport rate through the experimental beach at Abbotsham. These data provide novel insight into the longshore transport rate towards the Pebble Ridge and the importance of low-frequency, high-magnitude events in this process.

However, each component of the model incorporates uncertainties which propagate through to the final results. The discussion section of this chapter considers the model outputs and limitations, and finally the implications of the results for the future morphodynamics of the Pebble Ridge.

5.7.1 Model Outputs

5.7.1.1 Hydrodynamics

The nearshore wave climate was dominated by calm conditions, with increasingly powerful storms occurring at an exponentially-decreasing frequency. The magnitude of the negative longshore component of wave power adjacent to the experimental beach was generally small and the most powerful wave conditions consistently approached the beach with a positive angle of obliquity. Although Bideford Bay is exposed to powerful oceanic storm swells, significant amounts of storm energy could only reach the inner shore platform on a small number of days when there was a particularly large tidal range. Conversely, the entire beach occasionally remained sub-aerial during the most neap tidal cycles. Consequently, powerful oceanic storm waves were only effective in generating longshore transport when coincident with large spring tides.

Limitations

A major limitation to empirical models is that they provide limited insight into the processes leading to the particular response and their accuracy is reliant on the strength of the correlation between variables. The causative relationships governing the nearshore wave height are quite clear, but understanding of the precise relationship between offshore wave properties and the approach angle at the inner shore platform is somewhat weaker. Improved predictions of the mean nearshore approach angle of incident waves would be achieved by increasing the deployment time of the MAVS at the south shore platform. These data would not only enable the relationship between wave period and approach angle to be strengthened, but also make it possible to test the modelled approach angle against unrelated data, and therefore properly assess the accuracy of predictions.

The modelled nearshore wave properties are based largely on the concurrent conditions measured within Bideford Bay. The Bideford Bay wave buoy provides a relatively consistent record of the wave height, period and approach angle over the past four years, but these data are not without uncertainty. Ambiguity arises due to either a total absence of data or when measurements are 'flagged' by the Channel Coast Observatory. Important to the functioning of the model is the unbiased measurement of the entire spectrum of wave conditions. However, analysis of the failure rate shows wave buoy measurements are increasingly likely to be absent or 'flagged' during stormy conditions (see Figure 5.9). Removing these data from the analysis would results in an inherent bias towards quiescent conditions and ultimately the systematic underestimation of positive longshore transport.

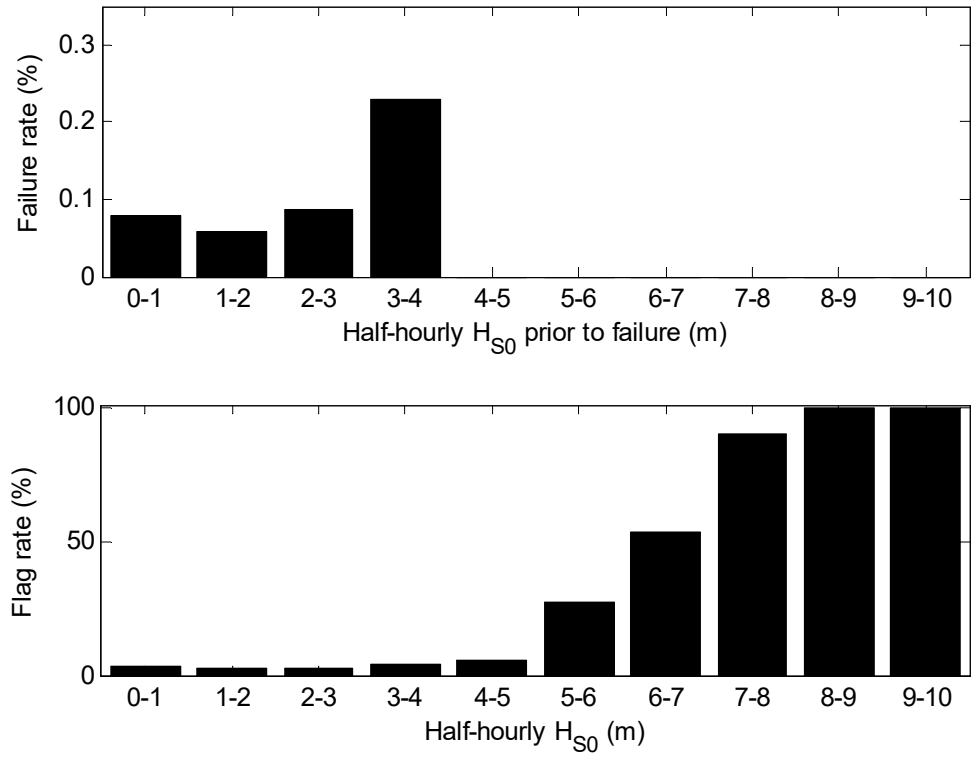

Figure 5.9: Percentage failure rate versus the significant offshore wave height measured prior to failure (top) and percentage flag rate versus concurrent measured offshore wave height (bottom).

The complete failure of the wave buoy is rare and, as demonstrated by Figure 5.9, increases from generally less than 0.1 % of half-hours following the successful measurement of wave heights of less than 3 m, to up to 0.3 % of half-hours following the successful measurement of wave heights of between 3 m and 4 m. Notably, the failure rate dropped to zero following measurement of

wave heights exceeding 4 m. Although, it should be noted that this might also indicate the tendency of the wave buoy to remain un-operational for longer periods of time during particularly powerful storm events. In any case, complete failure of the buoy is rare and amounts to less than 0.5 % of the four year deployment.

The wave buoy only failed on a small number of occasions and information on the CCO website indicates these interruptions were generally unrelated to the wave conditions (see Figure 5.9). However, a large proportion of the storm-based measurements were flagged due to uncertainty. One ameliorating factor is that the nearshore wave height is independent of that offshore when H_{S0} exceeds 80 % of the nearshore water depth. Erroneous storm-based wave height measurements will therefore be filtered out during the conversion to nearshore wave height. Of course, errors in the measured wave period and approach angle will influence the modelled the longshore component of wave power at the inner shore platform.

The flag rate, which is also presented in Figure 5.9, increases with significant wave height, with a clear threshold evident at 5 m. One hundred percent of measurements over 8 m are flagged due to uncertainty. Flagged measurements accounted for approximately 3 % of the half-hourly time series data used in the model. Although it is not possible to quantify sensitivity of outputs to these uncertain measurements, the tendency for energetic wave conditions to be flagged suggests these data will probably have a disproportionately large impact on the overall results. This problem could be addressed by modelling the Bideford Bay wave climate with a coupled ocean-atmospheric numerical model, which would not be vulnerable to storm damage.

5.7.1.2 Longshore Transport

The daily longshore transport rate varied in concert with the longshore component of wave power and generally ranged from minimal, bidirectional transport in calm conditions to strongly positive transport in energetic conditions. As expected, days in which the largest volume of material was transported were confined to spring tide conditions, when the greatest amount of wave energy could propagate across the shore platform and a large portion of the beach was subjected to wave action (see Figure 5.10).

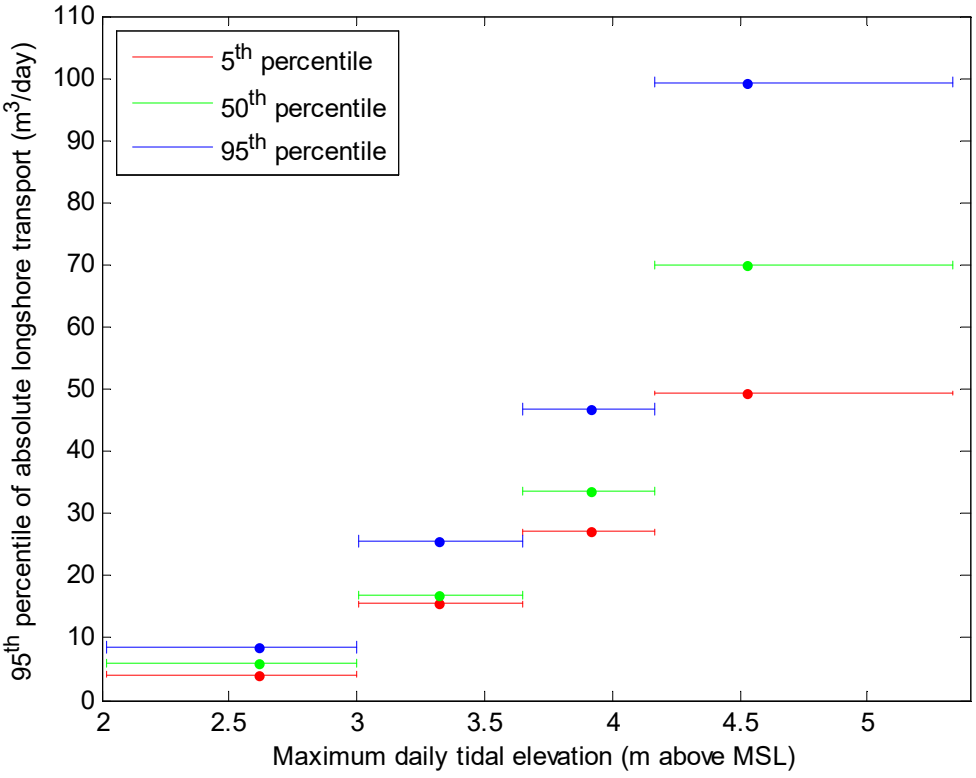

Figure 5.10: 95th percentile of the absolute daily longshore transport rate versus the daily maximum tidal elevation for Run 1A. Each bar represents the mean modelled longshore transport rate over a period of 423 days. The number of observations (423) made for each tidal elevation was kept uniform in an effort to ensure an approximate distribution of offshore wave conditions occurred for each of the tidal elevations bins. The horizontal extent of each bar indicates the minimum and maximum, daily-maximum tidal elevation within each bin.

The clast transport model incorporates uncertainties which were managed by systematically forcing the model with the many and varied combinations of the input variables. Each model run included 20 iterations of the hydrodynamic component, which were combined with 15 variants of the *K* coefficient. The systematic combination of the various configurations of the hydrodynamic and clast transport components produced 300 transport time series. The 5th, 50th and 95th percentiles of the numerous daily transport predictions were considered within the analyses.

The net annual transport estimates derived from the three time series were variable. Importantly, the 50th and 95th percentiles of the model iterations predict net transport in the positive direction and hence are consistent with direct observations. As displayed in Table 5.1, the 50th percentile of predicted net longshore transport was between 1339 m^3/yr and 2649 m^3/yr, depending on the DoA trend used. These annual net transport rates are somewhat smaller than

initial estimates made at the Pebble Ridge, which were based on the volume of clastic material recycled from the north to the south of the feature during a re-nourishment program that was run between 1986 and 1996. For instance, Kirby (1996) estimated between 3200 m^3 and 5000 m^3 of clastic material were recycled annually in order to maintain the integrity of the southern ridge. In contrast, the 50th percentile of model prediction correlate more closely with council estimates reported by Orford (2005), which are between 1000 m^3/yr and 2000 m^3/yr.

The recycle-based estimates should however be treated with caution. Notwithstanding the large variability in documented recycle rates, it seems likely that estimating the longshore transport rate based on the re-nourishment programme is erroneous. It is unlikely that a principal aim of the programme was to re-cycle the precise volume of material transported along the Pebble Ridge through natural processes. Indeed, the quite understandable desire to build-up areas of the Pebble Ridge beyond the previous natural level would lead to the overestimation of the longshore transport rate. Furthermore, the re-nourishment process itself could increase the volume of material available for transport (e.g. Orford, 2005). Precise details about the re-nourishment scheme are not available and currently no other longshore transport estimates exist.

The importance of low-frequency, high-magnitude events varies depending on the model iteration. The 5th percentile of daily transport estimates implies positive longshore transport is exclusive to infrequent, high-magnitude events. Alternatively, in the 95th percentile of model iterations, small-scale positive transport associated with modal, calm conditions contributes an increasing proportion of the total net positive transport, and hence the overall importance of storms is diminished. Despite this variability, all model iterations attribute a disproportionately large fraction of the total positive transport to infrequent powerful storm events.

The empirical model presented in this chapter not only indicates the disproportionate contribution of Atlantic storm swells to the positive transport of clastic material towards the Pebble Ridge, but also the moderating role of water depth on the proportion of wave energy that can access the beach. It is therefore important to explore the sensitivity of the longshore transport process

to mean sea level and storminess, which have both been linked to climate change.

5.7.2 Impact of Sea Level Rise

The combination of projected global marine transgression (due to both thermal expansion and the influx of melt water from terrestrial-based ice) and the current isostatic rebound of North Devon indicate relative sea level at Abbotsham will rise significantly within this century. Projections of global mean sea level rise are variable and dependent on future rates of warming and therefore greenhouse gas emissions. The 2009 UK Climate Projections report (UKCP09, 2009) considered the future relative sea level around the UK with respect to the predicted global mean sea level rise (from IPCC, 2007) and modelled isostatic rebound rates (from Bradley et al., 2009). The nearest forecast was made for Cardiff (Wales), 85 km west-north-west of Abbotsham. Here, a 'high emissions' scenario was forecast to result in a 0.46 m rise in mean sea level by 2095 (relative to the 2010 level). Considering this, the empirical model was re-run (Run B) with the same offshore wave climate, but with mean sea level increased by 0.46 m (see Electronic Appendix 2 for all B runs).

The rise in mean seal level increased, for each tidal half-cycle, the period for which the beach was subjected to wave action. Specifically, the proportion of time for which the beach was submersed (hereafter referred to as 'submersion time') increased from 31 % to 37 %. In addition, the maximum possible wave energy available at the inner shore platform increased non-linearly at each instant in time. Analysis of the offshore wave height and tidal record in Run A (i.e. for current sea level) showed that for between 51 % and 58 % of the submersion time, wave energy at the inner shore platform was to some extent moderated by water depth. The 0.46 m rise in mean sea level increased the access of incident wave energy to the beach and reduced these figures to between 43 % and 49 %. Indeed, the proportion of total offshore wave energy reaching the inner shore platform increased from approximately 10 % to 14 %.

The resulting increase in wave energy acting on the beach increased net positive longshore transport in each of the model runs by 61 %. Somewhat surprisingly, the relative contribution by the most powerful 10 %, 5 % and 1 % of wave conditions remained unchanged. This result is indicative of the general

moderating effect of water depth and that the substantial increase in positive net longshore transport appeared to be due to the general increase in wave energy at the inner shore platform. It follows that an increase in mean sea level consistent with the high emissions scenario would significantly increase net positive transport towards the Pebble Ridge regardless of a future change in the offshore wave conditions.

5.7.3 Impact of Increasing Storminess

An increase in the mean significant wave height has been measured by moored instruments in the north-east Atlantic Ocean over the last 50 years (Bacon & Carter, 1991, 1993). The change has been attributed to a systematic increase in the surface wind speeds as a result of climate change. A number of papers predict a further increase over the next century as the atmosphere continues to warm (e.g. Kushnir et al., 1997; Wang et al., 2003; Weiss et al., 2005; Dodet et al., 2010). However, Hemer et al. (2013) showed that when forced with a high greenhouse gas emission scenario their atmospheric-ocean general circulation model predicted a reduction in the mean height and period of waves as wind speeds reduced over the north Atlantic Ocean.

While the future wave climate of the north Atlantic remains uncertain, the range of projected outcomes include scenarios in which the significant height and period of waves increase considerably. Ideally, this section would present the outputs from further model runs exploring the potential impact of a systematic change in the offshore wave climate on longshore transport at Abbotsham. This process is made difficult by the lack of detail of wave climate projections. The majority of research has focussed on the long-term change to the annual-mean values. However, the empirical model is sensitive to the unreported processes by which the annual mean height and period increase. For instance, it is intuitive that net longshore transport predictions would differ where the increase in mean wave energy was the result of: (1) a proportional increase in the height and period of the entire distribution of waves; (2) an intensification of low-frequency, high-magnitude events only.

A logical approach to addressing this uncertainty would be to systematically vary the offshore wave climate and analyse the corresponding alteration to the modelled net annual longshore transport rate. For this, the distributions of the

offshore wave conditions would be altered to reflect the projected increase in the annual mean values. The shape of the distributions would also be systematically distorted so as to vary the intensity of low-frequency, high-magnitude events (whilst maintaining the distribution mean). Furthermore, the impact of these synthetic wave climates would be explored for a range of mean sea levels consistent with the projections for low, medium and high emissions scenarios. This approach would provide comprehensive insight to the sensitivity of longshore transport to variability in wave climate, but would be highly-laborious and is therefore beyond the scope of the current PhD research. Instead, the abovementioned storm sensitivity analysis is highlighted as future work.

The impact of an increase in storminess is explored here conceptually. In all model iterations, storm conditions were consistently coupled with large-scale net positive transport towards the Pebble Ridge. The term ‘storminess’ encompasses both the frequency and intensity of storm events. An increase in storm intensity (but not frequency) might have little impact on the longshore transport rate because the attenuation of wave energy across the shore platform would increase in proportion to offshore wave height. Only if the increase in storm intensity is couple with an increase in mean sea level (and hence water depth across the shore platform) might any surplus in the offshore storm energy reach the beach. Conversely, an increase in storm frequency could have a significant impact on the longshore transport rate regardless of a change in mean sea level. It follows that an increase in storm frequency and/or storm intensity - where coupled with mean sea level rise - would therefore increase the annual net positive longshore transport.

5.7.4 Pebble Ridge Nourishment & Future Dynamics

The wider implications of these results are dependent on the assumption that transport through the experimental beach is representative of the Abbotsham beach cell (see Figure 5.11 for boundaries) as a whole, and hence equal to the flux transported towards the Pebble Ridge. Given the systematic variability in wave condition along Abbotsham beach (demonstrated in Chapter 4), one might logically conclude assuming uniformity in longshore transport is erroneous.

However, the relative importance of longshore variability during the energetic conditions (when the majority of clast transport occurred) was small.

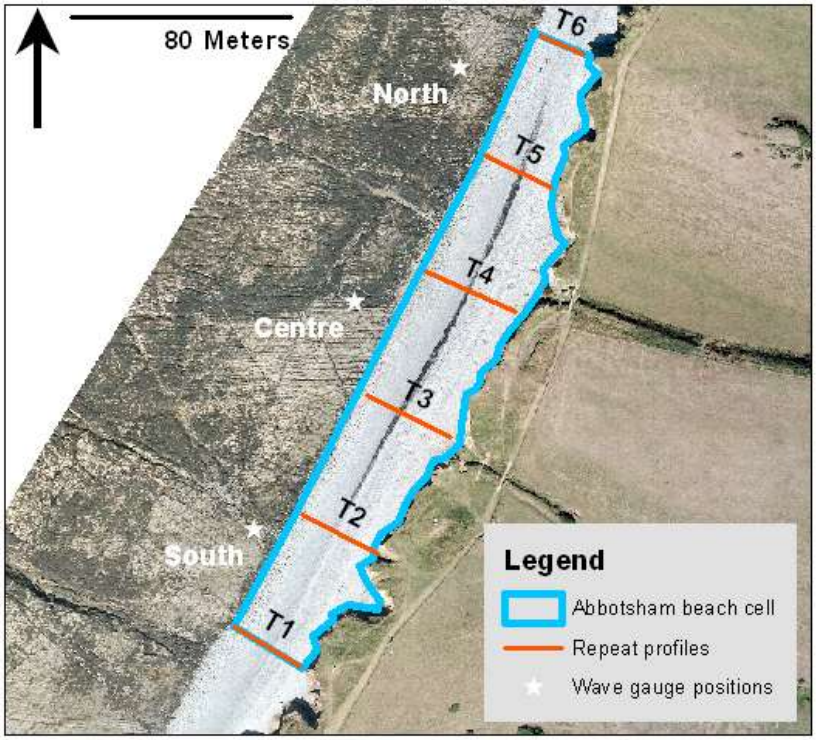

Figure 5.11: Aerial image of the Abbotsham displaying the boundaries of the Abbotsham beach cell and positions of the six transects across which repeat measurement of the beach profile were made.

Repeat measurement of the profiles across six predefined beach transects spanning the Abbotsham beach cell showed the volume remained relatively constant over the 18 month field campaign (see Figure 5.12). It is therefore assumed that longshore transport modelled through the experimental beach is largely representative of transport throughout the Abbotsham beach cell as a whole and therefore proportional to the flux in and out of the beach.

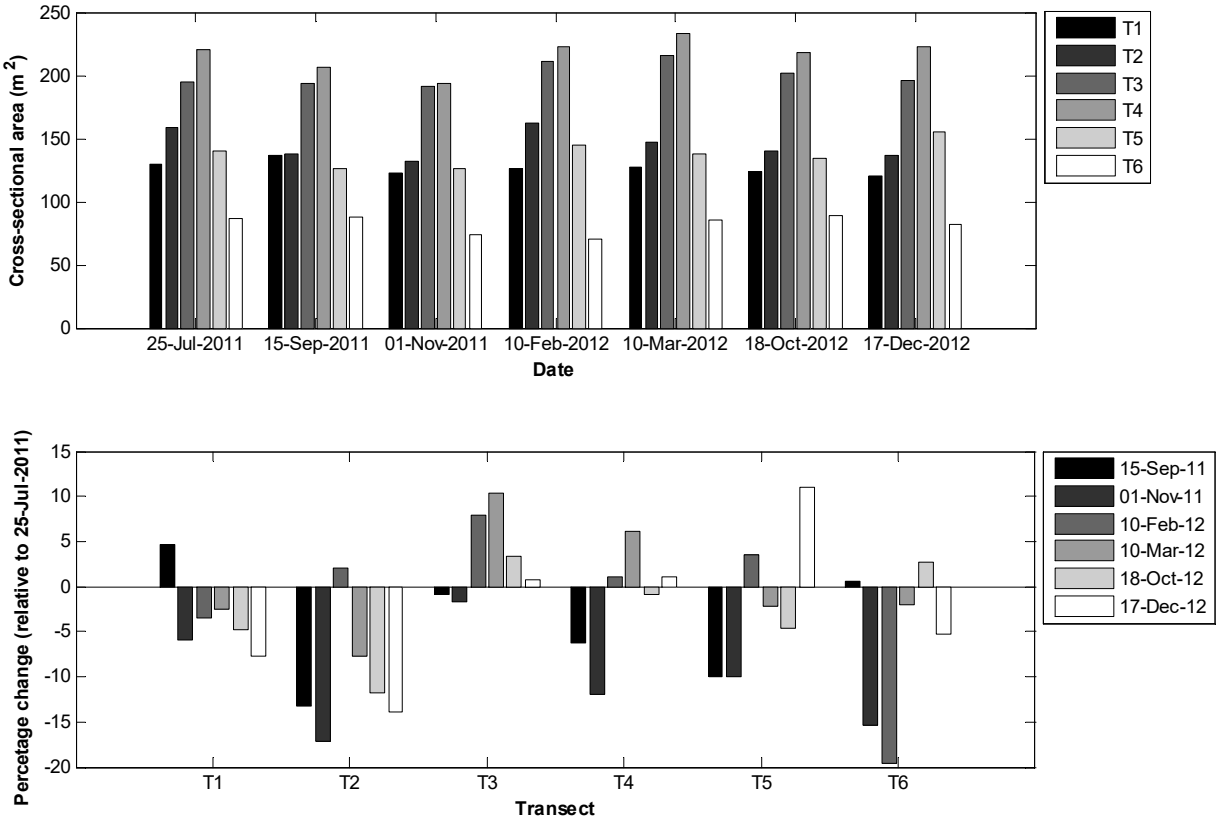

Figure 5.12: Cross-sectional area (top) and percentage change in cross-sectional area (bottom) of Abbotsham beach throughout the 18 month field campaign. The beach profiles remained relatively consistent over the 18 month field campaign. Variability in the cross-sectional area of each profile was generally less than 15 % between field visits. Importantly, no long-term accreting or eroding trend was consistently observed along the Abbotsham beach cell.

Longshore transport through Abbotsham beach is considered here in light of the volume of the beach itself. The volume of the Abbotsham beach cell was estimated based on a digital elevation model, constructed using LiDAR data from the Channel Coast Observatory. The boundaries of the Abbotsham beach cell were based on the entire survey area of the beach (see Figure 5.12). Despite the most recent LiDAR data being obtained almost a year prior to starting field work at Abbotsham, comparison between the repeat profiles of the beach measured in October 2010 closely matched the cross-sectional area of the beach measured over the subsequent 2.5 years. The combined cross-sectional area of all transects (903 m^2) from the LiDAR data was within the minimum and maximum (839 m^2 and 944 m^2 respectively) of the numerous *in-situ* measurements made throughout the field campaign. The base elevation was given as the mean elevation of the exposed platform fronting the

experimental beach (i.e. 1.8 m above MSL) and the gradient of the shore platform beneath the beach was considered to be negligible.

The Abbotsham beach cell was estimated to be 33,426 m^3 in volume. In all model iterations, the volume of material predicted to be transported through the beach during the stormiest day amounted to less the 3 % of the total beach volume. This result is consistent with repeat profile measurements, which suggested the morphology of the beach remained largely unchanged regardless of the intervening wave conditions. It is likely that the Abbotsham beach cell is therefore resilient to the impact of the most intense storms and significant morphological change would only result from a long-term alteration to the wave force or up-drift nourishment.

As described in section 2.2.2, the socially and economically valuable Pebble Ridge comprises the most northerly section of the system of coarse greywacke clasts that extends from the Gore to the mouth of the Taw-Torridge Estuaries. The Pebble Ridge provides natural protection for the town of Westward Ho! and Northam Burrows from erosion and inundation by powerful oceanic storm waves. The rapid retreat of the southern portion of the Pebble Ridge has been documented over the past 150 years, and has already resulted in land loss and property damage. A number of reports assessing the future dynamics of the Pebble Ridge have been published (e.g. Stuart & Hookway, 1954; Halcrow, 1980, 2008; Comber et al., 1993; Keene, 1996; Kirby, 1996; Orford, 2005; May, 2007; Pethick, 2007). They focus on its future morphodynamics in light of predicted sea level rise, but do not consider the potential change to the influx of clastic material to the feature. The implications of the modelled longshore transport for Pebble Ridge nourishment are discussed here with respect to predicted sea level rise and a potential increase in storminess.

Pethick (2007) noted that the anticlockwise rotation of the Pebble Ridge is not yet complete, and further re-orientation is required for swash-alignment to be achieved. He developed a conceptual model of the future morphodynamics of the Pebble Ridge within the context of sea level rise. He suggested the predicted sea level rise of 8 mm/yr (DEFRA, 2006), would increase the rate of retreat from the current 1.5 m/yr to greater than 2 m/yr. The retreat rate will increase exponentially thereafter and could reach 4 m/yr by 2100, when sea

level rise is predicted to approximate 14.5 mm/yr. Moreover, Pethick (2007) proposed the swash-aligned ridge would experience minimal longshore transport, and that the natural infilling of breaches in the feature would be minimised. The loss of the coherent structure of the Pebble Ridge would further compromise its function as a buffer against wave action, and would ultimately result in a significant loss of land.

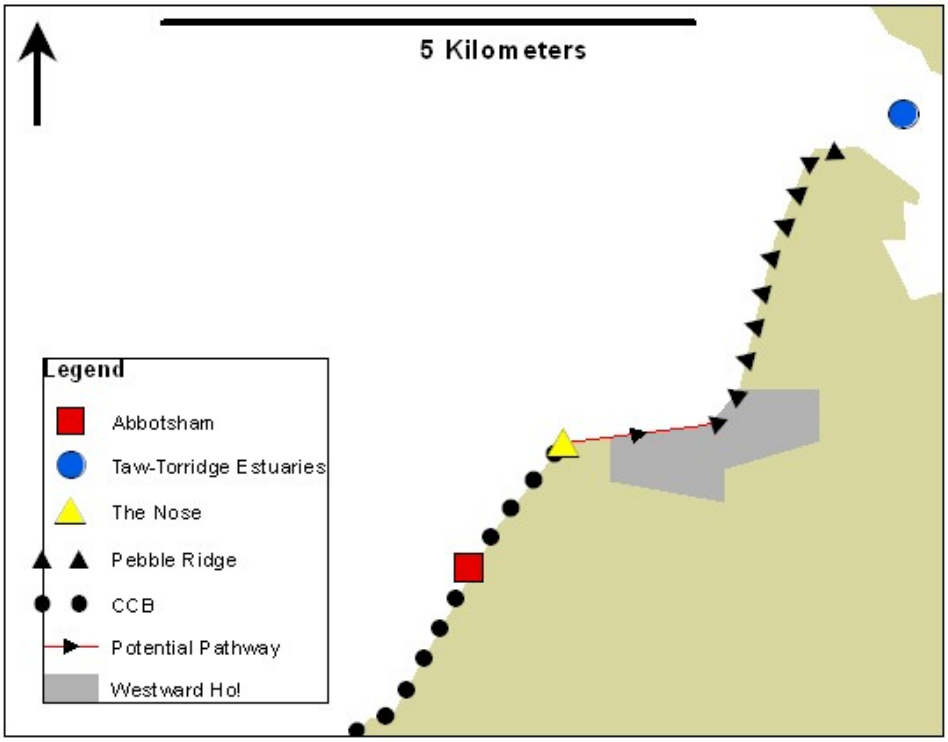

Figure 5.13: Map of a section of the Bideford Bay coastline displaying the positions of the Abbotsham beach, the Nose and the Pebble Ridge.

Pethick (2007) referred to Orford's (2005) assertion that the current disjoint between the Pebble Ridge and coarse clastic system further south has resulted from the rotation of the Pebble Ridge, and interrupted the southerly supply of clastic material from the Gore (see Figure 5.13). Orford (2005) proposed little or no clastic material can currently pass the Nose, and that the Pebble Ridge may only receive a relatively small amount of material from the erosion of a section of the raised beach at the Nose. Notwithstanding the potential major re-charge of clastic material from a further landslide, similar to that thought to have occurred between the 16th and 17th centuries, Pethick (2007) considered the Pebble Ridge as a relict feature that is cut-off from any significant clastic inputs.

However, direct observations of the time-varying position of a large number of tracer clasts at Abbotsham beach have demonstrated overwhelming net northward transport towards the Pebble Ridge. The 50th percentile of empirical model outputs estimates current annual volumetric transport rates to be at least 1339 m^3/yr (i.e. Run 1A). If, as Orford (2005) proposed, the Nose currently inhibits the conveyor of clastic material to the Pebble Ridge, it seems likely that clasts transported through the Abbotsham beach cell will accumulate within the short stretch between Abbotsham and the Nose. It is suggested here that the resulting extension of the developed beach would eventually re-establish the pathway for clastic material around the Nose and towards the Pebble Ridge.

The future morphodynamics of the Pebble Ridge will depend in part on the balance between the influx and outflux of clastic material. The current study focussed of the influx of clasts to the Pebble Ridge, and the only available outflux estimates are based on the volume of material recycled from the north to the south of the Pebble Ridge during a maintenance programme established almost 30 years ago. It should be noted that a more confident projection of the future dynamics of the Pebble Ridge is dependent on improved longshore transport estimates along the feature itself.

The considerable increase in the influx of material that is predicted to result from relative sea level rise and/or increased storminess will help offset the consequent demise of the Pebble Ridge. However, the Pebble Ridge is a large feature, estimated to be 6000,000 m^3 in volume (Pethick, 2007). Regardless of the unknown outflux rate, the influx of material required to maintain the integrity of the feature with increasing mean sea level and storminess would be vast. In all model runs, influx estimates remain small in comparison to the volume of the Pebble Ridge itself (< 0.2 %/yr), and it seems unlikely that the increased influx would be sufficient to halt, or even considerably reduce degradation. Instead, any ameliorating affects would most probably be small-scale. The Influx of clastic material will perhaps play an increasingly important role as the Pebble Ridge becomes more swash aligned and transport along the feature itself is minimised. Here, the enhanced influx of material could infill breaches in the feature and help maintain the integrity of the Pebble Ridge.

5.7.4.2 Key Recommendations for Future Research

- The empirical model was forced with direct measurements from the Bideford Bay wave buoy. Uncertainty with buoy measurements increased with wave height, and during the intense storms (e.g. H_{S0} > 6 m), all measurements were flagged by the CCO due to concern about their accuracy. A future recommendation would be to compare wave buoy measurements with predictions made with an ocean-atmospheric model to assess the nature of systematic errors that might occur in stormy conditions. Such analyses would mean the sensitivity model to erroneous buoy measurements could be quantified.
- As mentioned in the previous chapter (4), restricted access to a directional wave gauge limited the number of nearshore approach angle measurements and thus confidence with which the nearshore approach angle can be inferred from concurrent wave conditions offshore. Understanding of the relationship between the nearshore and offshore wave direction would be improved by simply prolonging the deployment time (to perhaps one month) of the directional wave gauge at the south shore platform. It is also recommended that a representative subset of measurements are excluded from the regression analysis and instead used as an independent dataset with which to robustly test the accuracy of the inferred wave variables.
- The ability to explore the sensitivity of the longshore transport process to a systematic change in the wave climate was precluded by a lack of detail about the precise nature of the predicted change. As outlined in section 5.7.3, an extension of this work would include a large-scale systematic investigation into the relative effects of varying the frequency/magnitude storms of the longshore transport rate.
- The thesis research focussed on the up-drift supply of clastic material to the Pebble Ridge and did not look at transport along the feature itself or between the Gore and Abbotsham. Improved understanding of the future dynamics of the Pebble Ridge would result from wider knowledge of the organisation and dynamics of the entire system. The implementation of similar empirical observations (Chapter 4) and models (Chapter 5) up-drift of Abbotsham and at the Pebble Ridge, would provide a more

holistic view of the system; with which improved predictions of the large-scale re-orientation and degradation of the Pebble Ridge would likely result.

5.8 Conclusion

Chapter 5 presents an empirical model, used to predict the daily longshore transport rate through the experimental beach over the last four years. The modelled annual net transport rates were variable and ranged from -390 m^3 to 5917 m^3. Although the minimum estimates were clearly in disagreement with the observed direction of net transport, the 50^{th} and 95^{th} percentile of each model run predicted a significant volume of material is transported towards the Pebble Ridge. It is not known whether clasts are accreting at the Nose, or continuing through to the Pebble Ridge. In any case, it seems likely that clastic material migrating through the Abbotsham beach cell will at some stage reach the Pebble Ridge.

Outputs from the empirical model showed longshore transport to be strongly influenced by the tidal elevation and storminess. Model runs in which mean sea level was raised by 0.46 m demonstrated a considerable increase in both the time for which the beach was subject to wave action and the maximum possible wave energy available at the inner shore platform at each instant in time. Forced with the same offshore wave climate, the 0.46 m increase in mean sea level increased positive annual net transport estimates by 61 %.

In the absence of detailed predictions of the future wave climate of the North Atlantic, the potential increase in storminess was explored conceptually. Evaluation of the net transport rate with respect to the entire spectrum of observed wave conditions indicates that a disproportionately large fraction of the total positive transport towards the Pebble Ridge was generated by low-frequency, high-magnitude storm conditions. The efficacy with which storm events generated longshore transport was dependent on water depth, and hence the spring-neap cycle. It was concluded that while an increase in storm intensity alone might have little impact on transport rates if not coupled with a significant rise in mean sea level, an increase in storm frequency would likely increase positive net annual transport regardless of sea level rise. Large-scale

storm sensitivity analysis is suggested as future work to quantify the impact of a systematic change in the wave climate.

The future dynamics of the Pebble Ridge will be determined by the balance between the influx and outflux of material. The current chapter focussed on the processes important to the influx rate, and the only available outflux estimates were based on the volume of material recycled in order to maintain the integrity of the southern ridge. The increased influx of material, as a result of sea level rise and increased storm activity, would act to mitigate the simultaneous retreat and degradation of the Pebble Ridge. In any case, the influx of material was small in comparison to the volume of the Pebble Ridge itself. It is therefore concluded that the likely increase in the influx as a result of sea level rise and/or increase in storminess would only partially offset the large-scale re-orientation and degradation of the Pebble Ridge.

6 : Synthesis and Conclusions

6.1 Introduction

This thesis presents a series of experiments designed to improve understanding of the relationship between the dynamics of coarse clastic beaches and nearshore wave conditions. The research questions addressed both fundamental aspects of beach morphodynamics and site-specific questions about particular processes considered important to the integrity of a coarse clastic barrier system that protects a vulnerable stretch of coastline in Bideford Bay, North Devon. The results of these studies have provided much needed insight into the relationship between the dynamics of coarse clastic beaches and nearshore wave conditions, which has hitherto been largely overlooked. In this synthesis chapter: (1) the results from the empirical portion of the thesis, and (2) the way in which they contribute to the current understanding of coarse clastic beach dynamics are discussed; (3) limitations and scope for future work are identified, and (4) the main thesis conclusions are drawn.

6.2 The Relationship between Coarse Clastic Beach Dynamics & Wave Force

The field-based experimental work presented in this thesis incorporated a range of observational techniques that enabled the analysis of various processes at: (1) a fine temporal scale which captured the entrainment process itself; (2) coarser temporal scale over which the net result of a series of transport events were considered. The thesis results are discussed below according to observational frequency.

6.2.1 Process-based Observations

The entrainment and transport process is dependent on the interrelationship between numerous complex variables. Analysis of the threshold-entrainment of ML clasts on a wave-by-wave basis demonstrated no relationship between the threshold-entrainment and wave power, and that clasts could occasionally be entrained by exceedingly weak threshold wave series. It was hypothesised that these results were an indication of the importance of unmeasured factors, including interactions between the various components of the wave spectrum within the short distance between the MAVS and ML clasts and the importance of the shoaling process and hence process zone. It was however not possible to explore further the abovementioned possibilities with the current data set. It is

however important to emphasise the fact that the questions raised by the experiment are the result of the novel, high-frequency measurements made, which had not previously been attempted in the natural littoral zone.

Despite the difficulties with which individual entrainment events could be linked to a threshold wave series, the real-time tilt and acceleration records from the ML clasts themselves provided new insight into the dynamics of clasts within the littoral zone. This was particularly true for the Abbotsham based motion logger experiment, where a misjudgement in the size of clasts selected to be implanted with motion loggers and the wave conditions during the field experiments were such that the threshold-entrainment of the entire ML sample was far exceeded. Here, an apparently random sub-sample of ML clasts were highly mobile while the others remained remarkably still. It was unclear whether the disparity in behaviour was due to the burial of some clasts, and hence indicates sheet flow conditions, or whether ML clasts remained at the beach surface but became stranded outside the breaker and swash zones on the flooding tide. In any case, these data were unsuitable for defining the threshold-entrainment, but indicated the highly dynamic state of the exposed beach at Abbotsham.

6.2.2 Net Observations

A strong, positive relationship was found between the mass of the heaviest clast entrained and the power of incident waves prevailing over each of the hour-long experiments. Importantly, the threshold-entrainment mass predicted by the force-balance equations of Lorang (2000) generally agreed with the field observations made over the experimental run.

Separate tracer experiments were conducted to consider the collective longshore displacement of clasts between daily, monthly and six monthly surveys. The mean daily longshore displacement of the tracer sample located on the experimental beach ranged from between –1.92±0.22 m/day to 11.91±0.17 m/day in calm and storm conditions respectively. The longshore displacement of tracer clasts was poorly related to the offshore wave conditions, but proportional to the estimated mean longshore component of wave power adjacent to the beach, which was a product of interactions between incident waves and shore platform morphology (as explained in full in section 6.3).

Tracer clasts, initially deployed at the beach surface, were rapidly (within one day) mixed into the beach by wave action. This finding is indicative of sheet flow conditions, where waves mobilise successive layers of clasts (Buscombe & Masselink, 2006). Results from the depth of activation experiments corroborate the observed burial rate and showed transport to a depth between approximately 0.04 m and 0.25 m below the beach surface in calm conditions, and deeper than 0.42 m around the MHWS mark during storm conditions. It was physically impossible for a lone worker to measure activation depths greater than 0.42 m, which hindered precise measurement of the thickness of the mobile layer during storm conditions. Accurate storm-based DoA measurements might however be achieved with a team of two or three dedicated workers, or with the development of an alternative method to insert the vertical column of tracer clasts deep within the beach matrix.

Combining the longshore transport and depth of activation results provided an estimation of the volume of material transported longshore through the experimental beach at Abbotsham each day. Longshore transport was found to vary from small-scale negative transport (the maximum magnitude of which ranged from -13 m^3/day to -30 m^3/day) to large-scale positive transport (the maximum magnitude of which ranged from 123 m^3/day to 247 m^3/day). Analysis of the daily longshore transport rate with respect to the longshore component of wave power enabled the derivation of the *K* coefficient. This process is standard practice on sand beaches but has rarely been attempted on a coarse clastic beach (e.g. Nicholls & Wright, 1991). In fact, the intermediate diameter of clasts at Abbotsham was almost an order of magnitude larger than the coarsest beach for which this analysis has been conducted. Comparison of the thesis results with the previous finding from a range of researchers (after Komar, 1997) indicated a reciprocal relationship between intermediate clast size and efficiency with which material is transported longshore.

An empirical model (based on the derived *K* coefficient) developed to predict the daily longshore transport rate through Abbotsham beach was used to provide valuable estimates of the net annual longshore transport rate towards the Pebble Ridge, as well as quantify the sensitivity of net annual longshore transport to storms and mean sea level. It is hoped these finding are of particular interest to the local coastal advisory groups for whom no detailed

influx estimates existed. The 50th percentile of model outputs indicated the longshore transport to be at least 1339 m^3/year and supports direct observation of the overwhelming positive displacement of tracer clasts along Abbotsham beach over a six month period. Further analysis of model outputs showed (1) a disproportionately large amount of the net positive transport was the results of infrequent high magnitude storm events but (2) the efficacy with which a particular storm event generates longshore transport is moderated by water depth across the shore platform and therefore the spring-neap cycle.

6.3 The Role of Nearshore Morphology

The extensive and irregular intertidal shore platform which fronts Abbotsham beach had a considerable effect on the energy and approach angle of incident waves at the shoreline. The important role of shore platform morphology on the attenuation of incident wave energy has been increasingly studied (e.g. Ogawa et al., 2011, 2012; Beetham & Kench, 2011; Bezerra et al., 2011; Marshall & Stephenson, 2011; Ogawa, 2013). In contrast to previous field studies, wave height measurements presented in this thesis spanned a wide range of conditions and were made adjacent to a beach on which comprehensive clast transport observations were also made. This meant it was not only possible to make a full assessment of the moderating effect of the shore platform on the nearshore wave conditions, but provide a novel assessment of the impact of shore platform moderation on longshore clast transport.

As the offshore significant wave height exceeded the water depth at the inner shore platform, the amount of incident wave energy reaching the shoreline became increasingly moderated. During storm wave events, incident wave energy along the inner shore platform was permanently saturated and therefore linearly related to water depth. Shore platform control on storm wave energy at the shoreline was mirrored by the crest height of the adjacent beach, which was inversely related to the elevation of the fronting shore platform. The moderating effect of the shore platform also lead (in Chapter 5) to the conclusion that a future increase in storm intensity, without a concurrent increase in storm frequency or mean sea level rise, would have little impact on the wave force acting on the beach and hence the net annual transport rate. Conversely, the moderating effect of the shore platform means an increase in mean sea level would result in a significant increase in wave energy acting on the beach,

particularly during storms. Model runs in which mean sea level was increased by 0.46 m predicted a 61 % increase in net annual transport toward the Pebble Ridge.

While the cross-shore attenuation of wave energy has recently gained some scientific attention, the current field study also identified (previously unreported) systematic variability in the refraction of incident waves in response to morphological irregularities in the shore platform. In contrast to the positive approach angles measured offshore, shorter period waves (6 s < T_P < 12 s) at the south position tended to have a negative mean approach angle. Incident waves with a negative angle of obliquity generated negative-directed clast transport. The magnitude of daily negative transport was at all times small, yet the prevalence of these conditions meant that over the course of a year, frequent negative transport events had a considerable impact on the magnitude of net positive transport towards the Pebble Ridge.

The strong refraction of incident waves coincided with a reduction in the expected wave height within the central embayment and an amplification of wave height at the north and south positions. This prompted the suggestion that shorter period waves were refracted away from the central embayment and resulted in a focussing of wave energy at the peripheral areas. Further empirical work is required to better understand how waves refract across the shore platform and the resulting spatial variability in the mean approach angle and wave energy along the inner shore platform fronting Abbotsham beach.

Field data presented in this thesis provide strong evidence of the influence of shore platform morphology on not only the magnitude, but also direction of net clast transport on the adjacent experimental beach. It was concluded that the wave force, and hence clast transport along the experimental beach, was geologically contingent, and should be considered in relation to nearshore wave transformations. It follows that, depending on the nearshore morphology, relating beach dynamics to the wave conditions measured some distance offshore could yield poor, and perhaps misleading, results.

6.4 Contribution of the Thesis to the Understanding of Beach Morphodynamics

The multiplicity of interrelated physical processes that govern the dynamics of a coarse clastic beach means they cannot be considered independently from one another (see Figure 1.3). Recent advances in tracing technology and compact wave measuring devices have improved the ease with which certain aspects of coarse clastic beach dynamics can be measured, however obtaining detailed field observations remains a challenge. This thesis presents novel field measurements that further understanding of coarse clastic beach dynamics and novel field methods that will help obtain detail field measurements in the future. The key contributions of each empirical chapter are outlined in this section.

The threshold-entrainment experiments (presented in Chapter 3) focussed on the interrelationship between intrinsic sediment characteristic and extrinsic incident wave force required to entrain individual clasts and initiate sediment transport. Although these experiments did provide valuable information on the threshold-entrainment of clasts, considerable uncertainty was associated with these data. Perhaps these experiments are most valuable as a 'proof of concept' of the application of motion loggers to measure clast motions in the littoral zone. The experiments represented a very modest step towards the ultimate ambition of tracing a clasts trajectory throughout time and highlighted the basic limitations imposed by: (1) the sampling frequency of motion loggers on the resolution of rapid rotations; (2) clast burial on retrieval of ML clasts; (3) relating particular entrainment events to a threshold wave series measured some distance away. Each of these points will need to be addressed to build on the current research.

The empirical experiments presented in Chapter 4 explored the complex, multifaceted relationships between the tide-dependent moderating effect of surf zone morphology on incident wave transformations and resulting sediment transport (see section 4.7). The main contribution of this empirical work was to demonstrate geological control on incident wave transformations and the magnitude and direction of longshore transport on the adjacent beach. The combination of the daily longshore displacement and depth of activation data enabled the estimation of the longshore transport rate and the derivation of the *K* coefficient. The latter of these two were of particular value because the

intermediate diameter of clasts composing Abbotsham beach was over an order of magnitude greater than coarsest beach for which a *K* coefficient has been previously derived. This enabled the extension of the fundamental relationship between the *K* coefficient and intermediated clast diameter of a beach, which was initially explored by Komar (1997).

The empirical model developed in Chapter 5 applied the quantitative relationships developed in Chapter 4 to explore the interplay between the incident wave conditions, ocean tides, surf zone morphology and processes on sediment transport. Combining the *K* coefficients (derived in Chapter 4) with the multiannual wave and tide time series provided hitherto unknown estimates of the longshore transport rate through Abbotsham beach and highlighted the sensitivity of this process to intense storm events and sea level rise. The novelty of the model's construction and the poignancy of the research question meant Chapter 5 has value from a scientific perspective and contributes to the general debate about impact of climate change on coastal processes. However, model outputs are particularly valuable to local coastal advisory groups (e.g. North Devon Biosphere Reserve) for whom the dynamics of the Pebble Ridge is of immediate concern.

6.5 Errors & Uncertainty

Each of the empirical components of this thesis included errors and uncertainties which had varying impact on the confidence with which data could be analysed and interpreted. Large errors and uncertainties were associated with the methodology of the threshold-entrainment experiment. Whilst the use of motion loggers enabled the measurement of real-time motions consistent with the frequency at which entrainment events occur, the inability to fully resolve particularly rapid rotations and the inherent insensitivity of the rotational entrainment criteria to non-rotational (sliding) events meant the threshold-entrainment was observed through a somewhat constricted lens.

The fastest rotation that could be resolved is dependent on the sampling frequency of the motion logger. An increase in the sampling frequency of the devices would improve the resolution of rapid rotations. However, the inclusion of non-rotational motions within the entrainment criteria would require an entirely new observational approach based on the total accelerations of clasts.

This would be particularly difficult due to the fine nature of acceleration signatures, which could only be resolved with an exceedingly high sample rate (e.g. Frank et al., 2013).

Further uncertainty arose when attempting to relate a particular entrainment event to an individual threshold wave series identified in the pressure record of the MAVS device, located up to 16 m and 30 m away in Flathead Lake and at Abbotsham respectively. Uncertainty, with defining the precise position of each motion logger at each instant in time complicated this process and it was consequently assumed that the ML clast was underlying the most competent (powerful) threshold wave series located between the MAVS and the shoreline.

Furthermore, this method considered the threshold wave series as a discrete entity and did not account for the effects of complex spectral interaction that might occur between the wave gauge and shoreline. It was hypothesized that the threshold wave series approach was highly sensitive to systematic errors resulting from complex spectral interactions within the short distance between the MAVS and motion Logger clasts. Further investigation into the potential significance of nearshore wave interactions would require a cross-shore array of wave gauges such as those deployed by Masselink et al (2010) and could not be explored further with present data set.

The adopted threshold-entrainment method worked only in the low-energy conditions of Flathead Lake. An attempt to execute the same experiment on the exposed maritime beach at Abbotsham was less successful. Here, the presence of secondary and tertiary frequencies complicated the wave spectrum and the ability to attribute entrainment to a specific threshold wave series. Moreover, the binary behaviour of the sample of ML clasts, which ranged from highly mobile to remarkably still, raised questions about whether some ML clasts were buried or left stranded below the energetic breaker zone during the experiment. Consequently these data were not considered suitable for the threshold entrainment analysis.

The high levels of vertical mixing on Abbotsham beach created uncertainty in the longshore transport experiment (in Chapter 4). This was particularly important in terms of locating the position of detected clasts during the beach surveys. Because it was not physically feasible to excavate the beach until each

tracer clast was found, the position of detected but unseen clasts was estimated based on their radio signal and could have been anything up to 1 m away from the actual position. However, the errors between the measured and actual position of tracer clasts are likely to have been random and have had little impact on the calculated mean transport of the 47-118 tracer clasts located on both of the coupled survey days.

The requirement of the worker to manually transfer data from the DGPS and RFID units to the field notebook introduced further, unquantifiable errors to the dataset. For two of the daily transport observations (between 12 and 13 February 2012 and 08 and 09 March 2012 respectively), the recorded displacement of a tracer clast was in conflict with the transport of the sample as a whole, and could not reasonably be assumed to have been the consequence of wave action. The relative isolation of the Abbotsham beach meant these results were unlikely to be due to human interference (e.g. someone throwing a tracer clast) but instead probably resulted from the errors of the worker. The potential for such errors would be considerably reduced by integrating the RFID and DGPS units so that data from the two devices was automatically combined and not reliant on the manual transcription of an often cold, wet and tired worker.

Further uncertainty arose from the longshore component of power being based on the modelled nearshore wave conditions rather than direct measurements made adjacent to the beach during the periods intervening successive surveys. Despite the modelled wave conditions providing a good description of variability in the mean longshore displacement of tracer clasts, the relationship between the hydrodynamics and the longshore transport of coarse clasts would be improved by relating clast transport to direct wave measurements.

However, most of the uncertainty in the longshore transport estimates emanated from the poor depth of activation data. Particularly large uncertainty surrounds the depth of activation during intense storm conditions, which was immeasurably deep. Gaps in this data set accommodated a wide range of possible trends, which were explored subjectively. Various depth of activation scenarios were trialled to quantify the sensitivity of the estimated longshore transport to the uncertainty within the data set. Significant improvements would

result from increasing the number of storm-based depth of activation measurements and the development of a more effective method of inserting the DoA column into the beach matrix.

The empirical model developed in Chapter 5 was founded on the field measurements made in the previous chapter (4). It follows that uncertainty and methodological improvements identified for the empirical work presented in Chapter 4 are relevant to the predicted net annual transport rates (Chapter 5). Additional uncertainty originated from the Bideford Bay wave buoy measurements that were used in the model. Uncertainty increased rapidly with prevailing wave height, and during storm conditions almost all measurements were 'flagged' by the CCO as being particularly uncertain. It was not possible to further explore the potential nature of ensuing errors and their impact on the modelled net annual transport rates. A comparison between wave buoy measurements and predictions from an ocean-atmospheric model were primary suggestions as a means of quantifying the impact of wave buoy errors on the modelled transport rate.

Aside from the uncertainty within the empirical model, ambiguity associated with the wider interpretation modelled net annual transport rate and the future dynamics of the Pebble Ridge arose from a lack of knowledge about the: (1) precise ways in which prevailing wave energy might increase; (2) current and future transport rates along the Pebble Ridge. Advanced predictions of the future dynamics of the Pebble Ridge is therefore dependent on: (1) more detailed predictions about the precise way in which the wave climate of the North Atlantic will change (i.e. storm intensity versus storm frequency); (2) greater knowledge of transport rate along the Pebble Ridge and wider coarse clastic system in Bideford Bay.

6.6 Limitations & Future Directions

The empirical work in this thesis used new, 'off-the-shelf' technologies to observe various processes on coarse clastic beaches. Implanting these new technologies within natural beach clasts has greatly improved the ability to make field-based measurements of clast transport. Combining the clast transport observations with nearshore wave measurements has improved understanding of the role of platform morphology and nearshore wave

transformations and the wave-related morphodynamics of coarse clastic beaches. However, fundamental limitations and challenges to understanding the dynamics of coarse clastic beaches remain, which are discussed here.

6.6.1 A Lagrangian Approach to Measuring Clast Transport

Radio Frequency Identification technology has made tracer clasts easily-identifiable, even when buried up to a meter below the beach surface. This is a significant improvement on traditional visual tracers, particularly with consideration to the rate of clast burial on Abbotsham beach. Yet, the RFID system does not negate the need for a person to actively search the beach to locate tracer clasts and thereby measure net transport. Consequently, the temporal frequency with which clast transport observations can be made is dependent on the ability of the worker(s) to repeat strenuous clast searches. The exposed and turbid nearshore, and extensive beach at Abbotsham made submersed RFID surveys impossible (e.g. Bertoni et al., 2010). Clast searches were instead confined to times when the beach was sub-aerial. Despite the semi-daily tides at Abbotsham, the exhaustive nature of clast searches meant that it was reasonable to only conduct beach surveys once a day.

It should be emphasised that the majority of previous tracer studies considered the net transport of clasts over a period of weeks and months (e.g. Allan et al., 2006; Curtiss et al., 2009; Bertoni et al., 2010; Dickson et al., 2011). The extensive daily observations presented in this thesis were therefore quite novel, and provide new insight into the net transport in response to specific nearshore wave conditions that prevailed over the relatively short intervening period. However, the observed daily net transport is the result of numerous complex interactions between the coarse clastic beach and the variable and non-linear hydraulic forces exerted by irregular incident waves. Despite being one of the highest temporal frequencies at which the collective displacement of clasts has been observed, the daily surveys provide limited insight into the fundamental processes leading to the observed net transport.

Alternatively, the motion loggers, which were integrated within natural beach clasts, surveyed at a rate of four hertz, enabled process-based measurement of individual entrainment events. However, the high-frequency acceleration and tilt time series was insufficient to fully-resolve the rapid motions of clasts within the

littoral zone and realise the ultimate aspiration; to internally track the real-time position of the tracer clast through its inertia. Indeed, no device currently exists that can actively record its real-time position within the natural littoral setting (Van Wellen et al., 2000; Naylor et al., 2010). The ability reconstruct, via the clasts inertial history, its transport pathway would therefore signify a major methodological advancement for research into the dynamics of coarse clastic beaches. The deployment of these 'smart' clasts would vastly improve the measurement of all beach processes addressed in this thesis. It therefore seems logical to pursue the design and manufacture of such devices suitable for deployment in the littoral and fluvial environment (e.g. Abeywardana et al., 2009).

6.6.2 Relating Clast Transport to the Wave Force

The hydrodynamics of coarse clastic beaches is complex and strongly related to process zone. However, it is incredibly difficult to measure wave dynamics across the beach face, not least because *in-situ* wave gauges are at risk of damage from impact with mobile clasts. Moreover, the Lagrangian nature of the swash zone means traditional fixed instruments are not suitable for measuring the up-rush and back-wash, which can dominate the dynamics of coarse clastic beach (Puleo et al., 2000). The experiments in this thesis relate the dynamics of tracer clasts to the height and approach angle of waves measured at a single point located between 10 m and 20 m away from the base of the experimental beach. These simple wave measurements were adequate for experiments concerned with the net transport of clasts across the beach face, which was the cumulative product of clast dynamics across all process-zones over an extended period of time (i.e. days to months). However, the importance of the process zone was indicated by the threshold-entrainment experiments, and it seems probable that significant advancement in process-based understanding of the dynamics of coarse clastic beaches will not be achieved without due attention to the complexities of the shoaling process.

While horizontal asymmetries in the profile of breaking waves have been observed to influence the threshold-entrainment of sand grains (e.g. Foster et al., 2006), extreme pore pressures have been measured under plunging breakers, which has been hypothesised to compromise the interlocking nature of the beach matrix and influence the depth of activation (Pedrozo-Acuña et al.,

2008, 2010). Further research has demonstrated a cross-shore gradient in the long-shore current of the wave swash generated by oblique wave fronts on coarse beaches (Austin et al., 2011). The forces exerted by a wave are intrinsically linked to the shoaling process and therefore process zone. Improvement to process-based understanding will result from considering clast transport as a function of process zone. Such advancement would result from the use of video analysis to measure the up-rush and back-wash of waves (e.g. Holman & Guza, 1984) and perhaps deploying a cross-shore array of wave gauges across the beach face (e.g. Masselink et al., 2010).

6.6.3 Clast Erosion

The dynamics of individual clasts is strongly related to clast mass and shape (e.g. Lorang, 2000). However clasts erode throughout time by impact fragmentation and/or more gradual abrasive action (Lorang & Komar, 1990). The experimental work presented in this thesis assumes the properties of the various tracer clasts to be consistent for the period over which observations were made (i.e. hours to months). This assumption was clearly accurate for the ML logger clasts, which were deployed in a series of up to five, hour-long experiments and safely stored during the intervening periods. However, tracer clasts deployed for the longshore displacement experiments were observed over a period of up to 6 months after deployment, and were not retrieved for re-measurement at any stage. It follows that the extent to which the mass and shape of tracer clasts could have varied is unknown.

Fragmentation on impact with another hard object (e.g. clast, rocky shore platform or cliff) can rapidly erode large clasts. Fragmentation generally occurs along natural fault lines and is therefore geologically-controlled (Cornish, 1898; Stephenson & Naylor, 2011). Notably, the holes drilled into each clast to accommodate an RFID tag would have surely weakened tracer clasts, which might lack any lithological irregularities. Depending on the position of the RFID tag in relation to the plane of fragmentation, the dimension of the newly-liberated fragment could be quite different to those of the original tracer.

Alternatively, clasts can be gradually abraded as a result of small-scale impacts with sand or other coarse clasts. Dobkins & Folk (1970) suggested clasts abrade as they graze within the littoral zones, which results in a tendency

towards an oval shape. Field experiments of Allan et al. (2006) and Dickson et al. (2011) support this assertion by demonstrating positive relationships between mass loss and displacement distance of tracer clasts.

The erosion rate is therefore a function of intrinsic clast properties (including size, shape and lithology) as well as extrinsic conditions (such as beach properties and the hydrodynamic regime). Although the greywacke clasts that make up Abbotsham beach generally lack obvious lithological irregularities, a small number of sampled clasts did incorporate clear quartz intrusions through one or more planes. Angular fragments of freshly broken clasts were a rare sight, indicating the infrequent occurrence of impact-fragmentation. However, it is not possible to assess the abrasion rate of tracers without retrieval and re-measuring their weight and axial lengths (similar to Allan et al., 2006; Dickson et al., 2011).

It should be re-emphasised, that analysis was only conducted on tracers located in a relatively confined area (250 m) of Abbotsham beach. These clasts are likely to have not been transported an extensive distance, which has been linked to erosion. Moreover, the extensive mixing depth across the beach face suggests transport is more closely related to the collective properties of the beach and not individual clasts. Measuring the erosion rate of tracer clasts would be intensive and is beyond the scope of the current thesis research. However, the erosion of a tracer clast is likely to have some effect on its dynamics, and is therefore a process that should be considered in the future.

6.7 Thesis Conclusions

This thesis aimed to develop a quantitative relationship between the dynamics of coarse clastic beaches and nearshore wave conditions. The research questions were addressed by a number of Lagrangian field experiments using newly-available ‘off-the-shelf’ technology. The majority of experiments were conducted on a short stretch of coarse clastic beach at Abbotsham, North Devon. However, process-based field experiments into the threshold-entrainment were also conducted in the low-energy environment of Flathead Lake, Montana USA.

Within each specific area of empirical research, the dynamics of clasts were closely related to the wave conditions measured between 10 m and 20 m

seaward of the beach base. The threshold-entrainment was observed using motion loggers implanted within up to 15 natural beach clasts, deployed in unison during a total of six 1.5 hour-long experiments. The sample rate of four hertz enabled the quasi real-time dynamics of clasts to be observed and entrainment events, defined from the analysis of the three-axial tilt time series, to be related to the threshold wave series estimated to be overlying the ML clast the time of entrainment. These experiments demonstrated the dynamic nature of clasts within the littoral zone, which could become entrained and re-settled numerous times within each experiment.

A positive relationship was found between the threshold-entrainment mass and the power of incident waves that prevailed over the experiments. This relationship could be accurately predicted by the force-balance equations of Lorang (2000). However, the weakest threshold wave series associated with the entrainment of each ML clast were far weaker than the power of the prevailing wave conditions. When forced with the weakest threshold wave series, the Lorang equations systematically underestimated the critical entrainment mass. It was hypothesised that the exceedingly weak threshold wave series could indicate limitations of the wave measurements, which were obtained a short distance away and did not account for the shoaling process. However, further detailed research is required to explore the significance of this assertion.

Further experiments measuring the net effect of all entrainment events intervening daily beach surveys were conducted with a sample of between 47 and 118 natural, RFID-traced clasts at the macro-tidal field site at Abbotsham, UK. The magnitude and direction of the mean daily longshore displacement of tracer clasts was proportional to the mean longshore component of power estimated at the inner shore platform during the intervening period. The rate of clast burial was high across the beach face and a series of experiments demonstrated a positive relationship between wave power and depth of activation, which during the stormiest day exceeded 0.42 m in the central beach face. The combined longshore displacement and depth of activation results suggested at least 123 m^3 clastic material was transported longshore during the stormiest 24 hour period that coincided with field observations.

The shore platform at Abbotsham was important as an intermediate between offshore incident waves and the beach. The elevation of the platform moderated the amount of incident wave energy at the beach base, which (within the central embayment) was half that measured offshore during the stormiest spring high tide period. In addition, longshore irregularities in platform morphology resulted in the refraction of incident wave fronts and therefore systematic variability in the local mean approach angle of incident waves at the beach base. Analysis of the half-hourly mean nearshore approach angle at the south position demonstrated systematic variability of up to 7 ° as a result of interactions with the underlying morphology. Strongly refracted wave fronts approached the experimental beach with a negative mean angle, which reverse the direction in which the longshore component of wave power acted and therefore the direction of net clast transport. It was concluded that the magnitude and direction of clast transport was geologically contingent and should not be considered in isolation from interactions between shoaling waves and shore platform morphology. Moreover, this particular result highlights the importance of obtaining nearshore wave measurements to improve understanding of the dynamics of CCBs.

Experiments monitoring components key to quantifying the longshore transport rate of coarse greywacke clasts through the Abbotsham beach cell were not only of intrinsic scientific value, but also have practical implications for the nourishment of the coarse clastic ‘Pebble Ridge’ that protects Westward Ho! and Northam Burrows from erosion and inundation by powerful storm waves. A simple empirical model was developed to estimate the longshore transport rate through the Abbotsham beach cell and run for the multiannual period (June 2009 to April 2014) during which the Bideford Bay wave buoy has been deployed and operational. Uncertainty in each component of the model was systematically explored resulting in a range of possible outcomes. The 50^{th} percentile of model predictions suggested the net annual longshore transport rate towards the Pebble Ridge was at least 1339 m^3.

In each model iteration, a disproportionately large fraction of positive longshore transport was attributed to storm swells. It was concluded that any future increase in storm intensity (but not frequency) without a significant rise is mean sea level would have little impact on the longshore transport rate at Abbotsham,

because the water depth across the shore platform limits the amount of wave energy reaching the experimental beach. Meanwhile, an increase in mean sea level, storm frequency and/or storm intensity coupled with mean level rise would likely result in an increase in the net annual longshore transport rate towards the Pebble Ridge. Despite this, it was concluded that any increase in the net annual longshore transport rate would be small in comparison to the volume of the feature itself and therefore unlikely to halt or significantly reduce future degradation.

The experiments presented in this thesis provide new insight into the dynamics of coarse clastic features, which have been hitherto understudied. The use of motion loggers implanted within natural beach clast provided much-needed field observations of the threshold-entrainment, which supported predictions made with the Lorang (2000) equations. High-frequency daily observation of the collective displacement and depth of action of a sample of traced clasts enabled the derivation of the *K* coefficient, to relate the longshore component of wave power to the immersed weight transport rate of coarse clasts. Meanwhile, comparisons between measurements from an alongshore array of wave gauges and offshore wave buoy showed the magnitude and direction in which the longshore component of wave power acted was strongly related to shore platform morphology. An empirical model developed to estimate longshore transport through Abbotsham beach showed the shore platform to limit the amount of wave energy that could reach the nearshore and thus the net annual longshore transport rate. It was concluded that a future increase in storm intensity in itself would have little effect on the nearshore wave force and clast transport. Conversely, an increase in storm frequency and/or mean sea level would likely result in a significant increase in the longshore transport rate towards the Pebble Ridge, yet not enough to halt its continuing degradation. It is hoped that these data will not only aid the understanding of the dynamics of coarse clastic features but also the management of such features at a time when predicted sea level rise and a potential increase in storminess is likely to increase reliance on sea defence systems globally.

Appendices

Appendix 1

BOLEAN SEARCH CRITERIA TO IDENTIFY LITERATURE ADRESSING COARSE CLASTIC BEACHES:

megaclast AND beach NOT river* NOT fluvial NOT alluvial OR megaclast AND barrier NOT river* NOT fluvial NOT alluvial OR megaclast AND wave NOT river* NOT fluvial NOT alluvial OR megaclast AND littoral NOT river* NOT fluvial NOT alluvial OR megaclast AND swash NOT river* NOT fluvial NOT alluvial OR megaclast AND coastal NOT river* NOT fluvial NOT alluvial...

clast* AND beach NOT river* NOT fluvial NOT alluvial OR clast* AND barrier NOT river* NOT fluvial NOT alluvial OR clast* AND wave NOT river* NOT fluvial NOT alluvial OR clast* AND littoral NOT river* NOT fluvial NOT alluvial OR clast* AND swash NOT river* NOT fluvial NOT alluvial OR clast* AND coastal NOT river* NOT fluvial NOT alluvial...

boulder* AND beach NOT river* NOT fluvial NOT alluvial OR boulder* AND barrier NOT river* NOT fluvial NOT alluvial OR boulder* AND wave NOT river* NOT fluvial NOT alluvial OR boulder* AND littoral NOT river* NOT fluvial NOT alluvial OR boulder* AND swash NOT river* NOT fluvial NOT alluvial OR boulder* AND coastal NOT river* NOT fluvial NOT alluvial...

cobble* AND beach NOT river* NOT fluvial NOT alluvial OR cobble* AND barrier NOT river* NOT fluvial NOT alluvial OR cobble* AND wave NOT river* NOT fluvial NOT alluvial OR cobble* AND littoral NOT river* NOT fluvial NOT alluvial OR cobble* AND swash NOT river* NOT fluvial NOT alluvial OR cobble* AND coastal NOT river* NOT fluvial NOT alluvial...

pebble* AND beach NOT river* NOT fluvial NOT alluvial OR pebble* AND barrier NOT river* NOT fluvial NOT alluvial OR pebble* AND wave NOT river* NOT fluvial NOT alluvial OR pebble* AND littoral NOT river* NOT fluvial NOT alluvial OR pebble* AND swash NOT river* NOT fluvial NOT alluvial OR pebble* AND coastal NOT river* NOT fluvial NOT alluvial...

shingle* AND beach NOT river* NOT fluvial NOT alluvial OR shingle* AND barrier NOT river* NOT fluvial NOT alluvial OR shingle* AND wave NOT river* NOT fluvial NOT alluvial OR shingle* AND littoral NOT river* NOT fluvial NOT alluvial OR shingle* AND swash NOT river* NOT fluvial NOT alluvial OR shingle* AND coastal NOT river* NOT fluvial NOT alluvial...

gravel* AND beach NOT river* NOT fluvial NOT alluvial OR gravel* AND barrier NOT river* NOT fluvial NOT alluvial OR gravel* AND wave NOT river* NOT fluvial NOT alluvial OR gravel* AND littoral NOT river* NOT fluvial NOT alluvial OR gravel* AND swash NOT river* NOT fluvial NOT alluvial OR gravel* AND coastal NOT river* NOT fluvial NOT alluvial

BOLEAN SEARCH CRITERIA TO IDENTIFY THE MIXED SAND & GRAVEL PAPERS WITHIN THE CLASTIC BEACH LITERATURE:

mixed sand OR sand

BOLEAN SEARCH CRITERIA TO IDENTIFY THE BOULDER & BLOCK PAPERS WITHIN THE COARSE CLASTIC BEACH LITERATURE:

megaclast OR boulder

Table A1: Boolean search criteria to find coarse clastic literature on ISI web of knowledge. Search executed to construct figure 1.2. The criteria have been sectioned for visual ease, '...' is used here to denote continuation and is excluded from the search criteria.

Appendix 2

BOLEAN SEARCH CRITERIA TO IDENTIFY THE SAND-BEACH LITERATURE:

sand AND beach* NOT river* NOT fluvial NOT alluvial NOT boulder* NOT cobble* NOT pebble* NOT shingle NOT gravel* NOT land NOT aeolian NOT DNA* NOT bacteri* NOT microb* NOT chemical* NOT toxic* NOT Radio* NOT dune NOT bio* NOT species NOT cliff* NOT gas NOT silicon NOT wind* NOT explo* NOT silt* NOT mud* NOT cohesive NOT seis* NOT electric* NOT ecolog* NOT *organism* NOT radar...

OR sand AND bar NOT fluvial NOT alluvial NOT boulder* NOT cobble* NOT pebble* NOT shingle NOT gravel* NOT land NOT aeolian NOT DNA* NOT bacteri* NOT microb* NOT chemical* NOT toxic* NOT Radio* NOT dune NOT bio* NOT species NOT cliff* NOT gas NOT silicon NOT wind* NOT explo* NOT silt* NOT mud* NOT cohesive NOT seis* NOT electric* NOT ecolog* NOT *organism* NOT radar...

OR sand AND wave* NOT fluvial NOT alluvial NOT boulder* NOT cobble* NOT pebble* NOT shingle NOT gravel* NOT land NOT aeolian NOT DNA* NOT bacteri* NOT microb* NOT chemical* NOT toxic* NOT Radio* NOT dune NOT bio* NOT species NOT cliff* NOT gas NOT silicon NOT wind* NOT explo* NOT silt* NOT mud* NOT cohesive NOT seis* NOT electric* NOT ecolog* NOT *organism* NOT radar...

OR sand AND littoral NOT fluvial NOT alluvial NOT boulder* NOT cobble* NOT pebble* NOT shingle NOT gravel* NOT land NOT aeolian NOT DNA* NOT bacteri* NOT microb* NOT chemical* NOT toxic* NOT Radio* NOT dune NOT bio* NOT species NOT cliff* NOT gas NOT silicon NOT wind* NOT explo* NOT silt* NOT mud* NOT cohesive NOT seis* NOT electric* NOT ecolog* NOT *organism* NOT radar...

OR sand AND swash NOT fluvial NOT alluvial NOT boulder* NOT cobble* NOT pebble* NOT shingle NOT gravel* NOT land NOT aeolian NOT DNA* NOT bacteri* NOT microb* NOT chemical* NOT toxic* NOT Radio* NOT dune NOT bio* NOT species NOT cliff* NOT gas NOT silicon NOT wind* NOT explo* NOT silt* NOT mud* NOT cohesive NOT seis* NOT electric* NOT ecolog* NOT *organism* NOT radar...

OR sand AND coast* NOT fluvial NOT alluvial NOT boulder* NOT cobble* NOT pebble* NOT shingle NOT gravel* NOT land NOT aeolian NOT DNA* NOT bacteri* NOT microb* NOT chemical* NOT toxic* NOT Radio* NOT dune NOT bio* NOT species NOT cliff* NOT gas NOT silicon NOT wind* NOT explo* NOT silt* NOT mud* NOT cohesive NOT seis* NOT electric* NOT ecolog* NOT *organism* NOT radar

Table A2: Boolean search criteria to find sand-based literature on ISI web of knowledge. Search executed to construct figure 1.2. The criteria have been sectioned for visual ease, '...' is used here to denote continuation and is excluded from the search criteria.

Appendix 3

```
function [AoR, maxrot, entrain, acceler] = CCALC_HOBO3Dtilt2rotation(HOBOtime, HOBOdata)
% [AoR, AbA,maxrot,entrain] = CCALC_HOBO3Ddegtilt2rotation(HOBOtime, HOBOdata)
% Uses the three-dimensional tilt vectors from the HOBO motion logger to
% calculate the event-based revolution of a clasts through an arbitrary
% axis, and records the magnitude and timing of entrainment events.

deg2radtilt = cos(HOBOdata(:,5:7).*pi/180); % converting 3D tilt vectors from degrees to
radians.

a = deg2radtilt(:,1); % defining the axes from tilt data.
b = deg2radtilt(:,2); % defining the axes from tilt data.
c = deg2radtilt(:,3); % defining the axes from tilt data.

%% Angle of Rotation (cross product)

[Xab, Xac, Xbc] = RCCALC_crossprod(a, b, c); % getting the cross product from the a, b &
c to give the vectors ab, ac & bc.

for i = 1:length(deg2radtilt)-1 % defining the loop to be the length of the tilt vectors
minus 1.
    zeronorma1 = (a(i)^2+b(i)^2+c(i)^2) * (a(1+i)^2+b(1+i)^2+c(1+i)^2); % normalising
the combination of the three axes to zero.
    AoR(i) = asin(sqrt((Xab(i)^2+Xac(i)^2+Xbc(i)^2)/zeronorma1))/pi*180; % overall AoR
'ANGLE OF ROTATION' between consecutive timesteps.

    if (a(i)*a(i+1) + b(i)*b(i+1) + c(i)*c(i+1))/zeronorma1 < 0
        AoR(i) = 180 - AoR(i);
    end
end

%% *** AoR to DISCRETE ROTATIONAL EVENTS ***
ii = 0; % driver of the 'Main Loop'.
count = 0; % ing' variable for the number of descrete entrainment events.
maxrot = 0; % maximum rotation made by the clast in the whole HOBO run.
entrain = NaN; % entrainment magnitude and time array.
%% *** TILT RECORD LOOP ***
while ii+1 <= length(AoR)
    ii = ii+1; % drive the Main Loop forward by one.

    if AoR(ii) > 0 % If clast rotates...
%% *** 'EVENT' LOOP ***
        iii = 1; % Event Loop driver.
        cont = 1; % continue into the Event Loop.
        inirot = AoR(ii); % 'initial rotation'.
        oldrot = inirot; % 'old rotation' = to initial rotation,  for the first time step only.

        while ii+iii < length(AoR)-1 & cont == 1 % consider rotation to be the start of a series of
consecutive motions andlook ahead in detail while...
            zeronorma3 = sqrt(Xab(ii)^2+Xac(ii)^2+Xbc(ii)^2) *
sqrt(Xab(iii+ii)^2+Xac(iii+ii)^2+Xbc(iii+ii)^2); % normalising the combination of the three axes to
zero.
            ABA = ((Xab(ii)*Xab(iii+ii)+Xac(ii)*Xac(iii+ii)+ Xbc(ii)*Xbc(iii+ii))/zeronorma3); %
cosin of 'ANGLE BETWEEN rotational AXES' (ABA) of the initial and current rotation.

            if ABA > 1 % if the cosine of the angle between rotational axes is greater than 1 (which
is impossible and results from MATLAB rounding errors)...
                ABA = 1; % force ABA to 1.
            elseif ABA < -1 % if the cosine of the angle between rotational axes is less than -1
(which is impossible and results from MATLAB rounding errors)...
                ABA = -1; % force ABA to -1.
            end

            if iii > 1 % if not the the first rotation in the event, where ABA = 1...
                newrot = AoR(iii+ii)* ABA; % Multiply the angle of rotation by the cosine of the
angle between rotational axes.
            else
                newrot = AoR(ii); % else ABA = 1
            end

            if  oldrot+newrot > oldrot | iii == 1 % if following rotational values are a succesion of
the initial change, then...
                halt = NaN; % update event status.

                if oldrot+newrot > maxrot(1) & oldrot ~= newrot % if current rotation is greater than
the maximum recorded rotation, and rotation isn't the first in the event where oldrot = newrot...
                    maxrot = ([HOBOtime(ii) HOBOtime(ii+iii) oldrot+newrot]); % record the magnitude
and timing of the rotation.
                end

%%  *** ENTRAINMENT RECORD ***
                if oldrot+newrot >= 180 % if the clast has executed/exceeded one half-rotation in a
single event...
```

```
                    if isnan(entrain) % if entrainment has not been declared in the current event...
                       count = 1;
                    elseif entrain(count,1) ~= HOBOtime(ii) % if this is a new sparate entrainment
event...(To check the best solution replace HOBOtime(ii) for 1 and plot3(entrain(:,1), entrain(:,2),
entrain(:,3), '*k'))
                       count = length(entrain(:,1))+1;
                    end
                    entrain(count, 1:3) = [HOBOtime(ii), HOBOtime(ii+iii), oldrot+newrot]; % record
the magnitude and timing of the entrainment event.
                    acceler(count, 1) = max(abs(HOBOdata(ii:ii+iii,4)));
                end

%% *** ROTATIONAL EVENT TERMINATION CONDITIONS ***
            elseif oldrot+newrot < 0 | iii+ii-halt > 4 % but if the new rotation is greater than the
event cumulative AND OF THE OPPOSITE SIGN, or a halt or small reversal in rotation occurs for greater
than 1 second (4 timesteps)...
                cont = 0; % CONTinue N(0)T!!! Terminate event and head back to Main Loop.
                if count > 0 & HOBOtime(ii) == entrain(count,1) % if the clasts has just been
entrained...
                    ii = ii+iii-1; % skip searching the rest of the entrainment event and continue
Main Loop from entrainment end.
                end
            else % finally, if there is a small halt or or reversal in rotation for the first time...
                if isnan(halt)
                   halt = iii+ii; % record the start time.
                end
            end
%% *** EVENT TIME DRIVER ***
            if iii > 1
                oldrot = oldrot+newrot; % shuffling time steps.
            end
            iii = 1+iii; % drive the Event Loop forward by one.
        end
    end
end
```

Figure A1: Algorithm (written in MATLAB) used to identify entrainment events. See section 3.6.3 for full description of the algorithm.

Appendix 4

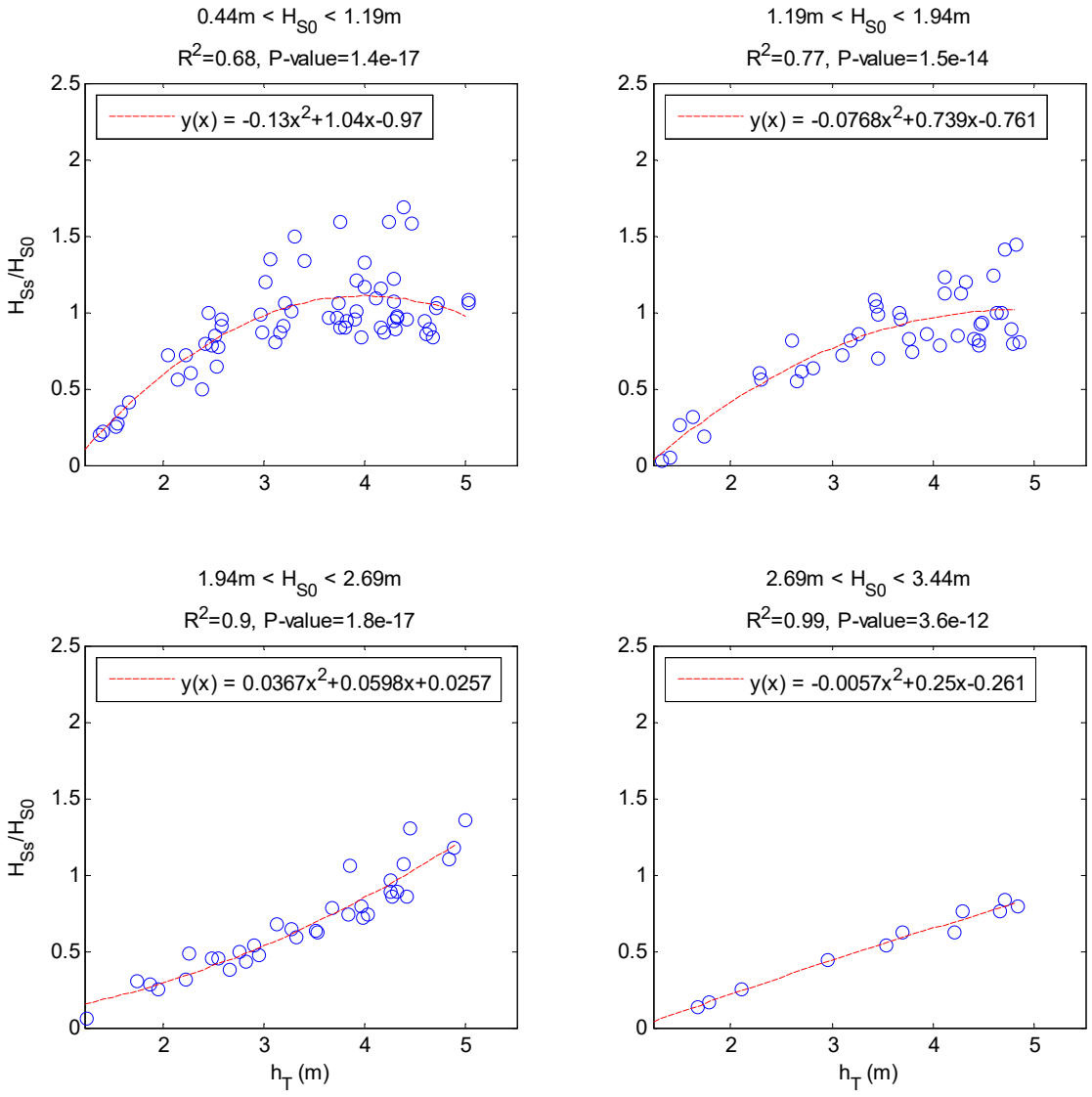

Figure A2: Ratio of the nearshore to offshore wave height versus tidal elevation. The data has been separated with respect to the concurrent offshore wave height (H_{S0}). The figure is constructed using all measurements made at the southern shore platform. In each plot, the distributions are represented with second order polynomials (red dashed lines). The nearshore wave height is, in each case, positively related to water depth. Where the offshore wave height is small (H_{S0} < 1.94 m), the trend is non-linear such that the rate at which the wave height increases reduces with tidal elevation. Larger waves are more strongly moderated by the water-depth, which is reflected by the increasingly linear trends and reduced variability where H_{S0} > 1.94 m.

References

Abeywardana DK, Hu AP, Kularatna N. 2009. Design Enhancements of the Smart Sediment Particle for Riverbed Transport Monitoring. *Proceedings of the 4th IEEE on Industrial Electronics and Applications*: 336-341.

Allan JC, Hart R, Tranquili JV. 2006. The use of Passive Integrated Transponder (PIT) tags to trace cobble transport in a mixed sand-and-gravel beach on the high-energy Oregon coast, USA. *Marine Geology* **232**: 63-86.

Almeida LP, Masselink G, Russell PE, Davidson MA. 2015. Observations of gravel beach dynamics during high energy wave conditions using a laser scanner. *Geomorphology* **228**: 15-27.

Anfuso G. 2005. Sediment-activation depth values for gentle and steep beaches. *Marine Geology* **220**: 101-112.

Arber MA. 1974. The Cliffs of North Devon. *Proceedings of the Geologists' Association* **85**: 147-151.

Archer WA. 2013. World's highest tides: Hypertidal coastal systems in North America, South America and Europe. *Sediment Geology* **284**: 1-25.

Austin MJ, Buscombe D. 2008. Morphological change and sediment dynamics of the beach step on a macro-tidal gravel beach. *Marine Geology* **249**: 167-183.

Austin MJ, Masselink G. 2006. Swash-groundwater interaction on a steep gravel beach. *Continental Shelf Research* **26**: 2503-2519.

Bacon S, Carter DJT. 1991. Wave climate changes in the north Atlantic and North Sea. *International Journal of Climatology* **11**: 545-558.

Bacon S, Carter DJT. 1993. A connection between mean wave height and atmospheric pressure gradient in the North Atlantic. *International Journal of Climatology* **13**: 423-436.

Backstrom JT, Jackson DWT, Cooper JAG. 2009. Shoreface morphodynamics of a high-energy, steep and geologically constrained shoreline segment in Northern Ireland. *Marine Geology* **257**: 94-106.

Bagnold RA. 1940. Beach formation by waves: some model experiments in a wave tank. *Journal of the Institute of Civil Engineers* **15**: 27-53.

Barbano MS, Pirrotta C, Gerardi F. 2010. Large boulders along the south-eastern Ionian coast of Sicily: Storm or tsunami deposits? *Marine Geology* **275**: 40-154.

Battjes JA. 1974. Computation of set-up, longshore currents, run-up and overtopping due to wind-generated waves. Report 74-2. Committee of Hydraulics, Department of Civil Engineering. Delft University of Technology, Delft, the Netherlands.

Bauer BO, Allen JR. 1995. Beach steps: an evolutionary perspective. *Marine Geology* **123**: 143-166.

Bauer BO, Lorang MS, Sherman DJ. 2001. Estimating Boat-Wake-Induced Levee Erosion using Sediment Suspension Measurements. *Journal of Waterway, Port, Coastal, and Ocean Engineering* **128(4)**: 152-162.

Beetham EP, Kench PS. 2011. Field observations of infragravity waves and their behaviour on rock shore platforms. *Earth Surface Processes and Landforms* **36**: 1872-1888.

Bertoni D, Sarti G. 2011. On the profile evolution of three artificial pebble beaches at Marina di Pisa, Italy. *Geomorphology* **130**: 244-254.

Bertoni D, Sarti G, Benelli G, Pozzebon A, Raguseo G. 2010. Radio Frequency Identification (RFID) technology applied to the definition of underwater and subaerial coarse sediment movement. *Sedimentary Geology* **229(3)**: 140-150.

Bezerra MM, Moura D, Ferreira Ó, Taborda R. 2011. Influence of Wave Action and Lithology on Sea Cliff Mass Movements in Central Algarve Coast, Portugal. *Journal of Coastal Research* **27**: 162-171.

Blair TC, McPherson JG. 1999. Grain-size and textural classification of coarse sedimentary particles. *Journal of Sedimentary Research* **69**: 6-19.

Bluck BJ. 1967. Sedimentation of beach gravels: examples from South Wales. *Journal of Sedimentary Research* **37**: 128-156.

Bluck BJ. 1999. Clast assembling, bed forms and structure in gravel beaches. *Transactions of the Royal Society of Edinburgh: Earth Sciences* **89**: 291-323.

Bluck BJ. 2011. Structure of gravel beaches and their relationship to tidal range. *Sedimentology* **58**: 994-1006.

Bouws E, Jannink D, Komen GJ. 1996. The Increasing Wave Height in the North Atlantic Ocean. *Bulletin of the American Meteorological Society* **77**: 2275-2278.

Bradley SL, Milne GA, Teferle FN. Bingley RM, Orliac EJ. 2009. Glacial isostatic adjustment of the British Isles: new constraits from GPS measurements of crustal motion. *Geophysical Journal International* **178**: 14-22.

Bruno RO, Dean RG, Gable CG. 1981. Longshore transport evaluations at a detached breakwater. *Coastal Engineering* **1980**: 1453-1475.

Bruun P, Günbak AR. 1977. Risk Criteria in Design Stability of Sloping Structures in Relation to $\xi = tan\frac{\alpha}{\sqrt{H/L_0}}$ risk criteria in design. *Coastal Engineering* **1**: 287-322.

Bryant EA, Haslett SK. 2002. Was the AD 1607 coastal flooding event in the Seven Estuary and Bristol Channel (UK) due to a tsunami? *Archaeology in the Severn Estuary* **13**: 162-167.

Buscombe D, Masselink G. 2006. Concepts in gravel beach dynamics. *Earth-Science Review* **79**: 33-52.

Caldwell JM. 1956. Wave action and sand movement near Anaheim Bay, California. U.S. Army Corps of Engineers. Beach Erosion Board. *Technical Memorandum* **68**. Washington D.C.

Carr AP. 1971. Experiments on longshore transport and sorting of pebbles: Chesil Beach, England. *Journal of Sedimentary Petrology* **41**: 1084-1104.

Carter RWG, Orford JD. 1993. The Morphodynamics of Coarse Clastic Beaches and Barriers: A Short- and Long-term Perspective. *Journal of Coastal Research* **15**: 158-179.

Chen B, Chen Z, Stephenson W, Finlayson B. 2011. Morphodynamics of a boulder beach, Putuo Island, SE China coast: The role of storms and typhoon. *Marine Geology* **283**: 106-115.

Chini N, Stansby P, Leake J, Wolf J, Roberts-Jones J, Lowe J. 2010. The impact of sea level rise and climate change on inshore wave climate: A case study for East Anglia (UK). *Coastal Engineering* **57**: 973-984.

Comber DPM, Hansom JD, Fahy FM. 1993. Taw-Torridge Estuary: Coastal Processes and Conservation. Report by the Coastal Research Group, University of Glasgow for English Nature, Peterborough 61.

Cornish V. 1898. On Sea-Beaches and Sandbanks. *The Geographical Journal* **11**: 528-543.

Curoy J, Moses CA, Robinson DA, Williams RBG. 2009. Profile evolution and active layer measurements on a macrotidal composite gravel beach, Somme Estuary, France. *Zeitschrift fuer Geomorphologie* **53**: 387-409.

Curtiss GM, Osborne PD, Horner-Devine AR. 2009. Seasonal patterns of coarse sediment transport on a mixed sand and gravel beach due to vessel wakes, wind waves, and tidal currents. *Marine Geology* **259**: 73-85.

Dean RG, Berek EP, Bodge KP, Gable CG. 1987. NSTS Measurements of Total Longshore Transport. *Proceedings of Coastal Sediments 1987, American Society of Civil Engineers*: 652-667.

Dean RG, Berek EP, Gable CG, Seymour RJ. 1982. Longshore Transport Determined by an Efficient Trap. *Proceedings of the 18th International Conference on Coastal Engineering, American Society of Civil Engineers*: 954-968.

DEFRA. 2006. Flood and coastal defence appraisal guidance. FCDPAG3 Economic Appraisal. Supplement Note to Operating Authorities – Climate change impacts.

Dickson ME, Kench PS, Kantor MS. 2011. Longshore transport of cobbles on a mixed sand and gravel beach, southern Hawke Bay, New Zealand. *Marine Geology* **287**: 31-42.

Dobkins JE, Folk RL. 1970. Shape Development on Tahiti-Nui. *Journal of Sedimentary Petrology* **40**: 1167-1203.

Dodet G, Bertin X, Taborda R. 2010. Wave climate variability in the North-East Atlantic Ocean over the last six decades. *Ocean Modelling* **31**: 120-131.

Doering JC, Bowen AJ. 1995. Parameterization of orbital velocity asymmetries of shoaling and breaking waves using bispectral analysis. *Coastal Engineering* **26**: 15-33.

Duane DB, James WR. 1980. Littoral Transport in the Surf Zone Elucidated by an Eularian Sediment Tracer Experiment: *Journal of Sedimentary Petrology* **50**: 929-942.

Duncan JR. 1964. The effects of water table and tide cycle on swash-backwash sediment distribution and beach profile development. *Marine Geology* **2**: 186-197.

Emery KO, Kuhn GG. 1982. Sea cliffs: Their processes, profiles, and classifications. *Geological Society of America Bulletin* **93**: 644-654.

Engel M, May SM. 2012. Bonaire's boulder fields revisited: evidence for Holocene tsunami impact on the Leeward Antilles. *Quaternary Science Reviews* **54**: 126-141.

Etienne S, Paris R. 2010. Boulder accumulations related to storms on the south coast of the Reykjanes Peninsula. *Geomorphology* **114**: 55-70.

Farrell EJ, Granja H, Cappietti L, Ellis JT, Li B, Sherman DJ. 2009. Wave Transformation across a Rock Platform, Belinho, Portugal. *Journal of Coastal Research* **56**: 44-48.

Ferreira Ó, Ciavola P, Taborda R, Bairros M, Dias JA. 2000. Sediment Mixing Depth Determination for Steep and Gentle Foreshores. *Journal of Coastal Research* **16**: 830-839.

Foster DL, Bowen AJ, Holman RA, Natoo P. 2006. Field evidence of pressure gradient induced incipient motion. *Journal of Geophysical Research* **111**: C05004.

Frank D, Diane F, Chou P, Kao Y, Calantoni J, Sou I. 2013. Direct Measurements of Sediment Response to Waves with “Smart Sediment Grains”. *Proceedings of 2013 Oceans*.

Gabriel S, Moura D, Jacob J, Horta J. 2013. Monitoring of waves in rocky shores: comparison between a shore platform and the adjacent pocket beach. *7th International Conference on Coastal Dynamics:* 683-694.

Gendaszek AS, Magirl CS, Konrad CP, Czuba CR, Marineau MD. 2012. Using Buried Accelerometers to Measure the Timing of Bed Movement, Scour, and Fill in Gravel-Bedded Rivers. *Proceedings of the Hydraulic Measurements and Experimental Methods Conference, Snowbird, Utah*: 12-15.

Goff J, Dudley WC, deMaintenon MJ, Cain G, Coney JP. 2006. The largest local tsunami in 20th century Hawaii. *Marine Geology* **226**: 65-79.

Goto K, Chavanich SA, Imamura F, Kunthasap P, Matsui T, Minoura K, Sugawara D, Yanagisawa H. 2007. Distribution, origin and transport process of boulders deposited by the 2004 Indian Ocean tsunami at Pakarang Cape, Thailand. *Sediment Geology* **202**: 821-837.

Goto K, Okada K, Imamura F. 2009. Characteristics and hydrodynamics of boulders transported by storm waves at Kudaka Island, Japan. *Marine Geology* **262**: 14-24.

Goto K, Kawana T, Imamura F. 2010 Historical and geological evidence of boulders deposited by tsunamis, southern Ryukyu Island, Japan. *Earth-Science Reviews* **102**: 77-99.

Halcrow. 1980. Pebble Ridge at Westward Ho! Torridge District Council.

Halcrow. 2008. North Devon and Somerset Coastal Advisory Group. Shoreline Management Plan SMP2. Hartland Point to Anchor Head.

Hattori M, Suzuki T. 1978. Field Experiment on Beach Gravel Transport. Proceedings of the 16th international Conference on Coastal Engineering. *American Society of Civil Engineers*: 1688-1704.

Hemer MA, Katzfey J, Trenham CE. 2013. Global dynamical projections of surface ocean wave climate for a future high greenhouse gas emission scenario. *Ocean Modelling* **70**: 221-245.

Hofmann MH, Hendrix MS. 2010. Depositional processes and the inferred history of ice-margin retreat associated with the deglaciation of the Cordilleran Ice Sheet: The sedimentary record from Flathead Lake, northwest Montana, USA. *Sediment Geology* **223**: 61-74.

Holman RA. 1986. Extreme value statistics for wave run-up on a natural beach. *Coastal Engineering* **9**: 527-544.

Holman RA, Guza RT. 1984. Measuring run-up on a natural beach. *Coastal Engineering* **8**: 129-140.

Hsu TW, Liang SJ, Young BD, Ou SH. 2012. Nonlinear run-ups of regular waves on sloping structures. *Natural Hazards and Earth System Sciences* **12**: 3811-3820.

Hudson RY. 1953. Wave forces on breakwaters. *Transactions of the American Society of Engineers* **118**: 653-685.

Hughes MG. 1995. Friction Factors for Wave Uprush. *Journal of Coastal Research* **11**: 1089-1098.

Hughes SA. 2004. Estimation of wave run-up on smooth, impermeable slopes using the wave momentum flux parameter. *Coastal Engineering* **51**: 1085-1104.

Hughes MG, Cowell PJ. 1987. Adjustment of Reflective Beaches to Waves. *Journal of Coastal Research* **3**: 153-167.

Hunt IA. 1959. Design of seawalls and breakwaters. *Transaction of the American Society of Civil Engineers* **85**: 123-152.

Iribarren R. 1938. Una formula para el calculo de los disques de escollera. Revista deObras Publicas, Madrid (A Formula for the Calculation of Rock-Fill Dykes, Translated by D. Heinrick, University of California, Department of Engineering T.R.-He-116-295 Berkely, 1948).

Iribarren R, Nogales Y Olano C. 1950. Generalizacion de la formula para el calculo de los diques de escollera y comprobacion de sus coefficients, Revista de Obras Publicas, Madrid, Spain.

Inman DL, Zampol JA, White TE, Hanes DM, Waldorf BW, Kastens KA. 1970. Field Measurements of Sand Motion in the Surf Zone. *Coastal Engineering* **1980**: 1215-1234.

Isla FI. 1993. Overpassing and armouring phenomena on gravel beaches. *Marine Geology* **110**: 369-376.

IPCC, 2007: Climate Change 2007: Impacts, Adaptation and Vulnerability. Contribution of Working Group II to the Fourth Assessment Report of the Intergovernmental Panel on Climate Change. [Editors: Parry ML, Canziani OF, Palutikof JP, van der Linden PJ, Hanson CE]. Cambridge University Press, Cambridge, UK.

IPCC, 2014: Coastal system and low-lying areas. In Climate Change 2014: Impacts, Adaptation, and Vulnerability. Part A: Global and Sectoral Aspects. Contributions of Working Group II to the Fifth Assessment Report of the Intergovernmental Panel on Climate Change [Editors: Field CB, Barros VR, Dokken DJ, Mach KJ, Mastrandrea MD, Bilir TE, Chatterjee KL, Ebi YO, Estrada RC, Genova B, Girma B, Kissel ES, Levy AN, MacCracken S, Mastrandrea PR, White LL.] Cambridge University Press, Cambridge, UK and New York, USA. 361-409.

Jamal MH, Simmonds DJ, Magar V. 2014. Modelling gravel beach dynamics with XBeach. *Coastal Engineering* **89**: 20-29.

Jackson DWT, Cooper JAG, del Rio L. 2005. Geological control of beach morphodynamic state. *Marine Geology* **216**: 297-314.

Jackson DWT, Cooper JAG. 2009. Geological Control on Beach Form: Accommodation Space and Contemporary Dynamics. *Journal of Coastal Research* **56**: 69-72.

Jackson NL, Nordstrom KF. 1993. Depth of activation of sediment by plunging breakers on a steep sandy beach. *Marine Geology* **115**: 143-151.

Johnston MR. 2001. Nelson Boulder Bank, New Zealand. *New Zealand Journal of Geology & Geophysics* **44**: 79-88.

Kamphuis JW. 1990. Alongshore Sediment Transport Rate. *Proceedings of the 22nd International Conference on Coastal Engineering: American Society of Civil Engineers*: 2402-2415.

Keene P. 1996. Classic Landforms of the North Devon Coast. The Geographical Association. Sheffield, UK.

Kennedy DM, Milkins J. 2014. The formation of beaches on shore platforms in micro-tidal environments. *Earth Surface Processes and Landforms* 2014.

King CAM. 1951. Depth of disturbance of sand on sea beaches by waves. *Journal of Sedimentary Petrology* **21(3)**: 131-140.

Kirby R. 1996. Hartland point to Brean Down: Summary of existing knowledge of coastal trends and stability. Ravensrodd Consultants.

Kirk RM. 1977. Rates and forms of erosion on intertidal platforms at Kaikoura Peninsula, South Island, New Zealand. *New Zealand Journal of Geology and Geophysics* **20**: 571-613.

Komar PD. 1997. *Beach Processes and Sedimentation*: Second Edition. Prentice Hall, New Jersey.

Komar PD, Inman D. 1970. Longshore sand transport on beaches. *Journal of Geophysical Research* **75**: 5514-5527.

Krumbein WC, Monk GD. 1943. Permeability as a Function of the Size Parameters of Unconsolidated Sand. *Transactions of the American Institute of Mining Engineers: Society of Petroleum Engineers* **151**.

Kuo CT, Kuo ST. 1974. Effect of wave breaking on statistical distribution of wave heights. *Proceedings of the Conference on Civil Engineering in the Oceans* **3**: 1211-1231.

Kushnir Y, Cardone VJ, Greenwood JG, Cane MA. 1997. The Recent Increase in North Atlantic Wave Heights. *Journal of Climate* **10**: 2107-2113.

LaFave JI, Smith LN, Patton TW. 2004. Ground-Water Resources of the Flathead Lake Area: Flathead, Lake, Missoula, and Sanders Counties, Montana. Part A – Descriptive Overview abd Water-Quality Data. Montana Ground-Water Assessment Atlas 2. Montana Bureau of Mines and Geology. 1-132. Billings, Montana, USA.

Lee K, Mizutani N, Hur D, Kamiya A. 2007a. The effect of groundwater on topographic changes in a gravel beach. *Ocean Engineering* **34**: 605-615.

Lee MWE, Sear DA, Atkinson PM, Collins MB, Oakey RJ. 2007b. Number of tracers required for the measurement of longshore transport distance on a shingle beach. *Marine Geology* **240**: 57-63.

Longuet-Higgins MS. 1952. On the statistical distributions of the heights of sea waves. *Journal of Marine Research* **9(3)**: 245-266.

Longuet-Higgins MS. 1970. Longshore Currents Generated by Obliquely Incident Sea Waves, 1. *Journal of Geophysical Research* **75(33)**: 6778-6789.

Lorang MS. 2000. Predicting threshold mass and stable boulder mass for a beach. *Journal of Coastal Research* **16**: 432-445.

Lorang MS. 2002. Predicting the crest height of a gravel beach. *Geomorphology* **48**: 87-101.

Lorang MS. 2011. A Wave-competence approach to distinguish between boulder and megaclasts deposits due to storm waves versus tsunamis. *Marine Geology* **283**: 90-97.

Lorang S, Komar PD. 1990. Pebble Shape. *Nature* **347**: 433-434.

Lorang MS, Stanford JA, Hauer FR. 1993a. Dissipative and Reflective Beaches in a Large Lake and the Physical Effects of Lake Level Regulation. *Ocean & Coastal Management* **19**: 263-287.

Lorang MS, Komar PD, Stanford JA. 1993b. Lake Level Regulation and Shoreline Erosion on Flathead Lake, Montana: A Response to the Redistribution of Annual Wave Energy. *Journal of Coastal Research* **9**: 494-508.

Lorang MS, Stanford JA. 1993. Variability of shoreline erosion and accretion within a beach compartment of Flathead Lake, Montana. *Limnology and Oceanography* **38(8)**: 1783-1795.

Madsen OS. 1974. Stability of a sand bed under breaking waves. *Proceedings of 14th Conference on Coastal Engineering*: 776-794.

MacDonald NJ, O'Connor BA. 1996. Changes in wave impact on the Flemish coast due to increased mean sea level. *Journal of Marine Systems* **7**: 133-144.

Maniatis G, Hoey T, Sventek J. 2013. A New Method for Rapid Prototyping of Purpose-Specific Sensor Enclosures: Example Application and Implications for Data Coherence. *Journal of Sensor and Actuator Networks* **2**: 761-779.

Maouche S, Morhange C, Meghraoui M. 2009. Large boulder accumulation on the Algerian coast evidence tsunami events in the western Mediterranean. *Marine Geology* **262**: 96-104.

Marshall RJE, Stephenson WJ. 2011. The morphodynamics of shore platforms in a micro-tidal setting: Interactions between waves and morphology. *Marine Geology* **288**: 18-31.

Masselink G, Russell P, Blenkinsopp C, Turner I. 2010. Swash zone sediment transport, step dynamics and morphological response on a gravel beach. *Marine Geology* **274**: 50-68.

Masselink G, Li L. 2001. The role of swash infiltration in determining the beach face gradient: a numerical study. *Marine Geology* **176**: 139-156.

Mastronuzzi G, Sansò P. 2004. Large boulder accumulations by extreme waves along the Adriatic coast of southern Apulia (Italy). *Quaternary International* **120**: 173-184.

Matias A, Williams JJ, Masselink G, Ferreira Ó. 2012. Overwash threshold for gravel barriers. *Coastal Engineering* **63**: 48-61.

May VJ. 2007. Westward Ho! Cobble Ridge. *Coastal Geomorphology of Great Britain* **28**: 1-6.

May CL, Pryor BS. 2014. Initial Motion and Bedload Transport Distance Determined by Particle Tracking in a Large Regulated River. *River Research and Applications* **30**: 508-520.

McNamara JP, Borden C. 2004. Observations on the movement of coarse gravel using implanted motion-sensing radio transmitters. *Hydrological Processes* **18**: 1871-1884.

Miller IM, Warrick JA, Morgan C. 2011. Observations of coarse sediment movements on the mixed beach of the Elwha Delta, Washington. *Marine Geology* **282**: 201-214.

Moore GW, Cole JY. 1960. Coastal processes in the vicinity of Cape Thompson, Alaska: Geologic Investigations in Support of Project Chariot in the Vicinity of Cape Thompson, Northwestern Alaska – Preliminary Report. [Editors: Kachadoorian R, Campbell RH, Moore GW, Cole JY, Lachenbruch AH, Greene GW, Barnes DF, Waller RM, Lamar WL, Slaughter MJ]. U.S. Geological Survey Trace Elements Investigation Report 753: 41-55.

Nandasena NAK, Paris R, Tanaka N. 2011. Reassessment of hydrodynamic equations: Minimum flow velocity to initiate boulder transport by high energy events (storms, tsunamis). *Marine Geology* **281**: 70-84.

Nandasena NAK, Tanaka N, Sasaki Y, Osada M. 2013. Boulder transport by the 2011 Great East Japan tsunami: Comprehensive field observations and whither model preditions? *Marine Geology* **346**: 292-309.

Naylor LA, Rodrigues BA, Tancock D, Brady A. 2010. Boulder Dynamics: Research to understand boulder transport pathways and supply to Northam Pebble Ridge. Pilot Study Results and Recommendations.

Naylor LA, Stephenson WJ, Trenhaile AS. 2010. Rock coast geomorphology: Recent advances and future research directions. *Geomorphology* **114**: 3-11.

Nicholls RJ. 1989. The Measurement of the Depth of Disturbance Caused by Waves on Pebble Beaches. *Journal of Sedimentary Research* **59**: 630-631.

Nicholls RJ, Wright P. 1991. Longshore transport of pebbles: experimental estimates of K. *Proceedings of the Conference on Coastal Sediments 1991*: *American Society of Civil Engineers*: 920-933.

Noormets R, Felton EA, Crook KAW. 2002. Sedimentology of rocky shorelines: 2. Shoreline megaclasts on the north shore of Oahu, Hawaii - origins and history. *Sedimentary Geology* **150**: 31-45.

Nott J. 2003a. Waves, coastal boulder deposits and the importance of the pre-transport setting. *Earth and Planetary Science Letters* **210**: 269–276.

Nott J. 2003b. Tsunami or storm waves? - determining the origin of a spectacular field of wave emplaced boulders using numerical storm surge and wave models and hydrodynamic transport equations. *Journal of Coastal Research* **19**: 348–356.

Oak HL. 1984. The Boulder Beach: A Fundamentally Distinct Sedimentary Assemblage. *Annals of the Association of American Geographers* **74**: 71-82.

Oak HL. 1986. Process inference from coastal-protection structures to boulder beaches. *Geografiska Annaler* **68A**: 25-31.

Ogawa H. 2013. Observation of wave transformation on a sloping type B shore platform under wind-wave and swell conditions. *Geo-Marine Letters* **33**: 1-11.

Ogawa H, Dickson ME, Kench PS. 2011. Wave transformations on a sub-horizontal shore platform, Tatapouri, North Island, New Zealand. *Continental Shelf Research* **31**: 1409-1419.

Ogawa H, Kench P, Dickson M. 2012. Field Measurements of Wave Characteristics on a Near-Horizontal Shore Platform, Mahia Peninsula, North Island, New Zealand. *Geographical Research* **50**: 179-192.

Orford JD. 1975. Discrimination of particle zonation on a pebble beach. *Sedimentology* **22**: 441-463.

Orford J. 2005. Further Geomorphological Advice in respect of Westward Ho! SSSI. Geomorphological & Shoreline Management Advice Contract (2003). English Nature.

Orford JD, Forbes DL, Jennings SC. 2002. Organisational controls, typologies and timescales of paraglacial gravel-dominated coastal systems. *Geomorphology* **48**: 51-85.

Orford JD, Anthony EJ. 2011. Extreme events and the morphodynamics of gravel-dominated coastal barriers: Strengthening uncertain ground. *Marine Geology* **290**: 41-45.

Osborne PD. 2005. Transport of gravel and cobble on a mixed-sediment inner bank shoreline of a large inlet, Grays Harbor, Washington. *Marine Geology* **224**: 145-156.

Packwood AR. 1983. The influence of beach porosity on wave uprush and backwash. *Coastal Engineering* **7**: 29-40.

Paris R, Fournier J, Poizot E, Etienne S, Morin J, Lavigne F, Wassmer P. 2010. Boulder and fine sediment transport and deposition by the 2004 tsunami in Lhok Nga (western Banda Aceh, Sumatra, Indonesia): A coupled offshore-onshore model. *Marine Geology* **268**: 43-54.

Paris R, Naylor LA, Stephenson WJ. 2011. Boulders as a signature of storms on rock coasts. *Marine Geology* **283**: 1-11.

Pawlowicz R, Beardsley B, Lentz S. 2002. Classical tidal harmonic analysis including error estimates in MATLAB using T_TIDE. *Computers and Geosciences* **28**: 929-937.

Pedrozo-Acuña A, Simmonds DJ, Reeve DE. 2008. Wave-impact characteristics of plunging breakers acting on gravel beaches. *Marine Geology* **253**: 26-35.

Pedrozo-Acuña A, Torres-Freyermuth A, Zou Q, Hsu T, Reeve DE. 2010. Diagnostic investigation of impulsive pressures induced by plunging breakers impinging on gravel beaches. *Coastal Engineering* **57**: 252-266.

Pethick J. 2007. The Taw-Torridge Estuaries: Geomorphology and Management. Report to Taw-Torridge Estuaries Officers Group. Internal report for North Devon's Biosphere Reserve.

Poate T, Masselink G, Davidson M, McCall R, Russell P, Turner I. 2013. High frequency in-situ field measurements of morphological response on a fine gravel beach during energetic wave conditions. *Marine Geology* **342**: 1-13.

Puleo JA, Beach RA, Holman RA, Allen JS. 2000. Swash zone sediment suspension and transport and the importance of bore-generated turbulence. *Journal of Geophysical Research* **105**: 17021-17044.

Reeds Nautical Almanac. 2003. A & C black publishers Ltd. London

Rodwell MJ, Rowell DP, Folland CK. 1999. Oceanic forcing of the wintertime North Atlantic Oscillation and European climate. *Letters to Nature* **398**: 320-323.

Ruiz de Alegria-Arzaburu A, Masselink G. 2010. Storm response and beach rotation on a gravel beach, Slapton Sands, U.K. *Marine Geology* **278**: 77-99.

Sallenger AH, Holman RA. 1985. Wave Energy Saturation on a Natural Beach of Variable Slope. *Journal of Geophysical Research* **90**: 11939-11944.

Sear DA, Lee MWE, Oakey RJ, Carling PA, Collins MB. 2000. Coarse sediment tracing technology in littoral and fluvial environments: a review. In: Tracers in Geomorphology.[Editors: Foster IDL]. John Wiley and Sons Ltd, Chinchester, England, 21–55.

Sherman DJ, Nordstrom KF. 1985. Beach Scarps. *Zeitschrift für Geomorphologie* **29**: 139-152.

Shields A. 1936. Anwendung der Aehnlichkeitsmechanik und der Turbulenzforschung auf die Geschiebebewegung (Application of similarity mechanics and turbulence research to bead load movement). Mitteilungen der Preußishchen Versuchsanstalt für Wasserbau (in English) 26. Berlin: Preußische Versuchsanstalt für Wasserbau.

Shoonees JS, Theron AK. 1991. Review of the field-data base for longshore sediment transport. *Coastal Engineering* **19**: 1-25.

Slade GO. 1962. Westward Ho! Pebbleridge. The Surveyor. June 1962: 812-814.

Sleath JFA. 1999. Conditions for Plug Formation in Oscillatory Flow. *Continental Shelf Research* **19**: 1643-1664.

Soward KS. 1965. Geology of Damsites on Flathead River Mouth to Flathead Lake Lake and Sanders Counties Montana. Geological Survey Water-Supply Paper 1550. U.S. Government Printing Office, Washington, D.C. 1-89.

Spazzapan M, Petrovčič J, Mikoš M. 2004. A New Tracer for Monitoring Dynamics of Sediment Transport in Turbulent Flows. *Acta Hydrotechnica* **22/37**: 135-148.

Stephenson WJ, Naylor LA. 2011. Geological controls on boulder production in a rock coast setting: Insights from South Wales, UK. *Marine Geology* **283**: 12-24.

Stuart A, Hookway RJS. 1954. Coastal Erosion at Westward Ho!. Report to the Coast Protection Committee (Special), Devon County Council, 13.

Sunamura T. 1992. Geomorphology of Rocky Coasts. Wiley, New York. 302.

Sunamura T, Kraus NC. 1984. Prediction of average mixing depth of sediment in the surf zone. *Marine Geology* **62**: 1-12.

Switzer AD, Burston JM. 2010. Competing mechanisms for boulder deposition on the southeast Australian coast. *Geomorphology* **114**: 42-54.

Thornton EB, Guza RT. 1983. Transformation of Wave Height Distribution. *Journal of Geophysical Research* **88**: 5925-5938.

Tremblay M, Marquis GA, Roy AG. 2010. A New Method for Tracking Individual Particles During Bed Load Transport in a Gravel-Bed River. *American Geophysical Union, Fall Meeting 2010*.

Trenhaile AS. 1987. Rock The Geomorphology of Rock Coasts. Clarendon Press, Oxford, UK.

UKCP09, 2009: Sea level change estimates. [Editors: Millin S]. Met Office, UK.

U.S. Army Corps of engineers, Shore Protection Manual (SPM). 1984. 4th ed. 2 vols. Coastal Engineering Research Center, Water-ways Experiment Station, Vicksburg, Mississippi. Government. Printing Office, Washington, D.C.

Van der Meer JW, Stam CM. 1992. Wave Runup on Smooth and Rock slopes. *Journal of Waterways, Ports, Coastal, and Ocean Engineering* **188**: 534-550.

Van Wellen E, Chadwick AJ, Mason T. 2000. A review and assessment of longshore sediment transport equations for coarse-grained beaches. *Coastal Engineering* **40**: 243-275.

Wang H. 1974 Synthesis of Breakwater Design and Design Review Procedures: Ocean Engineering Report Number 1. Department of Civil Engineering, University of Delaware, Newark, Delaware, US.

Wang XL, Zweirs FW, Swail VR. 2003. North Atlantic Ocean Wave Climate Change Scenarios for the Twenty-First Century. *Journal of Climate* **17**: 2368-2383.

Watts GM. 1953. A study of sand movement at South Lake Worth inlet, Florida. U.S. Army, Beach Erosion Board. Technical Memorandum 42: 24.

Weiss R. 2012. The mystery of boulders moved by tsunamis and storms. *Marine Geology* **295-298**: 28-33.

Weiss R, von Storch H, Feser F. 2005. Northeast Atlantic and North Sea Storminess as Simulated by a Regional Climate Model during 1958-2001 and Comparison with Observations. *Journal of Climate* **18**: 465-479.

Williams DM, Hall AM. 2004. Cliff-top megaclasts deposits of Ireland, a record of extreme waves in the North Atlantic – storms or tsunamis? *Marine Geology* **206**: 101-117.

Williams JJ, Ruiz de Alegria-Arzaburu A, McCall RT, Dongeren AV. 2012. Modelling gravel barrier profile response to combined wave and tides using XBeach: Laboratory and field experiments. *Coastal Engineering* **63**: 62-80.

Wolf J, Woolf DK. 2006. Waves and climate change in the north-east Atlantic. *Geophysical Research Letters* **33**: 1-4.

Wolman MG. 1954. A Method of Sampling Coarse River-Bed Material. *Transactions of the American Geophysical Union* **35(6)**: 951-956.

Young IR, Zieger S, Babanin AV. 2011. Global Trends in Wind Speed and Wave Height. *Science* **332**: 451-455.

Zingg T. 1935. Beiträge zur Schotteranalyse. *Schweizerische Mineralogische und Petrographische Mitteilungen* **15**: 39-140.